Evaporatively Cooled Atomic Hydrogen

Investigated by

One- and Two-Photon Optical Methods

ACADEMISCH PROEFSCHRIFT

ter verkrijging van de graad van doctor
aan de Universiteit van Amsterdam,
op gezag van de Rector Magnificus
prof.dr. J.J.M. Franse
ten overstaan van een door het college van dekanen
ingestelde commissie in het openbaar te verdedigen
in de Aula der Universiteit
op maandag 22 december 1997 te 9.00 uur

door

Pepijn Willemszn Harry Pinkse

geboren te Nieuwerkerk aan den IJssel

Promotor:	prof. dr. J.T.M. Walraven
Co-promotor:	dr. T.W. Hijmans
Commissie:	prof. dr. A. Lagendijk
	prof. dr. ir. H.B. van Linden van den Heuvell
	prof. dr. W. Hogervorst
	prof. dr. B.J. Verhaar
	prof. dr. H.G. Muller

Faculteit der wiskunde, informatica, natuur- en sterrenkunde

The work described in this thesis was part of the research program of the
Stichting voor Fundamenteel Onderzoek der Materie (FOM),
which is financially supported by the
Nederlandse Organisatie voor Wetenschappelijk Onderzoek (NWO)
and was carried out at the

Van der Waals-Zeeman Instituut
Universiteit van Amsterdam
Valckenierstraat 65
1018 XE Amsterdam
The Netherlands

Contents

Chapter 1

Introduction

1.1 Trapped atomic hydrogen

In the field of cold atomic gases, atomic hydrogen (H) holds a unique position. H is the simplest of all elements and its properties are well documented[1, 2]. Presently, the H-maser is the most stable short-term time base. Unlike other atomic systems, H can be stored as a cryogenic gas in a container if the walls are covered by liquid helium, due to the extremely low binding energy of H on liquid helium. By thermalizing with these walls, H can be cooled to sub-Kelvin temperatures, as was first demonstrated by Silvera and Walraven in 1980[3]. If the recombination of the H atoms to H_2 molecules is suppressed, H is a stable gas.

Historically, one of the main goals after the stabilization of atomic H was the creation of the conditions where Bose-Einstein condensation (BEC) is expected to occur. BEC is a purely quantum-statistical phase transition that occurs when the average distance between two atoms is less than their thermal De Broglie wavelength, which expresses the quantum-mechanical uncertainty in the position of the atoms. This requires a high density of sufficiently cold particles, such that the density in the 6-dimensional phase space (3 momentum and 3 spatial coordinates) exceeds a critical density. London suggested a relation between the phenomenon of BEC and the occurrence of superfluidity in liquid helium (^{4}He)[4].

BEC in a weakly interacting gas has been observed only recently, not in atomic H but in cold vapors of alkali atoms. In contrast to atomic H, where cryogenic methods are used, cooling of alkali gases relies on optical methods[5]. Optical cooling has progressed enormously in the last decade and is now a major field of research[6]. However, most optical methods fail at very low temperatures when the average kinetic energy of the atoms is comparable with the energy an atoms receives from the recoil of a photon emission. Therefore, in order to reach "sub-recoil" temperatures, non-optical methods, developed for H, were employed in experiments with cold alkali gases, culminating in 1995 by the observation of BEC in dense and cold rubidium, sodium and lithium vapors[7].

In magnetic compression experiments with spin-down polarized H (H$\downarrow$, i.e., electron spin antiparallel to the magnetic field) phase-space densities were reached that fell short approximately one order of magnitude from BEC[8]. In the compression experiments with atomic H$\downarrow$, the dominant decay mechanism was found to be three-body recombination on the surface of the liquid helium. Because this recombination scales with the third power of the density, it is thought to be very hard, if not impossible, to reach BEC by compression of H$\downarrow$ in contact with a surface of liquid helium.

To eliminate the surface-induced decay channel altogether, at the end of the 1980's the quest for BEC concentrated on spin-up polarized H (H$\uparrow$, i.e., electron spin parallel to the magnetic field). Though H$\uparrow$ is not as stable as H$\downarrow$, it has the advantage that it can be trapped in a magnetic field minimum. Such wall-free confinement of H$\uparrow$ was first realized by Hess *et al.*[9] and shortly afterwards in Amsterdam by van Roijen *et al.*[10, 11].

Optical methods have also been employed in the research of trapped atomic H. In the early experiments with trapped H$\uparrow$ the diagnostics was based on monitoring the flux of atoms leaving the trap. In Amsterdam, optical diagnostics was developped in the framework of the thesis of Luiten[12, 13]. Using narrow-band ultraviolet light, Lyman-α (L_α, wavelength $\lambda_L = 121.57\,nm$, resonant with the $1S - 2P$ transition in H), the trapped H$\uparrow$ could be studied *in situ*. The absorption spectra contain information about the spatial distribution because of Zeeman shifts, and the velocity distribution is reflected in the Doppler broadening of the resonance lines. By comparing L_α absorption spectra with those calculated from the differential equations describing the light propagation through the non-uniform gas[14, 12], L_α spectroscopy allows non-destructive determination of temperature and density with high sensitivity down to temperatures around 1 mK, where the Doppler broadening becomes comparable to the $2P$ natural line width. Moreover, optical detection discriminates between H$\uparrow$ and H$\downarrow$, and, due to the isotope shift, between ^{1}H and ^{2}H (deuterium, D); even the hyperfine composition of the gas can directly be obtained from the spectrum. Another optical diagnostic tool was developed at MIT. In 1996 the MIT group was able to observe magnetically trapped atomic H down to temperatures of 0.15 mK, using the $1S - 2S$ two-photon transition[15].

Using L_α spectroscopy as a diagnostic tool, Luiten made the first *in situ* measurements of evaporative cooling[12]. Evaporative cooling, first demonstrated in 1987 with H$\uparrow$ by Hess[9], relies on the preferential removal of atoms with energies higher than the average thermal energy, cooling the remaining gas. Thus far, evaporative cooling is the only technique capable of boosting the phase-space density towards values needed for BEC[16]. In atomic H, it pushed the attained phase-space density up to within one order of magnitude of the critical density for BEC[17]. The theoretical description of the evaporation process was investigated by Luiten *et al.*, using a model based on the assumption of a truncated Boltzmann distribution, which was put on solid ground by numerical solution of the Boltzmann equation[14].

In a subsequent series of trapping experiments in Amsterdam, the L_α source needed for the

optical detection of H was used for optical cooling of the trapped H↑ gas. In order to reduce the velocities in all three dimensions, optical cooling of a Knudsen gas requires at least four laser beams. In contrast, in the dense H samples one can rely on the thermalizing effect of the interatomic collisions to cool the H gas by irradiating it with a single beam of L_α, as was demonstrated in the thesis work of Setija[18]. In addition, Setija *et al.* combined evaporative cooling with optical pumping in a new optical cooling method: light-induced evaporation (LIE)[19, 18]. The pumping relies on the excitation of atomic levels with spontaneous decay to non-trapped H↓ states, effectively removing these atoms from the trap. Using this method, conditions were reached that were approximately four orders of magnitude away from the critical phase-space density for BEC. Insufficient diagnostics prohibited the observation of samples at lower temperatures. However, as was argued by Setija[18], the relatively large L_α photon-recoil on atomic H probably prevents reaching BEC with LIE.

The limitations of the diagnostics encountered by Setija also hindered the first attempts made in the framework of the present thesis to increase phase-space densities by evaporative cooling. They were pinned down to two causes. First, the L_α beam waist at the sample position was much bigger than the sample size, which reduces the ratio of the absorbed to the total light flux at low temperatures, when the sample is concentrated in a small region around the trap center. Second, the temperature sensitivity of L_α spectroscopy decreases around 2 mK, where the Doppler and the Zeeman shifts become of the same order as the spectral bandwidth of the L_α source and the radiative line width of the $2P$ state. The L_α beam waist and the bandwidth of the L_α source are mere technical issues, but the natural line width seems, at first sight, impossible to circumvent. The solution of these problems is a main part of this thesis, as will be addressed in the next section.

1.2 This thesis

The main goal of the work described in this thesis was the increase of the phase-space density of the trapped H. To achieve this, evaporative cooling over a magnetic barrier was implemented, studied, and optimized. In parallel, the diagnostics of the trapped gas had to be improved. On the technical side, this required major improvements on the optical apparatus. A more fundamental issue was the development of a two-photon method to overcome the intrinsic limitation of the L_α spectroscopy due to the large bandwidth of the $2P$ state.

The waist of the L_α beam was reduced by the construction of a new gas cell, where L_α is produced as the third harmonic of pulsed ultraviolet (UV) light at 364.8 nm, and the construction of a new monochromator, which separates the weak L_α from the much stronger UV background light. With these improvements, described in chapter 3, narrow L_α beams of a radius of ~ 0.1 mm could be made in a reliable way. The overlap of the narrow light beam and the H sample in the cryogenic cell required the improvement of several elements of the

apparatus. The optical access to the cryogenic cell was improved to allow the use of a sensitive room-temperature detector. The improvements made to the optical system allowed the determination of temperatures down to $\sim 0.5\,\mathrm{mK}$, almost an order of magnitude lower with respect to the work of Setija *et al.*[18].

The improved apparatus does not circumvent the limitation of the L_α spectroscopy associated with the broad natural line width of the $2P$ state. To overcome this intrinsic limitation of L_α spectroscopy, we developed resonance enhanced two-photon spectroscopy (RETS) [20], which is described in detail in chapter 5 of this thesis. RETS is based on the $1S - 3S$ or $1S - 3D$ transition via the near-resonant intermediate state $2P$ by stacking two co-propagating photons, one close to L_α, and one close to Balmer-α (H_α, with wavelength 656.47 nm). For the experiments on RETS, high-power tunable H_α light had to be generated and combined with the L_α light. It turned out that the overlap with the L_α beam was a critical issue for success of the experiment and required special attention. RETS provides high sensitivity due to the resonant enhancement of the transition matrix element by the $2P$ intermediate level. At present the resolution of our method is limited by our L_α source bandwidth ($120 - 150\,\mathrm{MHz}$), but ultimately the resolution is only limited by the lifetime of the $3S$ level (160 ns) and $3D$ level (16 ns), which are much longer than the $2P$ lifetime (1.6 ns).

In order to increase the phase-space density of the trapped H we applied evaporative cooling by removing hot particles over a magnetic barrier in the longitudinal direction of the trap. It turned out that this way of evaporative cooling is not as effective as expected on the basis of "ergodic" single-particle motion. The term "ergodic motion" is used here to indicate the situation where all points in phase space with the same energy are sampled with equal probability. In the case of evaporative cooling under ergodic conditions, all atoms with a total energy exceeding a given energy, the escape energy, are lost. This situation is referred to as "3-dimensional (3D) evaporation". In axisymmetric potentials where the Hamiltonian separates in a longitudinal and a radial part, the single-particle motion is not ergodic. If the escape mechanism only selects on longitudinal energy, the situation is referred to as "1-dimensional (1D) evaporation", which is a less effective process than 3D evaporation. In our experiments, there is an escape route for energetic atoms over a saddle-point in the magnetic trapping potential in a single direction only. It turns out that the evaporation process in our trap is better described by a 1D than a 3D evaporation model. Armed with this information, we were able to optimize the evaporative cooling trajectories assuming 1D evaporation, resulting in a phase-space density only a factor 50 short of the quantum degenerate regime. The analysis of evaporative cooling and the experimental results are described in chapter 7.

In pursuit of BEC, evaporative cooling is a very powerful tool to increase the phase-space density of a trapped gas with orders of magnitude. But it is also an inherently irreversible method, since it is based on the escape of particles. It would be very valuable to take profit of the adiabatic conditions in such an isolated system as a trapped gas and study, e.g., condensate

formation and destruction with a fixed number of particles, under reversible conditions. Hereto only small changes of the phase-space density are required. However, most adiabatic changes to the trapping potential do not change the phase-space density of a trapped gas. This holds, for example, for cooling by adiabatic expansion of a harmonic trap. The improved accuracy of the spectroscopic thermometry turned out to be very valuable in the demonstration of the fact that the phase-space density is *not* a conserved quantity in reversible adiabatic changes of the *shape* of the potential. Interestingly, this point has escaped attention in the literature[21]. As explained in chapter 6, shape is here related to the exponent in the relation between the potential energy and the spatial coordinates of the trap. For harmonic potentials $U_p \propto r$ and for a harmonic potential $U_p \propto r^2$, with r the distance to the center of the trap.

In the work described in this thesis, the range of attained phase-space densities was increased by two orders of magnitude with respect to the work of Setija *et al.*. This was made possible by significant improvements on the diagnostics and by theoretical and experimental study of evaporative cooling over a magnetic barrier, revealing that this was bottlenecked by the details of the escape mechanism. Moreover, it was demonstrated that the phase-space density of a trapped gas can be changed in a reversible adiabatic way. Resonance enhanced two-photon spectroscopy was developed for the study of cold atomic H. RETS overcomes the intrinsic limitations of L_α spectroscopy. The reduction of the L_α source bandwidth, also essential for the application of the two-photon method in trapped H at sub-millikelvin temperatures, is a technical issue yet to be solved. However, the intrinsic resolution of RETS is only limited by the natural line width of the $3S$ (1 MHz) and the $3D$ level (10 MHz).

1.2.1 Outline

The thesis starts with a general introduction to the basics of H trapping. Trapping geometries are discussed, including the Ioffe configuration used in the experiments described in this thesis. Details about loading the trap are given here. Part of the trapping basics is an introduction about the density distribution of the gas in the trap. Familiar quantities as the "temperature" and "volume" need a careful introduction in inhomogeneous trapping potentials, especially if the trap is of finite depth. The quantities introduced in this section provide the building blocks for the description of decay processes in the trap and evaporation out of the trap and are used in the subsequent chapters.

Chapter 3 deals with the experimental setup. The optical and cryogenic apparatus is described in detail, with focus on the improvements made since thesis work of Van Roijen[11], Luiten[12, 14], and Setija[18]. Here the improvements of the L_α beam quality needed for more accurate spectroscopy are explained, as well as the setup to generate and stabilize the H_α. The improvements on the cryogenic cell and the cryostat for the RETS experiments are discussed.

Chapter 4 is an intermezzo in which decay processes that limit the lifetime of a magnetically

trapped H↑ are discussed, both theoretically and experimentally. A large part of this chapter deals with the sample loss found in traps with a zero-magnetic-field region, where the magnetic moment of a passing atom cannot follow the rapid changes in the magnetic-field direction, causing so-called Majorana spin flips leading to loss from the magnetic trap. In traps of the Ioffe type Majorana decay is normally completely negligible. However, for some experiments it can be useful to reduce the magnetic field to values where Majorana decay becomes important. This situation is analyzed and compared with the experiment.

Chapter 5 is devoted to L_α spectroscopy and RETS of magnetically trapped atomic H. This includes a discussion of energy levels in the presence of an external magnetic field and the strength of the relevant one- and two-photon transitions. The line shifts near the simultaneous resonance of both a one- and a two-photon line is illustrated by the observation of an "Autler-Townes doublet" in the RETS spectrum of H. The line shapes and various broadening mechanisms are explained and the equations that form the basis of the spectrum calculation are discussed. To demonstrate its potential, RETS spectra taken from a single H sample during evaporative cooling are analyzed.

Chapter 6 deals with adiabatically changes of the phase-space density of trapped gases. Theory relating the phase-space density to trap changes, both in the Boltzmann regime and in the degenerate Bose regime is presented. The effect is experimentally verified by observing the phase-space density in a trapped gas of atomic H and changing the shape of the potential.

In chapter 7 theory and experiments on evaporative cooling are discussed. It is explained how the efficiency of evaporative cooling is bottlenecked by the low dimensionality of the escape mechanism for the evaporating particles. With this knowledge an optimized trajectory through phase space was calculated assuming 1D evaporation. The data of an experiment based on this optimized trajectory are in qualitative agreement with the model.

Chapter 6 and 7 are reproductions of the articles [22] and [23], respectively. Therefore, some overlap with the rest of the thesis is unavoidable. On the other hand, this has the advantage that these chapters can be read more or less independently from the rest of the thesis.

1.3 Outlook

In chapter 7 it is concluded that BEC in H is out of reach with the present apparatus, but it also provides a clear handle how to proceed in order to reach BEC in atomic H: the evaporation mechanism must be improved to 3D. This can, e.g., be arranged by removing atoms at an equipotential energy surface, for instance by applying a radio-frequency field, a method popular in evaporative cooling of alkali gases. Although it is quite a challenge to combine such a technique with a dilution refrigerator environment, it does not seem impossible.

The most obvious step in improving the diagnostics for the H sample at the low temperatures required for BEC, is to improve the bandwidth of the L_α source. If this bandwidth can be

reduced with one order of magnitude, RETS can be used to characterize the H sample down to BEC. The presence of a condensate is expected to be directly observable in the RETS spectrum.

A fascinating application of RETS might be future spectroscopy of antihydrogen[24]. Future symmetry tests on antihydrogen will most probably start with spectroscopic investigations of a trapped sample with a small number of atoms. RETS on the $1S - 3S$ transition offers the perspective of a spectral resolution that is two orders of magnitude better than L_α spectroscopy, with, at the same time, a resonant cross section of up to 50% of the $3\lambda^2/2\pi$ single photon L_α cross section.

For high density gases, an important property of RETS is that the absorption cross section for two-photon absorption can be adjusted at will, even on the center of the two-photon resonance, by choosing the detuning from the intermediate $2P$ state. Compared to one-photon spectroscopy, this tunable transparency offers important advantages for the investigation of very dense gases. In this respect a new experiment in Amsterdam is worth mentioning. The experiment is designed to study quantum degeneracy in a two-dimensional gas[25] of H$\downarrow$ adsorbed on the surface of liquid ^{4}He. An essential part of this experiment is the presence of a high density buffer gas of H$\downarrow$. Preliminary results show L_α spectra that are optically dense over 50 GHz and densities as high as $10^{16}\,\mathrm{cm}^{-3}$. For the investigation of these high-density samples, RETS has three advantages. The tunable transparency allows the optically very dense gas to be tuned to a suitable optical density, facilitating thermometry. A technical advantage is the following. Because of the large Zeeman shifts, the total band of L_α resonance lines is many 100 GHz wide. With L_α alone, only a few lines lie within the range over which the L_α source can scan without mode hops. Using RETS, the L_α source can be tuned near the resonance of, e.g., a line attributed to surface atoms, while thermometry can be done on a RETS line. The two-photon line can always be brought within the scan range of the L_α source by proper choice of the H_α frequency. Finally, in the inhomogeneous field of the experiment, all L_α lines are broadened by Zeeman broadening. A Zeeman-free RETS line is, even at the gas temperature of ~ 100 mK, narrow enough to discriminate the hyperfine structure, allowing the determination of the hyperfine composition of the H$\downarrow$ gas.

Bibliography

[1] T.J. Greytak and D. Kleppner, in *New Trends in Atomic Physics*, edited by G. Grynberg and R. Stora (North-Holland, Amsterdam 1984), p. 1125.

[2] I.F. Silvera and J.T.M. Walraven, in *Progress in Low Temperature Physics*, edited by D.F. Brewer (Elsevier, Amsterdam 1986), Vol. 10, p. 139.

[3] I.F. Silvera and J.T.M. Walraven, Phys. Rev. Lett. **44**, 164 (1980).

[4] F. London, Nature **141**, 643 (1938).

[5] Only recently, atomic europium was successfully trapped in a magnetic trap, by laser ablation in a cryogenic environment combined with He buffer gas cooling, as described in: Jinha Kim, Bretislav Friedrich, Daniel P. Katz, David Patterson, Jonathan D. Weinstein, Robert DeCarvalho and John M. Doyle, Phys. Rev. Lett. **78**, 3665 (1997).

[6] For an overview of the early days of lasercooling, see the special issue on laser cooling and trapping of atoms, J. Opt. Soc. Am. B **6**, No. 11, 1961-2278 (1989).

[7] The first observation of BEC was reported for Rb at Jila: M.H. Anderson, J.R. Ensher, M.R. Matthews, C.E. Wieman, and E.A. Cornell, Science **269**, 198 (1995). In Na, BEC was achieved at MIT: K.B. Davis, M.-O. Mewes, M.R. Andrews, N.J. van Druten, D.S. Durfee, D.M. Kurn, and W. Ketterle, Phys. Rev. Lett. **75**, 3969 (1995). The first evidence for BEC with Li at Rice university was published in: C.C. Bradley, C.A. Sackett, J.J. Tollet, and R.G. Hulet, Phys. Rev. Lett. **75**, 1687 (1995). The data in this publication has been reanalyzed in: C.C. Bradley, C.A. Sackett, and R.G. Hulet, Phys. Rev. A **55**, 3951, 1997.

[8] E. Tjukanov, A. Ya. Katunin, A.I. Safonov, P. Arvela, M. Karhunen, B.G. Lazarev, G.V. Shlyapnikov, I.I. Lukashevich and S. Jaakkola, Physica B **178**, 129 (1992).

[9] Harald F. Hess, Greg P. Kochanski, John M. Doyle, Naoto Masuhara, Daniel Kleppner, and Thomas J. Greytak, Phys. Rev. Lett. **59**, 672 (1987).

[10] R. van Roijen, J.J. Berkhout, S. Jaakkola, and J.T.M. Walraven, Phys. Rev. Lett. **61**, 931 (1988).

[11] R. van Roijen, Ph. D. thesis, University of Amsterdam (1989).

[12] O.J. Luiten, Ph. D. thesis, University of Amsterdam (1993).

[13] O.J. Luiten, H.G.C. Werij, I.D. Setija, M.W. Reynolds, T.W. Hijmans, and J.T.M. Walraven, Phys. Rev. Lett. **70**, 544 (1993).

[14] O.J. Luiten, M.W. Reynolds, and J.T.M. Walraven, Phys. Rev. A **53**, 381 (1996).

[15] Claudio L. Cesar, Dale G. Fried, Thomas C. Killian, Adam D. Polcyn, Jon C. Sandberg, Ite A. Yu, Thomas J. Greytak, Daniel Kleppner, and John M. Doyle, Phys. Rev. Lett. **77**, 255 (1996).

[16] A recent review of of evaporative cooling is: Wolfgang Ketterle and N.J. van Druten in *Advances in Atomic, Molecular and Optical Physics*, edited by B. Bederson and H. Walther (Academic Press, San Diego, 1996), Vol. 37, p. 181-236.

[17] John M. Doyle, Jon C. Sandberg, Ite A. Yu, Claudio L. Cesar, Daniel Kleppner, and Thomas J. Greytak, Phys. Rev. Lett. **67**, 603 (1991).

[18] I.D. Setija, Ph. D. thesis, University of Amsterdam (1995).

[19] I.D. Setija, H.G.C. Werij, O.J. Luiten, M.W. Reynolds, T.W. Hijmans, and J.T.M. Walraven, Phys. Rev. Lett. **70**, 2257 (1993).

[20] P.W.H. Pinkse, A. Mosk, M. Weidemüller, M.W. Reynolds, T.W. Hijmans, J.T.M. Walraven, and C. Zimmermann, Phys. Rev. Lett. **79**, 2423 (1997).

[21] Wolfgang Ketterle and David E. Pritchard, Phys. Rev. A **46**, 4051 (1992).

[22] P.W.H. Pinkse, A. Mosk, M. Weidemüller, M.W. Reynolds, T.W. Hijmans, and J.T.M. Walraven, Phys. Rev. Lett. **78**, 990 (1997).

[23] P.W.H. Pinkse, A. Mosk, M. Weidemüller, M.W. Reynolds, T.W. Hijmans, and J.T.M. Walraven, to be published.

[24] For a review see: M. Charlton, J. Eades, D. Horváth, R.J. Hughes, C. Zimmermann, Phys. Rep. **241**, 65 (1994); *Antihydrogen*, Proceedings of the Antihydrogen Workshop, held on 30-31 July 1992, Munich Germany, edited by J. Eades, Hyperf. Int., **76** (1993).

[25] Details about the experiment can be found in: A.P. Mosk, P.W.H. Pinkse, M.W. Reynolds, and J.T.M. Walraven, *Proceedings of the symposion on quantum fluids and solids*, Paris 1997, to appear in Journal of Low Temp. Phys.

Chapter 2

Basics of hydrogen trapping

2.1 Introduction

All experiments with cold trapped gases start with the production of the gas, and subsequent cool-down and trapping in a potential well. Most alkali vapors can be cooled down from room temperature by optical means and can be trapped in a magneto-optical trap, from which the gas can be transferred to a magnetostatic trap, if desired. In contrast, atomic hydrogen can be cooled to sub-Kelvin temperatures and loaded in a magnetostatic trap by non-optical means. Moreover, the densities in typical hydrogen trapping experiments are sufficiently high to have frequent interatomic collisions that thermalize the gas, enabling a thermodynamic description indispensable for proper treatment of the dynamics of the gas and the calculation of optical spectra.

The purpose of this chapter is to provide the basics for the experiments on, and the thermodynamic description of trapped hydrogen and therefore serves as an introduction to the discussion of adiabatically changing the phase-space density in chapter 6 and evaporative cooling in chapter 7. The chapter starts with a discussion of the potential energy that a H atom experiences when placed in a spatially inhomogeneous magnetic field (section 2.2). Next, in section 2.3, magnetic field geometries used for trapping neutral atoms will be discussed, including the one that is used for trapping H in the experiments described in this thesis. In section 2.4 it is explained how to create atomic H in a cryogenic dissociator and finally trap it in the potential well created by the magnetic field. Once trapped, the gas can be characterized in terms of occupied "volume", "density", internal energy etc. What these familiar quantities are in an inhomogeneous trapping potential will be the subject of section 2.5.

hyperfine state	energy	state
d	$a_h/4 + \mu^- B/2$	$\|\uparrow\uparrow\rangle$
c	$-a_h/4 + (a_h/2)[1 + (\mu^+ B/a_h)^2]^{1/2}$	$\cos\theta\|\uparrow\downarrow\rangle + \sin\theta\|\downarrow\uparrow\rangle$
b	$a_h/4 - \mu^- B/2$	$\|\downarrow\downarrow\rangle$
a	$-a_h/4 - (a_h/2)[1 + (\mu^+ B/a_h)^2]^{1/2}$	$\sin\theta\|\uparrow\downarrow\rangle - \cos\theta\|\downarrow\uparrow\rangle$

Table 2.1: Energy levels and eigenstates of the ground state hyperfine structure in a magnetic field, expressed in the $|m_s\, m_i\rangle$ basis, where $\mu^{\pm} = g_e\mu_B \pm g_n\mu_n$ which can be approximated by $2\mu_B$ with an error smaller than 1%. The hyperfine mixing angle is defined by $\tan 2\theta \equiv a_h/\mu^+ B \simeq a_h/2\mu_B B$. The barred arrows indicate the nuclear spin, i.e., $\downarrow$ means $m_i = 1/2$ and $\uparrow$ means $m_i = -1/2$.

2.2 Potential energy of a trapped atom

The energy shift that a single ground state hydrogen atom experiences in a magnetic field arises from the Zeeman interaction $E_z = -\vec{\mu}\cdot\vec{B}(\vec{r})$ between $\vec{\mu}$, the magnetic moment of the atom, and the position dependent external magnetic field $\vec{B}(\vec{r})$. This fact is used in a magnetostatic trap, which has a spatially inhomogeneous magnetic field with a minimum at $\vec{r} = \vec{r}_0$, creating a potential well for atoms with magnetic moments anti-parallel to the field. Usually it can be assumed that the magnetic field change experienced by a trapped atom $|\dot{\vec{B}}|/B \ll \mu_B B/\hbar$, in which case the assumption is justified that $\vec{\mu}$ follows $\vec{B}(\vec{r})$ adiabatically and the Zeeman energy only depends on the amplitude $|\vec{B}(\vec{r})|$ of the magnetic field. Only if an atom passes a region with a magnetic field very close to zero, the direction of the magnetic field can vary so rapidly that the atom can change over from one Zeeman sublevel to another, non-trapped state[1]. This process is called Majorana spin flipping and will be discussed in more detail in section 4.5.

The interaction of groundstate H atoms with the magnetic field is somewhat complicated by the hyperfine interaction between the electron spin $\vec{s}$ and the proton spin $\vec{\imath}$. The Zeeman energy can be obtained from the following Hamiltonian

$$H = (g_e\,\mu_B\,\vec{s} - g_n\,\mu_n\,\vec{\imath})\cdot\vec{B} + a_h\,\vec{\imath}\cdot\vec{s}, \tag{2.1}$$

with μ_B and μ_n the Bohr magneton and the nuclear magneton, g_e and g_n the corresponding g-factors, respectively. In zero field the hyperfine splitting is a_h, where $a_h/k_B = 0.068\,\mathrm{K}$. Diagonalizing H with respect to the $|m_s, m_i\rangle$ basis gives four hyperfine states, labeled a, b, c and d, in order of increasing energy. The states are listed in table 2.1, together with the eigenenergies, which are also plotted in Fig. 2.1.

Usually the potential energy of the atoms is defined with respect to the energy at the trap minimum $\vec{r}_0$

$$U_p(\vec{r}) = E_h(\vec{r}) - E_h(\vec{r}_0), \tag{2.2}$$

where h denotes one of the four possible hyperfine states. The four hyperfine states can be

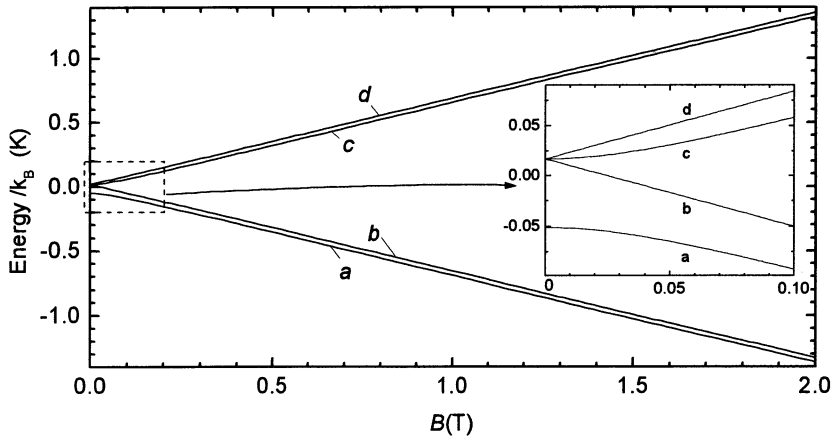

Figure 2.1: Zeeman effect of the hyperfine structure of atomic hydrogen: the energy of the Zeeman sublevels as a function of magnetic field. The inset shows an enlarged view of the low-field region.

devided in two "high-field seeking" (H↓) states, a and b, and two "low-field seeking" (H↑) states, c and d, for obvious reasons. Because Maxwell's equations do not allow a local magnetic field maximum in free space, only the low-field seeking c and d states can be trapped in a magnetostatic trap.

2.3 Trapping configurations

The first magnetostatic trapping of neutral atoms was realized by Migdall *et al.*[2] with sodium in a magnetic quadrupole trap. This simple trapping configuration is made of two coils with opposing currents, and has a magnetic field zero in its center from where $|\vec{B}|$ increases linearly in all directions. Mathematically, the quadrupole trap is an example of the class of power-law traps, analyzed by Bagnato *et al.*[3]. These potential wells are of the form

$$U_p(x,y,z) = (x/\lambda_x)^{1/\delta_x} + (y/\lambda_y)^{1/\delta_y} + (z/\lambda_z)^{1/\delta_z} \tag{2.3}$$

where, e.g., λ_x sets the length scale in the x direction and δ_x sets the power law. Note that these potentials can be written as $U_p(x,y,z) = U_x(x) + U_y(y) + U_z(z)$, i.e., the potential is separable in the three motional degrees of freedom. The harmonic trap is a special case, with $\delta_x = \delta_y = \delta_z = 1/2$, and, e.g., $\lambda_x = \omega_x\sqrt{2/m}$ for a particle with mass m. The power-law traps, and especially the harmonic trap, are important model geometries because many thermodynamic and kinetic properties of trapped gases have been calculated in these simple potentials, often leading to analytical expressions.

Unfortunately, the simplest magnetostatic power-law trap, the two-coil quadrupole trap, has a zero magnetic-field minimum, which becomes a problem at very low temperatures, when many

atoms reside near the minimum of the trap. Atoms passing the trap minimum experience a magnetic field that changes direction rapidly, which leads to the Majorana spin flips mentioned in section 2.2. This Majorana decay can be prevented by keeping the atoms away from the magnetic field zero, for instance by adding an extra repulsive potential using a far-off-resonant laser beam[4]. However, the best way to prevent Majorana decay is to use a trap with a non-zero magnetic field minimum. One of the simplest magnetostatic trapping configurations with a non-zero B minimum is the Ioffe trap, first used in plasma experiments in the 1960's and proposed by Pritchard for neutral atom trapping[5]. It consists of four parallel current bars and two dipole coils, as is sketched in Fig. 2.2. The bars ("Ioffe bars") are arranged symmetrically

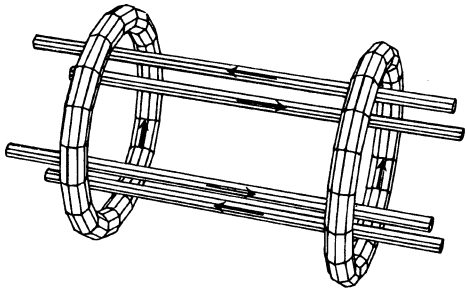

Figure 2.2: Sketch of the Ioffe configuration. The arrows indicate the current directions: the currents of two neighboring Ioffe bars have opposite directions; the currents in the two dipole coils run in the same direction.

around the symmetry (z-) axis of the dipole coils. The currents in neighboring bars run in opposite directions and create the radially confining magnetic field of quadrupolar symmetry, which is zero on the symmetry axis and the magnitude of which increases linearly with radial distance ρ. The quadrupole field is perpendicular to the axis, except near the end of the Ioffe bars. The Ioffe bars can be connected in several ways[6], for instance by making each one part of a separate oval shaped coil, as is done in the trap discussed in this thesis (see Fig 2.3).

Each of the dipole coils produces a magnetic field that points predominantly in the z-direction, peaking in the center of the coil. Hence, the z-component of the magnetic field produced by two coils placed far enough apart will have a minimum between the two coils. The amplitude of the sum field of the quadrupole field and the dipole fields will have a true minimum in free space.

Apart from preventing Majorana spin flips, a non-zero field minimum has the advantage that it separates the spectral lines used in the spectroscopic diagnostics of the trapped gas (see Chapter 5), facilitating the spectroscopy. The combination of these properties makes the Ioffe configuration ideal for trapping H↑.

2.3.1 The Ioffe trapping field

The trap that was used in the experiments described in this thesis was built and used by Van Roijen *et al.*[7]. It is of the Ioffe type with the four Ioffe bars being part of four elongated, racetrack-shaped (oval) coils. In addition, it has not two but four dipole coils. One of them, the dissociator coil, creates a large ($\simeq 4.5\,\mathrm{T}$) magnetic field outside the trapping region to force low-field seekers from the dissociator towards the trap. An extra trim coil in the center gives more control over the magnetic field at the trap center. The exact layout is depicted in Fig. 2.3. The trap operates at liquid helium temperatures and is made of wires that are superconducting

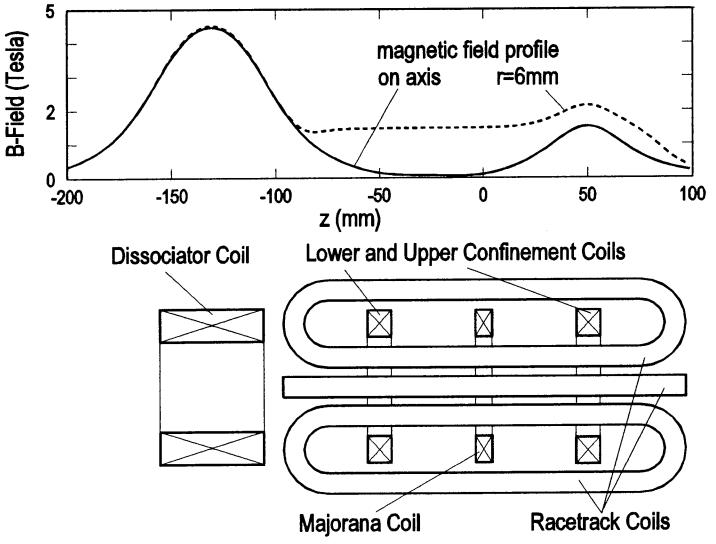

Figure 2.3: Cross section of the trapping magnet coils. The upper part of the figure shows a typical magnetic field configuration.

at that temperature, enabling relatively steep magnetic gradients and a well depth of maximally 1.5 T, corresponding to 1.0 K for H, comparable to the binding energy $\varepsilon_a/k_B = 1.011(10)\,\mathrm{K}$ of H on liquid ^{4}He [8], which covers the walls of the experimental cell.

Because of the axial symmetry of the trap, the magnetic field profile is usually expressed in a cylindrical coordinate system (ρ, ϕ, z), with ρ the distance to the central axis and ϕ the azimuthal angle. The axial position z is either given relative to a fixed point of the trap, or relative to the trap minimum ($\rho = 0, z = z_0$), which can shift if the trapping potential is changed.

The magnetic field $\vec{B}(\vec{r})$ produced by the combination of these coils can numerically be calculated straightforwardly from classical electrodynamics. Luiten gives useful approximations for the field as a power series in ρ and z[9]. For low temperatures, when the gas is concentrated

near the trap center, it suffices to take into account only the leading terms in the expansion of the field around this point

$$\begin{aligned} B_\rho(\rho,\phi,z) &= -\alpha\rho\sin 2\phi \\ B_\phi(\rho,\phi,z) &= -\alpha\rho\cos 2\phi \\ B_z(\rho,\phi,z) &= B_0+\beta(z-z_0)^2, \end{aligned} \tag{2.4}$$

where $\beta = \frac{1}{2}(\partial^2 B_z(0,0,z)/\partial z^2)_{z=z_0}$ and α is the radial field gradient due to the quadrupole coils. The magnetic field strength can be found easily by quadratically summing the three B-field components in Eq. 2.4 to

$$B = |\vec{B}(\vec{r})| = \sqrt{[B_0+\beta(z-z_0)^2]^2+\alpha^2\rho^2}. \tag{2.5}$$

For positions so close to the minimum that $(B-B_0) \ll B_0$, i.e., for temperatures $T \ll T_0 \equiv \mu_B B_0/k_B$, the field can be approximated to lowest order in ρ and z by

$$B = B_0+\beta(z-z_0)^2+\frac{\alpha^2}{2B_0}\rho^2. \tag{2.6}$$

This is called the "harmonic" approximation. In this thesis the words "Ioffe-quadrupole" (IQ) trap will be reserved for potentials of the form of Eq. 2.6. Also in IQ traps many thermodynamic quantities can be calculated analytically. Note that the IQ trap of Eq. 2.6 can be written as the sum of a radial and an axial part and is hence said to be separable, whereas a Ioffe trap in general is not.

2.4 Loading of the trap

As demonstrated for the first time in 1987[10], atomic hydrogen can be loaded into a magnetostatic trap without optical cooling, after production in a cryogenic dissociator[11]. This is a microwave resonator in which a discharge can be made in helium vapor. The walls are covered with a layer of several hundred monolayers of solid molecular H_2, which is covered with a thin saturated layer of superfluid helium. The exact mechanism is not completely understood, but it is believed that charged particles, which are accelerated in the discharge, penetrate the He film and strike the solid H_2 coating on the wall and release either H_2 or H. The molecules could be dissociated in the vapor. A magnetic field gradient separates the high-field seeking a and b states from the low-field seeking c and d states. The hot atoms cool down by collisions with the He gas in the dissociator (operating temperature $\sim 0.6\,\mathrm{K}$) and, after leaving the dissociator, by thermalization with the He covered cell walls, which are in our case at $\sim 0.1\,\mathrm{K}$. To prevent a jet of He originating from the dissociator spraying through the trapping region, there is no line of sight between the dissociator and the trapping region. In fact, a filling tube with three

90° angles is used in the experiments described in this thesis, to connect the dissociator with the trapping region. This design is the same as described by Luiten[9]. After leaving from the filling tube, the low-field seekers are accelerated towards the center of the trap. Because the superfluid He layer surrounding the trapping region reduces surface adsorption, a sufficiently high density can be build up to have frequent interatomic collisions to produce low-energetic atoms that are trapped while the hotter atoms will cool by thermalizing with the He-covered walls.

The free surface of liquid He supports only one bound state for a H atom with a binding energy e_a of only 1.011(10) K [8]. When a H atom hits a superfluid He film, two things can happen: 1) The atom will trapped in the bound state ("adsorbed"), but is free to move along the surface. The H atom floats on the He film so to say. 2) The atom will be reflected. The sticking probability s was measured by Berkhout *et al.*[12, 13] and in the temperature range $0.07\,\mathrm{K} \leq T \leq 0.5\,\mathrm{K}$ was found to be $s/T \approx 0.33\,\mathrm{K}^{-1}$. A H atom bound to the surface will desorb again after a characteristic time[13]

$$\tau_a = \frac{2\pi\hbar}{s\,k_\mathrm{B}\,T_w} e^{e_a/k_\mathrm{B}T_w}, \tag{2.7}$$

with a kinetic energy of the order of the wall temperature T_w. The low value of e_a permits the existence of a sub-Kelvin hydrogen gas in thermal equilibrium with its He covered walls.

The critical stage in the loading process is the transport through the tube connecting the dissociator with the trapping region. If the temperature is too low, the H↑ atoms will recombine due to two-body surface recombination[11, 14]. Because of the exponential dependence of the residency time on the temperature (Eq. 2.7), the loading efficiency is strongly temperature dependent.

The binding energy of H on liquid ^{3}He or mixtures of ^{3}He and ^{4}He is less than on pure liquid ^{4}He. If a monolayer of ^{3}He is formed on top of the liquid ^{4}He, the binding energy is only 0.34(3) K[15], much lower than e_a of H on ^{4}He. As a consequence, loading of H with ^{3}He covered walls works at lower temperatures than with ^{4}He covered walls. In the experimental setup described in this thesis, H↑ could not be loaded with cell temperatures below 105 mK with pure ^{4}He covered walls. The most efficient loading was observed at cell temperatures around $120 - 140$ mK. However, in the presence of a monolayer of ^{3}He, H↑ could be loaded at the base temperature (80 mK) of the apparatus.

It is interesting to compare the binding energy of H on liquid ^{4}He with that of atomic deuterium (D). The binding energy of D on liquid ^{4}He is, with 2.6 K, more than twice as large as that of H, resulting in much higher D surface densities as H densities at the same bulk gas density. Therefore, one expects the two-body surface recombination to hinder the loading of D into a magnetic trap. Indeed, so far nobody has succeeded in trapping D, although Luiten[9] managed to get sufficient amounts into the trapping region to get an optical signal of D. However, this signal disappeared within in a few seconds after stopping the dissociator.

2.5 Equilibrium thermodynamics

Modeling the thermodynamic properties of the trapped gas is essential for analyzing the optical spectra from the trapped gas, as well as the description of decay processes and evaporative cooling. The description is facilitated by the fact that a trapped gas of low-field seeking H atoms is in very good approximation an ideal gas because the interparticle interactions are not important: the gas parameter $na^3 \ll 1$, where $a = 0.72$ Å the s-wave scattering length[16], and the ratio of the mean field energy over the thermal energy $n\tilde{U}/k_{\rm B}T \ll 1$, with $\tilde{U} = 4\pi\hbar^2 a/m$ [17] for a H atom of mass m, and at temperature T. If the thermal De Broglie wavelength of the atoms, defined by $\Lambda = (2\pi\hbar^2/mk_{\rm B}T)^{1/2}$, is much smaller than the mean interparticle spacing ($n\Lambda^3 \ll 1$), the ideal Bose gas is well approximated by the ideal Boltzmann gas, as will be done in this section.

In all experiments described in this thesis, the H↑ was studied in magnetic traps of finite depth. This means that atoms are removed from the trap if their total energy, or, depending on the escape mechanism, their energy associated with one or more of the motional degrees of freedom, exceeds a threshold energy ϵ_t. It is assumed that this escape, or "evaporation" is fast compared to the characteristic collision time. As a result of this escape mechanism the distribution function is truncated in phase space.

The basic assumption that will be made in the thermodynamic description is that of "quasi-equilibrium", described by a single thermodynamic "temperature" T. It assumes that the phase-space distribution (position and momentum) *for trapped particles* depends only on the energy of the particle. This is for instance guaranteed by frequent interatomic collisions or by single-particle motion that is sufficiently ergodic, i.e., if the motion of an atom between two collisions is stochastic, and the atom samples all parts of the phase space with the same energy with equal probability. Whether the single-particle motion is ergodic or not is a non-trivial question with important consequences that will be treated in detail in chapter 7.

As an example, consider a power-law trap with a finite depth in the z-direction. Atoms with enough z-momentum p_z to escape over the magnetic barrier in the z-direction are considered not trapped and leave the trap within the time needed for one roundtrip. If the single-particle motion is not ergodic, the phase-space distribution will be truncated to contain only those particles with $U_z(z) + p_z^2/2m < \epsilon_t$. If the single-particle motion is ergodic, the barrier in the z-direction will remove all particles with *total* energy $\epsilon > \epsilon_t$. The situation in which the escape criterion only depends on the total energy was analyzed in detail by Luiten[9] and Walraven[18]. They assumed that the gas is characterized by a Boltzmann distribution function[17] that is truncated in phase space at a constant energy hypersurface and conserves that shape, as a result of the interatomic collisions, even if the single-particle motion is not ergodic.

The truncated Boltzmann approximation was put onto solid ground by Luiten *et al.*[19] who showed by numerical solution of the Boltzmann equation that for non-degenerate Bose

gases the evaporation process conserves the truncated Boltzmann evaporation indeed rather accurately. In this thesis a generalized truncated Boltzmann approximation is used, which assumes a Boltzmann distribution that can either be truncated based on the total energy, or based on the z-energy only.

In the following paragraphs the basics of the thermodynamic description of a magnetically trapped gas will be discussed, necessary to deal with trap decay or density profiles needed in the spectrum calculations such as presented in chapter 5. It serves as an introduction to the discussion about the adiabatic changes of the phase-space density in chapter 6 and the study of one- and three-dimensional cooling in chapter 7, where the thermodynamics will be treated in more detail.

2.5.1 Distribution functions

The trapped gas is described by its classical phase-space distribution

$$f(\vec{r},\vec{p}) = n_0\Lambda^3\, e^{-(U_p(\vec{r})+p^2/2m)/k_BT}, \tag{2.8}$$

which is normalized as in [19], such that the total number of atoms, N, is given by

$$N = (2\pi\hbar)^{-3}\int d^3r \int d^3p\; f(\vec{r},\vec{p}), \tag{2.9}$$

where the integration runs over the available phase space. The distribution function is characterized by two parameters: the phase-space density $n_0\Lambda^3$ at $(\vec{r},\vec{p}) = (\vec{r}_0, 0)$ and the temperature T. In the case of a finite trap depth, it will be assumed that trapped atoms are clearly distinguishable from non-trapped atoms based on their coordinates in phase-space. The distribution function is in that case truncated in the 6-dimensional phase space by a well defined hypersurface, i.e., it is zero outside this region.

2.5.2 Density profiles

In an infinitely deep trap the density profile of the gas is easily obtained by integrating the phase-space distribution function (Eq. 2.8) over momentum yielding

$$n_\infty(\vec{r}) = n_0 \exp[-U_p(\vec{r})/kT], \tag{2.10}$$

and n_0 is the true density at the center of the trap. If the distribution is truncated at $\epsilon = \epsilon_t$, the integral leads to a density profile given by

$$n(\vec{r}) = n_\infty(\vec{r})P\left(\frac{3}{2}, \frac{\epsilon_t - U_p(\vec{r})}{k_BT}\right). \tag{2.11}$$

Here $P(a,\eta) \equiv \Gamma^{-1}(a) \int_0^\eta dt\, t^{a-1}e^{-1}$ is the incomplete gamma function [20]. If the trapping potential is separable in an axial and a radial part and the truncation is only based on the z-energy, the following density profile is expected:

$$n(\vec{r}) = n_\infty(\vec{r}) P\left(\frac{1}{2}, \frac{\epsilon_t - U_z(z)}{k_B T}\right). \tag{2.12}$$

In the case of a truncated distribution, n_0 is not the true density at the center of the trap, but approaches it for $\epsilon_t \to \infty$.

2.5.3 The density of states

With the assumption of quasi-equilibrium and a truncation criterion that is a function of the energy ϵ only, all relevant information about the trapping potential is contained in the density of states $\rho(\epsilon)$, which is a function of energy only. It may be written as [19]

$$\rho(\epsilon) = \frac{2\pi(2m)^{3/2}}{(2\pi\hbar)^3} \int_{U_p(\vec{r}) \le \epsilon} d^3r\, \sqrt{\epsilon - U_p(\vec{r})}, \tag{2.13}$$

where $\rho(\epsilon)$ is normalized so that $\rho(\epsilon)\, d\epsilon$ is equal to the number of single-particle eigenstates with energies between ϵ and $\epsilon + d\epsilon$. The density of states often takes a simple form. For instance, for power-law traps (Eq. 2.3) it is simply

$$\rho(\epsilon) = A_{\mathrm{PL}}\, \epsilon^{1/2+\delta}, \tag{2.14}$$

with $\delta = \delta_x + \delta_y + \delta_z$ and A_{PL} a trap dependent constant. For the IQ trap (Eq. 2.6), with potential energy $U_p \equiv \mu_B B$ and $U_0 \equiv \mu_B B_0$, the density of states is

$$\rho(\epsilon) = A_{\mathrm{IQ}} \left(\epsilon^3 + 2U_0\epsilon^2\right), \tag{2.15}$$

with $A_{\mathrm{IQ}} = (2m\,\pi^2)^{3/2}/[(2\pi\hbar)^3 2\alpha^2\beta^{1/2}]$. Both for $\epsilon \gg U_0$ and $\epsilon \ll U_0$ the density of states of an IQ trap is equivalent to that of a power-law trap.

If the truncation of the distribution function is not only based on the total energy, but for instance on the energy related with the motion in the z-direction only, the density of states can not be used anymore and calculations should be based on integrals over the trapping potential.

2.5.4 Partition function and effective volume

The canonical partition function $\mathcal{Z} = \mathcal{Z}_1^N/N!$ of a classical ideal gas of N particles in an inhomogeneous potential U_p follows immediately from the definition of the single-atom partition function $\mathcal{Z}_1$ for a trapped ideal gas (see, e.g., [17]):

$$\mathcal{Z}_1 = (2\pi\hbar)^{-3} \int d^3r \int d^3p\, e^{-(U_p(\vec{r}) + p^2/2m)/k_B T}, \tag{2.16}$$

where the integration runs over available phase-space. For instance, in the case of a truncation in phase space that only depends on the total energy, the integration is limited to the volume in phase space where $U_p(\vec{r}) + p^2/2m \leq \epsilon_t$. It is important to note that the partition function is just as well defined for a truncated distribution.

From Eq. 2.16 and Eq. 2.9 it follows directly that the effective volume $V_e \equiv N/n_0$ is closely related to $\mathcal{Z}_1$:

$$V_e = \Lambda^3 \mathcal{Z}_1. \tag{2.17}$$

The importance of the effective volume is that, because all thermodynamic functions can be derived from the partition function, all this information is also contained in the effective volume.

In the case of separable potentials that are axisymmetric, the effective volume can be written as the product of an effective length L_e and an effective area A_e:

$$V_e = A_e \, L_e, \tag{2.18}$$

with

$$A_e = \int\int dx \, dy \, e^{-U_\perp(x,y)/k_B T} \tag{2.19}$$

$$L_e = \int dz \, e^{-U_z(z)/k_B T} \mathrm{erf} \sqrt{\frac{\epsilon_t - U_z(z)}{k_B T}}, \tag{2.20}$$

where the trap is assumed to be truncated in the z-direction only. If the truncation is removed ($\epsilon_t \to \infty$) then erf $\to 1$. The effective length L_e and the effective radius $\sqrt{A_e/\pi}$ are good indications for the dimensions of the sample. If the potential is not separable, still an indication of the effective linear dimension can be obtained by taking the integrals $\int_{-\infty}^{\infty} dz \, n(0,z)/n_0$ and $[\int_0^{\infty} d\rho \, 2\rho \, n(\rho, z_0)/n_0]^{1/2}$, for the effective length and effective radius, respectively. Here $n(\rho, z)$ is the density at point (ρ, z).

The effective volume V_e is sometimes called the single-particle effective volume to discriminate it from the higher-order effective volumes such as the second-order effective volume

$$V_{2e} \equiv \int \left(\frac{n(\vec{r})}{n_0} \right)^2 d^3 r, \tag{2.21}$$

where the integration runs over the available geometric volume. V_{2e} is useful for calculating trapped averaged processes that are proportional with the square of the density. An example are inelastic collisions, which will be discussed in more detail in section 4.2. For thermal distributions not truncated in momentum space, V_{2e} has a simple relation to the first order effective volume: $V_{2e}(T) = V_e(T/2)$.

2.5.5 Thermodynamic functions

The internal energy E of the trapped gas can be derived from the partition function via

$$E = N k_B T^2 \frac{1}{\mathcal{Z}_1} \frac{\partial \mathcal{Z}_1}{\partial T}, \tag{2.22}$$

giving

$$E = \left(\frac{3}{2} + \gamma\right) N k_B T, \tag{2.23}$$

where $\gamma = (T/V_e)\,(\partial V_e/\partial T)$, with the partial derivative evaluated at constant trapping potential and constant N. The parameter γ plays an important role in the discussion of adiabatic changes of the phase-space density in chapter 6. In a full thermal (not truncated) distribution an atom has an average kinetic energy $\frac{3}{2}k_B T$ (equipartition theorem[17]) and an average potential energy $\gamma k_B T$. For a truncated distribution, this interpretation of the two terms in Eq. 2.23 is not legitimate, although their sum is still the total energy.

In the case of separable axisymmetric potentials, it can be useful to split γ into two parts, $\gamma_\perp$ and γ_z, which are defined by

$$\gamma_\perp = \frac{T}{A_e}\frac{\partial A_e}{\partial T} \tag{2.24}$$

$$\gamma_z = \frac{T}{L_e}\frac{\partial L_e}{\partial T}. \tag{2.25}$$

For non-truncated distributions $\gamma_\perp$ and γ_z have the obvious meaning of the average potential energy corresponding to the movement in the radial, respectively the axial direction.

Analogous to Eq. 2.21 it is possible to define quantities that are obtained by averaging the potential energy over higher powers of the density distribution, as for instance

$$\gamma_2 \equiv \frac{1}{k_B T}\int U_p(\vec{r})\left(\frac{n(\vec{r})}{n_0}\right)^2 d^3r, \tag{2.26}$$

which is useful for calculating sample heating caused by processes depending on binary atomic collisions. In a non-truncated distribution γ_2 and γ have a simple relation: $\gamma_2(T) = \gamma(T/2)/2$.

The canonical partition function $\mathcal{Z}$ (see, e.g., Reif[21]) can be also be written as

$$\mathcal{Z} = \frac{\mathcal{Z}_1^N}{N!} = e^{-F/k_B T}, \tag{2.27}$$

where $F = E - TS$ is the Helmholtz free energy. Using $N/\mathcal{Z}_1 = n_0\Lambda^3$ (from Eq. 2.17) and Stirling's formula, $\ln N! \approx N \ln N - N$, one arrives at the following expression for the entropy:

$$S = N k_B \left(\frac{5}{2} + \gamma - \ln n_0\Lambda^3\right). \tag{2.28}$$

This expression has important consequences. Because entropy is conserved in adiabatic reversible processes, it follows from Eq. 2.28 that the phase-space density $n_0\Lambda^3$ cannot be altered in a reversible adiabetic process, unless γ changes. This will be discussed further in chapter 6. It should be stressed that the entropy is a well defined quantity, even in the case of a non-thermal distribution. Thermal equilibrium is a state of maximum entropy, and it is therefore a good check to see what happens if we begin with a truncated distribution, instantly set $\epsilon_t \to \infty$, and

allow the gas to thermalize. The entropy should increase in that case. Indeed, for instance for a power-law trap (Eq. 2.3), it is easily verified that the change of entropy ΔS is given by

$$\frac{\Delta S}{N k_B} = \left[\frac{3}{2} + \delta\right]\left[1 - \frac{P(5/2+\delta,\eta)}{P(3/2+\delta,\eta)} + \ln\frac{P(5/2+\delta,\eta)}{P(3/2+\delta,\eta)}\right] - \ln P(3/2+\delta,\eta), \tag{2.29}$$

with $P(a,\eta)$ the incomplete gamma function [20], $\eta \equiv \epsilon_t/k_B T$ and $\delta = \delta_x + \delta_y + \delta_z$. The entropy change on thermalization is a monotonically decreasing positive function of η, with $\Delta S \to 0$ for $\eta \to \infty$, as required.

2.5.6 Collision rates

The collisional properties of hydrogen can be calculated from first principles. Because of the four different spin states of ground state H, the full description of H-H interaction involves 16 interaction potentials. Neglecting the small nuclear spin reduces the number of interaction potentials to two: a singlet ($S = 0$) and a triplet potential ($S = 1$), where $\vec{S} = \vec{s}_1 + \vec{s}_2$ is the sum of the electron spins.

At the low temperatures relevant for the experiments described in this thesis, two d atoms interact via the s-wave scattering cross section for elastic collisions $\sigma_{dd} = 8\pi a_T^2$, where $a_T = 0.72\,\text{Å}$ is the triplet scattering length[16]. The elastic cross section for c-d collisions is $4\pi a_T^2$, a factor of two lower than the d-d case because of the distinguishability of the atoms. The elastic cross section for c-c collisions is B-dependent and contains the singlet scattering length a_S, but can be approximated by $8\pi a_T^2$ for $B \gg 0.05\,\text{T}$.

The elastic collision event rate is

$$\Gamma_c = \frac{1}{2m(2\pi\hbar)^6}\int d^3r \int d^3p_1 \int d^3p_2\, |\vec{p}_2 - \vec{p}_1|\, \sigma_{el}\, f(\vec{r},\vec{p}_1)\, f(\vec{r},\vec{p}_2), \tag{2.30}$$

where $f(\vec{r},\vec{p})$ is the thermal single-particle distribution function, Eq. 2.8, and the integration extends over the available phase space. For constant elastic cross sections the integral can be evaluated, giving

$$\Gamma_c = \frac{1}{\sqrt{2}} n_0^2\, \bar{v}\, \sigma_{el}\, V_{2e}(T), \tag{2.31}$$

where $\bar{v} = \sqrt{8k_B T/\pi m}$ is the average thermal velocity. The average time an atoms spends between two collisions, $\tau_c = N/2\Gamma_c$, is a good measure for the equilibration time of the sample. For instance, at a temperature of 50 mK and a density of $5 \cdot 10^{11}\,\text{cm}^{-3}$, $\tau_c \simeq 1.3\,\text{s}$. In order to remain close to thermal equilibrium, the rate of changing the trapping potential should not exceed τ_c.

Bibliography

[1] T.H. Bergeman, Patrick McNicholl, Jan Kycia, Harold Metcalf, and N.L. Balazs, J. Opt. Soc. Am. B **6**, 2249 (1989).

[2] Alan L. Migdall, John V. Prodan, William D. Phillips, Thomas H. Bergeman and Harold J. Metcalf, Phys. Rev. Lett. **54**, 2596 (1985).

[3] Vanderlei Bagnato, David E. Pritchard, and Daniel Kleppner, Phys. Rev. A **35**, 4354 (1987).

[4] K.B. Davis, M.-O. Mewes, M.R. Andrews, N.J. van Druten, D.S. Durfee, D.M. Kurn, and W. Ketterle, Phys. Rev. Lett. **75**, 3969 (1995).

[5] Y.V. Gott, M.S. Ioffe, and V.G. Tel'kovskii, Nucl. Fusion, 1962 Suppl., Pt. 3, 1045 (1962).

[6] T. Bergeman, Gidon Erez, and Harold J. Metcalf, Phys. Rev. A **35**, 1535 (1987).

[7] R. van Roijen, J.J. Berkhout, S. Jaakkola, and J.T.M. Walraven, Phys. Rev. Lett. **61**, 931 (1988).

[8] W.N. Hardy, M.D. Hürlimann, and R.W. Cline, Jap. J. Appl. Phys. **26**, Suppl. 26-3, 2065 (1987).

[9] O.J. Luiten, Ph. D. thesis, University of Amsterdam (1993).

[10] Harald F. Hess, Greg P. Kochanski, John M. Doyle, Naoto Masuhara, Daniel Kleppner, and Thomas J. Greytak, Phys. Rev. Lett. **59**, 672 (1987).

[11] R. van Roijen, Ph. D. thesis, University of Amsterdam (1989).

[12] J.J. Berkhout, E.J. Wolters, R. van Roijen and J.T.M. Walraven, Phys. Rev. Lett. **57**, 2387 (1986).

[13] J.J. Berkhout and J.T.M. Walraven, Phys. Rev. B **47**, 8886 (1993).

[14] I.F. Silvera and J.T.M. Walraven, in *Progress in Low Temperature Physics*, edited by D.F. Brewer (Elsevier, Amsterdam 1986), Vol. 10, p. 139.

[15] G.H. van Yperen, A.P.M. Matthey, J.T.M. Walraven, and Isaac F. Silvera, Phys. Rev. Lett. **47**, 800 (1981).

[16] D.G. Friend and R.D. Etters, J. Low Temp. Phys. **39**, 409 (1980).

[17] K. Huang, *Statistical Mechanics*, (John Wiley and Sons, New York, 1963).

[18] J.T.M. Walraven, in *Proceedings of the SUSSP 44 Summer School on Quantum Dynamics of Simple Systems*, edited by G.-L. Oppo, S.M. Barnett, E. Riis, and M. Wilkinson (Institute of Physics Publishing, Bristol, 1996), p. 315-352.

[19] O.J. Luiten, M.W. Reynolds, and J.T.M. Walraven, Phys. Rev. A **53**, 381 (1996).

[20] *Handbook of Mathematical Functions*, edited by Milton Abramowitz and Irene A. Stegun (Dover, New York, 1972).

[21] F. Reif, *Fundamentals of Statistical and Thermal Physics* (McGraw-Hill, New York, 1965).

Chapter 3

Experimental set-up

3.1 Introduction

Experiments on trapped atoms usually require a simple vacuum system and some lasers for cooling and trapping of the atoms. Although the details are different for commonly used atoms as Li, Rb, Na, the experimental setups are quite similar and often fit on a single optical table. The experiment can be especially compact if small diode lasers are available as narrow band light sources. Optical spectroscopy on magnetically trapped H↑, first demonstrated by Luiten[1], is quite different in this respect. Of all the possible wavelengths for exiting the ground state, Lyman-α (L_α) which excites a 1S ground state atom to the 2P excited state is experimentally the most accessible with a wavelength $\lambda = 121.57\,\text{nm}$. This is vacuum-ultraviolet (VUV) radiation, and is strongly absorbed in air. Typical windows transmit 50 % of the light. Narrow-band L_α sources are not commercially available. Although laser cooling of trapped H↑ was demonstrated recently [2, 3], obtainable light fluxes are still far too low to cool H↑ by optical means all the way down from room temperature to trapable temperatures of $\sim$ 1 Kelvin. Fortunately, this is not necessary because H can be trapped in a cryogenic environment without laser cooling (see chapter 2), although the combination of a sub 100 mK cryogenic environment, small sample space in the bore of a magnet in combination with VUV optical access provide major experimental challenges.

The total experimental setup necessary for the experiments described in this thesis, involves subsystems to generate, stabilize and diagnose L_α. For the two-photon experiments described in chapter 5, Balmer-α light (H_α, $\lambda = 656.47\,\text{nm}$ in vacuum) was needed, which also required stabilization and diagnosis. Moreover, the L_α and H_α light beams must be overlapped in an experimental cell. The cell is placed in a magnetic field created by superconducting magnets and is cooled by a dilution refrigerator.

The system used to generate L_α and the experimental cell are based on those used by Luiten [4], and Setija [3]. For completeness their description will be given here, but emphasis lies on

the changes with respect to references [4] and [3]. To improve the L_α beam quality, a new gas cell was constructed for frequency-tripling ultraviolet light (UV) to generate L_α, as well as a new monochromator to separate this L_α from the much stronger UV. To improve optical access, an optical path through the cryogenic cell and the rest of the cryostat was made. This allowed detection at room temperature with a solar-blind photomultiplier that is sensitive for L_α, but is almost blind for the strong H_α light.

3.2 The Lyman-α system

Despite the rapid progress in laser technology in the last few decades, cw lasers thus far have not been realized in the deep UV. The reason is a physical one: The ratio of spontaneous decay rate over the stimulated decay rate increases exponentially with frequency. Or, in other words, it is increasingly difficult to pump hard enough to compensate for the losses. Therefore, all narrow-band light sources in the UV rely on non-linear processes, such as frequency doubling or tripling. Because these processes depend in a non-linear way on the input intensity, pulsed operation is advantageous. This is the reason that all known schemes [5, 6, 7, 8, 9, 10, 11, 12] for generation of L_α are pulsed. The scheme that was built in Amsterdam was selected for relative simplicity and reliability[4, 12]. The scheme proposed by Marangos *et al.*[10] promises more L_α power, but is more complicated, and for non-invasive measurements (low intensity probing) the present scheme suffices. An interesting development is the attempt at the Max-Planck-Institut für Quantenoptik in Garching, Germany, to build a narrow-band cw L_α source based on four-wave mixing in Mg-vapor[13] or by surface-second-harmonic generation on a non-linear crystal[14].

The L_α source we use is based on pulsed dye amplification of light from a tunable narrow-band laser at 729.6 nm. The amplified light is frequency doubled, and the resulting UV is amplified once more. L_α light is then produced by third-harmonic generation in a phase-matched gas mixture of krypton and argon.

3.2.1 UV generation

A schematic diagram of the UV generation setup is shown in Fig. 3.1. A Ti-Sapphire ring laser (Coherent 899) generates 0.5 W of narrow-band cw light of 729.40 nm (bandwidth $\simeq$ 1.5 MHz). We use a single Ar^+-ion laser (Coherent Innova Sabre TSM 15) to pump both the Ti-Sapphire ring laser for the L_α system and the ring dye laser for the H_α (operating at 656 nm) simultaneously. Approximately 60 % of the 15 W multi-line power of the Ar^+-ion laser is used to pump the Ti-Sapphire laser, and the other 40 % is used for pumping the dye laser. A small fraction of the red 729 nm light is split off for stabilization and calibration (see section 3.4). The main part is directed to the pulsed dye amplifier (Lambda Physik 2003). To prevent back

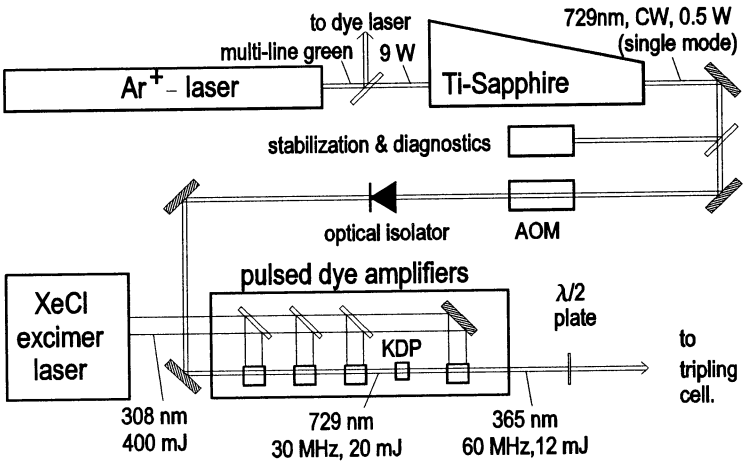

Figure 3.1: Optical set-up to generate the 365 nm, which is used as an intermediate frequency in the L_α source.

action of the amplified pulses on the Ti-Sapphire laser, we pass the light through a 30 dB optical isolator (Optics for Research IO-5-VIR) before entering the pulsed dye amplifier (PDA). The PDA is pumped by a XeCl-excimer laser (Lambda Physik LPX 210 i) which makes 300 mJ pulses of ultraviolet light (308 nm), at a maximum repetition rate of 100 Hz. In the pulsed dye amplifier the 729 nm is amplified in three cuvettes with a dye solution (Rhodamine 700 in methanol). The 729 nm light is amplified in three stages to enable efficient frequency doubling in a crystal of potassium dihydrogen phosphate (KDP). The ultraviolet (UV, 364.8 nm) generated in the KDP crystal is amplified once more in a UV dye (Radiant Dyes Chemie 'RDC-360 neu'), dissolved in a mixture of dioxane and ethylene glycol. The UV pulses that leave the PDA have a pulse energy of typically 12 mJ at 10 Hz repetition rate and last for approximately 20 ns. The maximum repetition rate of 100 Hz is set by the pump laser, but the system was usually operated in the $5 - 20$ Hz range, because of dye-lifetime considerations and the fact that the L_α yield depends on the sixth power of the amplifier pulse energy, which decreases with repetition rate. In practice the repetition rate was set by optimizing the signal-to-noise ratio in the L_α absorption spectrum.

When well aligned, the bandwidth of the UV, as determined by using a confocal etalon with a free spectral range (FSR) of 150 MHz, is $40 - 60$ MHz. From this we obtain an upper bound of the L_α bandwidth of 150 MHz. It turned out to be essential to have a bandwidth analyzer readily available during the alignment of the system, otherwise much broader line widths could be generated unnoticed.

3.2.2 Frequency tripling

The non-linear process in which the third harmonic of the fundamental frequency is generated is called frequency tripling. Assuming lowest order Gaussian beams, the generated power in the third harmonic is

$$P_3 \propto n^2 |\chi^{(3)}|^2 P_1^3 F, \tag{3.1}$$

where n is the density of the nonlinear medium, $\chi^{(3)}$ the third-order susceptibility, P_1 the power of the fundamental beam, and F a phase-match factor[8]. The phase matching is an important issue, which can be realized by considering a hypothetical gas with the same index of refraction for 365 nm light as for L_α. If the focus of the Gaussian beam entirely falls in the gas cell in which the tripling is achieved, *no* L_α is produced because the de Guoy phase slip of π radians makes all the L_α generated in the first part of the focus destructively interfere with the L_α generated in the second part. Efficient tripling can only be realized if this phase slip is compensated by a wave-vector mismatch, defined as the wave vector of the generated radiation minus three times the wave vector of the driving light. This phase-match depends on the gas constituents, but also on the shape of the focus of the fundamental light beam [8].

Krypton has a resonance at 123.58 nm, and therefore it has an appreciable $\chi^{(3)}$ at the L_α wavelength. Moreover, it has negative dispersion, required for phase matching. Phase matching can be obtained by adding a gas like argon with positive dispersion. As first demonstrated by Mahon *et al.*[5], a mixture of Kr and Ar is very suited to generate L_α (with a wavelength of 121.57 nm).

The generated L_α is separated from the much intenser UV in a monochromator. Previously a monochromator was used based on the dispersion of a lens being used off-axis, which eliminates the extra absorption losses in separate prisms, but gives poor control over the resulting beam quality. In order to improve beam quality, a new monochromator was built using prisms, as is described in the next section. Along with the monochromator a new tripling cell was built. To maintain gas purity the tripling volume was constructed of stainless steel and the windows are sealed off with metal seals only, using indium to seal both the entrance and exit windows as well as the inspection windows. The latter are important for checking dielectric breakdown of the gas, which is unwanted during normal operation because it leads to large fluctuations in generated VUV, but which can be useful for alignment. These measures were sufficient to make a single gas fill last for several weeks. For the new tripling cell a longer confocal parameter was chosen for a better L_α yield, following the suggestion of Luiten[4]. The beam is focused by a $f = 25$ cm lens in a 45 cm long tripling cell (Fig. 3.2). The lens is placed just outside the cell. The length of the cell chosen as long as possible for this focal length in order to maximize the beam size at the entrance and exit windows to avoid radiation damage. No window damage was observed, not even after several months of operation. In the focus of the UV beam L_α light is generated, imaged into the experimental cell in the cryostat by a MgF_2 lens with a focal

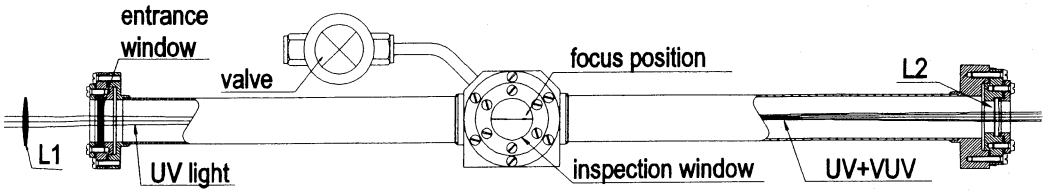

Figure 3.2: Drawing of the tripling cell. The UV enters from the left. The right side of the tripling cell fits in the monochromator.

length of $f = 19$ cm, which serves as exit window of the tripling cell. This lens is essential for the final beam quality.

The weak L_α beam exiting the tripling cell is co-propagating the high power UV beam. In principle L_α detection could be done at this place by using a gas detector. If, however, the L_α beam is separated from the UV, other more readily available detectors can be used and beam profiling can be realized. All diagnostics on the beam were, hence, done behind the monochromator described in the next section. Calculating back, however, one can infer the intensity of the $L_\alpha$beam *in* the tripling cell. The efficiency of the tripling process increases with the Kr pressure, but is limited by dielectric breakdown of the gas. The threshold for the breakdown is inversely proportional with the Kr pressure[15, 16]. For experimental convenience the system was therefore operated at a conservative Kr pressure of 240 Torr and phase matched with 620 Torr Ar. With this fill, breakdown of the gas was avoided under the worst alignment and optimal UV power conditions. Typically 5×10^9 L_α photons per pulse were created inside the tripling cell at an input power of 9 mJ per pulse. The efficiency of the third-harmonic generation is thus of the order 10^{-6}.

3.2.3 VUV Optics

LiF and MgF_2 are the only available window materials that transmit L_α. The transmission of both materials is of order 50 % for a window of 1 mm. However, we observed no significant lower transmission for elements two to three times thicker, which leads to the conclusion that the absorption is mainly surface bound. Using the Fresnel equations, we can calculate the reflection of the surface of a piece of VUV optic, using the known indices of refraction of LiF and MgF_2 (see table 3.1). This yields $5.4 - 5.9$ % between 0° and 45° for light polarized perpendicular to the surface, for both LiF and MgF_2. The only assumption in this calculation is that the extinction length of the material is much larger than the wavelength, which is certainly true for bulk LiF and MgF_2. Experimentally, however, we find a reflection of $\sim 10\%$, which supports the hypothesis of a surface-bound anomalous absorption. We also found that the transmission is quite sensitive to the surface treatment. Of many optical elements the transmission could be

wavelength (nm)	name	T (°C)	LiF n	MgF_2 n_o	MgF_2 n_e
643.9	HeNe (red)	20	1.391	1.37682	1.38858
656.47	H_α (red)	20	1.391	1.37663	1.38838
365	UV	20	1.4012	1.38614	1.39834
121.6	L_α (VUV)	25	1.624	1.6275	1.6320
		-193	1.6160	1.6150	
		-273	1.615	1.614	

Table 3.1: Index of refraction n of LiF and the ordinary and extraordinary indices of refraction n_0 and n_e respectively of the birefringent MgF_2 at several temperatures. The data is from references [18] and [19]. The indices of refraction at $T = -273$°C are extrapolations of the data in [19].

improved to up to 65 % by gently polishing the surface with diamond powder in ethylene glycol. Also a fast curing polymer which could be pealed off ('Opti-clean polymer'[17]) was useful for protecting and cleaning LiF or MgF_2 surfaces. The transmission of LiF is comparable to that of MgF_2, but LiF is not birefringent. Unfortunately, LiF is more hygroscopic than MgF_2 and its transmission deteriorates under normal laboratory conditions. In the final design all VUV optical elements were made of MgF_2.

The ordinary and the extraordinary index of refraction of the birefringent MgF_2 is tabulated in table 3.1. In order to avoid retardation effects, the optical axis of all the VUV optics is chosen parallel to the propagation direction. However, small angles are unavoidable when working with imaging optics. The setup contains several MgF_2 elements and it is found that their combined effect is an approximate retardation of a quarter wave. This is actually useful, because the L_α is linearly polarized when generated and circularly polarized light is needed for the closed cycle $1S - 2P$ transition (see chapter 5).

3.2.4 The monochromator

The L_α generated in the tripling cell must be separated from the much stronger co-propagating UV in a monochromator. In order to improve L_α beam quality, a setup was chosen using the dispersion of two prisms, at the expense of L_α loss in the extra optical elements compared with the off-axis lens set-up used by VonDrasek *et al.*[20] and Luiten[4, 12]. For easy access to the optics, the monochromator is shaped as a rectangular box, cut from a single block of an aluminum alloy, with a stainless steel cover. The cover has two large (75 mm diameter) inspection windows above the two prisms. Fig. 3.3 gives a top view. The light from the tripling cell first passes a 16 mm diameter aperture, before the L_α is deflected 12.8° by the first prism. Because of the dispersion of the prism, the UV is deflected over only 8.3° and leaves

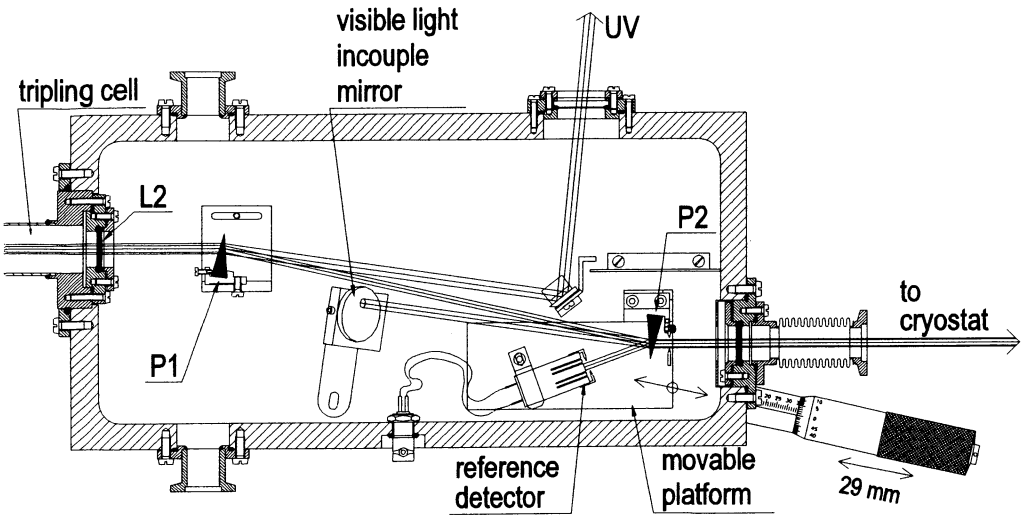

Figure 3.3: Drawing of the monochromator which separates the L_α from the much intenser UV light. On the left the end of the tripling cell is visible.

the monochromator via a high-reflective mirror and an anti-reflection coated window towards a beam dump.

The prisms are single crystals of MgF_2 supplied by Harshaw[21]. The prisms are equilateral with a top angle of 20°, 20 mm long sides and they are 20 mm tall. The optical axis of the MgF_2 prisms are parallel to their bases. Together with the tilt of 6.4° for the first prism with respect to the incoming beam, this guarantees that the L_α propagates parallel to the optical axis to avoid retardation effects in the birefringent MgF_2 crystals.

The L_α from the first prism is deflected by a second prism P_2 before it leaves the monochromator via a MgF_2 exit window. This second prism enhances the spectral separation by blocking the direct path of the scattered UV light into the cryostat. When looking from the cryostat into the monochromator 'with UV eyes' (or ordinary eyes, because the index of refraction is almost identical for UV and visible light, as can be seen in table 3.1), one does not see the brightly scattering first prism, but mirror M2. Via this mirror and an opening in the cover plate it is possible to feed in a visible beam and superimpose it on the outgoing L_α beam. This allows for visual inspection of the light path all the way through the cryostat, which turned out to be a vital option on several occasions.

Another advantage of this second prism is that the reflection of its front surface can be used to monitor the L_α intensity, providing a reference to divide out pulse to pulse fluctuations in the L_α yield. The reflection is observed by a solar-blind photodetector (Hamamatsu R1187). The availability of such a reflection saves the insertion loss of an extra MgF_2 beam splitter if a reference beam is needed. The second prism also assures that L_α exiting the monochromator

passed equal lengths of solid matter, canceling the position dependent absorption of a single prism in first order. Moreover, it assures that the L_α beam that is deformed to an elliptic beam by a single prism, is restored to a circular beam shape. The L_α beam is focussed by the lens which serves as output window of the triple cell. The focus is 1 m away, which limits the involved angles to several mrad.

The L_α beam is sent into the cryostat via an adjustable mirror (see section 3.5.2), which gives control over four degrees of freedom. This mirror, however, cannot translate the L_α beam parallel in the (horizontal) plane through the tripling cell and the monochromator. Therefore, P_2 and the reference detector were placed on a platform, movable parallel to the L_α beam between the two prisms over a range of 29 mm resulting in a parallel displacement of the outgoing L_α beam of 6.4 mm. The platform is placed on a crossed roller ("Schneeberger" [22]) bearing, and can be controlled from below by a micrometer. The micrometer is magnetically coupled to the platform.

Because L_α is absorbed in all but the purest noble gasses and vacuum, great care is taken to keep the monochromator interior clean and prevent ambient air to leak in. Apart from some teflon isolation and one epoxy feed-through, no plastics are used, to prevent outgassing. Possibly hidden volumes are ventilated to the main volume. All windows are sealed with indium, as is the cover. Only to seal the triple cell in the monochromator a rubber O-ring was used. The lubricants of the crossed roller bearing were replaced by a vacuum grease with a very low vapor pressure ("Fomblin RT15"[23]). Previously it was noticed that the L_α-transmittance of the VUV system decreased, unless a constantly refreshed buffer gas removed impurities sputtered by the strong UV pulses from the walls or the optics. For this reason we keep the interior filled with $\sim$ 30 mbar argon. We refresh the 3 liter volume at a rate of $\sim$ 10 mbar l/min.

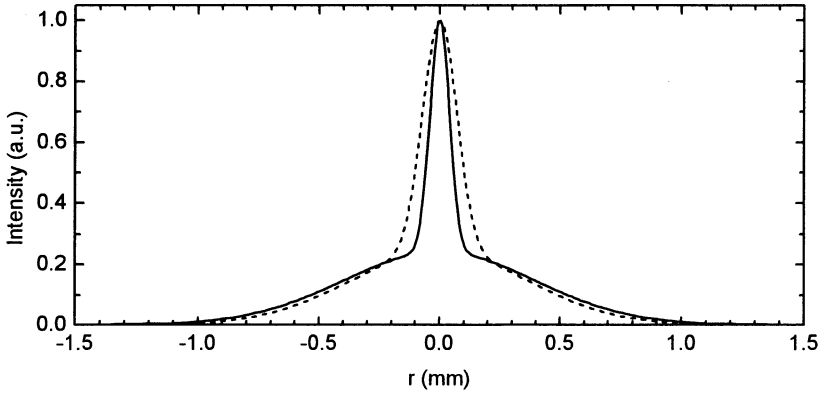

Figure 3.4: Typical beam profile as measured in the reference system with the knife edge method. The dashed and the solid line are cuts in two perpendicular directions.

The focus of the output L_α beam was measured behind the monochromator as described in section 3.5.1. Apart from the central peak a somewhat broader pedestal around the beam was visible (see Fig. 3.4). When fit to two concentric Gaussians we found a third of the intensity to fall in a central peak with a Gaussian parameter ($\omega_0^{(1)} = 1/e^2$ intensity-radius) of 0.11 mm, and the rest in a somewhat broader peak with $\omega_0^{(2)} = 0.8$ mm, typically.

3.3 The Balmer-α system

A ring dye laser (Coherent 699) pumped by 6 W multiline power of the Ar^+-ion laser, generates 0.5 W of narrowband cw light of 656 nm (bandwidth $\simeq$ 1.5 MHz). A schematic diagram of the H_α generation setup is shown in Fig. 3.5. A small fraction of this red light is split off for stabilization and calibration (see section 3.4). The main part is sent through a polarization compensator (Berek's compensator [24]). This is basically a thin plate of MgF_2 that can be rotated around two axes to obtain any arbitrary state of polarization. The L_α comes in pulses of $\sim$ 10 ns, with a time jitter of 5 ns with respect to the trigger pulse to the excimer laser. Since we do not want to dump any unnecessary heat in the cryostat, we chop the H_α beam by an acoustic optic modulator (AOM). With the present setup, the shortest pulses that can be generated conveniently by an AOM with a guaranteed flat intensity during the L_α pulse is $\sim 0.2\,\mu$s. This is long enough to compensate for any drift in the delay circuits during several hours of operation. By chopping the H_α first with a mechanical shutter with a rise and open time of less than 1 ms (Uniblitz), we block the 1 % of the H_α leaking through the AOM in the "closed" position. Because the low duty cycle ($2 \cdot 10^{-6}$) of the "open" state of the AOM, the leakage would otherwise far dominate the average light flux in the output. In this way, maximally 40μW of H_α light is sent through the cryostat. When well aligned, this causes negligible radiative heat input in the cell.

3.4 Stabilization and calibration

Two-photon spectroscopy of trapped atomic hydrogen requires two stable narrow-band sources, which are at the same time tunable. In this way one is able to average several spectra or compare data taken on different days. Ideally one would lock both sources to a stable absolute reference like an atomic line by means of an AOM or EOM (electro-optic modulator). The limited scan range of these optical modulators prohibit the desired many GHz tuning in our case. Instead, we rely on the combination of two references. One of them is very stable, but not tunable and will be called the primary standard. The other reference is called the secondary standard. As the primary standard a very stable cavity is used, for both the L_α as the H_α. The secondary standard for the L_α is a cavity with sufficient short term stability and is regularly calibrated against the primary standard. The secondary standard for the H_α is a diode laser, locked to the

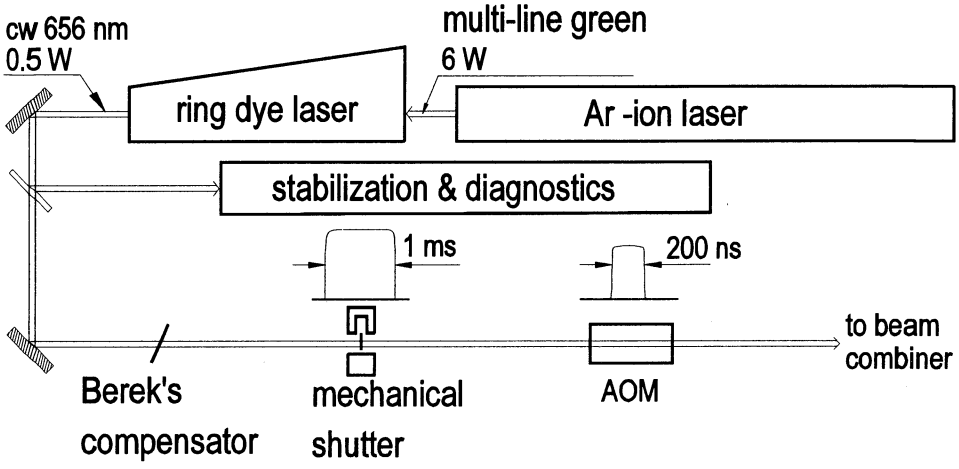

Figure 3.5: Optical set-up to generate H_α light with a wavelength of 656.47 nm.

primary standard. By counting a beat signal the H_α light can be compared to the laserdiode light over the desired long scan range.

A commercial wave meter (Burleigh WA-20 with an accuracy of 0.3 GHz) provides enough accuracy to be able to find the atomic H lines which then can be used to calibrate the stabilized sources. The next sections describe the details of the used locking and stabilization schemes.

3.4.1 Stabilization of the 729 nm light

The primary standard for the stabilization of the seeding light of the L_α generation, 729 nm from a Ti:Sapphire laser, is a simple etalon (etalon 1 in Fig. 3.6) with a free spectral range (FSR) of 2.983 GHz in an ultrastable thermostat. To increase stability, this cavity has no piezos to avoid their inherent creep. In order to have sufficient scan range, we use a scanning cavity (etalon 2) as a secondary standard. This secondary standard is a piezo-driven etalon with a FSR of 3.0 GHz that is continuously scanning in the same thermostat as etalon 1.

The resonance frequency of etalon 2 is scanned with a 10 Hz sawtooth over 6 GHz. Since this is much faster than any allowed laser scan, at least one resonance is recorded every cycle. The position of these resonances is compared with the expected values by a computer routine which updates the correction that is applied in the laser control software. Every time the lock failed, but at least once every day, this tunable etalon was calibrated against the primary standard. By comparing with a two-photon transition frequency in potassium ($4^2S_{1/2} \rightarrow 6^2S_{1/2}$, [25]), the drift of etalon 2 was found to be 365 kHz/hour, while the drift of etalon 1 was less than

1 MHz/day (see references [4, 12] for details).

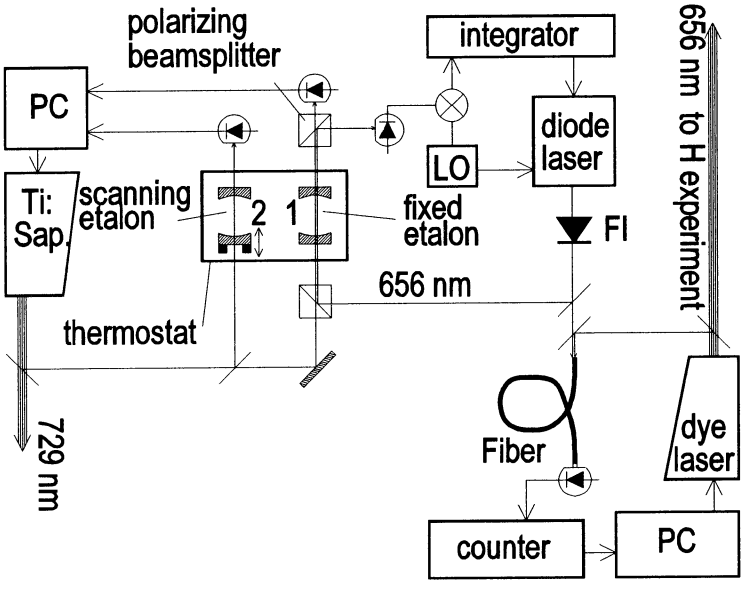

Figure 3.6: Outline of the stabilization set-up. LO=local oscillator, FI=Faraday isolator.

3.4.2 Balmer stabilization

The requirements for the H_α stabilization are quite similar to those of the 729 nm. Therefore, the stable etalon (etalon 1 in Fig. 3.6) is used as a primary standard for the H_α source as well.

As a secondary standard we used a diode laser at 656 nm locked by means of a radio-frequency side-band technique[26] to our stable reference etalon (see Fig. 3.6). Although the stable cavity is coated for 729 nm, resulting in a Q-factor of only 15 at 656 nm, it was possible to stabilize the diode laser to the cavity to within 10 MHz, which was narrow enough for the first two-photon experiments. The long term drift of the secondary standard is as good as the primary standard, the fixed etalon, to which it is locked. The short term linewidth, however, is of the order of 1 MHz.

The laserdiode setup is similar to the one build by Ricci *et al.*[27]. It is built around a 5 mW laser-diode chip (Toshiba TOLD9421), which acts as an intracavity etalon inside an external cavity formed by a grating and the chip itself. Since the internal cavity selects one of the 6 GHz spaced modes of the external cavity, the diode lases in a single mode. The whole setup is temperature controlled by a Peltier element with a block of aluminum as thermal mass. The

emerging beam is made circular by a pair of anamorphic prisms before it is sent through a 30 dB optical isolator (Optics for Research 'IO-2-656') to prevent feedback onto the laser diode.

In order to compare the frequency of the H_α source with that of the diode laser which serves as our secondary standard, a small fraction of the high power H_α is coupled into a very fast photodiode (New Focus '1534 Vis-IR') via an optical fiber, together with the diode laser light. The resulting beat frequency is counted by a 20 GHz microwave frequency counter (HP 5350B). The counter output is used to stabilize the H_α output. When locked to a fixed beat frequency, the drift in absolute frequency is less than 10 MHz, mainly determined by the uncertainty in the laser diode lock. If in future experiments a smaller bandwidth is needed, this can easily be accomplished by replacing the optics of the stable etalon by a properly coated set. Another way is to lock directly to an iodine line with a Doppler-free technique.

3.5 Beam control, overlap and diagnostics

3.5.1 VUV tools

To build and maintain a VUV system it is essential to have test and measurement equipment to diagnose the beams. With visible and IR setups it is common to work on an optical table with many standard tools like holders and translators for mirrors and lenses, detectors etc. Ideally one would have a similar toolbox for VUV optics, but one that works in vacuum. We have constructed a variety of VUV tools, based on the familiar 25 and 40 mm ISO-KF ("Klein"-flange) system. This has the advantage of flexibility that rubber O-rings give over metal seals, but where needed, e.g. in parts that are connected to the cryogenic optics, it is possible to use metal seals on the same steel flanges. The tubes are evacuated by an oil-free turbo-molecular pump. We found that after venting the system, for a change of detector for instance, only a few minutes were needed to evacuate the system enough to continue the experiment. For the transmission of the system to return to its equilibrium, however, $\sim$ 20 minutes of pumping is needed, probably due to traces of water absorbed on the walls.

Standard metal or glass X- and T- pieces serve as cornerstones connecting metal or glass tubes to form beam lines. Adjustable mirror holders that fit in the X- and T-pieces can be used to control the pointing of the (VUV) beam. Simple metal clamps are sufficient to position the tubes on a standard optics breadboard to interface with UV and visible light optics via windows that fit on the K-flanges. The glass pieces are particularly useful when using visible light simultaneously with the VUV. All detectors and windows are made to fit onto KF-flanges. For testing VUV optics it was particularly useful to have a test box available with several K-flange ports and the possibility to shift elements in and out the beam. A glass cover plate that sealed on a rubber O-ring provided an easy access to the test pieces.

A variety of room-temperature VUV detectors is employed in our apparatus, each selected

for its specific application: simple Si diodes, gas chambers, phototubes and photomultiplier tubes (PMT's). Because of the low intensity VUV light and the all-present UV light pulses, we relied mostly on solar-blind phototubes (Hamamatsu R1187) for room-temperature testing of the optics. They have a quantum efficiency of $\sim 10\%$, are convenient in use, but show some non-linear effects with our short and relatively intense pulses.

At liquid helium temperatures some photodiodes still work, notably the GaAsP ones used by Luiten *et al.*[4]. At cooling down, most photomultipliers cease operation slightly above 77 K[28, 29]. Microchannel plates have been used at 30 K[30]. Both detectors, however, do not work in high magnetic fields. On the other hand, at low temperatures other types of detectors become available, such as bolometers, which will be discussed in section 3.6.3.

Finally, one needs a tool to measure the VUV beam profile. Ideally, one would have a gated, sensitive, solar-blind CCD with a large surface of tiny pixels, which can be mounted on a vacuum system. However, camera systems that meet enough of the above requirements are expensive. Instead, we used two knife-edges on micrometer screws in front of an ordinary solar-blind photodetector. For characterizing the beam, we shift a knife edge slowly through the beam and repeat this procedure with the other knife edge. By differentiating the recorded pattern one can infer the original beam profiles. In this way, a 2D beam profile can be measured in about 20 minutes.

In order to check the L_α beam profile or its overlap (see section 3.5.3) with the H_α beam, we set up a permanent evacuated beam path into which the L_α beam could be directed by moving a VUV mirror into the main beam. This is depicted in Fig. 3.7 .

3.5.2 Beam control

The only way to move the overlapped light beams together, is to have an adjustable mirror in the evacuated light path behind the monochromator. The requirements for this mirror mount are quite stringent. Three degrees of freedom must be adjustable. Apart from the two angles θ and ϕ that define the orientation of the surface normal, it is also necessary that the beams can be displaced horizontally in the direction of the sample in the plane through the incoming and outgoing beams. In order to steer the beams in the cell with a resolution of the order of 10μm, the mirror mount must have an angular resolution of $\sim 10\mu$rad. A final requirement is the demand that the mirror mounts will not pollute the UHV. This excludes the use of plastics and limits the available mechanical feed-through systems severely. The design shown in Fig. 3.8 meets these criteria. The performance of the mount was measured with a visible light beam and a camera. The maximal angle the mirror can make is $2 \times 6\,^\circ$ in both the θ and the ϕ direction and the accuracy is better than $20\,\mu$rad, limited only by the micrometers. If necessary these can easily be replaced by more accurate transducers like piezo stacks. No significant hysteresis or cross-talk was observed.

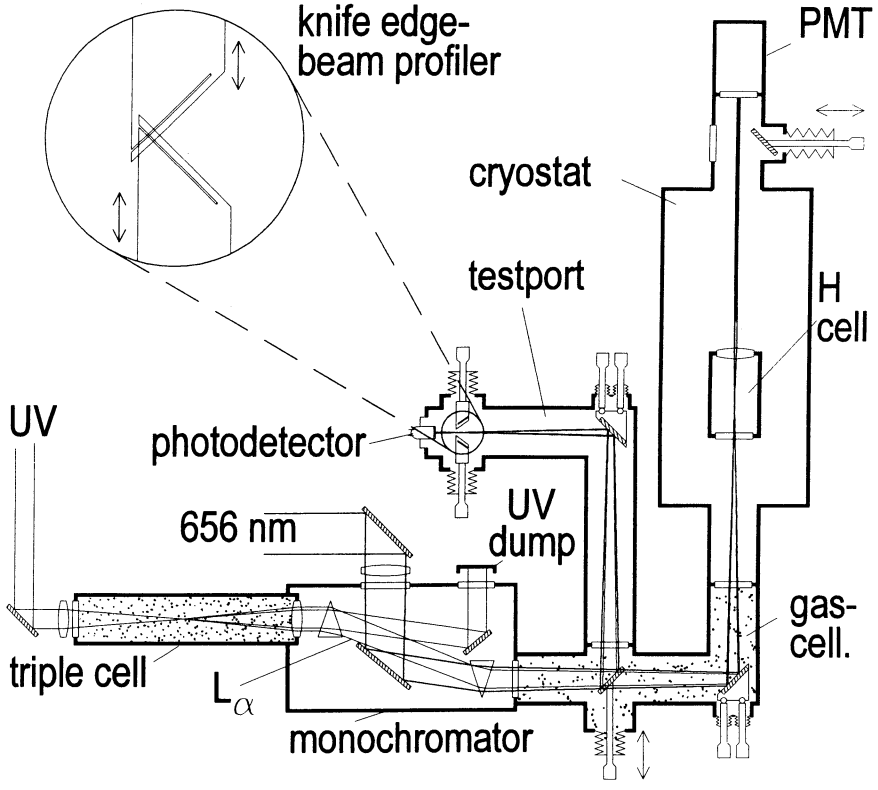

Figure 3.7: Path of the light beams through the testport en the cryostat. In the monochromator the intense UV (365 nm) is separated from weak L_α. Here also the H_α is coupled into the beam.

Another way to change the relative alignment of the beams and the H sample is moving the whole cryostat. Our cryostat is suspended from the ceiling above, the bottom side is only connected with the table with VUV optics via a thin-walled bellows. In order to fix this degree of freedom a heavy pole on the breadboard is clamped by micrometers connected with the lowest part of the cryostat. Sapphire plates guarantee flat, low friction non metallic surfaces which do not short-circuit the electrical disconnected cryostat and VUV breadboard.

The need to align the beam to a lateral precision of $10\,\mu$m, is mainly dictated by the requirement to coincide with the zero of the quadrupole field of the Ioffe trap. Hence, a simple improvement for future experiments would be to make the position of the magnetic field minimum adjustable. This could be accomplished by adding a little offset current to one or two of the radial confining coils. This method would have several advantages. First, one can find the optimal alignment for the beams without a H sample present and then align the sample on the axis of the beams, not disturbing the light path through the cryostat. Second,

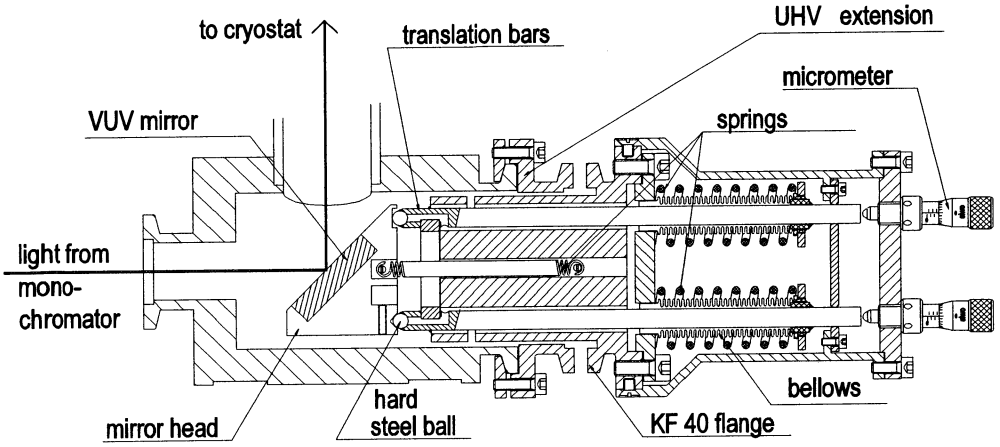

Figure 3.8: UHV compatible high-precision mirror mount. It consists of a body that can be mounted on a standard KF 40 flange. Three bars sliding through the body fix the position and orientation of a head containing the mirror. Lateral movement of these bars is prevented by three springs that push the bars aside. The axial motion of these bars is controlled from the outside by (differential) micrometers, where the vacuum seal is maintained by flexible metal bellows. The travel range of the bars, 6 mm, sets the possible displacement of the mirror. The head is pulled against hard metal spheres on the endpoints of these rods by two springs. By using two V shaped holes and one flat surface, every degree of freedom of the head is fixed exactly once.

the displacement of the minimum can be controlled very accurate; a differential current of a few amperes will shift the sample a few tenth of a millimeter. Third, the method would allow a simple way to make an (scanning) image of the H gas cloud.

3.5.3 Beam combination and overlap

A very important issue for seeing two-photon signals is to have overlap between the two colors in the focus in the cryogenic cell at all times. The beams are made co-propagating in the monochromator, where the dispersion of the second prism is used to combine the two beams from separate sources. The beams are both centered in the monochromator exit diaphragm. Secondly, they are overlapped in the evacuated reference port on a 0.3 mm sized hole. Once the two beams are overlapped, the mirror that directs them into the reference port can be retracted. In principle the beams then remain co-propagating, because they only pass through flat windows at (close to) normal incidence and are reflected once from a mirror.

However, because of the large difference in index of refraction for the two colors, ($n_{122\,\mathrm{nm}} - n_{656\,\mathrm{nm}} = 0.25$), wedge angles in the windows must be smaller than 0.1μrad in order not to

ruin the overlap. With these precautions taken into account, the method works so well that we were never able to increase the two-photon signal by adjusting the overlap after withdrawing the mirror.

Apart from positional overlap, the L_α and H_α pulses must have temporal overlap in the sample cell, while the gated detectors must be triggered synchronously. This was achieved by dividing the master trigger from the computer into two signals, each with its own series of various adjustable delays to accommodate the different switching times of the excimer laser, the shutters, AOMs and detector gates. Note the variation in time scale: The shortest time scale is the VUV pulse duration (10 ns), while the shutter must be triggered 1 ms before it must be open.

In order to discriminate a two photon signal in the L_α spectrum, the possibility was created to alternate between full and no temporal overlap. The situations of full and no overlap were checked by measuring the H_α pulses just before entering the monochromator and the UV scatter from the monochromator with the same detector. The difference in path length to the cell is then less than 10 cm, which reduces the measuring error to less than 0.3 ns. It was found that the L_α pulses drifted 100 ns relative to the H_α pulse in a few hours, caused by drifting of the potentiometers of the analog delay lines.

3.5.4 Adjustable L_α attenuation in a gas cell

For non-destructive detection of ultracold H gas, it is necessary to reduce the number of photons to a level where each atom absorbs on the average much less than one photon. However, reducing the L_α power by reducing the UV power is not a good idea, because the reference detector in the monochromator is not as sensitive as a PMT and its signal will become noisier with less VUV light. Therefore, the beams are led through a gas cell which will attenuate the L_α but is completely transparent for visible light. The transmission T of non-resonant VUV radiation through gases is well described by the law of Lambert-Beer

$$T = e^{-\mu p L}, \tag{3.2}$$

which is here written as a function of the pressure p and path length L. The only parameter is the extinction coefficient per unit length per unit pressure, μ. For a given gas, μ is almost constant[31]. In order to choose a suitable inert gas for our purpose, we measured the transmission of dry air, dry nitrogen and pure carbon dioxide. The results are shown in table 3.2. The measured CO_2 value coincides with literature values[32]. Ref. [32] gives a value of $\mu < 0.001\,\mathrm{cm}^{-1}$ for the L_α absorption coefficient of N_2. The discrepancy with our measurement is perhaps due to contamination of the nitrogen, obtained from liquid N_2 boil-off, with water vapor. The air was dried by leading it through $-20°$ coldtrap with all metal tubing. For comparison also the literature value for O_2 is given[33].

gas	μ ($atm^{-1}cm^{-1}$)
ambient air	>> 10
dry air	0.12
N_2	0.15
CO_2	1.9
O_2	0.23

Table 3.2: Measured absorption coefficients μ for L_α of several gases. The value for oxygen is a literature value[33].

The large absorption in ambient air is probably caused by water. Because it is known for adsorbing on clean surfaces, however, water is not very suited to be used as a medium for an absorption cell. CO_2 has a reasonable extinction length at convenient pressures, is inert and easy to store. That is why we relied on it as the effective medium in our L_α absorption cell.

The CO_2 was trapped in the volume between the monochromator, and a MgF_2 window just below the cryostat, as indicated in Fig. 3.7. If the maximum power is an issue and the gas cell is not needed, a factor two in L_α intensity can be gained by removing this last optical element. Since we do not continuously flow clean CO_2 through the gas cell, it is important to keep the interior very clean. The pressure in this volume was monitored by an oil free mechanical pressure gauge. It was filled with up to 30 mbar CO_2, attenuating the L_α with roughly a factor 10 per 10 mbar. After filling we noticed an increase of the L_α transmission on a time scale of a few minutes, probably due to disappearing contamination of water from the CO_2 source, but after approximately 5 minutes it was stable for the rest of the day. As a future improvement a gas flow system could be constructed to remove contaminations and to guarantee a constant gas composition and pressure.

3.5.5 Transmission measurement

To allow the use of convenient detectors at room temperature, the VUV and visible H_α light is sent entirely through the cryostat, as seen in Fig. 3.7. The optical detection above the cryostat can operate in two different modes. In the first one a mirror is placed in the beams to have a (indirect, i.e., via two mirrors) line of sight from the top of the cryostat entirely through the cryostat vacuum and the gas cell to the port for the visible-light input of the monochromator. This mode was essential for the coarse alignment and visible inspection of the light path in case of signal loss. In the second mode the mirror is pulled out and the L_α can fall on the solar-blind photomultiplier (Thorn EMI G26H315 with RF shielded housing). The PMT has its front surface at high voltage. The PMT housing is sealed with rubber O rings onto this surface and the cryostat vacuum was sealed with an extra MgF_2 window. This has the advantage that the

PMT can be replaced without much effort, and removing the PMT provides a line of sight into the cryostat which is more direct than via the mirror. Both of the properties turned out to be very useful during operation. The H cloud which is illuminated from below by the L_α is imaged onto a plane above the cryostat. In principle this enlarged image of the H cloud could be observed by a sensitive enough camera, but we placed a knife-edge beam profiler on this place. The knife edges allow the determination of the position of the L_α and H_α beam, as well as their spatial profile.

The quantum efficiency of the PMT was specified by the manufacturer to be 9.6 % at 122 nm. It has a 'solar blind' CsTe cathode behind a MgF_2 window. Nevertheless the PMT was found to respond to the intense H_α beam, be it with a quantum efficiency between 10^{-9} and 10^{-10}.

3.6 The cryostat

In order to attain the required low temperatures to have a superfluid film of helium on the walls with negligible background vapor, the sample cell inside the magnetic trap is cooled by a dilution refrigerator (Oxford Instruments "300 μW economy") to below 100 mK. The cryostat was modified to have optical access along the axis. Also a sealed magnet tank containing the trapping field coils was constructed below the mixing chamber[34].

3.6.1 The trap

The magnetic trap used in our experiments was designed and built by Van Roijen *et al.*[35, 34]. It consists of four axially symmetric coils and four racetrack-shaped (oval) coils. The four axially symmetric coils are referred to, from top to bottom, as the 'upper axial' (U), the 'Majorana' (M), the 'lower axial'(L) and the 'dissociator' (D), as can be seen in Fig. 3.10. The four oval coils are connected in series and are usually referred to as 'quadrupole' (Q). Together the coils form a trap of the Ioffe type[36], which was first proposed by Pritchard for neutral atoms[37]. The dissociator coil can generate fields up to 5 T, driving the low-field seeking H atoms produced in the dissociator towards the trap center situated near the Majorana coil. Therefore the Majorana coil is particularly suited to control the magnetic-field minimum. If this minimum is approximately zero, so called Majorana spin flips rapidly remove atoms from the trap. The cross sections of the four dipole coils are rectangular and their geometry is completely characterized by the numbers given in table 3.3. The racetracks have square cross-sections of thickness $t = 10$ mm. The centers of the four inner current bars are at a radius of 14 mm, the centers of the four outer bars are at a radius of 49 mm from the central axis of the trap. A more detailed description of the construction of the trapping magnet assembly is given by Van Roijen[34]. For a detailed description of the magnetic field calculation of the trap in general and in some specific current configurations in particular, the reader is referred to

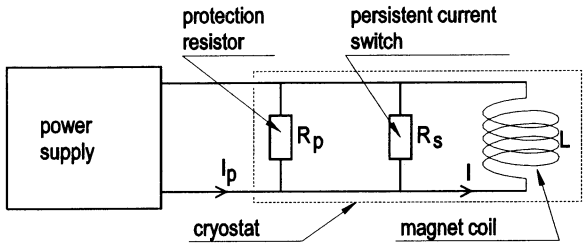

Figure 3.9: Circuit diagram of a superconducting magnet together with its superconducting switch and protection resistor.

the thesis of Luiten[4]. Here we would like to focus on some constructional aspects of the trap which are relevant when using it to reach low temperatures by forced evaporative cooling.

Apart from the high magnetic fields that are attainable, another advantage of superconducting magnets is that one can use them in persistent mode. In this mode the current loop is closed by a superconducting switch (see Fig. 3.9) and the current will circulate with negligible attenuation. The power supply can be removed and boiling off of the helium in the bath is reduced because the resistive wires up in the cryostat no longer dissipate. There is, however, always the risk of a quench, a self amplifying process in which a small part of the coil wire is no longer superconducting, which will then start dissipating, heating up neighboring superconducting wire to above their critical temperature, causing more dissipation etc. To prevent damage in case of a quench, every coil has its own protection resistor parallel to the coil (Fig.3.9). These resistors of typically $R_p = 0.5\,\Omega$, are placed high up in the helium bath and dissipate most of the heat stored in the magnetic field in case of a quench. During normal operation they do not carry any current because their impedance is much higher than that of the superconducting magnet. However, this situation changes during run up or down of the coils. The voltage U needed to make the current through a coil I change with a rate dI/dt is simply

$$U = L\frac{dI}{dt}. \tag{3.3}$$

The inductance L of a superconducting magnet coil is usually large, in our case of order 1 H. If one attempts to change the currents through the magnets rapidly, U can be large and a substantial amount of the current going through the leads to the cryostat will actually go through the parallel resistance R formed by the protection resistor R_p and the resistance R_s of the normal (i.e., not superconducting) persistent mode current switches. Another side effect of the finite parallel resistances and the large inductances is, that if one abruptly sets a new current I_p on a power supply, the current through the coil is approaching this only with a relaxation time

$$\tau = \frac{L}{R}, \tag{3.4}$$

which is of the order of 1 second for our trap coils. It can therefore take many seconds before the

coil	N	z_c (mm)	a (mm)	h (mm)	t (mm)	R (Ω)	L (H)	I_{max} (A)
Q	1680	0			10	0.37	1.41	36
U	1813	50	24	12	11.8	0.19	0.229	40
M	4335	0	24	8	9.3	0.42	1.4	5
L	1726	-50	24	12	12.5	0.46‡	0.206	40
D	7893	-131	22	50	16	0.14‡	2.24	40

Table 3.3: Some properties of the coils of the trap. Listed are the number of windings N, the position of the center z_c, the inner radius a, the length along the z-axis, h, the thickness t, the measured parallel resistance R, the inductance L and the maximum current I_{max}. The resistances are measured by observing current and voltage during (dis)charge, except for the R values marked with ‡, which are measured ac.

magnetic field B has equilibrated. This means that if one does not take these effects into account when programming a forced evaporation ramp reducing the trap depth to a few millikelvin, one can easily pass through a field geometry with no trap at all. This example demonstrates that it is necessary to know the resistances and inductances of the coils accurately. Therefore we measured the self inductances and the effective parallel resistances by charging and discharging a magnet, measuring the voltage across and the current through the magnet simultaneously. The self-inductance L follows then from Eq. 3.3. The exponential decay curves at the end of such a measurement immediately give the effective resistance R via Eq. 3.4. The results are tabulated in table 3.3. In principle also the mutual inductances can be measured in this way, but these are in general much smaller and were neglected. The results for the inductances of the dipole coils were compared with the results of a numerical calculation for simple circular coils with rectangular cross-sections matching the true shapes. The measured self-inductances L of the three small dipole coils confirmed the calculations within experimental accuracy. The self-inductance of the dissociator coil was not measured and for the four quadrupole coils no calculated L was available. The effective parallel resistances were also measured by an ac method. The results of both series of R-measurements coincided within 10 %. The trap can be improved to allow rapid magnetic field changes by removing (some of) the persistent current switches and using larger values for (some of) the protection resistors.

The entire trapping magnet assembly is fit into a stainless steel tank which is filled with liquid helium during operation. The magnet tank has a 16 mm diameter free bore in which the copper cell is centered. The stainless steel that is used is nominally non-magnetic (type "304"). However, with a small permanent magnet we noticed that it is not anymore. It is unknown if this is caused by the thermal cycling, the high magnetic fields or a combination of both. Obviously, this fact limits the calculability of the magnetic field. It is therefore advisable to

avoid stainless steel in a possible second generation trap and rely, for instance, on a titanium alloy.

3.6.2 The experimental cell

The atomic hydrogen is produced by cryogenic dissociation of molecular hydrogen. This dissociator is the same as the one used by Luiten[4] and its operation is described in chapter 2. Its location is indicated in Fig. 3.10. It is thermally linked to the heat exchangers of the dilution refrigerator. After being produced, the high-field seeking H atoms are removed on a pumping "bolometer"[34], situated in the high magnetic field near the dissociator. This is a thin resistive plate suspended between two thin conducting wires. By forcing a small current through the wires, the helium film on the plate can be evaporated, while the replacement flow of helium is limited by the very small cross section of the thin wires. If the helium film has been boiled off, the resulting bare surface will act as cryopump for atomic H. The word bolometer is put between quotes here because it is not used to measure the deposited heat, as the word bolometer would suggest. The cell in which the low-field seekers are trapped is depicted in Fig. 3.10. It is basically a hollow tube, made of high-purity copper for good thermal conductivity. The cell and the dissociator form an enclosed volume, apart from the filling capillary. The cell used by Luiten[4] and Setija[3] had a single MgF_2 window for optical access from below and a photodetector at the top. To improve optical access and in order to allow room-temperature detection, the cell was modified. A lens was inserted to guide the light out of the experimental cell and the cryostat, after passing through a 3 mm diameter hole in the mixing chamber.

After the removal of the photodetector out of the cell, there is a finite magnetic barrier over which the atoms can escape. For removal of these escaped atoms, a small pumping "bolometer" is installed near the lens on the upper side of the cell. It is made out of a $3.3 \times 3.0\,mm^2$ Kapton foil covered with aquadag, an aqueous dispersion of carbon powder, and suspended from two $16\,\mu m$ diameter tungsten wires (see Fig. 3.10).

3.6.3 Local cryogenic detectors

With the optical path through the cryostat, the main detection of light is conveniently done at room temperature. However, the cryogenic environment allows the application of some very sensitive additional detectors. These detectors are mounted on a thin walled tube inside the experimental cell. The electrical connections to the detectors are made of copper stripes on the surface of a $50\,\mu m$ thick Kapton sheet glued on the inside of the thin walled tube. Opposite to this Kapton sheet half of the circumference of the copper tube with a length of 13 cm length was removed for assembly of the detectors, making the hollow copper tube resemble an "apple corer".

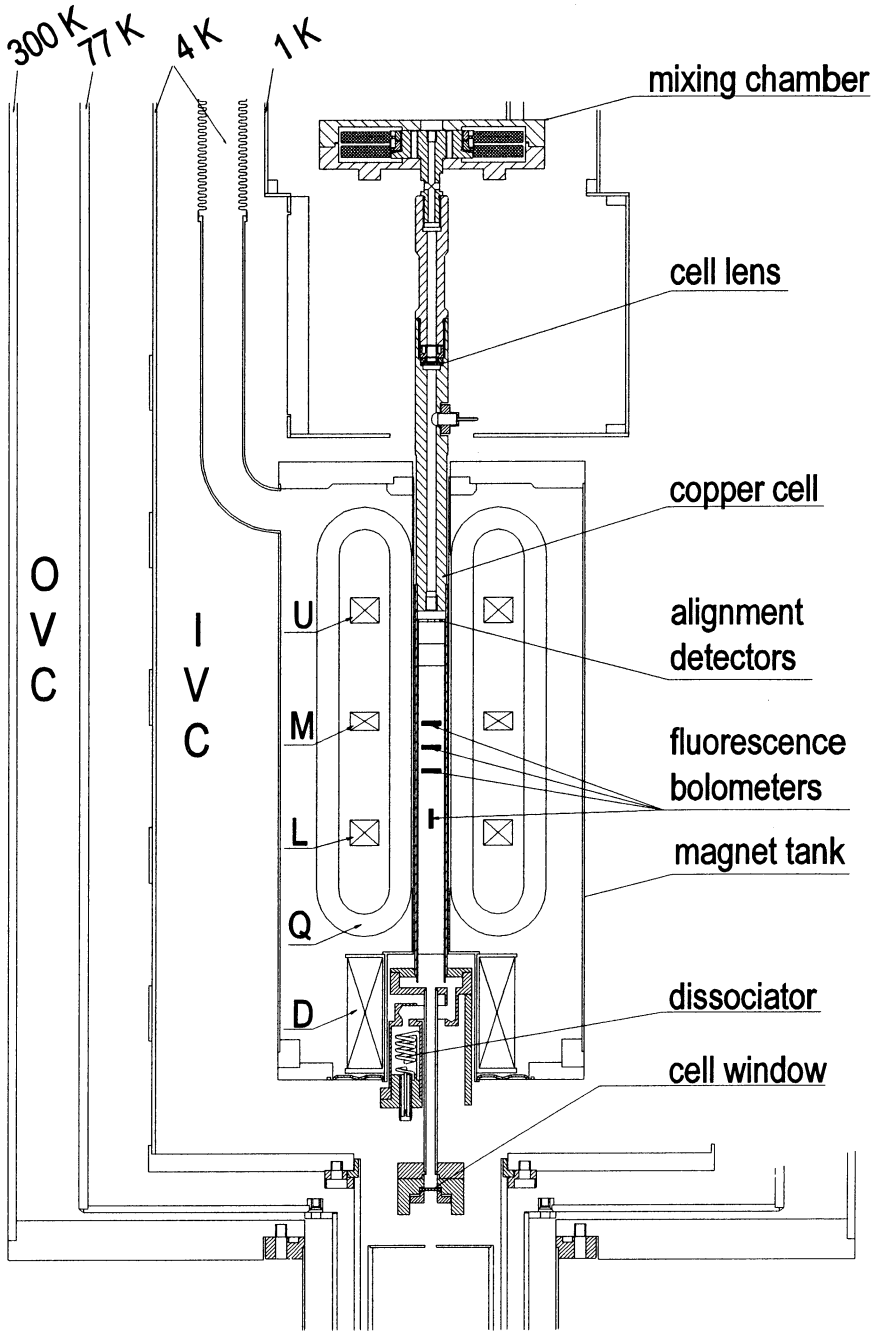

Figure 3.10: Drawing of the experimental cell inside the magnet tank and a part of the cryostat.

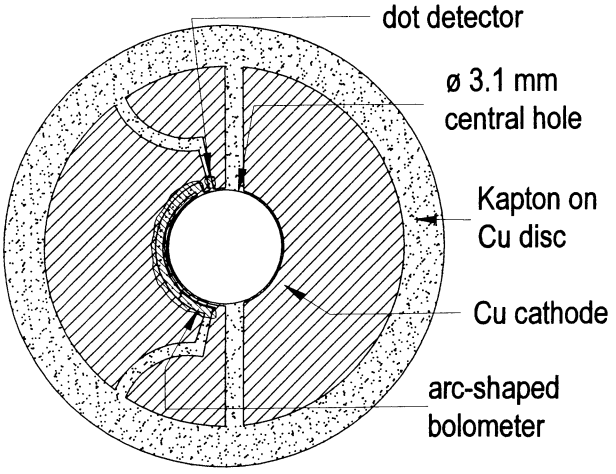

Figure 3.11: Drawing of the cryogenic alignment bolometers and the Cu electrode.

The first series of cryogenic detectors are 4 fluorescence detectors. These detectors are bolometers in the usual sense of the word, i.e., resistors with a large temperature coefficient dR_{bolo}/dT and a small heat capacity. When the bolometer is thermally poorly linked to its environment, a small amount of dissipated energy will result in a large change in resistance. This can be measured by observing the voltage drop over the bolometer through which a bias current is sent. The fluorescence detectors are made of Aquadag, painted directly on the Kapton sheet. They were read out by 4 cryogenic FET amplifiers. For a detailed discussion of the sensitivity and response time of these bolometers the reader is referred to Ref. [4]. Because the detected L_α fluorescence is masked by the much stronger H_α scatter, these detectors are not used during the two-photon measurements.

The second series of cryogenic detectors are designed to aid the alignment of the beams in the cell. They are situated on a 1 mm thick copper disk at the end of the 'apple corer' (see Fig. 3.10 for their location). A layout is shown in Fig. 3.11. The copper disc has a 3.1 mm diameter hole in the center to let the light beams pass. There are two Aquadag detectors and one bare copper photocathode. The copper electrodes of these detectors were made by photolithography on a 50 μm thick Kapton sheet, which was glued on the copper disk. Extra care was taken to place the detectors as close to the central hole as possible. Over and between three of the electrodes a few layers of Aquadag were painted. The resistance of the copper electrodes is negligible compared to the resistance of the Aquadag, and the sensitive area of the detectors is determined by the layout of the electrodes.

The largest of the alignment bolometers is an arc-shaped bolometer, as can be seen in Fig. 3.11. After preparation and drying it had a room temperature resistance of approximately 330 Ω. The room-temperature value fluctuates, probably because of the varying humidity in ambient atmosphere. At base temperature (85 mK) in the cryostat it had a resistance of 31 kΩ.

(This can only be measured with currents smaller than 10 nA. For higher currents the IV-curve is not linear because of Ohmic heating of the bolometer.) The gap between the electrodes of the arc-shaped bolometer is 0.16 mm wide and has a radius of curvature of 1.8 mm. It occupies 142° on the perimeter and is therefore relatively easy to hit with the L_α or the H_α light beam. Following the edge of this bolometer, one can then direct the beams onto the small dot-shaped bolometer, with an approximate rectangular shape of 0.2 mm×0.08 mm. After preparation this bolometer had a room-temperature resistance of approximately 725 Ω. At base temperature (85 mK) in the cryostat it had a resistance of 110 kΩ.

The alignment bolometers provide a method for overlapping the L_α and the H_α light. Because these bolometers are close to the actual sample position, uncertainties in the overlap caused by asymmetric contraction or stress in the MgF_2 windows after cool-down are eliminated. The alignment detectors could be read out without cryogenic amplifiers. The bolometers were all cooled down to < 100 mK and found to operate satisfactory. Fortunately, the overlapping and alignment in the room-temperature reference system worked so well that it was rarely necessary to use the cryogenic alignment detectors.

For room-temperature alignment one can use the copper photocathode which occupies almost half of the disc. The copper cathode was capable of detecting the L_α radiation until a helium film was admitted in the sample cell. Apparently, the He film prevents the photocurrent from the Cu substrate back to ground elsewhere in the cell.

3.6.4 Improved optical access

Since the MgF_2 optics sealing the cell (see Fig. 3.12) look out on the room-temperature vacuum systems above and below the cryostat, there are stringent vacuum requirements to prevent gases from condensing on the cold optics. To prevent contamination out of the outer vacuum can (OVC), the light passes the OVC through a tube separating the OVC from the inner vacuum can (IVC) of the cryostat. To check if the IVC provides a sufficiently clean vacuum, we measured the L_α transmission of the cryostat with a MgF_2 window near the mixing chamber. Prior to cooling down we flushed the IVC with pure nitrogen gas and pure helium to remove contaminations, always flushing in the direction of the oil diffusion pump. When cooling down we kept helium in the IVC at a few hundred millibars as a buffer gas to prevent contaminations to diffuse to the optics. Below nitrogen temperature, all likely contaminants are frozen and the buffer gas was removed. In addition, we kept the cell with the optics at a higher temperature than the rest of the cryostat as long as possible. Exercising this care with the gas handling, we observed no deterioration of the L_α transmission of the system during a test lasting a week. Later this was affirmed during the measurement run, lasting for several months.

The pipe guiding the light through the OVC (see Fig. 3.12), is made of thin walled (0.2 mm) stainless steel to minimize the heat conduction from the room-temperature part to the 4 K shield

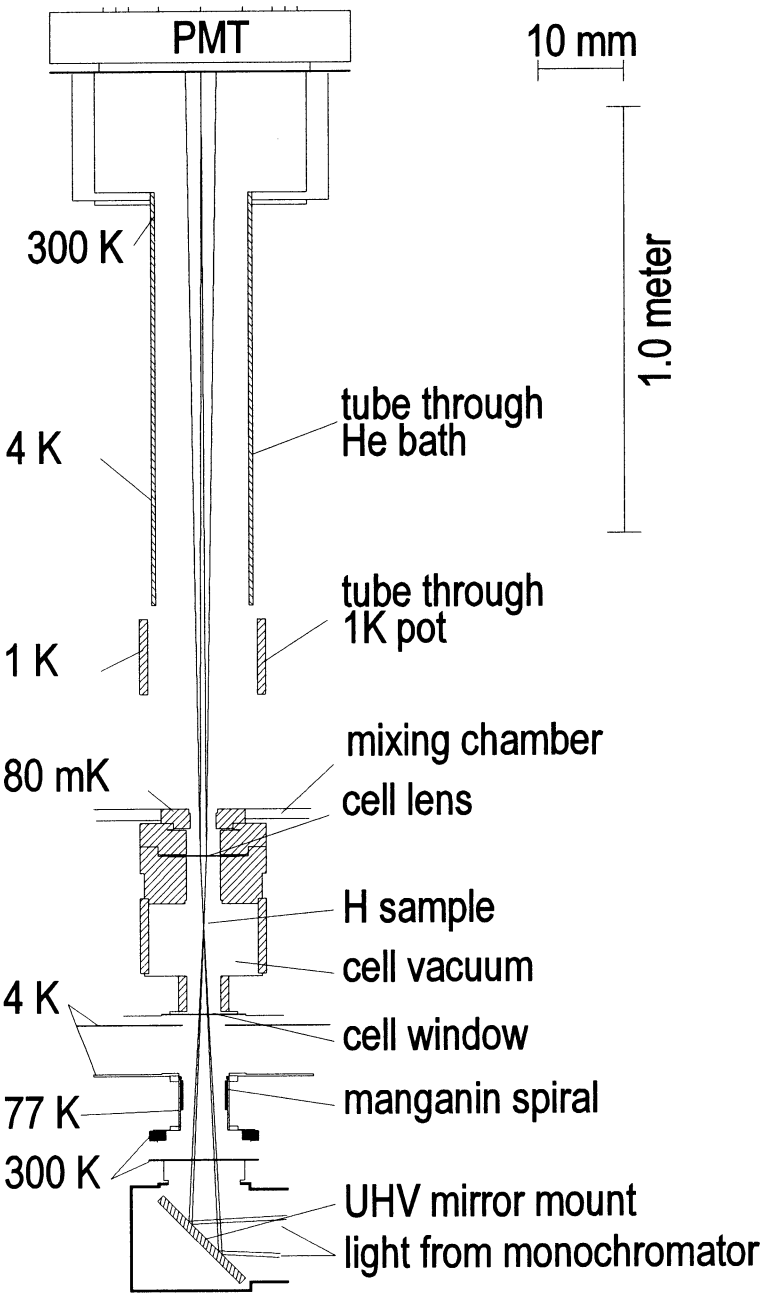

Figure 3.12: Drawing of the light path through the cryostat. The drawing is blown up with a factor 20 in the directions perpendicular to the light beams to emphasize the different aperture limiting elements.

of the cryostat. Half-way, the tube is thermally linked to the nitrogen shield of the cryostat. In order to prevent room-temperature infra-red radiation to funnel through the good reflecting 6 mm (outer diameter) stainless steel tube, a spiral of Manganin 0.28 mm diameter wire was inserted, soldered to the 4 K part of the tube and extending down to the 77 K link. The resulting free aperture was > 5 mm. Because the IVC can be kept clean enough to be used as VUV vacuum, no tubing was necessary above the pipe through the OVC. To reduce the radiative heat load on the cell even further, a 4 K radiation shield with an aperture of 5 mm diameter was placed in front of the window holder.

Because the distance between the mixing chamber and the top of the cryostat is 1.5 meter, the solid angle is small enough to make the direct radiation load from the top of the cryostat completely negligible. Funneling of infra-red radiation is effectively prevented by the gaps between the tubes through the He bath and the 1K pot, the cold plate and the mixing chamber.

Bibliography

[1] O.J. Luiten, H.G.C. Werij, I.D. Setija, M.W. Reynolds, T.W. Hijmans, and J.T.M. Walraven, Phys. Rev. Lett. **70**, 544 (1993).

[2] I.D. Setija, H.G.C. Werij, O.J. Luiten, M.W. Reynolds, T.W. Hijmans, and J.T.M. Walraven, Phys. Rev. Lett. **70**, 2257 (1993).

[3] I.D. Setija, Ph. D. thesis, University of Amsterdam (1995).

[4] O.J. Luiten, Ph. D. thesis, University of Amsterdam (1993).

[5] Rita Mahon, T.J. McIlrath, and David W. Koopman, Appl. Phys. Lett. **33**, 305 (1978).

[6] H. Langer, H. Puell, and H. Röhr, Opt. Commun. **34**, 137 (1980).

[7] R. Hilbig and R. Wallenstein, IEEE J. Quantum Electron. QE-**17**, 1566 (1981).

[8] Gary C. Bjorklund, IEEE J. Quantum Electron. QE-**11**, 287 (1975).

[9] L. Cabaret, C. Delsart, C. Blondel, Opt. Commun. **61**, 116 (1987).

[10] J.P. Marangos, N. Shen, H. Ma, M.H.R. Hutchinson, and J.P. Connerade, J. Opt. Soc. Am. B **7**, 1254 (1990).

[11] K. Hakuta, L. Marmet, B.P. Stoicheff, Phys. Rev. A **45**, 5152 (1992).

[12] O.J. Luiten, H.G.C. Werij, M.W. Reynolds, I.D. Setija, T.W. Hijmans and J.T.M. Walraven, Appl. Phys. B **59**, 311 (1994).

[13] Four-wave mixing in Mg-vapor, K.S.E. Eikema, personal communication.

[14] Tian-Jie Chen, R.N. Zitter, and R. Tao, Phys. Rev. A **51**, 706 (1995).

[15] Guy M. Weyl, David I. Rosen, Jack Wilson, and Wolf Seka, Phys. Rev. A **26**, 1164 (1982).

[16] Y.R. Shen, *The Principles of Nonlinear Optics*, chapter 27 (John Wiley & Sons, 1984).

[17] "Opti-clean polymer" by Merchantek, Inc., San Diego, California, USA.

[18] Handbook of Optics, Opt. Soc. Am. (Mc Graw-Hill, New York, 1978).

[19] P. Laporte, J.L. Subtil, M. Courbon, and M. Bon, J. Opt. Soc. Am. **73**, 1062 (1983).

[20] William A. VonDrasek, Shigeo Okajima, and Jan P. Hessler, Appl. Opt. **27**, 4057 (1988).

[21] Solon Technologies Inc. / Harshaw Crystal & dosimetry Products, Solon, Ohio, USA.

[22] W. Schneeberger AG Maschinenfabrik, CH-4914 Roggwil BE Switzerland.

[23] 'Fomblin', a perfluorinated grease, type RT15. Available from: Edwards high vacuum international, England.

[24] "Berek's compensator" from New Focus, Inc., Santa Clara, California, USA.

[25] D.C. Thompson, M.S. O'Sullivan, B.P. Stoicheff, and Gen-Xing Xu, Can. J. Phys. **61**, 949 (1983).

[26] G.C. Bjorklund, M.D. Levenson, W. Lenth, C. Ortiz, Appl. Phys. B **32**, 145 (1983); Wilfried Lenth, Opt. Lett. **8**, 575 (1983).

[27] L. Ricci, M. Weidemüller, T. Esslinger, A. Hemmerich, C. Zimmermann, V. Vuletic, W. König, T.W. Hänsch, Opt. Comm. **117**, 541 (1995).

[28] Andrew T. Young, Appl. Opt. **2**, 51 (1963).

[29] H.M. Araújo, V.Yu. Chepel, M.I. Lopes, R. Ferreira Marques, and A.J.P.L. Policarpo, Rev. Sci. Instrum. **68**, 34 (1997).

[30] J.M. Doyle and J.C. Sandberg, private communications.

[31] James A.R. Samson *Techniques of Vacuum Ultraviolet Spectroscopy* (J. Wiley & Sons, New York, 1967).

[32] R.W. Ditchburn, Proc. Roy. Soc. (London) **A236**, 216 (1956).

[33] Po Lee, J. Opt. Soc. Am. **45**, 703 (1955).

[34] R. van Roijen, Ph. D. thesis, University of Amsterdam (1989).

[35] R. van Roijen, J.J. Berkhout, S. Jaakkola, and J.T.M. Walraven, Phys. Rev. Lett. **61**, 931 (1988).

[36] Y.V. Gott, M.S. Ioffe, and V.G. Tel'kovskii, Nucl. Fusion, 1962 Suppl., Pt. 3, 1045 (1962).

[37] David E. Pritchard, Phys. Rev. Lett. **51**, 1336 (1983).

Chapter 4

Decay mechanisms

4.1 Introduction

Magnetically trapped atomic hydrogen is very stable and single gas samples have been observed to live for hours. On the other hand, very high density samples decay on the time scale of seconds. In this section various decay mechanism that influence the lifetime of a trapped gas of H↑ will be discussed, both theoretically and with the help of experimental results.

At high densities the dominant loss channels are inelastic H-H collisions, while at lower densities the gas is intrinsically more stable and external decay processes become more important. Examples of external decay processes are collisions with background (He) atoms and sample loss due to the influence of the (probe) light. As explained in chapter 2, magnetic trapping relies on the Zeeman energy shift of atoms with magnetic moments parallel to the magnetic field. The magnetic moments follow the direction of the field adiabatically, unless the magnetic trapping potential has a zero or near-zero magnetic-field minimum, leading to spin flips to non-trapped states. When considering trapping geometries, this Majorana decay is an important aspect. The effect of surface recombination on a magnetically trapped sample of which only the high energy atoms can reach the wall is discussed by Setija[1]. Evaporation of atoms out of a trap certainly reduces the number of atoms, but as evaporation cools the remaining gas, is not considered a decay process here. Moreover, in a trap of finite depth, evaporation of an otherwise stable gas automatically slows down because the repopulation of the high energy tail is exponentially suppressed by the diminishing temperature. Details about evaporation are given in chapter 7.

4.2 Intrinsic decay

The lifetime of low-field seeking hydrogen atoms stored in a magnetic trap is intrinsically limited by inelastic collisions between the trapped atoms. The fastest mechanism for these two-body

processes is spin-exchange relaxation. For this process to occur, admixture of the opposite electron spin is required, as is present in a or c atoms. Therefore, in a mixture of c and d atoms, the c atoms decay faster, leading to an almost doubly spin-polarized (i.e., pure d) H gas. The lifetime of the remaining gas is limited by dipolar decay, induced by the interaction between the magnetic moments of the two electrons involved.

The event rates for the various decay channels in inelastic H-H collisions have been calculated by Lagendijk *et al.*[2] and Stoof *et al.*[3]. Van Roijen *et al.* measured the collisional decay of a sample of trapped d state atoms and found it to be in agreement with theoretical predictions for dipolar decay [4, 5].

Consider a homogeneous system with constant temperature T, magnetic field B and density n_h of atoms in hyperfine state h (e.g., c or d). The number of events per unit time in which an atom in hyperfine state h_1 collides with an atom in hyperfine state h_2 leading to a pair of atoms in states h_3 and h_4, is simply $n_{h_1} n_{h_2} G_{h_1 h_2, h_3 h_4}(B,T)$, with $G_{h_1 h_2, h_3 h_4}(B,T)$ the two-body event rate constant associated with this decay channel. Usually one is only interested in the total loss rate constant $G^{h_3}_{h_1 h_2}$ for atoms of hyperfine state h_3 due to relaxation of two atoms in initial hyperfine states h_1 and h_2. $G^{h_3}_{h_1 h_2}$ is easily obtained by summing the involved event rate constant, as in the following example of the rate constant for loss of d atoms due to d-d collisions:

$$G^d_{dd} = 2(G_{dd,aa} + G_{dd,ac} + G_{dd,cc}) + G_{dd,ad} + G_{dd,cd}, \tag{4.1}$$

where the G's are functions of T and B.

In a magnetic trap matters are complicated somewhat by the inhomogeneous magnetic fields and density distribution. For a pure d state gas the decay of the density is then described by

$$\dot{n_0} = n_0^2 \langle G^d_{dd} \rangle \frac{V_{2e}}{V_e}, \tag{4.2}$$

or, equivalently,

$$\dot{N} = N^2 \langle G^d_{dd} \rangle \frac{V_{2e}}{V_e^2}, \tag{4.3}$$

where $\langle G^{h_3}_{h_1 h_2} \rangle \equiv V_{2e}^{-1} \int d^3r \, G^{h_3}_{h_1 h_2}(B(\vec{r}))[n(\vec{r})/n_0]^2$ is the trap-averaged rate constant, with V_e and V_{2e} the first- and second-order effective volume described in section 2.5.4. The trap averaging is important if the sample is contained in a deep trap at a relative high temperature so that the atoms sample a large range of magnetic fields. If $k_B T \ll \mu_B B_0$, with B_0 the magnetic field at the trap minimum, $\langle G^{h_3}_{h_1 h_2} \rangle$ is well approximated by $G^{h_3}_{h_1 h_2}(B_0)$. A better approximation to $\langle G^{h_3}_{h_1 h_2} \rangle$ is to evaluate $G^{h_3}_{h_1 h_2}$ at the average magnetic field experienced by the trapped atoms: $\langle G^{h_3}_{h_1 h_2} \rangle \approx G^{h_3}_{h_1 h_2}(B_0 + \gamma k_B T/\mu_B)$, where $\gamma k_B T$ is the average potential energy per particle as discussed in section 2.5.5.

If the fraction of the atoms in hyperfine state c is approximately constant, a rate constant G can be defined which describes the dipolar decay of the total density. For a given c-fraction

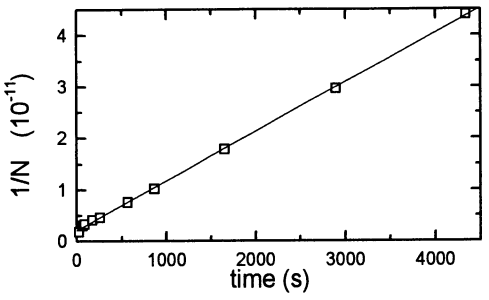

Figure 4.1: Inverse of the number of atoms N versus time in a Ioffe trap, indicating dipolar decay. The line is a fit giving an effective second-order decay constant $G_2 = (0.96 \pm 0.01) \cdot 10^{-14}\,\mathrm{s}^{-1}$. The average gas temperature during the measurement is 60 mK.

$\hat{c} \equiv N_c/N_d$, with N_c and N_d the number of c and d atoms, G is the weighed sum

$$G = (1-\hat{c})^2(G^d_{dd} + G^c_{dd}) + \hat{c}(1-\hat{c})(G^d_{cd} + G^c_{cd}) + \hat{c}^2(G^d_{cc} + G^c_{cc}), \tag{4.4}$$

evaluated at $B = B_0 + \gamma k_B T/\mu_B$. Due to spin exchange, the $\hat{c}$ in a typical H sample is quickly reduced from $\sim 50\,\%$ just after loading to $\sim 10\,\%$ after a minute, slowly decreasing further to the equilibrium value of order $3\,\%$ [5]. Therefore, the assumption of constant c-fraction is usually a good approximation for samples of more than a few minutes old.

4.2.1 Observation of dipolar decay

As an example, in Fig. 4.1 the evolution of the number of atoms is plotted. Here the trap (currents[6]: D35.0 L0.0 M0.0 U33.6 Q35.0) has a depth of 740 mK. The slow decay of N in time was found to be described by $N(t) = N(0)/[1+N(0)\,G_2\,t]$ as one would expect for a second-order decay process. The effective second-order decay rate constant $G_2 = (0.96 \pm 0.01) \cdot 10^{-14}\,\mathrm{s}^{-1}$ was found by following this particular sample for more than an hour. The fit is shown in Fig. 4.1. The observed decay rate translates (see section 4.2), for the average temperature of 50 mK, to a decay rate constant of $G = (4.0 \pm 0.8) \cdot 10^{-15}\,\mathrm{cm}^3\mathrm{s}^{-1}$. The error bar is due to the uncertainty in the temperature and, hence, the effective volumes. If we assume the expected $\hat{c} \approx 5\,\%$, the theoretical two-body decay rate evaluated at the average experienced magnetic field $B_0 + \gamma k_B T/\mu_B$ is $G = 3.5 \cdot 10^{-15}\,\mathrm{cm}^3\mathrm{s}^{-1}$, consistent with the data.

4.3 Background gas induced decay

In experiments with trapped alkali atoms, the main loss mechanism is usually collisions with background gas particles. At room temperature, the gas lifetime is usually limited to $\sim 100\,\mathrm{s}$ due to residual background gas, even in ultrahigh vacuum systems at the lowest attainable

pressures (of order 10^{-9} Pa). In a cryogenic environment the vacuum can be much better. In a dilution refrigerator even the vapor pressure of ^{4}He can be reduced to a negligible amount. For example, at the temperature where the refrigerator operated in the experiments described in this thesis, 80 mK, the equilibrium vapor pressure of ^{4}He is $< 10^{-37}$ Pa, truly negligible.

In the experiments of Setija[1], the ^{4}He vapor pressure was reduced to an extent that the sample decay was not limited anymore by the background gas. In some of the experiments described in this thesis, however, ^{3}He was admitted to allow higher densities of H to be loaded (see section 2.4). One might wonder if the much higher vapor pressure of ^{3}He does not cause extra losses, spoiling the gain in density resulting from the lower binding energy with the surface. In order to study the loss due to the ^{3}He background vapor, the cell temperature was stabilized at temperatures slightly above the normal operation temperature of $\sim$ 80 mK. A H$\uparrow$ sample was loaded in the experimental cell covered with a ^{3}He/^{4}He mixture film and evaporatively cooled to a temperature of 0.9 mK in a 10 mK deep trap. In this way a relatively low density sample was created, which was well isolated from the walls. At a cell temperature of 114 mK an exponential decay was observed with a decay time $\tau = 1.8 \cdot 10^3$ s. The saturated ^{3}He vapor pressure at 114 mK is $\sim 2 \cdot 10^4$ higher than at 80 mK. Under normal operation temperatures, in conclusion, the sample loss due to equilibrium ^{3}He background gas is completely negligible.

4.4 Light induced decay

In the experiments described in this thesis the trapped H$\uparrow$ is probed with light resonant with the Lyman-α (L_α) $1S - 2P$ transition in atomic H (see chapter 5), with a wavelength of $\lambda_L = 121.57$ nm. Ideally, the light necessary for observing the trapped H does not influence the sample at all. However, reality is less ideal. The light can directly influence the sample basically in two ways:

1. The L_α can pump c or d atoms to a non-trapped (a or b) state. Only the $d \leftrightarrow 2P_{3/2}(3/2)$ closed cycle transition is immune for this type of decay. Groundstate d atoms excited in all other transitions have a finite probability to decay to a non-trapped state.

2. Atoms that fall back to trapped states experienced two momentum kicks: one in the absorption process and one with the emission of a L_α photon. This can be exploited for laser cooling as in the demonstration of Doppler cooling of magnetically trapped H$\uparrow$ by Setija *et al.*[7]. However, usually the recoil increases the energy of the atom on the average with $2E_r$, where $E_r = \hbar^2 k^2/2m$ is the recoil energy, with m the mass of the atom and k the wave vector of the light. For the L_α transition in atomic H, $E_r/k_B = 0.64$ mK. If the trap in which the atom is excited is much deeper than 1.28 mK, the atom is not lost, but the extra heat is distributed over the entire sample by thermalizing collisions. On

the average this will lead to the evaporation of $2E_r/\epsilon_t$ atoms for each atom that returns to a trapped state.

In normal operation the number of photons scattered in a measurement should therefore be kept low in comparison with number of trapped atoms, especially at low temperatures, and preferably the $d \leftrightarrow 2P_{3/2}(3/2)$ closed-cycle transition should be used for non-destructive probing.

The optical pumping to non-trapped states, usually considered a nuisance, can be turned into a useful tool for cooling dense samples of trapped gas. The optical density prevents the light to penetrate the dense cloud. Hence, the light will be absorbed by atoms in the outer wings of the sample and remove a substantial fraction of them by optical pumping. This so called "light-induced evaporation" (LIE) was studied in detail by Setija *et al.*[7, 1] .

4.5 Majorana decay

In a magnetic trap the amplitude as well as the direction of the magnetic field are necessarily functions of position. As explained in section 2.2 the spins of the atoms usually follow the direction of the field adiabatically. For a trap with $B_0 \gg 0$ this is a very good approximation. However, if $B_0 \approx 0$, this adiabatic approximation breaks down leading to a finite spin-flip probability. These Majorana spin flips occur when the rate of change of the magnetic field is faster than the Larmor frequency associated with the spin-flip transition.

Bergeman *et al.*[8] performed a theoretical study of the decay in a (two-coil) magnetostatic quadrupole trap due to Majorana spin flips. They concluded that the decay of the lowest levels is probably too rapid for studying Bose-Einstein condensation (BEC) in such a trap. Indeed, BEC was first observed in traps where the zero-field region was "plugged"[9, 10]. BEC is also observed in traps which have an intrinsic non-zero minimum: in a so called "cloverleaf trap" with sodium[11], with lithium in a permanent magnet trap[12], and with sodium in a magnetostatic "baseball" trap[13]. All these traps create magnetic field configurations that are essentially of the Ioffe type and, hence, suppress Majorana spin flips.

In a Ioffe trap with an extra trim coil near the center of the trap, the magnetic field at the trap minimum can be tuned close to zero. Doing so increases the confinement near the trap center. This is for instance necessary when making a potential resembling a power-law potential with a large γ to study the effect of the shape of the potential on the phase-space density as is discussed in chapter 6. If $B_0 \approx 0$, also in a Ioffe trap Majorana decay can be expected. One can go further and locally invert the magnetic field, in which case there are always two true magnetic field zeros resembling small magnetic quadrupole traps. By inverting the current in one of the dipole coils of a Ioffe coil configuration, also a quadrupole trap can be made. In contrast to the simple anti-Helmholtz (two-coil) quadrupole trap, the Ioffe-based quadrupole can be very elongated.

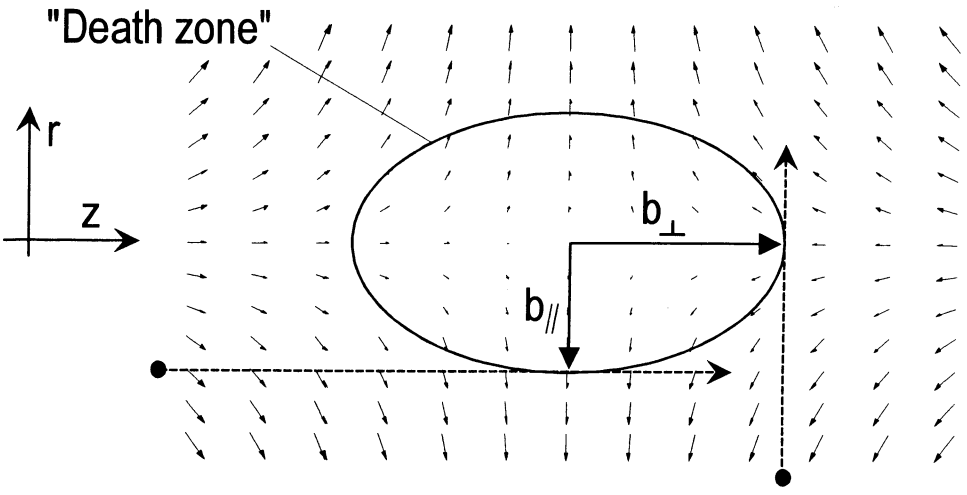

Figure 4.2: Cut through the xz plane of the region around the zero of a quadrupole trap. The arrows indicate the size and the direction of the magnetic field. Depicted are two possible trajectories of an atom skimming the "death zone", in which they will be lost from the trap because of Majorana spin flips.

In the following sections a first step will be made towards predicting the Majorana decay rates for H in various trapping configurations. A rough but zero-parameter estimation is made for the Majorana decay time in a quadrupole trap made with the coils of a Ioffe trap, which is relatively easy to analyze. The decay time in the case of a Ioffe trap with B_0 trimmed to or close to zero, is more difficult to analyze because it depends on the exact shape of the low-field region and is not examined in great depth. For both the quadrupole trap and the $B_0 \approx 0$ Ioffe trap a decay constant will be introduced and compared with data.

4.5.1 Estimation of Majorana decay rate

In a magnetic trap most H↑ is in the doubly polarized d state. The d atoms that experience an electron spin flip will end up in the c state, and will likely be lost from the trap rapidly because of spin exchange, which offers a fast decay channel for c atoms, as explained in section 4.2, especially at low magnetic field values[3]. The Larmor frequency associated with this transition is $B\mu_B/\hbar$, with $\mu_B/\hbar = 8.8 \cdot 10^{10}$ rad s^{-1}T^{-1} the gyromagnetic ratio of the transition. Consider an atom moving with thermal velocity $\bar{v}$ parallel to the z-axis of the quadrupole trap, at a distance $b_{||}$ of the z-axis (the particle moving horizontally in Fig. 4.2). The maximal rate at which the magnetic field vector changes, $\dot{\theta}_{max} = |\dot{\vec{B}}(\vec{r})|/B(\vec{r})$, occurs at $z = z_0$ and is roughly equal to $\bar{v}\alpha_z/B$, where $B = |\vec{B}|$. A d atom is likely to become a c atom if $\dot{\theta}_{max}$ exceeds $B\mu_B/\hbar$.

Furthermore, $B = \alpha b_{\|}$ if $z = z_0$. Hence, the atom is lost if it passes the minimum of the field closer to the z-axis than the critical distance

$$b_{\|} = \sqrt{\frac{\hbar\,\bar{v}\,\alpha_z}{\mu_B\,\alpha^2}} \tag{4.5}$$

In the same way, for an atom moving perpendicular through the z-axis, one can estimate the critical distance $b_\perp$ from the plane $z = z_0$:

$$b_\perp = \sqrt{\frac{\hbar\,\bar{v}\,\alpha}{\mu_B\,\alpha_z^2}}. \tag{4.6}$$

The above estimated points, where the flip probability becomes high may be connected and extrapolated to form a cigar like surface. Anywhere inside this surface the magnetic field will change its direction more rapidly than on this surface. The probability of hitting this volume can be quantified by the cross section σ. An indication of σ can be obtained by taking the surface area of a cut through this volume. Assuming an ellipsoidal shape, this leads to

$$\sigma = \pi\, b_{\|}\, b_\perp = \frac{\pi\,\hbar\,\bar{v}}{\mu_B\,\sqrt{\alpha\,\alpha_z}}. \tag{4.7}$$

From the cross section the lifetime of the gas is obtained via

$$\tau = \frac{V_e}{\sigma\,\bar{v}}. \tag{4.8}$$

For a quadrupole trap with constant radial gradient α and constant axial gradient $\alpha_z \ll \alpha$, the effective volume is

$$V_e = 4\pi \frac{(k_B T)^3}{{\mu_B}^3\,\alpha^2\,\alpha_z} = 4\pi\, r_e^2\, l_e, \tag{4.9}$$

with $r_e \equiv k_B T/\mu_B \alpha_z$ and $l_e \equiv k_B T/\mu_B \alpha$ the effective radius and length, respectively. Let us take a radial magnetic field gradient $\alpha = 172\,\mathrm{T\,m^{-1}}$ and an axial magnetic field gradient $\alpha_z = 6.9\,\mathrm{T\,m^{-1}}$, corresponding to the parameters of the experiment described in section 4.5.2. Substituting a typical loading temperature of 80 mK and a thermal velocity $\bar{v} \equiv \sqrt{8 k_B T/\pi m} = 41\,\mathrm{m\,s^{-1}}$ a decay time of $\tau = 60\,\mathrm{s}$ is expected for this quadrupole trap.

It should be stressed that this is only an order of magnitude estimate, because if the exact shape of the three dimensional ellipsoid were known, it is not clear which cut-through will give the effective cross section for thermal ensemble of particles moving in an anisotropic trap. Simply a particular choice was made. Moreover, the typical dimensions of the "death zone" depend on the direction of the velocity of the passing atom, and here only two test trajectories are taken.

The temperature dependence of the Majorana process follows a simple relationship as can be seen from the following argument: the cross section is linear in the thermal velocity: $\sigma \propto \bar{v}$.

Hence, $\tau = V_e/\sigma\bar{v} \propto T^3/v^2 \propto T^2$ and it makes sense to use a Majorana decay constant G_Q, for a given quadrupole trap defined by

$$\tau \equiv G_Q T^2 \tag{4.10}$$

for comparison with experiments. In the simple model sketched above, the Majorana decay constant amounts to

$$G_Q = \frac{m \pi k_B^2}{2\mu_B{}^2 \alpha^{3/2} \sqrt{\alpha_z} \hbar}, \tag{4.11}$$

which is a function of the hydrogen mass and the magnetic field gradients. The above estimated $\tau = 60\,\mathrm{s}$ at $80\,\mathrm{mK}$ corresponds with a Majorana decay constant of $G_Q = 9 \cdot 10^3\,\mathrm{s\,K^{-2}}$. The quadratic dependence on the temperature indicates that in a trap with a quadrupole-like minimum, Majorana decay will be particularly serious at very low temperatures.

As explained above, we do not try to estimate the Majorana decay in the case of a Ioffe trap where B_0 is reduced to zero. However, one qualitative remark can be made. Because $V_e \propto T^{5/2}$ for a Ioffe trap with $B_0 = 0$, the Majorana decay time is expected to scale with $T^{3/2}$. Because of the different scaling behavior, we introduce a new symbol, G_I, for the decay constant in a Ioffe $B_0 = 0$ trap:

$$\tau \equiv G_I T^{3/2}. \tag{4.12}$$

The constant G_I is expected to be dependent on the exact shape of the potential in the zero-field region(s).

4.5.2 Observation of Majorana decay

The first measurements of the inherent storage time limitations in a quadrupole trap due to the Majorana spin flips were reported for rubidium, by Petrich *et al.*[14]. Here, results will be presented on Majorana decay in magnetically trapped hydrogen, induced by creating a zero-field region for this purpose. The magnetic field profiles of the quadrupole trap that was used for the decay experiment are depicted in Fig. 4.3. It has a radial gradient of $\alpha = 172\,\mathrm{T\,m^{-1}}$ and an axial gradient of $\alpha_z = 6.9\,\mathrm{T\,m^{-1}}$. The effective volume $V_e = 0.38\,\mathrm{cm^3}$ is numerically obtained for the average temperature during the measurement 118 mK.

The trap of Fig. 4.3 was loaded with H↑ and the decay of the number of atoms was observed by L_α spectroscopy. The number of atoms is plotted versus time in Fig. 4.4. Just after loading the sample was still relatively hot (145 mK) but cooling down to $\sim 80\,\mathrm{mK}$ after 43 s by thermalization with the walls, in combination with evaporative cooling over the magnetic barrier in the z direction. At the same time, the sample is heated by the Majorana spin flips, which remove, preferentially, the cold atoms in the center of the trap. Because the Majorana heating scales linearly with the density n, but the evaporation proportional to n^2, the temperature rises again. At the end of the measurement we find $T = 157\,\mathrm{mK}$. As a consequence of the magnetic-field zero, the spectral lines overlap. This does not prohibit the spectroscopic thermometry at these

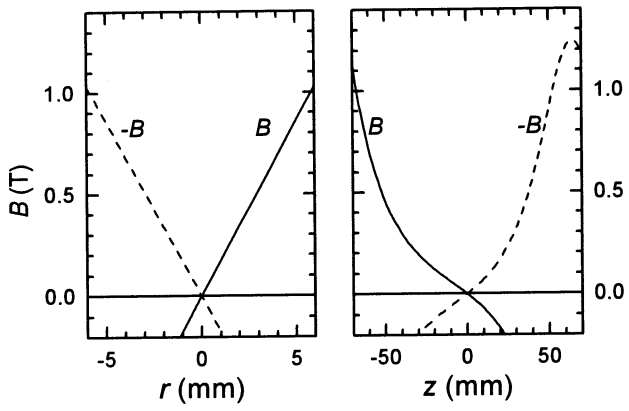

Figure 4.3: Magnetic field profiles of a quadrupole trap made by the magnets of our Ioffe trap with the current in one of its dipole coils inverted (current settings [6]: D35 L0 M0 U-33.7 Q28, depth 690 mK). Plotted is the magnetic field B as a function of radial distance r from the minimum (left graph) and as a function of the position on the z-axis (right graph) relative to the trap minimum. The dashed lines represent $-B$.

temperatures, but it is not possible to get an indication of the fraction of c atoms. The optical spectra are consistent with any c fraction between 0 and 50 %.

To obtain G_Q from the measured decay, the data was compared with theoretical decay curves, generated by integrating $\partial N/\partial t = N(t)[-1/G_Q T^2]$, taking into account the known time dependence of T. The result, $G_Q = (4.9 \pm 0.3) \cdot 10^3\,\mathrm{s\,K^{-2}}$ is plotted in Fig. 4.4 and is in agreement with the order of magnitude estimation made in the previous section. For the average decay temperature this G_Q corresponds to $\tau = (68 \pm 4)\,\mathrm{s}$. For comparison, in Fig. 4.4 also the evolution of the number of atoms in an "ordinary" ($B_0 \gg 0$) Ioffe trap is plotted, as was analyzed in section 4.2.1.

It is interesting to compare the results of the Majorana decay with the numbers reported by Petrich *et al.* for the case of cold ^{87}Rb in a spherical quadrupole trap[14]. These authors assume a two-coil quadrupole trap and define a decay constant A by the following relation with the lifetime of the gas:

$$\tau \equiv A r^2, \tag{4.13}$$

with r the radius of the gas cloud. Note that, assuming Eq. 4.9 and $l_e = r_e = r$, Eq. 4.13 gives the same temperature dependence for the decay time as Eq. 4.10. The constant A is only proportional to the atomic mass. Hence, the ratio between the mass of H and ^{87}Rb translates their observed $A = (3.7 \pm 0.7) \cdot 10^4\,\mathrm{s\,cm^{-2}}$ in an equivalent constant for H of $A_H = (4.3 \pm 0.8) \cdot 10^2\,\mathrm{s\,cm^{-2}}$. If l^2 is approximated by $(V_e/4\pi)^{2/3}$, a decay time of $\tau = (40 \pm 8) \cdot 10^2$ s is obtained for our situation at $T = 118\,\mathrm{mK}$. The small difference with the observed $\tau = 68 \pm 4\,\mathrm{s}$

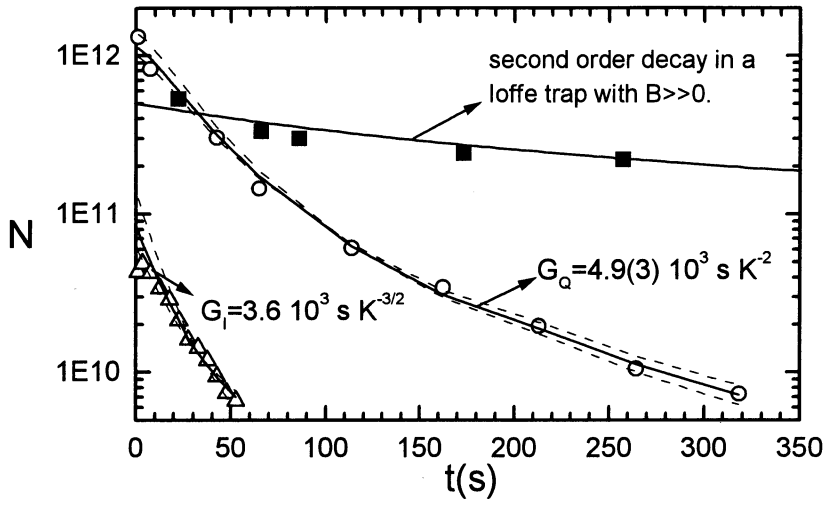

Figure 4.4: Majorana decay in a quadrupole trap (circles) and in a Ioffe trap where the minimum was trimmed to zero (triangles). The solid lines are fits to the data. The dashed lines correspond to the lower and the upper bounds to the fitted G's. For comparison also the decay of a sample loaded in an "ordinary" Ioffe trap is plotted (squares).

should lay in the anisotropy of our trap in combination, perhaps, with the different hyperfine structures of H and ^{87}Rb.

Majorana decay was also observed in a Ioffe trap where B_0 was set to ~ 0. After a H$\uparrow$ sample was loaded in the trap and had evaporatively cooled to an equilibrium temperature of $\sim 50\,\mathrm{mK}$, one of the magnet currents was changed to make $B_0 \approx 0$. Due to the Majorana decay the temperature increased monotonically to $T = 110\,\mathrm{mK}$ after 50 s, with an average of 77 mK. The observed decay of the number of atoms was fitted in the same way as the decay measured in the quadrupole trap above. The known temperatures were again taken into account, but this time using relation 4.12. The data and the fit curve are also plotted in Fig. 4.4. The result of the fit is $G_\mathrm{I} = (1.0 \pm 0.2) \cdot 10^3\,\mathrm{s\,K^{-3/2}}$. We attribute the small discrepancy at the start to the sensitivity of G_I to the exact shape of the zero-field region in combination with the time the superconducting magnets need to relax to their set value, which is of the order of 1 s, as described in section 3.6.1 of chapter 3.

The dependence of G_I on the exact shape of the zero-field region has not been studied. However, it was observed that G_I indeed depends critically on the exact shape of the magnetic potential. Trapping potentials with magnetic field minima that were 0.5 mT higher than in the above described experiment, showed no clear Majorana trap loss. On the other hand, when a change, barely exceeding the relative experimental accuracy of $\sim 1\,\mathrm{mA}$, was made in one of

the magnet currents, values of G_1 were found larger by a factor two, while the reduction in the magnetic field due to this current was less than 0.1 mT.

4.5.3 Observation of decay products

One expects that d atoms which experienced a Majorana spin flip and became a c atom, will be lost from the trap as an a or b atom because of spin exchange. The c atoms might also undergo another Majorana spin flip and turn into a b atom directly. Whatever the case, they will leave the trap as high-field seekers. To test if this could be observed, a sample of $\sim 4 \cdot 10^{11}$ H atoms was prepared in a trap with a small B_0. The L_α source was setup to scan over the frequency region in the optical absorption spectrum where a resonance line $[b \rightarrow 2P_{1/2}(1/2)]$ (see chapter 5) of the high-field seeking b atoms in the high-field region is expected. The high-field region was heated to prevent surface-catalyzed losses of H$\downarrow$, and after loading of the trap the H$\downarrow$-pumping "bolometer" (discussed in section 3.6.2) was switched off. Once the Majorana decay was triggered by reducing B_0, weak absorption lines could be seen at the expected frequency, with a maximal absorption of $\sim 10\,\%$ after approximately 50 s, consistent with the Majorana decay time measured in section 4.5.2. Here, the integrated surface under the asymmetrically broadened peak was found to be 0.445 GHz. Because the absorption was practically constant the next half minute, we neglect the decay in the produced H$\downarrow$ atoms and assume that the absorption is proportional to the total produced number of H$\downarrow$ atoms. Using the resonant cross section $\sigma_0 = 3\lambda_L/2\pi$ the column density of high-field seekers needed for this absorption is estimated to be $\sim 2.3 \cdot 10^{14}\,\mathrm{m}^{-2}$.

To get a lower bound on the total number of produced high-field seekers, let us for the moment assume that the H$\downarrow$ atoms only reside in the tube on the axis of the cryostat where the light enters the cell (see Fig. 3.10 in chapter 3 for a drawing of the cell). This tube has a cross section of $13\,\mathrm{mm}^2$, leading to a lower bound on the number of produced high-field seekers of $5 \cdot 10^9$ atoms, about 1% of the loaded low-field seekers. The real value must be higher 1) because we have neglected recombination, 2) because H$\downarrow$ will be pulled away from the axis, out of the L_α beam and 3) because, as can be seen in Fig. 3.10, there is more volume available in the high-field region than just the above mentioned tube.

Bibliography

[1] I.D. Setija, Ph. D. thesis, University of Amsterdam (1995).

[2] A. Lagendijk, I.F. Silvera, and B.J. Verhaar, Phys. Rev. B **33**, 626 (1986).

[3] H.T.C. Stoof, J.M.V.A. Koelman, and B.J. Verhaar, Phys. Rev. B **38**, 4688 (1988).

[4] R. van Roijen, J.J. Berkhout, S. Jaakkola, and J.T.M. Walraven, Phys. Rev. Lett. **61**, 931 (1988).

[5] R. van Roijen, Ph. D. thesis, University of Amsterdam (1989).

[6] The following convention is used for denoting the current settings of the trap: the current settings are preceded by a capital letter indicating through which coil the currents flow. "D" stands for the dissociator coil, "L" for the lower axial coil, "U" for the upper axial coil, and "Q" for the set of four racetrack-shaped (oval) coils, which are connected in series.

[7] I.D. Setija, H.G.C. Werij, O.J. Luiten, M.W. Reynolds, T.W. Hijmans, and J.T.M. Walraven, Phys. Rev. Lett. **70**, 2257 (1993).

[8] T.H. Bergeman, Patrick McNicholl, Jan Kycia, Harold Metcalf, and N.L. Balazs, J. Opt. Soc. Am. B **6**, 2249 (1989).

[9] K.B. Davis, M.-O. Mewes, M.R. Andrews, N.J. van Druten, D.S. Durfee, D.M. Kurn, and W. Ketterle, Phys. Rev. Lett. **75**, 3969 (1995).

[10] M.H. Anderson, J.R. Ensher, M.R. Matthews, C.E. Wieman, and E.A. Cornell, Science **269**, 198 (1995).

[11] M.-O. Mewes, M.R. Andrews, N.J. van Druten, D.M. Kurn, D.S. Durfee, and W. Ketterle Phys. Rev. Lett. **77**, 416 (1996).

[12] C.C. Bradley, C.A. Sackett, and R.G. Hulet, Phys. Rev. Lett. **78**, 985 (1997); C.C. Bradley, C.A. Sackett, J.J. Tollett, and R.G. Hulet, Phys. Rev. Lett. **75**, 1687 (1995).

[13] C.J. Myatt, E.A. Burt, R.W. Ghrist, E.A. Cornell, and C.E. Wieman, Phys. Rev. Lett. **78**, 586 (1997).

[14] Wolfgang Petrich, Michael H. Anderson, Jason R. Ensher and Eric A. Cornell, Phys. Rev. Lett. **74**, 3352 (1995).

Chapter 5

One- and two-photon spectroscopy

5.1 Introduction

5.1.1 Lyman-α spectroscopy

In situ diagnostics of magnetically trapped atomic H was first demonstrated by Luiten *et al.*[1, 2] who used a resonant optical technique to determine temperature and density of the cold gas in a non-destructive way. The method relies on narrow-band light with a wavelength $\lambda_L = 121.57\,\text{nm}$, which is resonant with the $1S - 2P$ transition (L_α, the first of the Lyman series) in H.

The L_α transition is electric-dipole allowed. If the atoms are polarized and the L_α light has the correct polarization, the maximal resonant cross section $3\lambda_L^2/2\pi$ applies. The L_α transition has a broad natural line width of $\Gamma/2\pi = 100\,\text{MHz}$, caused by the $1/\Gamma = 1.6\,\text{ns}$ radiative lifetime of the $2P$ state. For a gas of atoms in an inhomogeneous magnetic field, as present in a magnetic trap, the absorption spectra contain information about the spatial distribution because of Zeeman shifts. The velocity distribution is reflected in the Doppler broadening of the resonance lines. By comparing L_α transmission data with spectra calculated by integrating the differential equations describing the light propagation through the non-uniform gas[2], L_α spectroscopy allows the independent non-destructive determination of temperature and density with high sensitivity.

During the thesis work of Luiten[2] and Setija[3], the use of L_α spectroscopy for thermometry was limited to temperatures down to $\sim 3\,\text{mK}$. With the improved optical apparatus, described in chapter 3 of this thesis, measurements could be made down to approximately 0.5 mK, almost an order of magnitude lower. Examples of results obtained with this method are given in chapter 6 and 7. In order to extend the range of the L_α-based thermometry to even lower temperatures, the spectral resolution must be increased to resolve the smaller Doppler and Zeeman broadening at lower temperatures. The first step for the achievement of this goal was the development of a technique that is not limited by the natural line width of the $2P$ state.

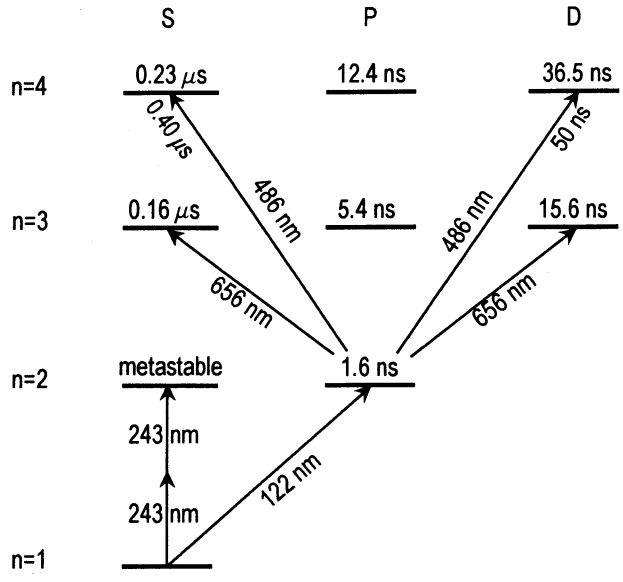

Figure 5.1: Level diagram of atomic hydrogen. Indicated are the levels with principal quantum number $n = 1, 2, 3$, and the wavelengths corresponding to the transitions. The numbers on top of the levels are the total lifetimes. For the relevant $n = 4 \rightarrow n = 2$ transitions the partial lifetimes are indicated.

The technique relies on a two-photon method, which is introduced in the next paragraph and will be the main focus of this chapter. The second step needed to take full advantage of this method, is reduction of the bandwidth of the L_α source, a technical rather than a physical problem, which has yet to be tackled. Some possibilities to achieve this are mentioned in the discussion in section 5.11.

5.1.2 Resonance-enhanced two-photon spectroscopy

To overcome the intrinsic limitation to the spectral resolution of L_α spectroscopy due to the 100 MHz radiative line width of the $2P$ state, we introduce resonance enhanced two-photon spectroscopy (RETS) of magnetically trapped atomic hydrogen[4]. In this method, the transition $1S - 3S$ or $1S - 3D$ (See Fig. 5.1) is excited via the near-resonant intermediate state $2P$ by stacking two co-propagating photons, one close to L_α (wavelength $\lambda_L = 121.57$ nm), and one close to Balmer-α, the first transition in the Balmer series (H_α, wavelength $\lambda_B = 656.47$ nm). The RETS method provides high sensitivity due to the resonant enhancement[5] of the transition matrix element by the $2P$ intermediate level. This enhancement depends on the detuning from the $2P$ level, which can be chosen at will. Hence, the absorption on the two-photon

resonance is adjustable; we speak of "tunable transparency", a very useful property when dealing with high density gases. At present the resolution of RETS is limited by our L_α source bandwidth (120 – 150 MHz), but ultimately the resolution is only limited by the lifetime of the $3S$ level ($\Gamma_{3S}^{-1} = 160$ ns) and $3D$ level ($\Gamma_{3D}^{-1} = 16$ ns), which are much longer than the $2P$ lifetime ($\Gamma_{2P}^{-1} = 1.6$ ns). Hence, RETS overcomes the intrinsic limitation of the resolution of L_α spectroscopy due to the broad natural line width of the L_α transition.

The small $3S$ line width in principle enables determination of the momentum distribution in H gas samples by Doppler spectroscopy down to temperatures below 1 μK, i.e., well below the BEC transition temperature at typical achievable densities (10^{14} cm^{-3}) in traps. In addition, the $1S(m_j = 1/2)-3S(m_j = 1/2)$ transition has no significant Zeeman shift. Therefore, the $1S-3S$ transition is an ideal reference line for calibration of the frequencies of the light beam used. Moreover, the insensitivity to the magnetic field can be a very useful property for thermometry in very dense gases in strong inhomogeneous fields: from the purely Doppler-broadened line shape the temperature is easily derived. The observation of the $1S-3S$ transition is described in section 5.3.4. The insensitivity to the magnetic field is observed qualitatively. However, the integrated intensity of this line is 30 times weaker than of the strongest $1S-3D$ transition, as is explained in section 5.4.1, and the signal-to-noise ratio on this line was too low to use the $1S-3S$ transition as a reliable thermometer during the work described in this thesis. Only after a reduction of the bandwidth of the L_α source, can a significant improvement in low temperature thermometry be expected.

RETS should not be confused with the Doppler-free $1S-2S$ two-photon spectroscopy, which was demonstrated for trapped H in 1996 at MIT[6]. This method uses two photons of wavelength $2\lambda_L = 243$ nm to excite the metastable $2S$ state. It has the potential of a very high resolution, because the $2S$ state has a very long radiative lifetime (~ 0.12 s), corresponding to a natural line width of 1.3 Hz. In contrast to RETS, $1S-2S$ two-photon spectroscopy is not resonance-enhanced. Consequently, large intensities are required. In the discussion (section 5.11) the two methods are compared.

In principle, RETS spectra can be recorded by varying either the L_α frequency or the H_α frequency. In the measurements described in this thesis, usually the H_α frequency was fixed and the L_α frequency was scanned. In the L_α spectra taken in the presence of strong H_α light, both the one- and the two-photon lines are expected. This has the advantage that we could record the one-photon L_α spectra almost simultaneously, simply by switching off the H_α beam. The L_α spectrum provides a useful reference frame to find the approximate positions of the levels used as resonant enhancer for the two-photon lines. Usually the resonant enhancement of a two-photon transition is dominated by a single $2P$ sublevel, which we will call the "resonant-enhancer level". With second-order perturbation theory, the strength of the two-photon lines can be calculated to a good approximation, in the limit that the one- and two-photon lines are well separated. However, the strong H_α light causes ac-Stark shifts on the single-photon L_α

lines and the two-photon lines. Actually, the strong H_α light mixes the one- and two-photon lines and it is no longer legitimate to speak of one- and two-photon transitions and the whole system is better described in the "dressed-states" formalism[7].

The precise calculation of the RETS spectra turns out to be quite involved. Fortunately, the experimental situation is well described by a weak L_α beam probing atomic states "dressed" by the strong H_α light. Therefore, we can use the complex susceptibility approach developed by Luiten *et al.*[2] to describe the propagation of the weak L_α through the H sample. In addition to the dependence of the susceptibility to the local magnetic field and density in the L_α spectroscopy case, the RETS susceptibility is also a function of the local H_α intensity.

5.1.3 Outline of this chapter

In this chapter L_α spectroscopy and RETS are explained. Because RETS relies on many of the details needed to understand L_α spectroscopy, the two methods are treated on equal footing. First, the relevant states of atomic H will be reviewed, especially their magnetic-field dependence. In section 5.3, the possible one- and two-photon transitions between the H levels are discussed. The relative strengths of the various L_α and H_α single-photon transitions are the subject of section 5.4. In section 5.5 the transition probabilities are discussed in a perturbative approach. The positions of the resonances is treated in the dressed-atom picture in section 5.6. By including the finite lifetime of the excited states, the line shapes of the RETS transitions in a uniform gas at zero temperature are calculated in section 5.7. In the case of well separated lines the line shapes can be understood as the consequence of several broadening mechanisms, which is the subject of section 5.8. The spectrum calculation using a description with a complex susceptibility tensor will be discussed in section 5.9, and the experimental results will be presented in section 5.10. The chapter concludes with a discussion of the limitations and future prospects of RETS.

5.2 Atomic hydrogen levels

Hydrogen is the simplest element of the periodic system and many of its properties can be calculated from first principles. Historically, the understanding of the H spectrum therefore stimulated the development of quantum theory. The gross structure of the H atom, already found in 1913 by Bohr, was subsequently refined by introducing the coupling between the angular momentum of the orbiting electron and the spin of the electron (fine structure), the influence of the spin of the nucleus (hyperfine structure), and the Lamb shifts, for which quantum-electrodynamical (QED) calculations were indispensable. Nowadays, high precision determination of the various Lamb shifts continues to push the correspondence of experiments[8, 9, 10] and theory[11] to unprecedented accuracies.

High resolution spectroscopy, however, is not the purpose of this thesis work. For diagnostics of the trapped gas it is sufficient to know the energy states of atomic H up to the experimental accuracy set by the L_α source bandwidth of about 120 MHz. However, to anticipate future improvements to the L_α source bandwidth, in this chapter the energies of the relevant levels will be calculated with an accuracy slightly better than the intrinsic line widths of those states. The nuclear spin is only important in the S (i.e., $l = 0$) states. For example, in the $1S$ ground state it leads to a splitting between the two low-field seeking hyperfine states of maximally 655 MHz. The hyperfine structure of most other excited states is less than their natural line width, can therefore not be resolved and will be neglected here.

The common spectroscopic notation of the atomic levels is $n\,^kL$ or $n\,^kL_J$, with n the principal quantum number, L the orbital quantum number (S, P, D, etc.), J the quantum number of the total angular momentum and k the spin multiplicity. Because the spin multiplicity is always 2 for H, this number will be omitted in the notation of the levels throughout this thesis. Later in this chapter the notation will be extended to include the magnetic quantum number m_j, leading to the notation $nL_J(m_j)$, as in the example $1S_{1/2}(1/2)$.

5.2.1 Zero-field energies

The Bohr formula[12] for the electronic levels of atomic hydrogen, states that the energy of a level relative to the ionization limit, which is taken as the zero of the energy scale, has a simple $1/n^2$ relation on the principal quantum number n:

$$E_{\text{Bohr}} = -\frac{hcR_\infty}{1 + m_e/m_\text{p}}\frac{1}{n^2}, \tag{5.1}$$

where h is Planck's constant, and $R_\infty = 109737.315685\,\text{cm}^{-1}$ is the Rydberg constant[13, 9]. The $(1 + m_e/m_\text{p})^{-1} = 0.999455679433$ factor[14] is a correction for the finite nuclear mass, with m_e and m_p the mass of the electron and the proton, respectively. Because E_{Bohr} only depends on the principal quantum number n, it is sometimes chosen as a reference energy for the fine structure. The Bohr energies of the ground state and the first two excited levels are -109677.583407, -27419.395852 and $-12186.398156\,\text{cm}^{-1}$, respectively.

Coupling between the magnetic moment of the electron spin and the magnetic field produced by its orbital momentum (for levels with orbital quantum number $l > 0$) gives rise to additional splitting. This effect is known as the fine-structure splitting, and involves treatment of the Dirac Hamiltonian, which is beyond the scope of this thesis. The Dirac values for the energy are quoted from the literature[15]

$$E_\text{D}(n,j) = \frac{2hcR_\infty}{(1 + m_e/m_\text{p})\alpha^2}\left\{\left[\left(\frac{\alpha}{n - j - 1/2 + \sqrt{(j+1/2)^2 - \alpha^2}}\right)^2 + 1\right]^{-1/2} - 1\right\}, \tag{5.2}$$

level	Lamb shift (MHz)	Reference	level	Lamb shift (MHz)	Ref.
$1S_{1/2}$	8172.80(5)	[10, 8]	$3S_{1/2}$	311.403(2)	[8]
$2S_{1/2}$	1045.003(9)	[17]	$3D_{3/2}$	-1.294	[19]
$2P_{1/2}$	-12.8367(3)	[18]	$3D_{5/2}$	1.211	[19]
$2P_{3/2}$	12.521	[19]			

Table 5.1: Experimental values for the $1S_{1/2}$, $2S_{1/2}$, $2P_{1/2}$, and $3S_{1/2}$ Lamb shifts, from various experimental [10, 8, 17] references. The $2P_{3/2}$, $3D_{3/2}$, and $3D_{5/2}$ Lamb shifts are calculated from the expressions in [19]. The error in these calculation is expected to be < 1 kHz, as estimated from comparison with the experimental value for the $2P_{1/2}$ Lamb shift. Note that the accuracies of these Lamb shifts exceed our present experimental resolution with orders of magnitude.

where α is the fine-structure constant. The Dirac energy also depends on the total angular momentum $j = l \pm 1/2$ of the atom. An important correction to this is a relativistic correction due to the non-separability of the Dirac equation for two charged particles into a center of mass and reduced mass system, which leads to an additive energy of

$$E_M(n) = -\frac{hcR_\infty \alpha^2}{4n^4}\frac{m_e}{m_p}. \tag{5.3}$$

The determination of the precise energy levels further includes corrections for the finite size of the nuclear charge distribution, a correction for the finite nuclear mass, and a correction arising from the full quantum-electrodynamical (QED) calculation. The combination of the nuclear mass, charge-distribution and the QED corrections is also known as the "Lamb" shift[16]. Precise values for the Lamb shifts are tabulated in table 5.1. The Lamb shifts are especially large in the S levels where there is a finite amplitude of finding the electron in the nucleus.

The results of the full calculation, i.e., the absolute energies of the atomic hydrogen levels, are listed in table 5.2. The energies are calculated using the equations of Ref. [19], but evaluated with the latest value of the Rydberg constant[9] and the modern values for the speed of light ($c = 299792458\,\mathrm{m\,s^{-1}}$, by definition), the fine-structure constant ($\alpha = 0.00729735308(33)$) and the electron-proton mass ratio ($m_e/m_p = 0.000544617013$), obtained from Ref. [14]. Finally, the latest experimental values were used for the Lamb shifts, if available (see table 5.1).

The hyperfine structure of the atomic hydrogen levels is caused by the interaction of the nuclear spin with the electron spin. An approximate solution can be obtained by treating the ordinary fine structure as a perturbation and the hyperfine structure as an even smaller perturbation. For brevity we just quote the approximate solution for the hyperfine splitting from the literature[15]:

$$a_\mathrm{h} = \frac{hcR_\infty}{(1 + m_e/m_\mathrm{p})}\frac{m_e}{m_p}\frac{2\alpha^2 g_n (j + 1/2)}{n^3(2l+1)j(j+1)}, \tag{5.4}$$

n	S	P		D	
4	102823.85302	102823.87907	102823.89432	102823.90340	102823.90950
			102823.84858		102823.89425
3	97492.22173	97492.28350	97492.31964	97492.34114	97492.35559
			97492.21122		97492.31946
2	82258.95440	82259.16304	82259.28500		
			82258.91912		

Table 5.2: Zero-field values of the energy levels in cm^{-1} above the ground state. For the P and D levels the energy is given for the two fine-structure levels separately, as well as for the center of gravity. Hyperfine splitting does not affect the position of the centroid of the hyperfine lines and is therefore neglected in the above values. The $2S$ experimental value is 82258.9543991(15) cm^{-1} [13]. The difference suggests an accuracy of the tabulated values of the order of $2 \cdot 10^{-6}$ cm^{-1} or 0.1 MHz.

fine-structure levels	Δ_{nl} (GHz)	fine-structure levels	Δ_{nl} (GHz)
$2P_{3/2} - 2P_{1/2}$	10.96905	$4P_{3/2} - 4P_{1/2}$	1.37112
$3P_{3/2} - 3P_{1/2}$	3.25010	$4D_{5/2} - 4D_{3/2}$	0.45704
$3D_{5/2} - 3D_{3/2}$	1.08333		

Table 5.3: The relevant fine-structure splittings. The error is less than 10 kHz, based on the accuracy of the Lamb shifts used. For comparison: the theoretical prediction of Ref. [20] for the $2P_{3/2} - 2P_{1/2}$ splitting is 10.9690542 GHz.

with $g_n = 5.56$ the nuclear g-factor for a proton[15]. For ground-state H, the upper of the two hyperfine levels is 3-fold degenerate and the lower is not degenerate. The hyperfine interaction does not influence the centroid of the lines. This automatically means that the upper hyperfine level lies at $a_h/4$ and the lower at $-3a_h/4$ with respect to the centroid. Some relevant hyperfine splittings are listed in table 5.4. Only in the case of S levels the hyperfine splitting is larger than the radiative line width of that level (the line widths are the inverse of the upper-state lifetimes, indicated in Fig. 5.1). The hyperfine splitting is therefore neglected for the P and the D levels of H.

$1S_{1/2}$	$2S_{1/2}$	$2P_{1/2}$	$2P_{3/2}$	$3S_{1/2}$	$3D_{3/2}$	$3D_{5/2}$
1.42041	0.1776	0.0592	0.0237	0.0526	0.0042	0.0027

Table 5.4: Hyperfine splittings in GHz of selected levels of atomic hydrogen in zero magnetic field.

5.2.2 The Zeeman effect

In the presence of a magnetic field $B \neq 0$ the degeneracy in $m_j = m_l + m_s$ is lifted and the optical resonance lines split. This effect is named after Pieter Zeeman who first observed it in 1896[21]. In a magnetic field, j is no longer a good quantum number – only the projection of the total angular momentum onto the z-axis, with quantum number m_j, is conserved. The general wave function can then be expressed as a superposition of two linearly independent spin wave functions. We will choose a basis in which s_z is diagonal. Neglecting the nuclear spin, relativistic corrections and the Lamb shifts, the interaction with the field is described by the fine-structure Hamiltonian

$$H_{\mathrm{FS}} = \tfrac{2}{3}\Delta_{n,l}\ \vec{l}\cdot\vec{s} + \mu_{\mathrm{B}}(\vec{l} + g_{\mathrm{e}}\vec{s})\cdot\vec{B}, \tag{5.5}$$

with μ_{B} the Bohr magneton and g_{e} the electron g-factor and $\Delta_{n,l}$ the fine-structure splitting of the manifold characterized by the quantum numbers n and l. The eigenstates and eigenvalues can be obtained by diagonalization of this Hamiltonian if treated as a small perturbation of the total Hamiltonian. They are listed in table 5.5 and table 5.6. Note that if $B = 0$ Eq. 5.5 will lead to a perturbative approximation to the zero-field fine-structure splitting.

The energy levels are expressed in terms of the dimensionless parameter

$$x \equiv \frac{(g_{\mathrm{e}} - 1)\mu_{\mathrm{B}}B}{\Delta_{n,l}}, \tag{5.6}$$

where $\Delta_{n,l}$ is the fine-structure splitting of that particular manifold. For convenience the electron g-factor is usually set to 2. This only makes a small error in the field dependence, since the true value[12] is 2.0023192. The eigenstates are expressed in the $|m_l, m_s\rangle$ basis, which is an abbreviation of the $|n, l, m_l, s, m_s\rangle$ basis. The fine-structure admixture angle is defined as

$$\sin\theta_m \equiv \sqrt{\frac{1+\delta_m}{2}}, \tag{5.7}$$

where

$$\delta_m = \frac{x + \frac{2m}{2l+1}}{\sqrt{1 + \frac{4m}{2l+1}x + x^2}}, \tag{5.8}$$

and m is an abbreviation for m_j.

The energy levels are listed are listed relative to the manifold centers of gravity in zero field, i.e., after averaging over all the lines of the n, l manifold, with the degeneracy $2j + 1$ as weighing coefficient. These centers of gravity as well as the absolute energies of the two zero-field fine-structure levels can be found in table 5.2. The Zeeman magnetic-field dependence is a function of the zero-field fine-structure splittings which are listed in table 5.3.

In principle, the Zeeman energy levels presented here are perturbative solutions of the Hamiltonian without hyperfine, relativistic or QED corrections. In the same approximation,

	m_j	Upper level ($j = l + \frac{1}{2}$)	Lower level ($j = l - \frac{1}{2}$)
nD	$\frac{5}{2}$	$\frac{2}{5}\Delta_{nD} + (2 + \frac{1}{2}g_e)\mu_B B$	
	$\frac{3}{2}$	$-\frac{1}{10}\Delta_{nD} + \frac{3}{2}\mu_B B + \frac{1}{2}\Delta_{nD}\sqrt{1 + \frac{6}{5}x + x^2}$	$-\frac{1}{10}\Delta_{nD} + \frac{3}{2}\mu_B B - \frac{1}{2}\Delta_{nD}\sqrt{1 + \frac{6}{5}x + x^2}$
	$\frac{1}{2}$	$-\frac{1}{10}\Delta_{nD} + \frac{1}{2}\mu_B B + \frac{1}{2}\Delta_{nD}\sqrt{1 + \frac{2}{5}x + x^2}$	$-\frac{1}{10}\Delta_{nD} + \frac{1}{2}\mu_B B - \frac{1}{2}\Delta_{nD}\sqrt{1 + \frac{2}{5}x + x^2}$
	$-\frac{1}{2}$	$-\frac{1}{10}\Delta_{nD} - \frac{1}{2}\mu_B B + \frac{1}{2}\Delta_{nD}\sqrt{1 - \frac{2}{5}x + x^2}$	$-\frac{1}{10}\Delta_{nD} - \frac{1}{2}\mu_B B - \frac{1}{2}\Delta_{nD}\sqrt{1 - \frac{2}{5}x + x^2}$
	$-\frac{3}{2}$	$-\frac{1}{10}\Delta_{nD} - \frac{3}{2}\mu_B B + \frac{1}{2}\Delta_{nD}\sqrt{1 - \frac{6}{5}x + x^2}$	$-\frac{1}{10}\Delta_{nD} - \frac{3}{2}\mu_B B - \frac{1}{2}\Delta_{nD}\sqrt{1 - \frac{6}{5}x + x^2}$
	$-\frac{5}{2}$	$\frac{2}{5}\Delta_{nD} - (2 + \frac{1}{2}g_e)\mu_B B$	
nP	$\frac{3}{2}$	$\frac{1}{3}\Delta_{nP} + (1 + \frac{1}{2}g_e)\mu_B B$	
	$\frac{1}{2}$	$-\frac{1}{6}\Delta_{nP} + \frac{1}{2}\mu_B B + \frac{1}{2}\Delta_{nP}\sqrt{1 + \frac{2}{3}x + x^2}$	$-\frac{1}{6}\Delta_{nP} + \frac{1}{2}\mu_B B - \frac{1}{2}\Delta_{nP}\sqrt{1 + \frac{2}{3}x + x^2}$
	$-\frac{1}{2}$	$-\frac{1}{6}\Delta_{nP} - \frac{1}{2}\mu_B B + \frac{1}{2}\Delta_{nP}\sqrt{1 - \frac{2}{3}x + x^2}$	$-\frac{1}{6}\Delta_{nP} - \frac{1}{2}\mu_B B - \frac{1}{2}\Delta_{nP}\sqrt{1 - \frac{2}{3}x + x^2}$
	$-\frac{3}{2}$	$\frac{1}{3}\Delta_{nP} - (1 + \frac{1}{2}g_e)\mu_B B$	
nS	$\frac{1}{2}$	$\frac{1}{2}g_e\mu_B B$	
	$-\frac{1}{2}$	$-\frac{1}{2}g_e\mu_B B$	

Table 5.5: Energy of the S, P, and D fine-structure levels of atomic hydrogen in a magnetic field for arbitrary principal quantum number n. The energies are given relative to their center of gravity which can be found in table 5.2. Fine-structure splittings Δ_{nl} are given in table 5.3.

the fine-structure splitting would be

$$\Delta E_{n,l} = \frac{hcR_\infty}{(1 + m_e/m_p)} \frac{\alpha^2}{n^3 l(l+1)}. \tag{5.9}$$

The real splittings are listed in table 5.3, including the difference in the Lamb shift of the two

	m_j	Upper level ($j = l + \frac{1}{2}$)	Lower level ($j = l - \frac{1}{2}$)
nD	$\frac{5}{2}$	$\|2\uparrow\rangle$	
	$\frac{3}{2}$	$\sin\theta_{\frac{3}{2}}\|1\uparrow\rangle + \cos\theta_{\frac{3}{2}}\|2\downarrow\rangle$	$-\cos\theta_{\frac{3}{2}}\|1\uparrow\rangle + \sin\theta_{\frac{3}{2}}\|2\downarrow\rangle$
	$\frac{1}{2}$	$\sin\theta_{\frac{1}{2}}\|0\uparrow\rangle + \cos\theta_{\frac{1}{2}}\|1\downarrow\rangle$	$-\cos\theta_{\frac{1}{2}}\|0\uparrow\rangle + \sin\theta_{\frac{1}{2}}\|1\downarrow\rangle$
	$-\frac{1}{2}$	$\sin\theta_{-\frac{1}{2}}\|-1\uparrow\rangle + \cos\theta_{-\frac{1}{2}}\|0\downarrow\rangle$	$-\cos\theta_{-\frac{1}{2}}\|-1\uparrow\rangle + \sin\theta_{-\frac{1}{2}}\|0\downarrow\rangle$
	$-\frac{3}{2}$	$\sin\theta_{-\frac{3}{2}}\|-2\uparrow\rangle + \cos\theta_{-\frac{3}{2}}\|-1\downarrow\rangle$	$-\cos\theta_{-\frac{3}{2}}\|-2\uparrow\rangle + \sin\theta_{-\frac{3}{2}}\|-1\downarrow\rangle$
	$-\frac{5}{2}$	$\|-2\downarrow\rangle$	
nP	$\frac{3}{2}$	$\|1\uparrow\rangle$	
	$\frac{1}{2}$	$\sin\theta_{\frac{1}{2}}\|0\uparrow\rangle + \cos\theta_{\frac{1}{2}}\|1\downarrow\rangle$	$-\cos\theta_{\frac{1}{2}}\|0\uparrow\rangle + \sin\theta_{\frac{1}{2}}\|1\downarrow\rangle$
	$-\frac{1}{2}$	$\sin\theta_{-\frac{1}{2}}\|-1\uparrow\rangle + \cos\theta_{-\frac{1}{2}}\|0\downarrow\rangle$	$-\cos\theta_{-\frac{1}{2}}\|-1\uparrow\rangle + \sin\theta_{-\frac{1}{2}}\|0\downarrow\rangle$
	$-\frac{3}{2}$	$\|-1\downarrow\rangle$	
nS	$\frac{1}{2}$	$\|0\uparrow\rangle$	
	$-\frac{1}{2}$	$\|0\downarrow\rangle$	

Table 5.6: Eigenstates of the S, P, and D Zeeman levels, neglecting hyperfine structure, of H in a magnetic field for arbitrary principal quantum number n in the $|m_l, m_s\rangle$ basis, where $\uparrow$ should be read as $m_s = 1/2$ and $\downarrow$ as $m_s = -1/2$. Note that the mixing angles θ_m are functions of n, l and $m = m_j$. The sign convention is identical to that in Luiten[2] and is based on the definitions of the spherical harmonics by Wigner[22].

fine-structure levels. In a good approximation one can take the true zero-field centers of gravity and true splittings as input for the calculation of the energy levels in an external magnetic field. In reality the hyperfine, relativistic and QED corrections are themselves field dependent[15].

However, the external magnetic field corrections to the Lamb shifts are of negligible order: $(\mu_B B/hcR_\infty)\Delta_{\text{Lamb}} < 10^{-5}\Delta_{\text{Lamb}}$, with Δ_{Lamb} the Lamb shift[20].

The hyperfine structure of the atomic levels is caused by the interaction of the electron spin with the proton spin and the magnetic field. Only for the $l = 0$ levels the hyperfine correction exceeds the natural line width. These S states do not have fine structure and the hyperfine and Zeeman interaction are given by the following Hamiltonian

$$H_{\text{HF}} = a_h \vec{i} \cdot \vec{s} + (g_e \mu_B \vec{s} - g_n \mu_n \vec{i}) \cdot \vec{B}, \tag{5.10}$$

with $\mu_n = \mu_B/1836.13$ the nuclear magnetic moment[15, 12]. For $B = 0$ the $1S_{1/2}$ state consists of a triplet and a singlet, separated by energy a_h. The magnetic field lifts the degeneracy of the triplet state. For finite B-field, diagonalization of H_{HF} leads to four nondegenerate hyperfine states, labeled by convention as a, b, c, d (in order of increasing energy for $B < 16\,\text{T}$) as listed in table 5.7. The energies are also plotted in chapter 2 in Fig. 2.1. The magnetic moments

hyperfine state	energy	state
d	$a_h/4 + \mu^- B/2$	$\|\uparrow\ddagger\rangle$
c	$-a_h/4 + (a_h/2)[1 + (\mu^+ B/a_h)^2]^{1/2}$	$\cos\theta\|\uparrow\ddagger\rangle + \sin\theta\|\downarrow\ddagger\rangle$
b	$a_h/4 - \mu^- B/2$	$\|\downarrow\ddagger\rangle$
a	$-a_h/4 - (a_h/2)[1 + (\mu^+ B/a_h)^2]^{1/2}$	$\sin\theta\|\uparrow\ddagger\rangle - \cos\theta\|\downarrow\ddagger\rangle$

Table 5.7: Energy levels and eigenstates of the ground state hyperfine structure in a magnetic field, expressed in the $|m_s m_i\rangle$ basis. The barred arrows indicate the nuclear spin, i.e., $\ddagger$ means $m_i = 1/2$ and $\ddagger$ means $m_i = -1/2$.

$\mu^\pm = g_e\mu_B \pm g_n\mu_n$ may be approximated by $\mu^\pm \approx 2\mu_B$ with only a small ($< 1\,\%$) error. The hyperfine mixing angle θ is defined by $\tan 2\theta = a_h/(\mu^+ B)$. The energy splitting between the c and d hyperfine levels is plotted in Fig. 5.2. The $c - d$ splitting has a maximum of 0.655 GHz at a magnetic field $B = 0.648\,\text{T}$, due to the nuclear Zeeman effect. At $B = 16.7\,\text{T}$ the c and the d levels cross, and in the high-field limit the splitting is proportional to $-g_n\mu_n B$. Note, that in the high-field limit, the nuclear Zeeman effect cannot be neglected in the excited states, and the observed hyperfine splittings of the transitions are not identical to the $c - d$ splitting.

Figure 5.3 shows the magnetic sublevels of the $1S_{1/2}$, $2P_{1/2}$, $2P_{3/2}$, $3S_{1/2}$, $3D_{3/2}$ and $3D_{5/2}$ states together with a number of relevant transitions connecting them.

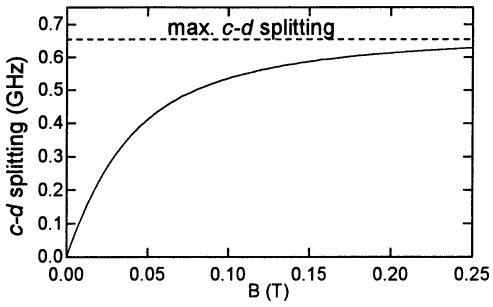

Figure 5.2: Energy difference between the ground state c and d levels of atomic H in frequency units. The maximum splitting is 0.655 GHz at a magnetic field $B = 0.65$ T.

5.3 Optical transitions

Once the atomic energy levels are known, the transition frequency is simply found from the energy difference between the levels involved in the transition. Which transitions are allowed under electric-dipole interaction can be found from the selection rules. For electric-dipole transitions, in which the motion of the electron couples to the electric field of the light, the electron-spin projections are conserved: $\Delta m_s = 0$. The selection rule for the angular momentum is $\Delta l = \pm 1$ and for its angular momentum projection $\Delta m_l = 0, \pm 1$. The transitions allowed by these rules have been labeled by the letter σ (*senkrecht*) to describe the $\Delta m_l = \pm 1$ transitions, which can be induced by light with an electric-field vector perpendicular to the quantization axis of the atom, and by the letter π (*parallel*) to describe the $\Delta m_l = 0$ transitions, which can be excited by light with an electric field parallel to the quantization axis. In an external magnetic field, the quantization axis is set by the direction of this field. On the symmetry axis of our magnetic trap (the z-axis), the magnetic field is parallel to the z-axis, which is also the propagation direction of the light. Therefore, π transitions are only observed off-axis, where $\vec{B}$ makes small angles with the propagation direction of the light. For $\Delta m_l = +1$ (σ^+ transition) one needs radiation with the polarization vector rotating clockwise for an observer looking along the quantization axis. For $\Delta m_l = -1$ (σ^- transition) radiation with the opposite helicity is required, i.e., the polarization vector should rotate anti-clockwise.

So far the hyperfine structure is neglected. Hyperfine structure does not complicate matters much because also the nuclear-spin projection is conserved in electric-dipole transitions: $\Delta m_i = 0$. Because the hyperfine splitting is a small correction in H which becomes rapidly smaller with increasing n, l and j, it is usually sufficient to take into account the ground-state hyperfine structure and neglect that of the excited levels. In this way all allowed transitions will have a satellite line at a distance of maximally one ground-state hyperfine splitting. More detailed analysis will show that some lines that are forbidden by the selection rules neglecting the hyperfine structure will become weakly allowed because of the hyperfine admixture of the

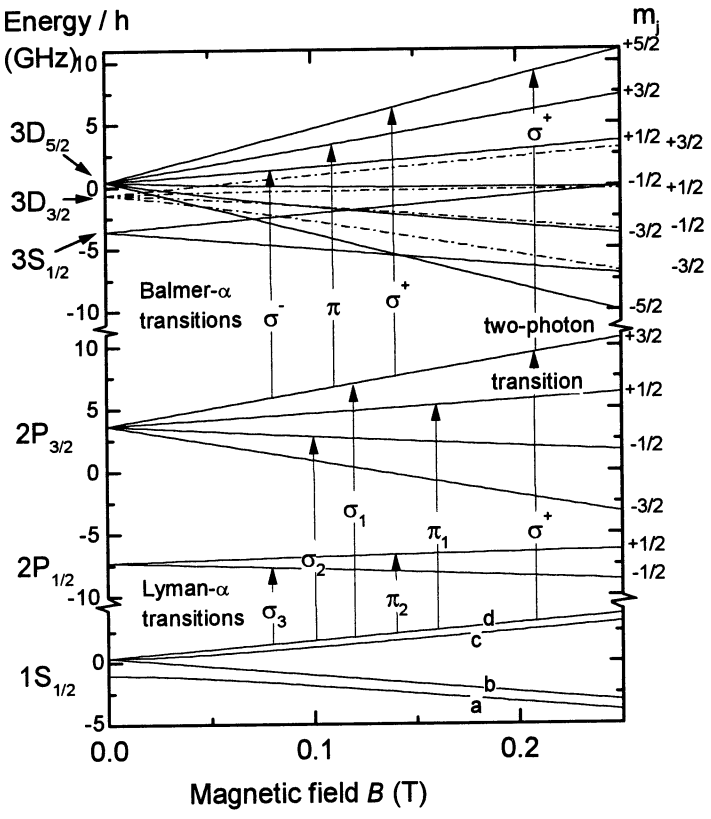

Figure 5.3: Energy of relevant levels of atomic H as a function of magnetic field. The energies are given relative to the manifold centroids (see table 5.2) of the $1S$, $2P$ and $3D$ levels, respectively. The magnetic quantum number m_j of the P and D levels is indicated right from the graph. All L_α transitions from the d state are indicated with the labels introduced in the text. As an example, three H_α transitions starting from the $2P_{3/2}(3/2)$ state are indicated. The two-photon closed cycle $d \leftrightarrow 3D_{5/2}(5/2)$ transition is also indicated.

opposite electron spin[2].

5.3.1 Lyman-α transitions

Under ordinary measuring conditions (a few minutes after loading the magnetic trap and assuming no intentional optical pumping), between 85% and 100% of the ground-state atoms can be found in the d hyperfine state. The transitions from the d state therefore dominate the spectrum and will be treated first. From the d state five L_α transitions are allowed (one σ^+

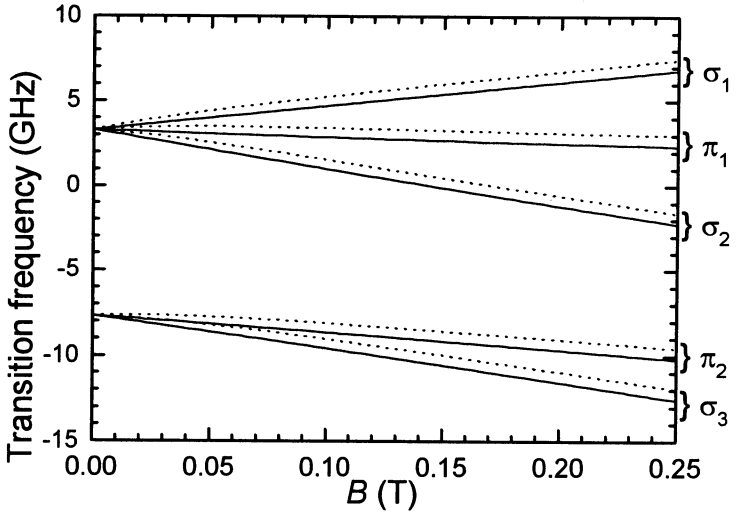

Figure 5.4: Transition frequencies for the five allowed L_α transitions from the d state (solid lines) and from the c state (dotted lines) as a function of magnetic field.

transition, two σ^- transitions and two π transitions). The transitions from the $1S_{1/2}(1/2)$ state have been labeled by convention (Fig. 5.4) as follows: σ_1 connects $1S_{1/2}(1/2)$ to the $2P_{3/2}(3/2)$ state, π_1 to the $2P_{3/2}(1/2)$ state, σ_2 to the $2P_{3/2}(-1/2)$ state, π_2 to the $2P_{1/2}(1/2)$ state and σ_3 to the $2P_{1/2}(-1/2)$ state.

The exact transition frequency for the d-$2P_{3/2}(3/2)$ transition in zero field is 82259.279 cm^{-1}. However, for convenience we will sometimes plot the experimental spectra relative to the transition frequencies of the Bohr approximation (82258.187555 cm^{-1} for the $n = 1 \rightarrow n = 2$ transition, and 15232.997695 cm^{-1} for the $n = 2 \rightarrow n = 3$ transition). In zero field the true σ_1 transition frequency is approximately 30 GHz above the Bohr reference value. The magnetic field dependence of the transition frequencies is plotted in Fig. 5.4. Of these transitions only the σ_1 transition forms a closed cycle: a ground-state atom excited to the state $2P_{3/2}(3/2)$ can only decay back to the same ground state. This makes this transition very suitable for Doppler cooling since no particles are lost due to optical pumping to non-trapped states. On any of the other transitions the atom has a finite probability of decaying to the high-field-seeking ground state after which it will be ejected from the trap.

If c atoms are present, five new transitions become possible which are, due to the electron-spin-up part of the c state ($|\uparrow\downarrow\rangle$), similar to the five allowed d lines. The difference in the transition frequency with respect to the five d lines is approximately the c-d splitting (see Sec. 5.2.1). Because the hyperfine splitting changes most noticeably in the low-field regime, it can be a useful probe for the magnetic field near the minimum of the trap. Note that we

neglected the nuclear Zeeman effect in the $2P$ state. It only becomes important in higher magnetic fields, and cancels the nuclear Zeeman effect in the $1S$ state. Therefore, the splitting of the L_α transition due to hyperfine structure has a constant value (0.70 GHz) in the high field limit, unlike the $c - d$ splitting, which is $-g_n\mu_n B$ in the high-field limit (see section 5.2.2). However, in the $0 - 0.25$ T range, the L_α splitting differs from the $c - d$ splitting plotted in Fig. 5.2 by less than 17 MHz, much less than the $2P$ natural linewidth.

Due to the electron-spin down part of the c state ($|{\downarrow}{\uparrow}\rangle$), additionally two σ^+, one σ^-, and two π transitions are allowed. The σ^- transition excites the $2P_{3/2}(-3/2)$ state, which cannot be reached from the d state. If the hyperfine structure of the ground state would be ignored, this state would be inaccessible. This transition is therefore sometimes called "hyperfine-allowed". However, this line as well as the other four transitions originating from the ($|{\downarrow}{\uparrow}\rangle$) part of the c state, are quite weak for all but the lowest fields, because they are suppressed relative to the other c lines, by a factor $\sin^2\theta$, which is less than 0.05 for $B \geq 10$ mT.

5.3.2 Balmer-α transitions

The excitations from the $2P$ state to the $3S$ or the $3D$ state are Balmer-α transitions, the first transition in the Balmer series. These transitions are denoted with H_α with a (vacuum) wavelength of 656.47 nm. Together with the L_α transitions, these H_α transitions form the "building blocks" of the resonance-enhanced two-photon lines. It is therefore important to understand the magnetic field dependence of these transitions. The transition frequencies are obtained by subtraction of the $n = 3$ and $n = 2$ Zeeman energies, tabulated in table 5.5. The number of possible transitions is too large to plot them all in a clear way in a single plot, therefore only the strongest transitions are drawn in Fig. 5.5 as a function of magnetic field. Furthermore, the choice is limited to the three Zeeman sublevels of the $2P_{3/2}$ state that can be reached from the d ground state and to the Zeeman sublevels of the $3D_{5/2}$ fine-structure manifold. As a reference frequency the frequency difference between the centroids of the $3D$ and $2P$ states is chosen. Also the five allowed transitions from the three selected $2P$ states to the $3S$ manifold are plotted with the $2P - 3D$ centroids as reference frequency. From the $2P_{3/2}(3/2)$ state there is a closed cycle to $3D_{5/2}(5/2)$. The $3S$ level can also be reached. It has a ten times longer lifetime than $3D$ (160 ns instead of 15.6 ns) and therefore the transition to the $3S$ level has a ten times smaller natural line width.

5.3.3 Two-photon transitions

For two-photon transitions the "transition frequency" can be defined analogously to the single-photon case, namely as the difference of the energy of the final state and the ground state, which is identical to the sum of the involved L_α and H_α transition frequencies. Selection rules for the two-photon transitions can be constructed from the electric-dipole selection rules for the two

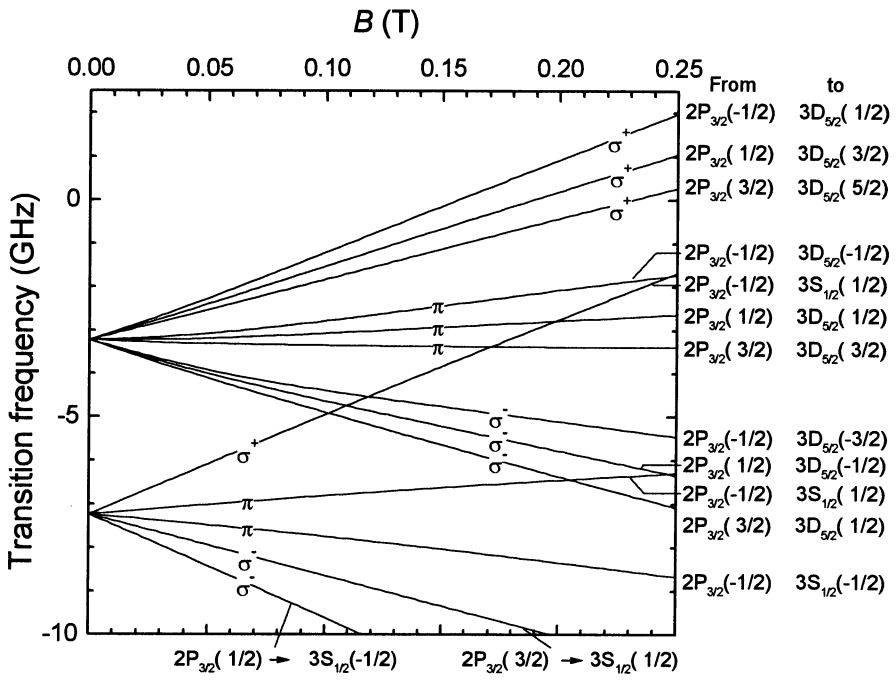

Figure 5.5: Transition frequencies for Balmer-α (H_α) transitions from the $2P_{3/2}$ states with $m_j = -1/2, 1/2$ and $3/2$ [notation $nL_j(m_j)$] to the $3D_{5/2}$ and $3S_{1/2}$ state, as a function of magnetic field, relative to the frequency difference of the $2P$ and the $3D$ manifold centroids (see table 5.2).

one-photon transitions involved. This restricts the changes in the orbital angular momentum to $\Delta l = 0, \pm 2$ and the changes in the projection of the total orbital angular momentum to $\Delta m_j = 0, \pm 1, \pm 2$. The electron- and nuclear-spin projections are still conserved quantities ($\Delta m_s = 0$ and $\Delta m_i = 0$). Applying these rules for atoms in the d ground state, eleven allowed two-photon lines can be counted.

The availability of two photons that both carry an angular-momentum quantum has consequences for the magnetic-field dependencies of the two-photon transitions. Starting in the d state and using, for instance, two σ^+ polarized photons, the $3D_{5/2}(5/2)$ state can be reached. Compared with the $d \rightarrow 2P_{3/2}(3/2)$ L_α transition, the $d \rightarrow 3D_{5/2}(5/2)$ transition has a dependence on the magnetic field that is two times higher. In an inhomogeneous magnetic field this two-photon spectral line therefore has a Zeeman broadened blue wing twice as broad as the σ_1 (L_α, $d \rightarrow 2P_{3/2}(3/2)$) transition. The magnetic field dependence of the transition frequencies of the eleven two-photon transitions from the d ground state are indicated in Fig. 5.6.

Also interesting is the two-photon transition from d to the doubly polarized ($|\uparrow\uparrow\rangle$) $3S_{1/2}$

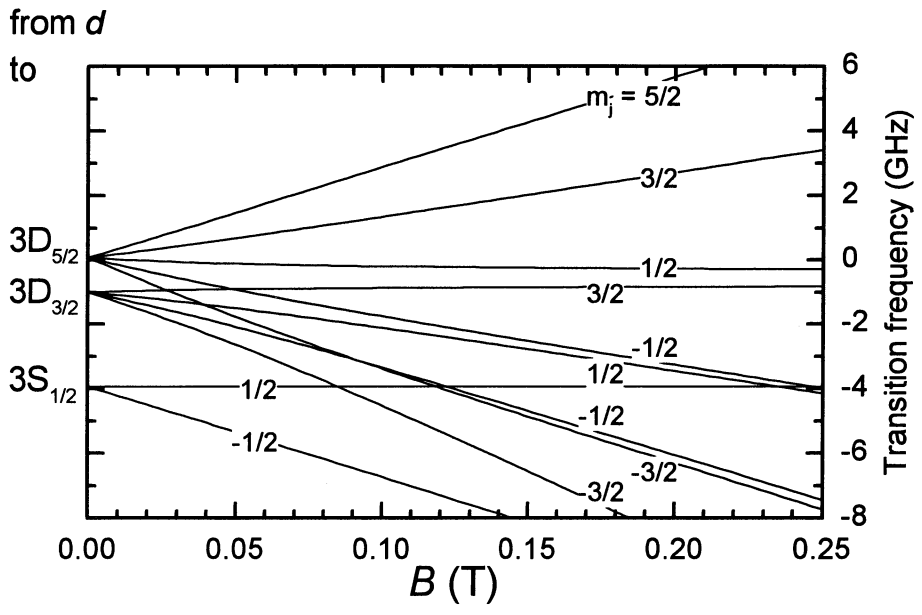

Figure 5.6: Transition frequencies for all possible two-photon transitions from the d ground state to the $3S$ and $3D$ excited states as a function of magnetic field B, relative to the frequency difference of the ground state and the $3D$ manifold centroids.

state. Because of the identical symmetry of the $1S$ and $3S$ wave functions, this transition has virtually no magnetic-field dependence. The small residual magnetic-field dependence is caused by the fact that the g-factor for a bound electron is slightly less than for an electron in free space due to relativistic effects. This correction is proportional to the binding energy[23], leading to a frequency shift of $0.22\,\mathrm{MHz\,T^{-1}}$, which is negligible for our purposes.

If also c atoms are present, every two-photon line for a d-state atom has a satellite line at a higher frequency. Neglecting the hyperfine structure of the excited state and the Zeeman effect of the nucleus, the distance to this c-state satellite line is given by the hyperfine splitting between the c and d ground states, as plotted in Fig. 5.2.

5.3.4 Observation of two-photon lines

To demonstrate the features of RETS, in this section two examples of experimental spectra will be discussed. The first example (Fig. 5.7) is a spectrum showing two-photon lines as they can be observed under typical conditions with the present apparatus. Conditions for this experiment were chosen such that many two-photon lines could be observed in a single spectrum. This

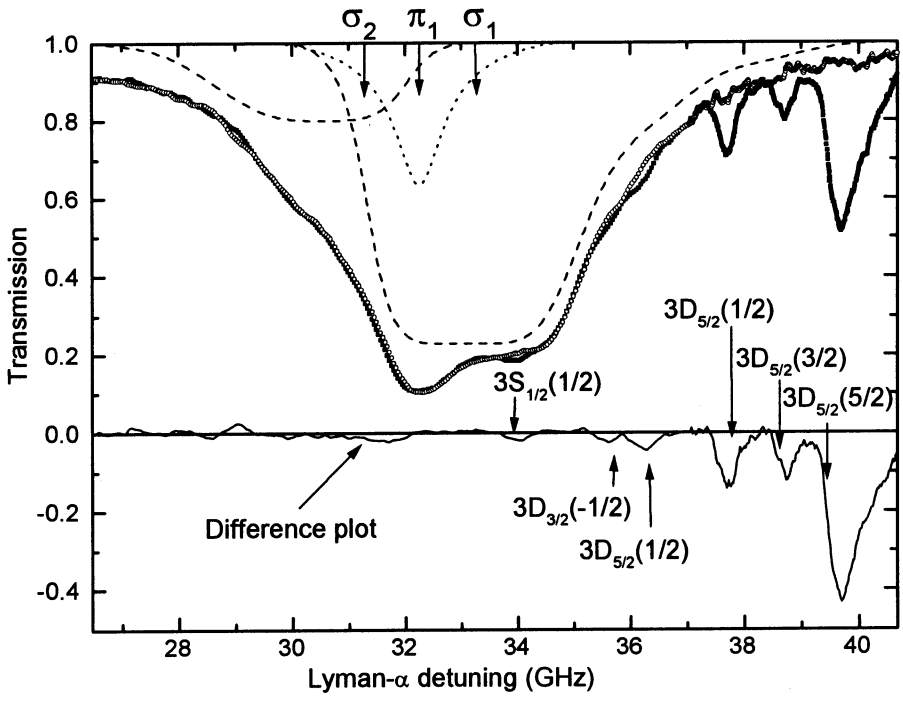

Figure 5.7: L_α absorption spectrum without (open circles) and with (solid squares) H_α light present, and their difference spectrum, as a function of the L_α frequency. The contours of the three lines that contribute to the L_α spectrum (σ_1, σ_2 and π_1) are sketched (dashed lines). The transition frequencies of these lines at the magnetic field of the trap center (53 mT) are indicated by three arrows at the top. The L_α frequency is given relative to 82258.187555 cm^{-1} (the Bohr frequency difference between the $1S$ and the $2P$ level). The H_α has an intensity of 1.5 $W\,mm^{-2}$ and a frequency of 15232.889 cm^{-1}. The transition frequencies at the trap center of the dominant two-photon lines are indicated by arrows.

situation was created by evaporative cooling a H sample to 9 mK and a central density of $1.13 \cdot 10^{13}\,cm^{-3}$. Moreover, the amplitude of the magnetic field at the trap center was chosen relatively low (53 mT), keeping the resonance lines from splitting far apart. The spectrum (see Fig. 5.7) is completely optically dense for the strong L_α lines (each transition itself absorbs all the light of the correct polarization over a few GHz, as indicated with the dashed lines). At the same time the two-photon lines are well resolved. The L_α light was σ^+ polarized for 78 %. The strongest two-photon transition visible is $1S_{1/2}(1/2) \rightarrow 3D_{5/2}(5/2)$, but as indicated in the figure, many more states of the $3D$ manifold were excited.

The expected positions of the lines for the magnetic field at the trap center are indicated

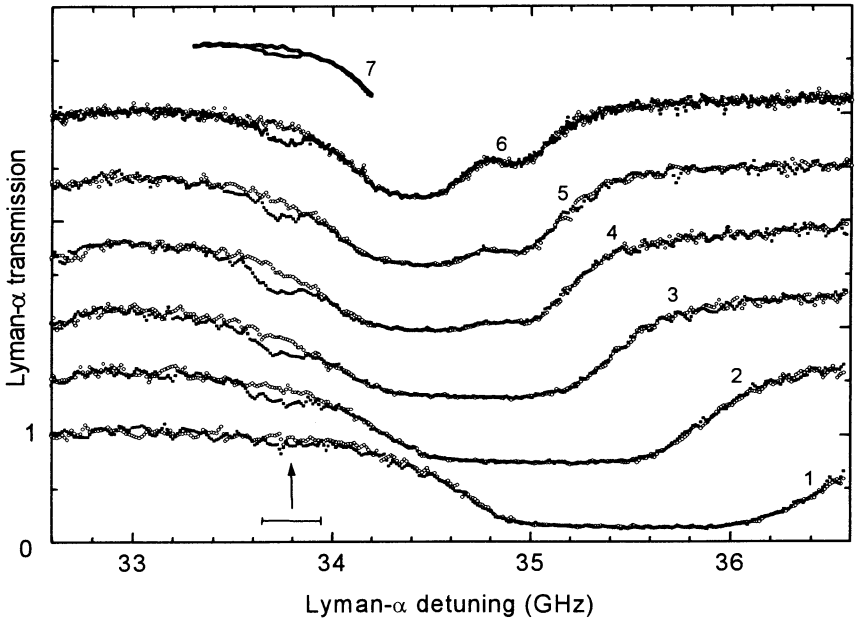

Figure 5.8: Sequence of L_α absorption spectra without (open circles) and with (solid squares) red light present, as a function of the L_α frequency (relative to the $1S - 2P$ Bohr frequency difference), while the trap depth is being reduced from 154 mK (spectrum 1) to 14 mK (spectra 6 and 7). The curves 2-7 are shifted upwards for clarity. The position of the $1S_{1/2}(1/2) - 3S_{1/2}(1/2)$ two-photon line at the (constant) H_α frequency of 15232.895 cm^{-1}, is indicated with an arrow, where the error bar is indicative of the uncertainty in the H_α value.

with arrows. However, because everywhere in the trap the magnetic field is larger than at the trap center, the peak of the observed resonance structures will in general not coincide with these arrows. Because the L_α and the H_α light are both dominantly σ^+ polarized, the strongest lines will have Zeeman shifts towards higher frequencies. The different magnetic-field dependencies of the two-photon lines are clearly visible. The two-photon line to $3D_{5/2}(5/2)$ has the strongest Zeeman dependence as can be seen from its shape which is asymmetrically broadened with a longer slope to the blue wing.

The two-photon transition from the d ground state to the $3S_{1/2}(1/2)$ state has a negligible magnetic field dependence, as was discussed in section 5.3.3. This insensitivity to the magnetic field is clearly visible in the second set of experimental data of this section, Fig. 5.8. In this figure, a number of spectra are shown, taken while evaporative cooling the sample by reducing the magnetic barrier that determines the trap depth. In this process, the magnetic field at the minimum of the trap is reduced from 190 mT in curve 1 to 115 mT in curve 7. Whereas the L_α

lines shift with changing magnetic field, the $1S - 3S$ two-photon line maintains its position on the frequency axis. Because the absolute L_α and H_α frequency are known, the position of this line in the spectrum can be calculated. The expected position of this line is indicated in the graph. For the calculation, the $1S$ and $3S$ hyperfine structures are taken into account. The residual error is explained by the ac-Stark shift due to the strong H_α light, $-0.04\,\mathrm{GHz}$, and falls well within the error margin of the H_α frequency during this measurement ($\pm 0.005\,\mathrm{cm}^{-1}$).

As explained in the introduction (section 5.1.2), the relevance of this Zeeman-free line is that it has the potential of being a high-resolution probe. In the example demonstrated here, the absolute $2P - 3S$ transition frequency was measured with an accuracy of the order of 100 MHz. However, the natural width of this resonance line is 100 times narrower, 10 times narrower than the resonance lines in the $3D$ manifold. Moreover, if far enough detuned from the resonant-enhancer level, it is only broadened by the Doppler effect. This makes the line shape in principle easy to calculate, making it an ideal temperature indicator. The FWHM line width of the RETS line in curve 7 of Fig 5.8 is 173 MHz. With the present L_α source bandwidth of $100 - 150$ MHz, it is very hard to measure the Doppler width, which is 0.06 GHz (FWHM) at 1 mK. Hence, it is not yet possible to make full use of this line. However, if the L_α bandwidth can be reduced with a factor 10, this resonance would be clearly visible below 1 mK, with the present H_α intensity. Moreover, because the integrated intensity of the RETS line scales linearly with the H_α power, any gain in H_α power directly increases the visibility of this line, also at higher temperatures.

5.4 Transition probabilities

Transition probabilities for atoms can be obtained from Fermi's golden rule. If the wave functions of the two involved states are known, the transition matrix element can be calculated. The total decay rate of a state, $2\gamma = 1/\tau$, with τ the lifetime of the state, can be obtained by summing over the transition rates of all transitions by which the state can decay. The lifetime of the excited levels of H that are relevant for us, are dominated by the spontaneous emission of a single photon. In general, more than one decay channel is possible. With each decay channel a partial lifetime can be associated. The partial lifetime τ_{ij} and the decay rate $\Gamma \equiv 2\gamma_{ij}$ of the corresponding channel from state i to state j are related by $2\gamma_{ij} = 1/\tau_{ij}$. The excited levels $3S$ and $3D$ decay only to the $2P$ state, and the $2P$ state decays back to the ground state. Hence, no ambiguity exists to which $(nl \rightarrow n'l')$ transition the decay rates γ_{2P}, γ_{3S} and γ_{3D} refer. The lifetimes of these states can be found in Fig. 5.1. Note that already the $n = 4$ levels can decay to more than one (nl) manifold.

Einstein found that there is a fixed relation between the coefficients for absorption and emission of a photon (his well known A and B coefficients[24]). Hence, once the total spontaneous decay rates γ_i are known, the absolute absorption probabilities can be calculated, as will be

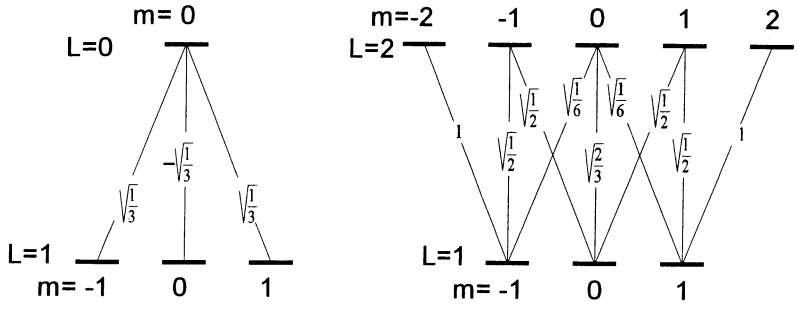

Figure 5.9: Clebsch-Gordan coefficients for $l = 0 \rightarrow l = 1$ (left) and $l = 2 \rightarrow l = 1$ (right) fluorescence transitions.

done in section 5.5. First, the relative decay rates within a multiplet will be examined.

5.4.1 Relative transition probabilities

The total spontaneous decay rates γ_i in zero magnetic field will be taken as input for the calculation of the absorption probabilities, and are available in the literature[15] . In a finite magnetic field the levels split into Zeeman sublevels and the transition from a level nl to $n'l'$ splits into a Zeeman multiplet. The ratio of the intensities in a Zeeman multiplet were already derived in 1925 [25]. It was found that the lifetime of a state does not depend on the orbital quantum number m_l. This allows the definition of branching ratios γ_{ij}/γ_i. The selection rule $\Delta m_l = 0, \pm 1$ limits the number of states to which an atom can make a transition, to a maximum of three per manifold (or six if one includes the spin degeneracy).

The matrix elements giving the relative decay probabilities for the three possible polarizations of the spontaneously emitted photon [15] are tabulated in table 5.8. In principle, they are Clebsch-Gordan coefficients arising from the coupling of two angular moments. The values are also schematically indicated in Fig. 5.9. The Clebsch-Gordan coefficients for the $l = 1 \rightarrow l = 0$ fluorescence transitions are not indicated in the figure because they all evaluate to unity.

The signs of the matrix elements are important if there is interference between different channels, e.g., in the case of a two-photon transition with two light beams of mixed polarization. The sign convention is that of E.P. Wigner[22]. The minus signs can be omitted when calculating one-photon transition probabilities.

It is not difficult to include the spin-orbit coupling in the calculation of the relative absorption coefficients, because all states can be expressed as linear superpositions of pure spin-up ($\uparrow$) and spin-down ($\downarrow$) wave functions (table 5.6). Note that spin is conserved in an electric-dipole transition. As an example, let us calculate the relative probability γ_{ij}/γ_i of fluorescence of

	$l' = l - 1$	$l' = l + 1$
π	$\sqrt{\frac{l^2-m^2}{l(2l-1)}}$	$-\sqrt{\frac{(l+1)^2-m^2}{(2l+3)(l+1)}}$
σ^-	$\sqrt{\frac{(l-m)(l-m-1)}{2l(2l-1)}}$	$\sqrt{\frac{(l+m+2)(l+m+1)}{2(2l+3)(l+1)}}$
σ^+	$\sqrt{\frac{(l+m)(l+m-1)}{2l(2l-1)}}$	$\sqrt{\frac{(l-m+2)(l-m+1)}{2(2l+3)(l+1)}}$

Table 5.8: Clebsch-Gordan coefficients for an atom fluorescing from $|l, m\rangle$ to $|l', m'\rangle$, with $m \equiv m_l$. The σ^- and σ^+ labels refer to the photon involved, i.e., $m' = m + 1$ corresponds to a σ^- emitted photon and $m' = m - 1$ to a σ^+ emitted photon. The quadratic sum of the π, σ^- and σ^+ contributions in each column add up to unity.

initial state $i = 3D_{5/2}(1/2)$ to the final state $j = 2P_{3/2}(1/2)$ in zero magnetic field. Because the lifetime of the upper state does not depend on m_l or m_s, the total decay rate is simply $\gamma_i = \gamma_{3D}$. Decomposed in pure spin states and expressed in the $|n\, l\, m_l\, m_s\rangle$ basis, the final and initial states are, respectively:

$$2P_{3/2}(1/2) = \sqrt{\tfrac{2}{3}}|2P\,0\uparrow\rangle + \sqrt{\tfrac{1}{3}}|2P\,1\downarrow\rangle \tag{5.11}$$

$$3D_{5/2}(1/2) = \sqrt{\tfrac{3}{5}}|3D\,0\uparrow\rangle + \sqrt{\tfrac{2}{5}}|3D\,1\downarrow\rangle, \tag{5.12}$$

and the relative fluorescence probability is given by

$$\begin{aligned}\gamma_{ij}/\gamma_{3D} &= \left|\left\langle 2P_{3/2}(1/2)\,|H_{\rm I}|\,3D_{5/2}(1/2)\right\rangle\right|^2/\gamma_{3D} \\ &= \left|\left(\langle 2P\,0\uparrow|\sqrt{\tfrac{3}{5}} + \langle 2P\,1\downarrow|\sqrt{\tfrac{2}{5}}\right) H_{\rm I}\left(\sqrt{\tfrac{2}{3}}\,|3D\,0\uparrow\rangle + \sqrt{\tfrac{1}{3}}\,|3D\,1\downarrow\rangle\right)\right|^2/\gamma_{3D} \\ &= \left|\langle 2P\,0\uparrow|\sqrt{\tfrac{3}{5}}H_{\rm I}\sqrt{\tfrac{2}{3}}|3D\,0\uparrow\rangle + \langle 2P\,1\downarrow|\sqrt{\tfrac{2}{5}}H_{\rm I}\sqrt{\tfrac{1}{3}}|3D\,1\downarrow\rangle\right|^2/\gamma_{3D} = \frac{3}{5},\end{aligned} \tag{5.13}$$

where $H_{\rm I}$ is the dipole interaction Hamiltonian, and $\langle 2P\,0\uparrow|H_{\rm I}|3D\,0\uparrow\rangle$ and $\langle 2P\,1\downarrow|H_{\rm I}|3D\,1\downarrow\rangle$ are the product of $\sqrt{\gamma_{3D}}$ and a Clebsch-Gordan coefficient which can be found in table 5.8.

In finite magnetic field the branching ratios are in general not rational numbers. Moreover, because the decomposition in terms of the two spin states depends on B, a magnetic field dependence is introduced in the transition probability. The calculation, however, is similar to the example given above, the only difference being that the proper field dependent mixing angle should be substituted (see table 5.6).

In our experimental situation we are more interested in the probability of the inverse process, i.e., absorbing a photon, rather than the probability of emission of a photon in fluorescence. The

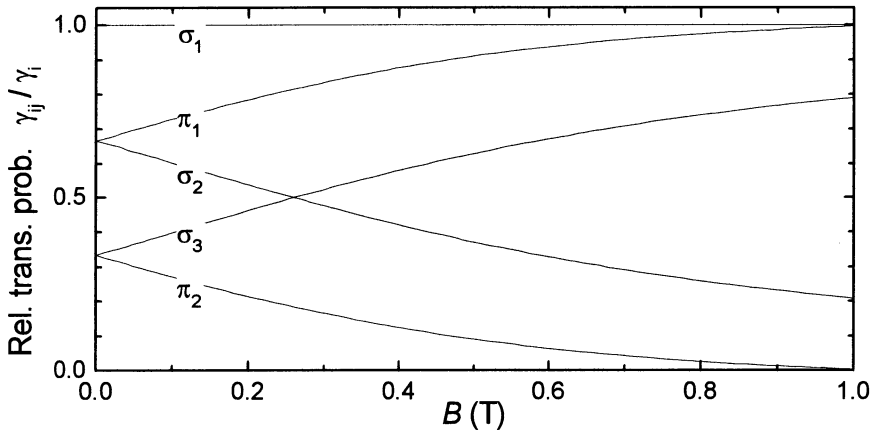

Figure 5.10: Relative (scaled to σ_1) transition probabilities of the L_α transitions from the d (b) state as a function of magnetic field.

relative probability, within a multiplet, for exciting an atom with a laser beam of the correct polarization is proportional to the fluorescence branching ratio. For the L_α and a number of H_α transitions, the relative absorption probabilities are plotted in Fig. 5.10 and Fig. 5.11, respectively. The transition probabilities of the L_α transitions depend on the fine-structure mixing angles $\theta_{\pm 1/2}$ of the $2P$ manifold and therefore show variations on the scale of 0.8 T, where the quantity $\mu_B B$ is of the order of the fine-structure splitting Δ_{2P}. The H_α transition probabilities depend, in general, on the fine-structure mixing angles of both the $2P$ and the $3D$ states. These probabilities will therefore show variation on two different field scales, one determined by the fine-structure splitting of the $2P$ state (corresponding to 782 mT) and one determined by the fine-structure splitting of the $3D$ state (corresponding to 77 mT).

As a consequence of the interplay between two fine-structure admixture angles (of the $2P$ and the $3D$ states), several weak lines exist that are forbidden in both the zero-field limit and the high-field limit, but are weakly allowed in the intermediate regime. They are not indicated in the figures. An example of such a line is the transition from $2P_{1/2}(1/2)$ to $3D_{5/2}(1/2)$. In the low-field limit the $2P_{1/2}(1/2)$ eigenstate can be approximated by $|1,\downarrow\rangle$ and $3D_{5/2}(1/2)$ by $|0,\uparrow\rangle$ (where the quantum numbers n and l are omitted). In the high-field limit, it is the $3D_{5/2}(1/2)$ state which becomes a pure electron-spin down wave function ($|1,\downarrow\rangle$) and the $2P_{1/2}(1/2)$ state becomes a pure electron-spin up state ($|0,\uparrow\rangle$). Because m_s is conserved in an electric-dipole transition, the transition probability vanishes in these two limits. In the intermediate regime both the $2P_{1/2}(1/2)$ state and the $3D_{5/2}(1/2)$ state are linear superpositions of electron-spin-up and down wave functions and a transition is allowed.

The transition from the $2P_{3/2}(3/2)$ state to the $3D_{5/2}(5/2)$ state is a closed cycle with the

fields is nearly resonant with the intermediate state $|a\rangle$, that contribution will dominate all the others and the absorption probability is given by

$$W_2(\Delta,\delta) = \frac{\pi}{8}\frac{\Omega_L^2\Omega_B^2}{\Delta^2}F_L(\Delta+\delta,\gamma_b), \tag{5.18}$$

where $\delta = \omega_B - \omega_2$ is the detuning of the H_α frequency ω_B from the unperturbed Balmer transition frequency ω_2, and γ_b is the HWHM natural line width of the upper level (i.e., γ_{3S} or γ_{3D}). The H_α Rabi frequency Ω_B is related to the H_α intensity analogous to Eq. 5.17: $\Omega_B^2/2\gamma_b = 3I\lambda_B^3/4\hbar c\pi^2$.

In the far detuned limit ($|\Delta| \gg \gamma_a$), the ratio of the two-photon over the one-photon transition rate is:

$$\frac{W_2(\Delta,\delta)}{W_1(\Delta)} = \frac{\pi\Omega_B^2}{4\gamma_a}F_L(\Delta+\delta,\gamma_b). \tag{5.19}$$

On the two-photon resonance this reduces to

$$\frac{W_2(\Delta,0)}{W_1(\Delta)} = \frac{\Omega_B^2}{4\gamma_a\gamma_b}, \tag{5.20}$$

independent of Δ. From Eq. 5.20, it can be realized that in the far detuned limit ($|\Delta| \gg \gamma_a$), the two-photon transition probability has the same form as a single-photon transition, with an effective Rabi frequency

$$\Omega_{ef} = \frac{\Omega_L\Omega_B}{2|\Delta|}. \tag{5.21}$$

We can estimate the minimum required value for Ω_B as follows. In our experiments the L_α light is much weaker than the H_α and depletion of the H_α light is negligible. The absorption of the L_α is monitored. In order to have a well resolved two-photon signal, one typically would like to be in the Lorentz tail of the L_α resonance that is used as resonant enhancer. Assuming a L_α tail with an absorption of $\sim 1\%$, a H_α Rabi frequency $\Omega_B/2\pi$ of order 0.2 GHz is needed to have a L_α absorption of 10 % on the two-photon resonance. Moreover, around 2 mK a $1S \rightarrow 3D$ two-photon line is Doppler broadened to $\sim$ 100 MHz, reducing this peak height to 1 %. The present L_α source bandwidth has the same broadening effect. Therefore, a Rabi frequency $\Omega_B/2\pi$ at least of order 1 GHz is required for useful RETS signals for thermometry.

In our present experimental setup, the H_α beam was focused to a Gaussian beam with radius of the order of 0.2 mm. The waist of the L_α beam was chosen smaller ($\sim$ 0.1 mm), guaranteeing an approximately constant Ω_B over the L_α cross section and thus reducing broadening due to different H_α light-shifts (see section 5.8.1) at different positions within the L_α beam. In order to realize the desired 1 GHz Rabi frequency with this beam waist, Balmer power of the order of 0.2 W is required in the sample cell. Because the H_α light co-propagates with the L_α, it passes several uncoated VUV-optics, reducing the intensity of the H_α light by reflection losses. Hence, a light source capable of providing $\sim$ 0.3 W of narrow band H_α is needed. As explained in chapter 3, this was realized with a ring dye-laser.

5.5.1 Range of validity of the perturbative expressions

Strong H_α light causes an ac-Stark shift of both the one- and two-photon lines. This is not reflected in the perturbative expressions, nor do they predict the changing line shape if δ approaches 0. The range in which the perturbative expressions are reasonable approximations depends, of course, on the application. For instance, one could require that the light shift (which is absent in the perturbative expressions), must be smaller than the natural width of the upper state, which is expressed by

$$\left|\frac{\Omega_B^2}{4\delta}\right| < \gamma_b. \tag{5.22}$$

To illustrate this condition, consider for instance the $3D$ state. With $\Omega_B/2\pi = 2\,\mathrm{GHz}$ (the present maximum), the H_α detuning $\delta/2\pi$ must be larger than approximately 100 GHz. This is a very large detuning which will reduce the absorption probability orders of magnitude.

If one is not interested in the exact position of the resonance lines, but only in a reasonable approximation of the absorption probability, condition 5.22 can be relaxed. It suffices then to demand that

$$|\delta| \gg \sqrt{\frac{\gamma_a}{2\gamma_b}}\Omega_B \tag{5.23}$$

which expresses the condition that the two-photon line must have a negligible admixture of the one-photon line. In this regime $|\delta|$ is not so small that the notion of "one-photon" and "two-photon" transitions will become ill defined, as will be discussed in the next section.

To illustrate condition 5.23, consider again the $3D$ state. With $\Omega_B/2\pi = 2\,\mathrm{GHz}$, the condition states that for $|\delta/2\pi| \gg 5\,\mathrm{GHz}$ the perturbative expressions give a fair approximation of the absorption probability.

5.6 Dressed-atom picture

In general, the evolution of an atom in several light fields can be found by solving the optical Bloch equations [24, 7, 26]. The "dressed-atom" picture[27, 28, 7, 29] gives a more transparent tool to handle absorption and emission by atoms in a strong light field. In this approach the light beam is considered as a single-mode quantum field. The combined Hamiltonian of the atom "dressed" with the light field is time independent. Since there is strong coupling between the intense H_α light and the $n = 2$ and $n = 3$ levels of H, the solution is sought of this two-level subsystem. The combined system, atoms "dressed" by the H_α light, is then probed by the weak L_α, coupling both the dressed states to the $1S_{1/2}$ ground state.

Consider the strong monochromatic H_α light field and the two levels it couples to. For the moment we neglect the finite lifetime of the levels involved. The Hamiltonian H describing the system is the sum of three parts, $H = H_B + H_A + H_I$, associated with the light field (H_B),

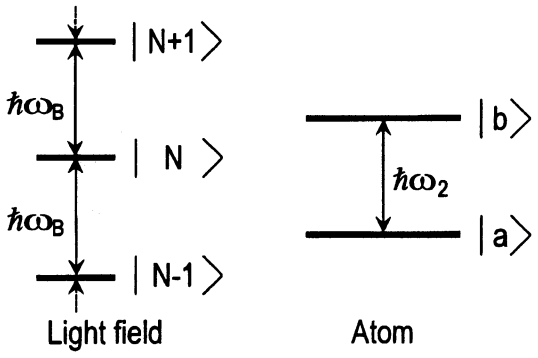

Figure 5.12: Graph of the energy eigenstates of the light field (left) and the atomic states $|a\rangle$ and $|b\rangle$ (right).

the atomic (H_A) and the interaction part (H_I). Neglecting the energy of the vacuum, the eigenvalues of H_B are $N\hbar\omega_B$ with $\hbar\omega_B$ the energy of a photon, and N the number of photons in the field. The levels of the unperturbed atom are labeled $|a\rangle$ and $|b\rangle$. The eigenvalues of H_A are the energies of the ground and excited state of the unperturbed atom, 0 and $\hbar\omega_2$ respectively.

H_I couples the ground and excited state of the unperturbed atom. The matrix element defines the Rabi frequency Ω_B:

$$\langle b|H_I|a\rangle = \tfrac{1}{2}\hbar\Omega_B \tag{5.24}$$

Figure 5.12 shows the idealized starting situation. The eigenstates of the field form a ladder with $\ldots, N-1, N, N+1, \ldots$ photons. It is assumed that the light is quasi-resonant with the atomic transition, i.e., $|\omega_B - \omega_2| \ll \omega_2$. Therefore, the combined energy of the ground state atom in a field with N photons is nearly degenerate with the energy of an excited state atom in a field with $N-1$ photons. To be precise, the energy difference is the detuning $\hbar\delta = \hbar(\omega_B - \omega_2)$.

The dressed-states picture can now be visualized by graphically merging the two diagrams of Fig. 5.12, resulting in the diagram on the left hand side of Fig. 5.13. In this dressed-states picture, a ladder of manifolds $\mathcal{E}(N)$ exists, each consisting of two nearly degenerate atom-field states. The energy distance between the manifolds $\mathcal{E}(N)$ and $\mathcal{E}(N+1)$ is $\hbar\omega_B$. If the interaction term in the Hamiltonian vanishes (i.e., for vanishing light intensities), the combined atom-field states ($|a, N\rangle \equiv |a\rangle|N\rangle$) become eigenstates of the total Hamiltonian H. Each manifold then has two nearly degenerate states $|a, N+1\rangle$ and $|b, N\rangle$, separated by the detuning δ. If the interaction term is turned on, the eigenstates become linear superpositions of the eigenstates of $H_B + H_A$. Therefore we now label them $|1, N\rangle$ and $|2, N\rangle$. As sketched on the right-hand side of Fig. 5.13, the interaction always increases the splitting between the levels. The combined atom-field eigensystem can be found by straightforward diagonalization of the Hamiltonian

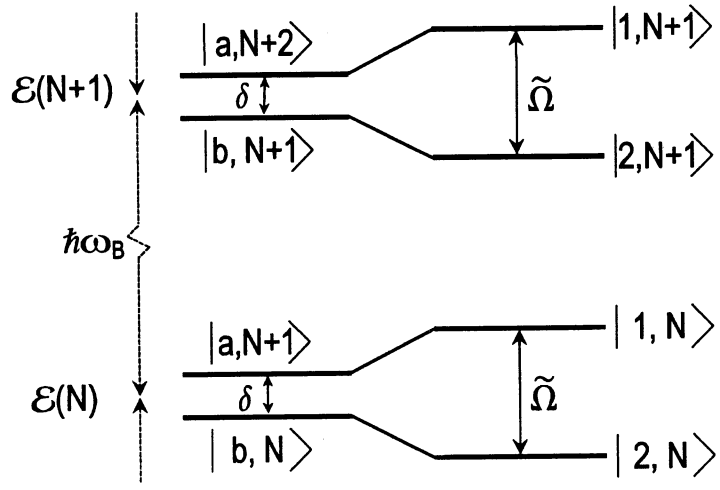

Figure 5.13: Ladder of dressed states. On the left the states are drawn without atom-field coupling, spaced by the detuning from the light with respect to the unperturbed atomic transition. The diagram is given for $\delta > 0$. Switching on the coupling will increase the splitting to $\tilde{\Omega}$, the generalized Rabi frequency.

leading to the eigenenergies relative to the energy of $|a\rangle$

$$E_{1N} = (N+1)\hbar\omega_B - \frac{1}{2}\hbar\delta + \frac{1}{2}\hbar\tilde{\Omega} \tag{5.25}$$

$$E_{2N} = (N+1)\hbar\omega_B - \frac{1}{2}\hbar\delta - \frac{1}{2}\hbar\tilde{\Omega}, \tag{5.26}$$

where the convention is adopted that $|1,N\rangle$ represents the state with the highest energy. The difference between these two energies is $\hbar\tilde{\Omega}$, where the generalized Rabi frequency $\tilde{\Omega} = \sqrt{\Omega_B^2 + \delta^2}$. If, for large δ, Ω_B is increased, the two levels in a manifold shift in opposite directions, each proportional to the light intensity, as $\Omega_B^2(4\delta)^{-1}$. This shift is known as the light shift or the ac-Stark shift. The corresponding eigenvectors (the dressed states) can be written as

$$|1,N\rangle = \sin\theta|\mathrm{a},N+1\rangle + \cos\theta|\mathrm{b},N\rangle \tag{5.27}$$

$$|2,N\rangle = \cos\theta|\mathrm{a},N+1\rangle - \sin\theta|\mathrm{b},N\rangle. \tag{5.28}$$

The mixing angle is defined by

$$\cos^2\theta = \frac{1}{2} - \frac{\delta}{2\tilde{\Omega}}\,, \quad 0 \le \theta \le \pi/2, \tag{5.29}$$

For positive δ, the state $|\mathrm{a},N+1\rangle$ has a higher energy than $|\mathrm{b},N\rangle$ and therefore in the weak coupling limit ($\Omega_B \to 0$) $\theta \to \pi/2$ and $|1,N\rangle$ can be identified with the unperturbed $|\mathrm{a},N+1\rangle$ state. For negative detuning $\theta \to 0$ in the weak coupling limit and $|1,N\rangle$ can be identified with the unperturbed $|\mathrm{b},N\rangle$ state.

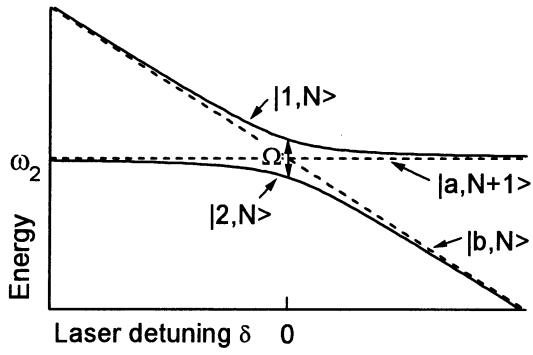

Figure 5.14: Energies of the dressed levels $|1, N\rangle$ and $|2, N\rangle$ relative to the energy of the unperturbed $|a, N+1\rangle$ as a function of detuning $\delta = \omega_B - \omega_2$.

The ladder system gives rise to a three component fluorescence spectrum, corresponding to radiative cascade of the dressed atom[7]. For the description of RETS this is, however, not of concern. The energies of the dressed levels are plotted in Fig. 5.14 as a function of the laser frequency ω_B, expressed as the detuning δ. The figure clearly shows how the $|1, N\rangle$ state changes continuously from the uncoupled state $|b, N\rangle$ to the uncoupled state $|a, N+1\rangle$. For $\delta = 0$ the $|1, N\rangle$ state is a symmetric superposition of both the uncoupled states. The dressed states repel each other upon increased coupling and show an avoided crossing as a function of δ, in contrast to the uncoupled states (the dashed lines in the graph) that simply cross. The central splitting is the Rabi frequency Ω_B.

The energies of the dressed atoms can be probed with weak light from a third unperturbed level $|g\rangle$. The situation is depicted in Fig. 5.15. With each state of the ladder of dressed states we associate a state $|g, N\rangle$. The distance between $|g, N+1\rangle$ and $|a, N+1\rangle$ is $\hbar\omega_1$. Under influence of the strong light field the unperturbed states $|a, N+1\rangle$ and $|b, N\rangle$ change into the dressed states $|1, N\rangle$ and $|2, N\rangle$, depicted on the right-hand side of Fig. 5.15. In contrast, $|g, N+1\rangle$ remains unchanged, as long as the probe is indeed weak.

The probe beam excites transitions from $|g, N+1\rangle$ to those levels that have an admixture of $|a, N+1\rangle$. Because both dressed states $|1, N\rangle$ and $|2, N\rangle$ contain admixture of $|a, N+1\rangle$ for non-zero $\tilde{\Omega}$, we see two transitions: a transition to $|1, N\rangle$ with frequency $\omega_L + (\tilde{\Omega} - \delta)/2$ and a transition $|2, N\rangle$ with frequency $\omega_L - (\tilde{\Omega} + \delta)/2$. In the far detuned limit of large $|\delta|$ these transitions are readily identified as the one- and two-photon transitions of the previous section. In addition, the dressed-atom picture also predicts what happens near $\delta = 0$: if a transition is probed from a unperturbed state $|g\rangle$ to a state $|a\rangle$, which is coupled to a third level $|b\rangle$ by an intense laser, the resonance line is expected to split into two components. The symmetric central doublet which is expected if $\delta = 0$ is called the "Autler-Townes doublet", after the microwave analog first described by Autler and Townes[30].

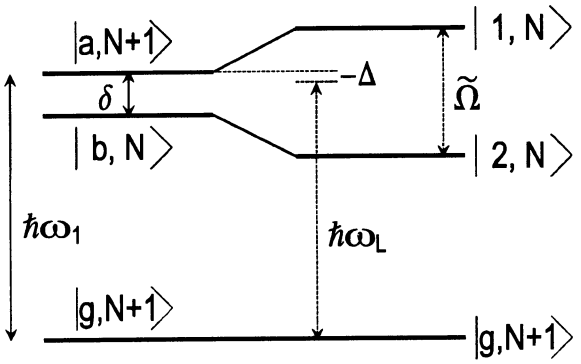

Figure 5.15: Graph of two dressed states $|1, N\rangle$ and $|2, N\rangle$ of the $\mathcal{E}(N)$ manifold, drawn for $\delta > 0$, together with a third state $|g, N+1\rangle$, which is weakly coupled to $|a, N+1\rangle$ by probe light of frequency ω_L of detuning Δ. On the left side the unperturbed levels $|a, N+1\rangle$ and $|b, N\rangle$ are indicated.

5.6.1 Observation of the Autler-Townes doublet

The avoided crossing which was discussed above, is directly visible in the experimental results depicted in Fig. 5.16. Plotted is the transmission of the VUV light with and without H_α light as a function of the detuning Δ of the VUV from the $d \rightarrow 2P_{3/2}(3/2)$ transition frequency at the trap center, for five different detunings δ from the $2P_{3/2}(3/2) \rightarrow 3D_{5/2}(5/2)$ resonance frequency at the trap center. Both light beams are σ^+ polarized. The trap was chosen with an offset field $B_0 = 115\,\mathrm{mT}$ in combination with relatively weak radial confinement ($31\,\mathrm{T\ m^{-1}}$), resulting in small angles between the magnetic field and the propagation direction of the light. In this way the nearby $d \rightarrow 2P_{3/2}(1/2)$ transition was suppressed to ensure a three-level system.

In the case where $\delta = 0$, the L_α line is split symmetrically into an "Autler-Townes doublet" [30] with peaks at $\pm\Omega_B/2$. The difference frequency of the two doublet components equals the Rabi frequency of the red beam (Ω_B) and thus allows the experimental determination of this important quantity.

If the H_α detuning δ increases, the two-photon spectrum shows an asymmetric profile (see the curve at $\delta/2\pi = 1\,\mathrm{GHz}$ in Fig. 5.16). The two peaks that are visible are the resonances of the two dressed states that now contain unequal amplitudes of the $2P$ and the $3D$ state. The largest of the two peaks at $\Delta \approx 0$ is the resonance of the dressed state that has more amplitude of the $2P$ state, and the smallest is that of the dressed states that has more $3D$ character.

For larger δ (e.g., $\delta/2\pi = 2\,\mathrm{GHz}$ in Fig. 5.16), the strong resonance represents the one-photon transition, shifted from the pure one-photon transition in the absence of H_α by a light shift (see section 5.8.1) from the strong H_α light. The weaker resonance at $\Delta \approx -\delta$ is the two-photon transition $d \rightarrow 3D_{5/2}(5/2)$. The corresponding transition probability in this limit scales as Ω_B^2/δ^2. This shows how the resonant optical thickness of the sample can be adjusted

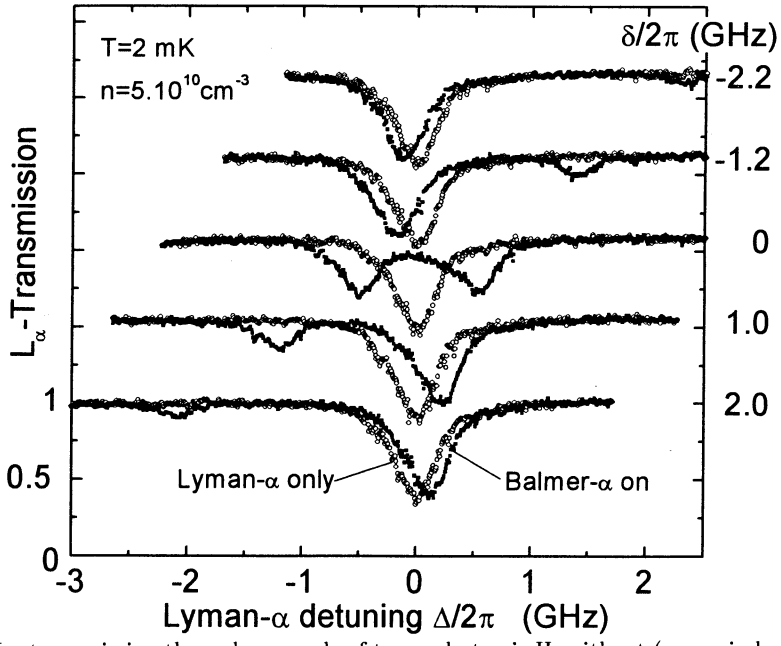

Figure 5.16: L_α transmission through a sample of trapped atomic H, without (open circles) and with (solid squares) red light of various detunings δ from the H_α (656 nm) transition. The symmetric double peak structure at $\delta = 0$ is known as the "Autler-Townes doublet". The 1 GHz splitting between the two peaks at $\delta = 0$ is the Rabi-frequency $\Omega_B/2\pi$. The curves have been displaced vertically for clarity.

by simply changing δ.

5.7 Line shapes

In section 5.6, we found the positions of the lines. To calculate line shapes, the spontaneous decay of the levels should be taken into account. A full description of the evolution of all coherences and populations, can be obtained from the optical Bloch equations. However, we are not interested in the evolution of the populations, because we probe ground-state atoms with weak (L_α) light. Therefore, it suffices to consider only a subsystem of the total quantum system and use a more convenient description with an effective Hamiltonian[7, 26] restricted to two excited states dressed by the strong H_α light. It can be shown that the result obtained in this way is a solution of the Bloch equations with the boundary condition that almost all population resides in the ground state.

In this section we will derive the polarizability, which contains all the information to calculate the line shapes, using the effective Hamiltonian method, based on the dressed-atom approach. From the polarizability the absorption probability per unit time is derived explicitly,

which will be the basis for the discussion of the shift and broadening mechanisms in section 5.8.

5.7.1 Atomic polarizability

The Hamiltonian used for calculation of the line shapes resembles the Hamiltonian used in the dressed-atom calculation of the line positions. However, to account for spontaneous decay, the energies of the unperturbed levels are given an imaginary component proportional to their spontaneous decay rate. Moreover, we leave out the terms counting the energy of the N photons in the intense laser beam. This leads to the effective Hamiltonian

$$H = \hbar \begin{pmatrix} -i\gamma_a & \frac{\Omega_B}{2} \\ \frac{\Omega_B}{2} & -\delta - i\gamma_b \end{pmatrix}, \tag{5.30}$$

where $2\gamma_a$ is the radiative decay rate of state $|a\rangle$ and $2\gamma_b$ that of state $|b\rangle$. Because of the complex values on the diagonal, this Hamiltonian is non-Hermitian. Physically the imaginary terms should be interpreted as accounting for loss of population due to spontaneous emission. The non-Hermitian Hamiltonian leads to two complex eigenenergies

$$E_1 = -\frac{1}{2}\hbar[\delta + i(\gamma_a + \gamma_b)] + \frac{1}{2}\hbar\sqrt{[\delta + i(\gamma_b - \gamma_a)]^2 + \Omega_B^2}, \tag{5.31}$$

$$E_2 = -\frac{1}{2}\hbar[\delta + i(\gamma_a + \gamma_b)] - \frac{1}{2}\hbar\sqrt{[\delta + i(\gamma_b - \gamma_a)]^2 + \Omega_B^2}. \tag{5.32}$$

The energy difference $E_1 - E_2$ is a complex number. For non-Hermitian Hamiltonians it is not possible to create an orthogonal set of eigenvectors in the usual sense. However, left-hand eigenvectors $\langle\phi_i|$ and right-hand eigenvectors $|\psi_i\rangle$ can still be found by the eigenvalue relations

$$H|\psi_i\rangle = E_i|\psi_i\rangle, \qquad \langle\phi_i|H = \langle\phi_i|E_i. \tag{5.33}$$

To a single eigenvalue E_i belong a left- and a right-handed eigenvector. The eigenvectors may be normalized in a bi-orthonormal set, defined by the relation

$$\langle\phi_i|\psi_j\rangle = \delta_{ij}. \tag{5.34}$$

With these notation considerations in mind, the right-hand eigenvectors are easily found to be

$$|\psi_1\rangle = S|a\rangle + C|b\rangle \tag{5.35}$$

$$|\psi_2\rangle = C|a\rangle - S|b\rangle, \tag{5.36}$$

with the complex coefficients

$$C = \sqrt{1/2 - [\delta + i(\gamma_b - \gamma_a)]/2\tilde{\Omega}}\,, \tag{5.37}$$

$$S = \sqrt{1/2 + [\delta + i(\gamma_b - \gamma_a)]/2\tilde{\Omega}}\,, \tag{5.38}$$

where $\tilde{\Omega}^2 = \Omega_B^2 + [\delta + i(\gamma_b - \gamma_a)]^2$. These coefficients are complex-valued, unless the unperturbed levels have equal (partial) lifetimes. In that case the absorption spectrum is just the sum of two Lorentzians. The left-hand eigenvectors are

$$\langle\phi_1| = S\langle \mathrm{a}| + C\langle \mathrm{b}| \tag{5.39}$$

$$\langle\phi_2| = C\langle \mathrm{a}| - S\langle \mathrm{b}|. \tag{5.40}$$

Note that despite their complex values, the coefficients C and S appear again, and not C^* and S^*.

To calculate the absorption probability for a weak probe beam, which couples a third state $|\mathrm{g}\rangle$ to the unperturbed $|a\rangle$ state, we consider the atomic polarizability α[26], generalized for our case of a non-Hermitian Hamiltonian. It describes the response of the dressed system to the weak probe beam and is defined by

$$\alpha = \frac{\langle \mathrm{g}|D|\psi_1\rangle\langle\phi_1|D^\dagger|\mathrm{g}\rangle}{E_1 - \hbar\Delta} + \frac{\langle \mathrm{g}|D|\psi_2\rangle\langle\phi_2|D^\dagger|\mathrm{g}\rangle}{E_2 - \hbar\Delta}, \tag{5.41}$$

where D is the electric-dipole operator coupling $|\mathrm{g}\rangle$ with $|a\rangle$. This polarizability is a scalar quantity, indicating that at this point the light beams and the atoms are considered to have well defined polarizations that are matched to each other. In the limit of large δ, when the two dressed states resemble the two unperturbed states, the numerator of the two terms in Eq. 5.41 will be real and Eq. 5.41 will be a sum of two complex Lorentzians. Substitution of Eqs. 5.35, 5.36, 5.39, and 5.40, in Eq. 5.41, and using $\langle \mathrm{g}|D|\mathrm{a}\rangle\langle \mathrm{a}|D^\dagger|\mathrm{g}\rangle = \hbar\alpha_0$, leads to

$$\alpha = \alpha_0 \left\{ \frac{\frac{1}{2} + [\delta + i(\gamma_b - \gamma_a)]/2\tilde{\Omega}}{\frac{1}{2}\left[-\delta - i(\gamma_a + \gamma_b) + \tilde{\Omega}\right] - \Delta} + \frac{\frac{1}{2} - [\delta + i(\gamma_b - \gamma_a)]/2\tilde{\Omega}}{\frac{1}{2}\left[-\delta - i(\gamma_a + \gamma_b) - \tilde{\Omega}\right] - \Delta} \right\}, \tag{5.42}$$

with $\alpha_0 = 3\lambda_L^3\gamma_a/4\pi^2$. With some tedious but straightforward algebra this can be simplified to

$$\alpha = \alpha_0 \left[-\Delta - i\gamma_a + \frac{\Omega_B^2/4}{\Delta + \delta + i\gamma_b} \right]^{-1}. \tag{5.43}$$

which describes the response of a three-level atom in its ground state to a weak probe beam in the presence of a strong light field coupling the upper two states. The real part of α describes dispersion effects and its imaginary part is the absorption probability.

It is also possible to derive Eq. 5.43 with resonant scattering theory. Here, this will not be discussed, and the reader is referred to an article by Fano[31].

5.7.2 Absorption cross section

The absorption cross section is easily derived from the the polarizability expression (Eq. 5.43) by taking the imaginary part. The result is:

$$\sigma = \sigma_0\gamma_a \left[\gamma_a + \frac{\gamma_b\Omega_B^2/4}{(\delta + \Delta)^2 + \gamma_b^2} \right] \left[\left(\Delta - \frac{(\delta + \Delta)\Omega_B^2/4}{(\delta + \Delta)^2 + \gamma_b^2} \right)^2 + \left(\gamma_a + \frac{\gamma_b\Omega_B^2/4}{(\delta + \Delta)^2 + \gamma_b^2} \right)^2 \right]^{-1}, \tag{5.44}$$

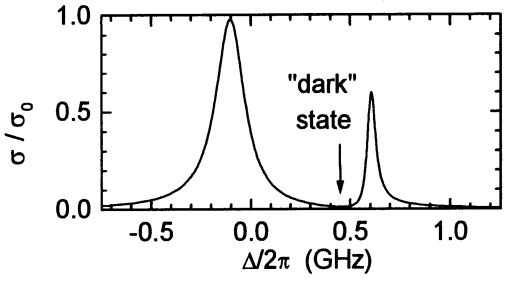

Figure 5.17: Plot of the absorption cross section σ relative to the resonant L_α value, as a function of L_α detuning Δ, for H_α detuning $\delta/2\pi = -0.5\,\mathrm{GHz}$. The arrow indicates the "dark" state.

after normalization to have a resonant cross section of $\sigma_0 = 3\lambda^2/2\pi$ for the pure L_α absorption ($\Omega_B = 0$ and $\Delta = 0$). Note that δ only appears in combination with Δ. Their sum $\delta + \Delta$ is the detuning of the two-photon resonance.

As an example the cross section is plotted in Fig. 5.17 as a function of L_α detuning $\Delta/2\pi$ for a H_α detuning $\delta/2\pi = -0.5\,\mathrm{GHz}$ from the $2P - 3D$ transition. The graph shows a "dark" state, i.e., at a certain point almost no light is absorbed. If the lifetime of the upper state were infinite, a true dark state would be formed when the detuning fulfills the two-photon resonance condition $\Delta + \delta = 0$. The dark state is a linear-superposition state that is completely uncoupled from the light.

In section 5.8 the various broadening mechanisms in the regime where the one- and two-photon transitions are well separated, will be discussed, starting from this equation. To calculate a true spectrum, also Doppler broadening, Zeeman broadening and the effect of a finite source bandwidth should be taken into account, as will be discussed in section 5.8.

5.7.3 Multiple dressed states

So far, only two levels were strongly coupled by the light. In a general experimental situation many more states can be involved. For instance the $2P_{3/2}(3/2)$ state might be coupled to the $3D_{5/2}(1/2)$, $3D_{5/2}(3/2)$, and $3D_{5/2}(5/2)$ states by H_α light. The Hamiltonian can still be diagonalized analytically for the general case of four coupled states. The dressed states should then be expressed in terms of the four unperturbed states and three avoided crossings can be observed. However, the solution in lengthy and does not give much insight.

In a situation where more than four levels are coupled at the same time, numerical diagonalization is unavoidable. Assuming N levels that are being coupled, the numerical task is to diagonalize a $N \times N$ complex non-Hermitian matrix. Having found the N complex eigenvalues E_n, where n labels the dressed states, and the N left- and N right-hand eigenvectors $\langle\phi_n|$ and $|\psi_n\rangle$, the polarizability for a weak beam probing from a state $|g\rangle$ this N level system is a

straightforward generalization of Eq. 5.41:

$$\alpha = \sum_{n=1}^{N} \frac{\langle g|D|\psi_n\rangle\langle\phi_n|D^\dagger|g\rangle}{E_n - \hbar\Delta}. \tag{5.45}$$

If the L_α polarization is a mixture of σ^+ and σ^- light, or the L_α beam makes a small angle with the magnetic-field vector, more $2P$ sublevels are involved, and the L_α propagation through the H gas can no longer be described by a scalar polarizability. A tensor description will be necessary. This will be done in section 5.9.

5.8 Well separated two-photon lines

For sufficiently large detuning δ the three-level system breaks up in the ordinary one-photon transition ($\Delta \approx 0$), now hardly perturbed by the strong H_α light because it is far off-resonance, and the two-photon transition ($\Delta + \delta \approx 0$).

As discussed in section 5.5, the requirement that the light shift must be smaller than the natural line width of the transition is a very strong condition. There is a broad intermediate regime where the one- and two-photon resonances are already well separated and the lines are well described by slightly modified Lorentzians. Moreover, in most cases it is justified to assume only one resonant enhancer per two-photon line. Spectroscopic thermometry relies on the numerical calculation of the exact shape and width of the spectral lines, but in order to get some physical insight in this process, it is important to understand all broadening mechanism separately. Therefore, corrections to the perturbative results will be discussed in the next paragraphs. They include important effects as light shifts, admixture broadening, power broadening and Doppler broadening.

A practical approach to find a more accurate approximation in the limit of large δ than the perturbative expressions of section 5.5, is to start from the full solution for the two-photon line shape and approximate it for small Ω_B^2/δ^2. Near the two-photon resonance ($|-\delta| \approx |\Delta| \gg \gamma_a$) the three-level system becomes an effective two-level system on the background of the weak Lorentzian tail of the one-photon transition:

$$\sigma = \sigma_0 \left\{ \frac{\gamma_a^2}{\Delta^2} + \frac{\gamma_a\gamma_b\Omega_B^2}{4\Delta^2} \left[(\Delta + \delta - \frac{\Omega_B^2}{4\Delta})^2 + \gamma_b^2 + 2(\gamma_a - \gamma_b)\gamma_b \frac{\Omega_B^2}{4\Delta^2} \right]^{-1} \right\}. \tag{5.46}$$

The cross section is the sum of a Lorentzian tail from the one-photon resonance and a Lorentzian describing the two-photon resonance. On the peak of the (light-shifted) two-photon resonance ($\Delta + \delta = \Omega_B^2/4\Delta$), the cross section is easily evaluated to be

$$\sigma = \sigma_0 \left[2 + \frac{\gamma_b}{\gamma_a} \frac{4\Delta^2}{\Omega_B^2} \right]^{-1}, \tag{5.47}$$

where the Lorentz tail of the one-photon transition is neglected. Obviously, this can never exceed $\sigma_0/2$. The reason is that for large Ω_B and small δ, the dressed states become symmetric superpositions of the $|a\rangle$ and the $|b\rangle$ state. Hence, the dressed states can have only a 50 % admixture of the $|a\rangle$ state to which the L_α couples.

Compared with the perturbative expressions, the denominator of the Lorentzian in Eq. 5.46 (the term within the square brackets) has extra terms which are responsible for some of the shift and broadening mechanisms which shall be discussed, one by one, in the following paragraphs.

5.8.1 Light shift

The second term in Eq. 5.46 peaks if $\Delta + \delta = \Omega_B^2/4\Delta$. In the perturbative expressions a resonance was predicted for $\Delta + \delta = 0$. The difference,

$$\frac{\Omega_B^2}{4\Delta}, \tag{5.48}$$

is known as the "light shift" or the ac-Stark shift, caused by the strong H_α light.

In an inhomogeneous light beam, the intensity I of the H_α light and, hence, the Rabi frequency (because $\Omega_B^2 \propto I$) vary. In a spatially inhomogeneous H_α intensity, the light shift varies across the L_α beam profile, leading to a broadened two-photon absorption line. This broadening can be prevented partially by choosing a L_α beam which is much thinner than the H_α beam. However, making the H_α beam larger is limited by the need for high H_α intensity in order to detune far to reduce admixture broadening (which will be discussed below). Narrowing down the cross section of the L_α beam will be limited by the condition that the L_α must be weak, otherwise the strong L_α will cause a (inhomogeneous) light shift and possibly power broadening. It is not difficult to include the light shift due to the L_α. The L_α light causes a light shift in the two-photon resonance of $-\Omega_L^2/4\Delta$, i.e., with a sign opposite to the shift caused by the H_α. The quantity Ω_L is the Rabi frequency of the L_α. Interestingly, this suggests that the light shift caused by the H_α can be compensated by an opposite light shift due to the L_α light. If the two light beams have the same shape and size at the sample, even the broadening due to the inhomogeneous Rabi frequencies could be counterbalanced in this way. However, this cannot be a practical solution because increasing the L_α power to compensate for the inhomogeneous-light-shift broadening due to the H_α, will also increase the power broadening, as is discussed in section 5.8.3.

5.8.2 Admixture broadening

The dressed states are linear superpositions of the unperturbed atomic states combined with the light field. If the lines are well separated, the dressed states can be approximated by the original unperturbed levels with an admixture of the other unperturbed state which becomes

weaker when approaching the far-detuned limit. This will influence the width of the observed resonance lines. In the case of well separate two-photon lines in hydrogen with L_α and H_α, the $2P$ intermediate level is much broader than the $3D$ or $3S$ upper state. As a consequence, the L_α one-photon resonance will be a little narrower than the natural width of the $2P$ state (if other broadening mechanisms can be neglected), due to admixture of the narrower $3S$ or $3D$ state. This effect can usually be neglected because the natural width of the $2P$ state is 10 or 100 times broader than that of the $3D$ and the $3S$, respectively. The two-photon resonance, however, can be significantly broader than the natural width of the upper state, due to the admixture of the broad $2P$ state. We call this "admixture broadening".

The admixture broadening is reflected in Eq. 5.46 by the last term in the denominator of the Lorentzian. By comparing with the natural width of the upper state γ_b it is easily realized that Eq. 5.46 gives rise to a Lorentzian of effective HWHM

$$\gamma_{\text{eff}} = \gamma_b \sqrt{1 + \frac{(\gamma_a - \gamma_b)\Omega_{\text{B}}^2}{2\gamma_b \Delta^2}}. \tag{5.49}$$

Therefore, if one permits not more than a doubling in the natural line width of the upper state, the following condition should be fulfilled:

$$|\Delta| > \sqrt{\frac{\gamma_a - \gamma_b}{2\gamma_b}}\, \Omega_{\text{B}}. \tag{5.50}$$

The consequence of this is that if one wants to observe, e.g., the two-photon closed-cycle transition to the $3D_{5/2}(5/2)$ state, with a width that is less than two times the $3D$ natural line width, the detuning from the resonant enhancer should be $|\Delta| > 2.1\,\Omega_{\text{B}}$. For the $3S$ level this will be $|\Delta| > 7.0\,\Omega_{\text{B}}$, but the Rabi frequency for the H_α transition to the $3S$ state will for the same intensity be $\sqrt{30}$ times smaller.

5.8.3 Power broadening

So far, the assumption was made that the L_α was a weak probe. This assumption is valid if the L_α Rabi frequency $\Omega_{\text{L}} \ll \gamma_a$, as follows from the correction that one can make to the line width due to saturation[32]

$$\gamma = \gamma_a \sqrt{1 + \left(\frac{\Omega_{\text{L}}}{\gamma_a}\right)^2}. \tag{5.51}$$

A similar argument can be made for the power broadening of the two-photon resonance, if we use the effective Rabi frequency from section 5.5 in stead of Ω_{L}. This leads to

$$\gamma = \gamma_b \sqrt{1 + \left(\frac{\Omega_{\text{L}}\Omega_{\text{B}}}{2\Delta\gamma_b}\right)^2}. \tag{5.52}$$

Saturation broadening of the two-photon line can therefore be neglected if the following condition is fulfilled:

$$\left|\frac{\Omega_L \Omega_B}{2\Delta\gamma_b}\right| \ll 1. \tag{5.53}$$

If one assumes a L_α beam which is just saturating the one-photon transition on resonance ($\Omega_L \approx \gamma_a$), the condition for not having power broadening on the two-photon line is $|\Delta| > \Omega_B\gamma_a/2\gamma_b$. For typical detunings in the present measurements ($\Delta \approx 4\,\mathrm{GHz}$), this means that too intense L_α light leads to approximately the same broadening on the two-photon lines as on the one-photon lines, expressed in fractions of the natural line width of the relevant upper state. Note that if condition 5.53 is not fulfilled, the two-photon transition will also suffer from admixture broadening.

Power broadening sets a lower limit to the L_α beam waist. The argument is the following. Approximately 10^4 electrons per pulse are needed for a signal-to-noise ratio of 100 on the photo detector that measures the transmitted L_α. Taking into account 10 % quantum efficiency of common photo-multiplier tubes and transmission losses in the VUV optics, 10^6 photons are required in the sample cell. In 10 ns, our present pulse length, this is an average power of 0.16 mW. In order not to exceed the saturation intensity of $3.6\,\mathrm{W\,cm^{-2}}$, the L_α ($1/e^2$-intensity-radius) beam waist must be larger than $53\,\mu$m. This is only a factor of two below the present beam waist. Hence, with the present L_α pulse length, the beam radius cannot be reduced much further without getting significant power broadening or poor signal-to-noise ratios. However, two remarks are in order. The first is that the above considerations about power broadening are only approximations for effective two-level systems that are derived for continuous-wave light. For pulsed light sources, the absorption probability depends on the exact pulse shape. The second remark is that future experiments may circumvent this beam-waist limit by using longer L_α pulses, which will come as an almost natural by-product of a reduction of the bandwidth of the L_α source, because of the Fourier limitation on the bandwidth of short pulses.

5.8.4 Doppler broadening

So far, the atoms were assumed to be at rest. Since they move in a real trap at finite temperatures, each atom will sense a Doppler-shifted light frequency (alternatively, one can say that the atomic transitions frequencies change for a moving atom). The frequency shift as observed by the moving atom will be

$$\kappa \equiv -\omega_L \frac{v_z}{c}, \tag{5.54}$$

with ω_L the frequency of the light (L_α in our case) in the lab frame, v_z the velocity of the atom in the propagation direction of the light beam, and c the speed of light. Since the atoms will have thermally distributed velocities, the observed transmission line profile will be the convolution of the Lorentzian natural line shape (or a power- or admixture-broadened Lorentzian) and a

Gausian reflecting the Maxwell-Boltzmann velocity distribution. Assuming for the moment a delta-function natural line, the resulting line shape after convolution will be

$$F_{\mathrm{G}}(\Delta, b) = \frac{1}{\sqrt{\pi}\, b} e^{-(\Delta/b)^2}, \tag{5.55}$$

with $\Delta = \omega_{\mathrm{L}} - \omega_1$ the detuning of the laser frequency ω_{L} from the atomic transition frequency ω_1, and $b = (\omega_{\mathrm{L}}/c)\sqrt{2k_{\mathrm{B}}T/m}$ a wavelength and temperature dependent parameter which is the $1/e$ half width of a Doppler broadened delta function. The FWHM line width of a purely Doppler broadened line is $2b\sqrt{\ln 2}$. The Gaussian is normalized as $\int_{-\infty}^{\infty} F_{\mathrm{G}}(\Delta, b) d\Delta = 1$. Substituting the values for the L_α transition in hydrogen, one evaluates $b/2\pi = 1.0567\sqrt{T}\,\mathrm{GHz\,K^{-1/2}}$, or, equivalently, a FWHM Doppler line width of $\Delta_{\mathrm{G}}/2\pi = 1.76\sqrt{T}\,\mathrm{GHz\,K^{-1/2}}$. Eq. 5.55 is a good approximation to the Doppler broadened line shape for $b \gg \gamma$, where 2γ is the natural width of the excited state, which evaluates to the condition $T \gg 2.2\,\mathrm{mK}$. For temperatures $T \ll 2.2\,\mathrm{mK}$, the Doppler broadening can be neglected and the L_α resonance will be approximately a Lorentzian $F_{\mathrm{L}}(\Delta, \gamma)$, which was introduced in section 5.5.

For temperatures where the Doppler broadening is of the same order as the L_α natural line width ($T \approx 2.2\,\mathrm{mK}$), the convolution of the L_α Lorentzian natural line with the Maxwell-Boltzmann velocity distribution will lead to a line shape which is called the "Voigt" profile. This convolution is most easily done if the Lorentzian is expressed in complex form:

$$F_{\mathrm{L}}(\Delta, \gamma) = \frac{1}{\pi} \mathrm{Im}\left(\frac{1}{\Delta - i\gamma}\right), \tag{5.56}$$

because

$$(2\pi k_{\mathrm{B}}T/m)^{-1/2} \int_{-\infty}^{\infty} dv_z \frac{1}{\kappa - \Delta - i\gamma} e^{-mv_z^2/k_{\mathrm{B}}T} = \frac{i\sqrt{\pi}}{b} w(\zeta), \tag{5.57}$$

where the complex error function

$$w(\zeta) = e^{-\zeta^2} \mathrm{erfc}(-i\zeta), \tag{5.58}$$

with $\zeta = (\Delta + i\gamma)/b$ and γ the natural radiative half width. Hence, the resulting normalized Voigt absorption profile is $\mathrm{Re}\,(iw(\zeta)/\sqrt{\pi}b)$.

The two-photon transitions will also experience Doppler broadening. In the general case, both the detuning from the two-photon resonance ($\Delta + \delta \approx 0$) and the detuning from the resonant enhancing intermediate level(s) ($\delta \approx -\Delta$) that are experienced by the moving atom depend on its velocity. For the general case of several two-photon lines each having several resonant enhancers, the resulting line shape will be very complicated and numerical convolution seems the only way to calculate the spectrum. Fortunately, some important approximations can be made. In the far-detuned limit, for instance, one can approximate the Doppler-broadened line shape by neglecting the shift in the detuning from the resonant enhancer. With this approximation the Doppler broadening can be found in a way similar to the Doppler broadening

of a one-photon transition. Consider again an atom moving with velocity v_z in the direction of the two light beams, which are assumed to be co-propagating as in our experimental situation. The atom will experience a shift in the sum frequency of the two beams

$$-(\omega_{\mathrm{L}}+\omega_{\mathrm{B}})\frac{v_z}{c}=\kappa\eta, \tag{5.59}$$

with $\omega_{\mathrm{L}}+\omega_{\mathrm{B}}$ the sum frequency of the two light beams in the lab frame and $\eta = 32/27$ the ratio of Lyman-β to Lyman-α frequencies. (Because the sum frequency of the L_α+H_α two-photon transition is identical to the of a Lyman-β transition frequency, the Doppler shift in the two-photon case is identical to the shift the atom would see on the Lyman-β transition). The $1/e$ half width of the Doppler broadening is given by $b_2/2\pi = 1.2525\sqrt{T}\,\mathrm{GHz\,K^{-1/2}}$, or, equivalently, a FWHM Doppler width of $\Delta_{\mathrm{D}}/2\pi = 2.09\sqrt{T}\,\mathrm{GHz\,K^{-1/2}}$. The line shape of a real resonance is well approximated by this Gaussian if $b_2 \gg \gamma_b$, with γ_b the natural line width of the upper state. This Doppler broadening is not very different from the L_α Doppler broadening. However, the natural line widths of the $3D$ state and the $3S$ are much narrower than the $2P$ line width. Therefore, the H_α lines are described by pure Gaussians to much lower temperatures than the $2P$ state, $16\,\mu\mathrm{K}$ and $0.16\,\mu\mathrm{K}$ for the $3D$ and the $3S$ state, respectively. This is a very important property of RETS, and it permits, in principle, Doppler thermometry down to temperature well below the BEC transition temperature (approximately $30\,\mu\mathrm{K}$ at a density of $10^{14}\,\mathrm{cm^{-3}}$). If the condition $b_2 \gg \gamma_b$ is not met, the Voigt profile should be used to describe the line profile, in a similar way as in the one-photon line.

If the one- and two-photon lines are well separated, the dressed states resembling the $n = 3$ states have small admixtures of the $2P$ state, which results in a somewhat broader Lorentzian. In principle, the Doppler broadening should be considered independently for both the unperturbed states of which the dressed state is composed. However, the difference in Doppler shift for a one-photon L_α transition and a two-photon L_α + H_α transition is only 20 %, and the admixture is usually small. Therefore, in most cases it suffices to approximate the line shapes of the dressed states by first calculating the admixture- and power-broadened Lorentzian and then Doppler broaden this to a Voigt profile, using the Lyman-β shift for the lines with mainly a two-photon character and the L_α shift for the lines that have a predominant one-photon character.

As long as each two-photon line has a single resonant enhancer, the full convolution can be done analytically, too. Consider, for instance, Eq. 5.43. For an atom moving with velocity v_z, this can be written in the following way:

$$\alpha(\kappa)=\alpha_0\left[\kappa-(\Delta+i\gamma_a)+\frac{\Omega_{\mathrm{B}}^2/4\eta}{(\Delta+\delta+i\gamma_b)/\eta-\kappa}\right]^{-1}. \tag{5.60}$$

It is not difficult to show[33] that this can be written as

$$\alpha(\kappa)=\frac{C_0}{\kappa-\kappa_0}+\frac{C_1}{\kappa-\kappa_1}, \tag{5.61}$$

where κ_0 and κ_1 are the roots of $0 = [\kappa - (\Delta + i\gamma_a)][\kappa - (\Delta + \delta + i\gamma_b)/\eta] - \Omega_B^2/4\eta$ and C_0 and C_1 are given by

$$C_0 = \frac{(\Delta + \delta + i\gamma_b)/\eta - \kappa_0}{\kappa_1 - \kappa_0}, \quad C_1 = \frac{\kappa_1 - (\Delta + \delta + i\gamma_b)/\eta}{\kappa_1 - \kappa_0}. \tag{5.62}$$

Note that the partial fraction expansion of α (Eq. 5.61) is a function of Doppler shift, in contrast to Eq. 5.41, which is expressed as a function of the L_α detuning. Having written α as a sum of complex Lorentzians, the convolution with a Maxwell-Boltzmann velocity distribution directly leads to

$$\langle \alpha(\kappa) \rangle = \alpha_0 \frac{i\sqrt{\pi}}{b} \left[C_0 w(\kappa_0/b) + C_1 w(\kappa_1/b) \right], \tag{5.63}$$

where the $\langle\rangle$ brackets denote the average over the thermal distribution.

5.9 Light propagation through a dilute gas

The atomic H gas is, from the point of view of the probing light beam, an inhomogeneous cloud of resonant scatterers. In order to predict the absorption spectra, a semi-classical theory will be used to calculate the propagation of the light beams through the sample. This model treats the electric-field vector $\vec{E}(\vec{r})$ classically. On the other hand, the interaction between the atoms and the light is described quantum mechanically. Because the L_α light can have arbitrary polarization and this polarization can change due to dispersive effects as Faraday rotation, the spectrum calculation should keep track of the polarization of the L_α when propagating through the gas. It is therefore necessary to reach beyond the scalar polarizability description which was used for the description of the line shapes. Instead, it will be assumed that the L_α light propagation can be described by a complex susceptibility tensor, depending on the local conditions in the gas. This susceptibility will in general depend on the local magnetic field, and in the two-photon case, also on the frequency and local intensity of the H_α beam. Because the H_α light intensity dominates over the L_α light intensity, the H_α attenuation is neglected.

The electric field and the polarization should obey the wave equation which directly follows from Maxwell's equations[34]:

$$\nabla^2 \vec{E} - \frac{1}{c^2} \frac{\partial^2 \vec{E}}{\partial t^2} = \frac{1}{\epsilon_0 c^2} \frac{\partial^2 \vec{P}}{\partial t^2} - \frac{1}{\epsilon_0} \vec{\nabla}(\vec{\nabla} \cdot \vec{P}). \tag{5.64}$$

The L_α light that passes through the sample is an electromagnetic wave of which the (complex) electric field $\vec{E}(\vec{r}, t)$ and induced polarization $\vec{P}(\vec{r}, t)$ in a dilute polarizable medium can, to a very good approximation, be written as

$$\begin{aligned} \vec{E}(\vec{r}, t) &= \vec{E}_0(\vec{r}, t) e^{i(kz - \omega t)} \\ \vec{P}(\vec{r}, t) &= \vec{P}_0(\vec{r}, t) e^{i(kz - \omega t)}, \end{aligned} \tag{5.65}$$

where $k = |\vec{k}| = \omega/c$ is the wave vector of a plane wave in vacuum with frequency ω. By substituting Eqs. 5.65 in Eq. 5.64 and by making the assumption that $\vec{E}_0(\vec{r},t)$ and $\vec{P}_0(\vec{r},t)$ are slowly varying complex amplitudes, i.e., they change on a much longer length scale than the wavelength of the light (slowly-varying-envelope approximation), we arrive at

$$\frac{\partial \vec{E}_0}{\partial z} = \frac{ik}{2\epsilon_0}\left[\vec{P}_0 - (\vec{P}_0 \cdot \vec{e}_z)\vec{e}_z\right]. \tag{5.66}$$

This equation describes the attenuation and dispersion of an electromagnetic wave as a result of the induced polarization. It will be the basis of the calculation of the propagation of the L_α light through the sample.

It is assumed that the medium is linear, i.e., the induced polarization has a linear dependence on the electric field vector. The complex electric susceptibility tensor $\overleftrightarrow{\chi}$, defined by

$$\vec{P}_0 = \epsilon_0 \overleftrightarrow{\chi}\, \vec{E}_0, \tag{5.67}$$

is the medium-dependent proportionality constant between the electric field vector and the induced polarization. Eq. 5.66 allows the complete determination of the propagation of the light through the gas, as soon as the complex susceptibility tensor is known. The expression of $\overleftrightarrow{\chi}$ in terms of the atomic properties will be the subject of the next sections.

5.9.1 Complex susceptibility tensor

The susceptibility for a weak beam probing a N level system at rest, is:

$$\overleftrightarrow{\chi}_0 = \frac{1}{\epsilon_0}\sum_{g,n}\rho_g(\vec{r})\frac{\langle g|\vec{D}|\psi_n\rangle\langle\phi_n|\vec{D}^\dagger|g\rangle}{E_n - E_g - \hbar\omega_L}, \tag{5.68}$$

with ω_L the frequency of the L_α probe laser, E_n the (complex) eigenenergy of the n^{th} dressed state, and $\rho_g(\vec{r})$ the local density of atoms in ground state g (that is, c or d atoms in the case of magnetically trapped atomic H). The susceptibility has a simple relation to the polarizability α discussed earlier: $\overleftrightarrow{\chi}_0 = \rho\, \overleftrightarrow{\alpha}$, with density ρ, and $\overleftrightarrow{\alpha}$ the tensor generalization of α.

To calculate the absorption spectrum, $\overleftrightarrow{\chi}_0$ has to be convoluted with a Gaussian corresponding to the Maxwell-Boltzmann velocity distribution. Because of the dependence on two light beams with different colors, $\overleftrightarrow{\chi}_0$ should be considered a function of both Doppler-shifted frequencies explicitly when performing the convolution

$$\overleftrightarrow{\chi}\,(\omega_L,\omega_B) = (2\pi k_B T/m)^{-1/2}\int_{-\infty}^{\infty} dv_z\, \overleftrightarrow{\chi}_0\,(\omega_L',\omega_B')e^{-mv_z^2/k_B T}, \tag{5.69}$$

with $\omega_L' = \omega_L(1 - v_z/c)$ and $\omega_B' = \omega_B(1 - v_z/c)$.

As explained in section 5.8.4, if all two-photon lines are well separated and have only a single resonant enhancer, this convolution can be done analytically. In the case of a tensor susceptibility, the convolution should be performed for all entries of the susceptibility matrix independently.

5.9.2 Spectrum calculation

When the susceptibility is known as a function of magnetic field and H_α intensity, the absorption spectrum can be calculated by propagating light rays through the sample based on Eq. 5.66, using the local magnetic field as discussed in chapter 2, as well as the density distribution of the gas. The problem is rather involved, because both magnitude and direction of the magnetic field and the gas density depend on position. The one-photon absorption spectrum can be calculated completely by numerical methods identical to those used by Luiten [2], which take into account all absorption lines as well as dispersive effects. In our experimental situation, we focus the L_α beam onto the sample, but because the depth of focus is of the order of 10 cm, much larger than the sample length, the light can be approximated by a parrallel beam. In the two-photon case, we usually restrict our selves to detunings such that the earlier mentioned approximation of a single resonant enhancer is quite good. This keeps the calculation tractable.

The polarization vector of the light is most easily expressed in the linear $(\vec{e}_1, \vec{e}_2, \vec{e}_3)$ basis, defined by

$$\begin{aligned} \vec{e}_3 &= \vec{k}/k, \\ \vec{e}_2 &= (\vec{e}_3 \times \vec{B})/B, \\ \vec{e}_1 &= \vec{e}_2 \times \vec{e}_3, \end{aligned} \tag{5.70}$$

with $\vec{k}$ the propagation direction of the probe beam. The axis $\vec{e}_3$ is identical to the z-axis, the symmetry axis of the trap. Eq. 5.70 guarantees that $\vec{B}$ lies in the plane defined by $\vec{e}_1$ and $\vec{e}_3$. The electric field amplitude $\vec{E}_0$ can be expressed in this linear basis as

$$\vec{E}_0 = E_{01}\vec{e}_1 + E_{02}\vec{e}_2, \tag{5.71}$$

or in the circular polarization basis $(\vec{e}_+, \vec{e}_-, \vec{e}_3)$ as

$$\vec{E}_0 = E_{0+}\vec{e}_+ + E_{0-}\vec{e}_-, \tag{5.72}$$

where $\vec{e}_+$ and $\vec{e}_-$ are circular unit vectors, defined by $\vec{e}_\pm \equiv (\vec{e}_1 \pm i\vec{e}_2)/\sqrt{2}$.

One more basis is useful: $(\vec{e}_+', \vec{e}_-', \vec{e}_3')$, defined by $\vec{e}_3' = \vec{B}/B, \vec{e}_2' = \vec{e}_2, \vec{e}_1' = \vec{e}_2' \times \vec{e}_3'$ and $\vec{e}_\pm' = (\vec{e}_1' \pm i\vec{e}_2')/\sqrt{2}$. This is nothing else than the circular polarization basis $(\vec{e}_+, \vec{e}_-, \vec{e}_3)$ rotated in the plane defined by $\vec{k}$ and $\vec{B}$ such that $\vec{e}_3'$ points in the direction of the local magnetic field. The transformation matrix describing this rotation[2] depends on the local direction of the magnetic field. In the one-photon case, and with the approximation that for each two-photon line only a single resonant enhancer is important also in the two-photon case, the complex susceptibility tensor $\overleftrightarrow{\chi}$ takes a simple diagonal form in the $(\vec{e}_+', \vec{e}_-', \vec{e}_3')$ basis:

$$\left[\overleftrightarrow{\chi}\right]' = \begin{pmatrix} \chi_+ & 0 & 0 \\ 0 & \chi_- & 0 \\ 0 & 0 & \chi_z \end{pmatrix}, \tag{5.73}$$

where $\chi_+ = \rho_g(\vec{r})\alpha_+$ and α_+ is defined as in Eq. 5.45, but with the dipole operator restricted to couple two states only if $\Delta m_j = 1$ (σ^+ transitions). The quantity $\rho_g(\vec{r})$ is the local density of ground-state atoms. Similarly, χ_- and χ_z are restricted to $\Delta m_j = -1$ (σ^- transitions) and $\Delta m_j = 0$ (π transitions), respectively.

We restrict ourselves to axially symetric beam profiles. In that case the calculation of the spectrum only requires the numerical integration of few rays for one azimuthal angle about the z-axis, as is discussed in detail in [2]. Such a calculation turned out to be fast enough, on a standard 1996 desktop computer (90 MHz Pentium), to calculate a two-photon spectrum with two two-photon lines in, typically, 10 minutes.

For the calculation of a ray of light exactly on the z-axis a further approximation can be made. On the z-axis, the magnetic field is parallel to the light, $\chi_z = 0$ and the π lines are absent. Therefore, the propagation of the light can be described in scalar form by the following two uncoupled equations:

$$\frac{\partial E_{0\pm}}{\partial z} = \tfrac{1}{2} i k \chi_\pm E_{0\pm}. \tag{5.74}$$

The calculation of the propagation of a light ray on the z-axis is much faster than that of rays parallel to the z axis but at an arbitrary distance, where the finite angles with the magnetic field come into play. This on-axis ray is therefore useful as a first indication of the shape of the absorption spectrum, but it is in general not sufficient.

In the general two-photon case, where the condition of a single resonant enhancer is relaxed, the spectrum can be calculated as well, but one should be more careful. For instance, in the presence of H_α light of *arbitrary* polarization, there is no obvious basis in which $\overleftrightarrow{\chi}$ is diagonal. The reason is that for a mixed H_α polarization the dressed states will in general have admixtures of several $2P$ sublevels with different magnetic quantum numbers m_j so that the ground state will be coupled to such a dressed state no matter which L_α polarization is used.

Hence, to avoid complications when using RETS for (Doppler) thermometry, it should be attempted to arrange a fully circularly polarized H_α beam, so that only one resonant enhancer should be considered per two-photon line, in addition to choosing the detuning from this level small compared to the Zeeman-shifts of the other transitions.

5.10 RETS during evaporative cooling

The unique combination of high resolution and high sensitivity enables rapid non-perturbative *in situ* studies of the trapped gas. As an example, the evolution of a gas cloud was observed during forced evaporative cooling, induced by lowering the field of one of the axial confinement coils. As shown in Fig. 5.18(a), at a density of $10^{13}\,\mathrm{cm}^{-3}$ the one-photon spectrum is strongly broadened by optical thickness, obscuring the effects of Zeeman and Doppler broadening.

The cooling process is monitored by taking spectra approximately every 10 seconds, scanning

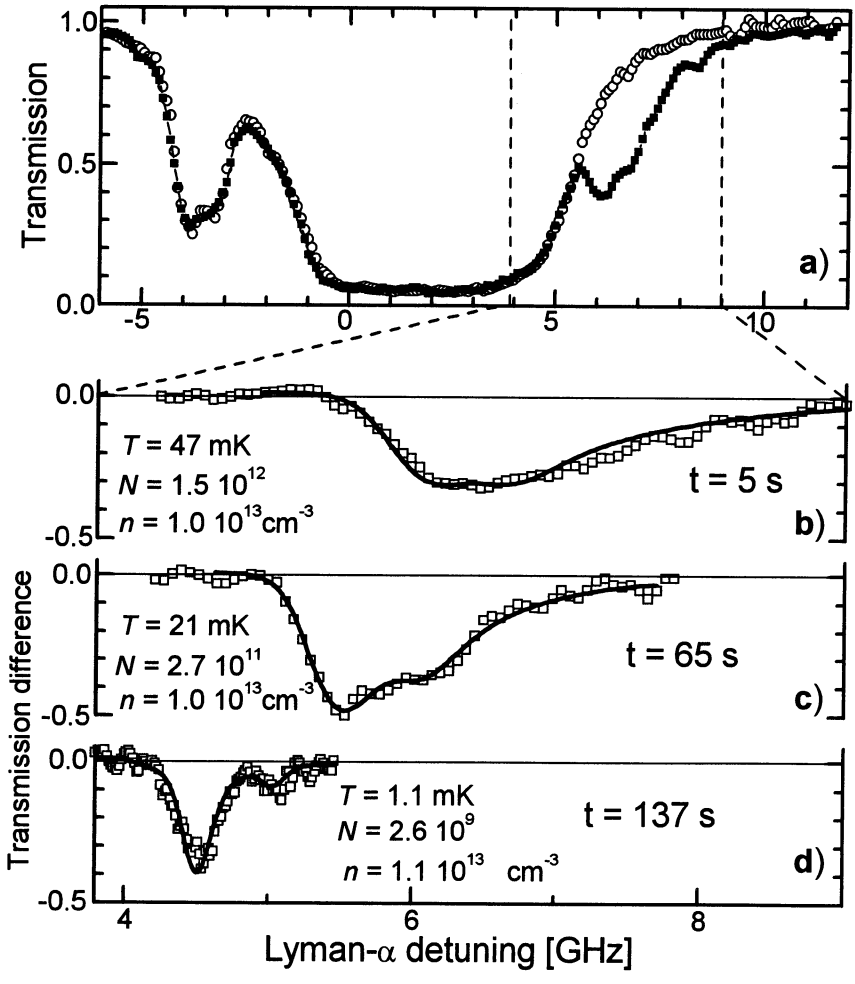

Figure 5.18: (a) L_α absorption spectrum without (open circles) and with (solid squares) red light present. The L_α detuning is given relative to the $1S_{1/2} - 2P_{3/2}$ transition at the magnetic field minimum. (b-d) Difference spectra (L_α absorption with minus without red light) showing two-photon resonances during forced evaporative cooling of a single sample. Cooling starts at time $t = 0$ in (b), The temperature (T), the central density (n), and the number of atoms (N) are derived from the fits (solid lines). Accuracies are of the order of 20 %, except in the final spectrum (d), where the error is of the order of 50 %. One scan takes ~ 5 s.

the L_α frequency for fixed H_α frequency and recording the L_α absorption alternatingly with H_α light present and absent. A selection of spectra recorded during such a sequence can be seen in Fig. 5.18(b-d). The two-photon transition used is the $1S_{1/2}-3D_{5/2}$. The two-photon resonances visible in Fig. 5.18(b-d) shift to lower detunings, since the magnetic offset field decreases during the forced evaporation. At the starting conditions, Fig. 5.18(b) the temperature is 47 mK with the Zeeman broadening dominating over the Doppler effect, yielding the asymmetric two-photon resonance line with a long tail towards higher frequencies. As the sample cools, the cloud shrinks as does the Zeeman broadening which can be seen in the series of spectra in Figs. 5.18(b-d). Spectrum (d) at (1.1 ± 0.5) mK, shows two almost symmetric resonances. The splitting between them, 0.52 GHz, is caused by the hyperfine structure, mainly that of the $1S$ ground state. The larger of the two peaks originates from the d atoms, which outnumber the c atoms. Absorption of c atoms causes the smaller peak. A fit to the double-peak spectrum gives a ratio of the number of c to the number of d atoms of $7 \pm 2\,\%$.

The fit to the two peaks in Fig. 5.18(d) gives a FWHM of 0.33 GHz. This width is determined by a number of properties and processes. Power and admixture broadening are not important: because of the large detuning (4.5 GHz) from the $2P$ state, the $3D$ state (natural linewidth 10 MHz) has almost negligible admixture of the $2P$ state, broadening the $3D$ natural linewidth of 10 MHz to $\sim$11 MHz. Also the broadening caused by the light shift, which varies across the L_α beam profile because of the H_α beam profile, does not contribute much, because the light shift is only 20 MHz at the center of the line. More important is Doppler broadening of the RETS line, which amounts to 69 MHz (FWHM) at 1.1 mK. At this temperature, the average Zeeman-shift of the two-photon lines for the trapped atoms with respect to an atom at the trap minimum is 66 MHz, indicative for the asymmetric broadening of the two-photon lines. The L_α source width was estimated to be 150 MHz during this measurement. All these contributions together constitute only about 60 % of the total observed line width. This discrepancy can be traced back to optical thickness. The physical picture of this broadening is the following. On resonance the gas is optically thick. The fact that only part of the impinging light beam is absorbed just reflects the fact that the light beam is not an infinitely narrow ray (here, both the gas cloud and the L_α beam had a radius of 0.10 mm). Some of the light leaks around so to say. If one detunes away from resonance, the gas cloud ultimately becomes transparent. The width of the line reflects how far one has to be away from resonance before this transparency sets in, something that obviously depends on density. The interplay with the other broadening mechanisms such as Zeeman broadening can be modeled reasonably well numerically if the optical thickness is not too great.

The example given here demonstrates that RETS can be used to obtain information on temperature and density in a way that complements L_α spectroscopy. In particular the tunable transparency is an important asset (compare, e.g., the optical density of the one- and two-photon contributions to the spectrum in Fig. 5.18(a)). The narrow line with of the $3D$ or $3S$

upper state can only be exploited in future generations of experiments, in which the presently dominating instrumental broadening effects have been eliminated.

5.11 Discussion

In this chapter we presented the first results with resonance enhanced two-photon spectroscopy as a diagnostic tool for cold trapped atomic hydrogen. With the demonstration of RETS, we have circumvented the intrinsically limited resolution of L_α spectroscopy due to the short radiative lifetime of the $2P$ state. For the $1S - 3S$ two-photon transition, the resolution of RETS is in principle only limited by the 1 MHz natural line width of the $3S$ state. At present the resolution is still limited by the $\sim 100 - 150$ MHz L_α source bandwidth.

In fact, the resolution of RETS on atomic hydrogen is not even limited by the width of the $3S$ state. The intrinsic resolution of RETS is only limited by the lifetime of the upper state. Hence, instead of using the H_α transition to excite the $3S$, one could take any other transition from the Balmer series. By using, for instance, the second transition in the Balmer series, Balmer-β, with a wavelength of 486 nm, one has access to the $4S$ level which has a partial lifetime of $\tau_{4S\rightarrow 2P} = 0.40\,\mu$s. However, no orders of magnitude can be gained here, and since narrower lines are more difficult to observe, especially when they are broadened and the maximum absorption becomes very weak, we have selected H_α as the preferred transition.

It is important to be aware of the limitations of RETS. As was mentioned in section 5.10, power and admixture broadening, and the effect of spatially inhomogeneous light shifts are not important, with the present L_α source bandwidth. Once the L_α source bandwidth is reduced, these broadening mechanisms should be reconsidered. Fortunately, the reduction of the L_α source width will necessarily result in longer pulses, so that power broadening of both the L_α as the RETS lines will probably still be negligible. The line shapes of the RETS lines are completely described by the dressed atom formalism discussed in this chapter, so the effect of admixture broadening and varying light shifts should not hinder the spectrum calculation, as long as these effects do not start dominating the observed line widths. With the present H_α Rabi frequency of 1 GHz the admixture broadening is already smaller than the $3D$ natural line width for detunings of 2.2 GHz, and scales with Ω_B^2/Δ^2. Note, however, that the two-photon signal decreases as Ω_B^2/Δ^2, too. Hence, to reduce admixture broadening, further detuning with more H_α power does not help. More H_α power does enable larger H_α beam waists and therefore smaller broadening due to the varying light shifts.

The relative dimensions of the light beams and sub-millikelvin H sample remain a point of concern. The sample radius can easily be increased by adiabatic expansion. However, this reduces temperature, increasing the need for a smaller L_α source bandwidth. A solution is to reduce the L_α beam waist further, e.g. by placing the focusing lens much closer to the sample than the present distance (approximately 1 m). As was discussed in section 5.8.3, reducing the

L_α beam waist implies higher L_α intensities. Therefore, in order to avoid power broadening, decreasing the L_α beam waist can only be useful with longer L_α pulses.

The next step towards the use of RETS as a sensitive and accurate diagnostic tool for atomic hydrogen, is to reduce the bandwidth of the L_α source. There are several options to achieve this. The most straightforward way is to increase the pulse length and reduce the bandwidth of the UV which is frequency tripled to produce L_α (see chapter 3). Another idea might be to use frequency tripling inside a cavity, using the strong dispersion of, e.g., MgF_2 to couple out the L_α. Completely new L_α production schemes are an option, too: as mentioned in section 3.2, at the Max-Planck-Institut für Quantenoptik in Garching, Germany, one is studying the feasibility of a narrow band *continuous wave* L_α source[35].

It is interesting to compare RETS with $1S-2S$ two-photon spectroscopy, which was demonstrated in a magnetic trap in 1996 at MIT[6]. Two photons of wavelength $2\lambda = 243\,\text{nm}$ can excite a transition from the $1S$ ground state to the $2S$ first excited state. By using two counter-propagating photons, this transition is Doppler-free. The temperature of the gas can be obtained from the transit time broadening of the two-photon resonance. This method potentially has a very high resolution, because the metastable $2S$ state has a very long radiative lifetime ($\sim 0.12\,\text{s}$), corresponding to a natural line width of $\sim 1.3\,\text{Hz}$. However, to get reasonable signals, one needs a very narrow band light source ($\sim 1\,\text{kHz}$) with relatively high laser power. The generation of the high-power continuous-wave narrow band 243 nm light is of comparable complexity as the generation of the L_α light. Another technical complication is that the $1S-2S$ two-photon absorption cannot be observed in absorption, and has to rely on counting fluorescent L_α photons produced by quenching the $1S$ state. These L_α photon are observed with a low detection efficiency ($4 \cdot 10^{-6}$)[6], and many atoms must be excited and quenched to get a reasonable signal. Typical integration times needed are $> 60\,\text{s}$. Compared with this $1S-2S$ scheme, L_α spectroscopy and RETS have several advantages. Closed cycle transitions can be used for the detection. Because the absolute cross section is well known, the absolute column density can be obtained directly. Moreover, relatively few atoms need to be excited because the absorption can efficiently be observed in transmission. Therefore, for fast non-destructive measurements of cold trapped gas, RETS offers the better perspective.

For high density gases, an important property of RETS is that the absorption cross section for two-photon absorption can be adjusted, even on the center of the two-photon resonance, by choosing the detuning from the intermediate $2P$ state. Compared to one-photon spectroscopy, this tunable transparency offers important advantages for the investigation of inhomogeneous dense gases. One may investigate the densest parts of the sample near their resonance frequency without being limited by optical thickness. It is clear that for optical investigations on high density samples of $H\downarrow$, with densities varying between $10^9\,\text{cm}^{-3}$ and $10^{19}\,\text{cm}^{-3}$, tunable transparency may be a key advantage.

Finally, a fascinating application of RETS should be mentioned which lies, perhaps, a little

further away in the future. Symmetry tests on antiatoms will most probably start with a spectroscopic investigation[36], once antihydrogen is created and stored in sufficient quantities. Resonance enhanced $1S - 3S$ spectroscopy offers the perspective of a spectral resolution that is two orders of magnitude better than one-photon L_α spectroscopy, with, at the same time, a resonant cross section of up to 50% of the $3\lambda^2/2\pi$ single-photon L_α cross section.

Bibliography

[1] O.J. Luiten, H.G.C. Werij, I.D. Setija, M.W. Reynolds, T.W. Hijmans, and J.T.M. Walraven, Phys. Rev. Lett. **70**, 544 (1993).

[2] O.J. Luiten, Ph. D. thesis, University of Amsterdam (1993); O.J. Luiten, H.G.C. Werij, M.W. Reynolds, I.D. Setija, T.W. Hijmans and J.T.M. Walraven, Appl. Phys. B **59**, 311 (1994).

[3] I.D. Setija, Ph. D. thesis, University of Amsterdam (1995).

[4] P.W.H. Pinkse, A. Mosk, M. Weidemüller, M.W. Reynolds, T.W. Hijmans, J.T.M. Walraven, and C. Zimmermann, Phys. Rev. Lett. **79**, 2423 (1997).

[5] That the presence of a resonance can greatly enhance a two-photon transition was demonstrated in an experiment with sodium: J.E. Bjorkholm and P.F. Liao, Phys. Rev. Lett. **33**, 33 (1974).

[6] Claudio L. Cesar, Dale G. Fried, Thomas C. Killian, Adam D. Polcyn, Jon C. Sandberg, Ite A. Yu, Thomas J. Greytak, Daniel Kleppner, and John M. Doyle, Phys. Rev. Lett. **77**, 255 (1996).

[7] *Atom-Photon Interactions: Basic Processes and Applications*, Claude Cohen-Tannoudji, Jacques Dupont-Roc and Gilbert Grynberg (John Wiley & Sons, USA, 1992).

[8] S. Bourzeix, B. de Beauvoir, F. Nez, M.D. Plimmer, F. de Tomasi, L. Julien, F. Biraben, and D.N. Stacey, Phys. Rev. Lett. **76**, 384 (1996).

[9] M. Weitz, A. Huber, F. Schmidt-Kaler, D. Leibfried, W. Vassen, C. Zimmermann, K. Pachucki, T.W. Hänsch, L. Julien and F. Biraben, Phys. Rev. A **52**, 2664 (1995). This reference contains the latest value of Rydberg constant.

[10] D.J. Berkeland, E.A. Hinds, and M.G. Boshier, Phys. Rev. Lett. **75**, 2470 (1995).

[11] Krzysztof Pachucki, Phys. Rev. Lett. **72**, 3154 (1994).

[12] G.K. Woodgate, *Elementary Atomic Structure* (Oxford University Press, USA 1980).

[13] T. Andreae, W. König, R. Wynands, D. Leibfried, F. Schmidt-Kaler, C. Zimmermann, D. Meschede, and T.W. Hänsch, Phys. Rev. Lett. **69**, 1923 (1992).

[14] *Symbols, Units, Nomenclature and Fundamental Constants in Physics* prepared by E. Richard Cohen and Pierre Giacomo, Physica **146 A**, 1 (1987).

[15] Hans A. Bethe and Edwin E. Salpeter, *Quantum Mechanics of One- and Two-Electron Atoms* (Plenum Publishing Corporation, New York, 1977).

[16] J.R. Sapirstein and D.R. Yennie, in *Quantum Electrodynamics*, edited by T. Kinoshita (World Scientific, Singapore, 1990).

[17] S.R. Lundeen and F.M. Pipkin, Phys. Rev. Lett. **46**, 232 (1981); E.W. Hagley and F.M. Pipkin, Phys. Rev. Lett. **72**, 1172 (1994).

[18] R.G. Beausoleil, D.H. McIntyre, C.J. Foot, E.A. Hildum, B. Couillaud and T.W. Hänsch, Phys. Rev. A **35**, 4878 (1987).

[19] J.D. Garcia and J.E. Mack, J. Opt. Soc. Am. **55**, 654 (1965).

[20] Stanley J. Brodsky and Ronald G. Parsons, Phys. Rev. **163**, 134 (1967).

[21] See, e.g., *Atomic Physics 15*, proceedings of the 15th international conference on atomic physics, Zeeman-effect centenary, Amsterdam, The Netherlands, 5-9 August 1996, H.B. van Linden van den Heuvell, J.T.M. Walraven and M.W. Reynolds, eds. (World Scientific, Singapore 1997).

[22] Eugene P. Wigner, *Group Theory* (Academic Press, New York 1959).

[23] D. Kleppner, in *The Hydrogen Atom*, edited by G.F. Bassani, M. Inguscio, and T.W. Hänsch (Springer-Verlag Berlin, Heidelberg 1989).

[24] Rodney Loudon, *The Quantum Theory of Light* (Oxford University Press, New York, 1983).

[25] Helmut Hönl, Zeits. für Phys. **31**, 340 (1925); R. de L. Kronig, Zeits. für Phys. **31**, 885 (1925).

[26] Bruce W. Shore, *The Theory of Coherent Atomic Excitation* (John Wiley & Sons, USA, 1990).

[27] C. Cohen-Tannoudji and S. Haroche, Journal de Physique **30**, 153 (1969).

[28] Claude Cohen-Tannoudji and Serge Reynaud, J. Phys. B **10**, 345 (1977).

[29] Y.R. Shen, *The Principles of Nonlinear Optics* (John Wiley & Sons, USA, 1984).

[30] S.H. Autler and C.H. Townes, Phys. Rev. **100**, 703 (1955).

[31] U. Fano, Phys. Rev. **124**, 1866 (1961).

[32] K. Shimoda, *Introduction to Laser Physics* (Springer-Verlag, Berlin, 1984).

[33] Wilfred Kaplan, *Advanced Calculus* (Addison-Wesley, USA, 1973).

[34] See any good textbook on electromagnetism, e.g., W.J. Duffin, *Electricity and Magnetism* (McGraw-Hill, UK, 1980), or J.D. Jackson, *Classical Electrodynamics* (John Wiley & Sons, USA, 1975).

[35] Four-wave mixing in Mg-vapor, K.S.E. Eikema, personal communication.

[36] *Antihydrogen*, Proceedings of the Antihydrogen Workshop, held on 30-31 July 1992, Munich Germany, edited by J. Eades, Hyperf. Int., **76** (1993).

Chapter 6

Adiabatically changing the phase-space density of a trapped Bose gas

We show that the degeneracy parameter of a trapped Bose gas can be changed adiabatically in a reversible way, both in the Boltzmann regime and in the degenerate Bose regime. We have performed measurements on spin-polarized atomic hydrogen in the Boltzmann regime demonstrating reversible changes of the degeneracy parameter (phase-space density) by more than a factor of two. This result is in good agreement with theory. By extending our theoretical analysis to the quantum degenerate regime we predict that, starting close enough to the Bose-Einstein phase transition, one can cross the transition by an adiabatic change of the trap shape.
[This chapter was published as: P.W.H. Pinkse, A. Mosk, M. Weidemüller, M.W. Reynolds, T.W. Hijmans, and J.T.M. Walraven, Phys. Rev. Lett. **78**, 990 (1997).]

The observation of Bose-Einstein condensation (BEC) in magnetically trapped atomic vapors of rubidium [1], sodium [2], and lithium [3] has opened a new field of study at the intersection of atomic and condensed matter physics. Presently, condensates are produced routinely and detailed studies of condensate properties, such as collective excitations [4] and interaction of two condensates [5], are being made. The BEC phase transition itself is especially intriguing. Open questions include the kinetics of condensate formation and the effect of interatomic interactions and finite number of particles. Thus far, measurements have relied upon evaporative cooling to prepare the sample at the desired density below the critical temperature. Evaporative cooling, however, is inherently irreversible since it is based on the loss of hot particles from the trap [6, 7, 8]. To tackle the above questions it would be extremely valuable to vary the degeneracy of the trapped gas adiabatically in a reversible manner, with a fixed number of particles, especially since non-destructive detection methods have become available [9].

The possibility of increasing phase-space density and reaching BEC by changing the trapping potential was investigated by Ketterle and Pritchard [10]. For a collisionless gas they showed

that it is impossible to influence phase-space density by manipulating the trapping potential. An example is cooling by adiabatic expansion in a harmonic trap: one does not lose any atoms, but one does not get closer to BEC either.

In this paper we show that this "no pain, no gain" principle is not true for a collisional gas. We experimentally demonstrate that the degeneracy parameter of a trapped gas can be changed adiabatically (without exchange of heat) and reversibly, without sacrificing atoms, by changing the shape of the trap slowly compared to the internal equilibration time. Our experiments are done in the Boltzmann regime where the degeneracy parameter $n\Lambda^3$ coincides with phase-space density. Here n denotes the density of the gas at the minimum of the potential and $\Lambda \equiv (2\pi\hbar^2/mT)^{1/2}$ is the thermal de Broglie wavelength at temperature T (with m the atomic mass and Boltzmann's constant $k_B = 1$). We observed a change of $n\Lambda^3$ by a factor of two, which agrees well with a quantitative prediction based on statistical thermodynamics applied to a trapped gas. We point out that, given suitable starting conditions, this approach is also suited to cross the BEC phaseline. This follows from analytical expressions for heat capacity, entropy and condensate fraction of a Bose gas as a function of the trap shape.

Our experiment is performed with atomic hydrogen in the cryogenic Ioffe trap described by Van Roijen *et al* [11]. To determine quantities like temperature and density we measure the Lyman-α absorption spectrum of the gas and fit calculated spectra to the experimental one (see [12] for details). It takes a measuring time of 40 seconds to reach a 10% level of accuracy under present conditions. To minimize heating by photon recoil, we used our Lyman-α source at low intensity (typically 10^6 photons at the sample per pulse, 20 pulses per second). In order to assure sufficient signal to noise ratio, we replaced the photodiode used in previous experiments [12] by a photomultiplier. This method offers a non-destructive way to follow the evolution of a trapped gas *in situ* under changing conditions.

The character of the Ioffe trap can be controlled via the magnetic field at the trap center, B_0. For $\mu_B B_0 \gg T$ (with μ_B the Bohr magneton), the trap is essentially harmonic. For $\mu_B B_0 \ll T$, the trap is close to linear in the radial direction and nearly harmonic axially. We selected two magnetic field configurations, **A** and **B**, shown in Fig. 6.1, that maximize the change in phase-space density within the constraints of our apparatus.

After loading the trap from a cryogenic dissociator the sample is evaporatively cooled by ramping down the magnetic barrier at one of the longitudinal ends of the trap (at $z = 5$ cm, see Fig. 6.1). Evaporation is then stopped by raising this barrier. Hereafter we let the sample decay and equilibrate for about 1000 s to prepare a thermal sample that is better than 95% doubly spin polarized with typical densities around 10^{11} atoms/cm^3 [11]. This density was selected to assure negligible sample loss during measurement of the spectrum. We gradually change from trap **A** to trap **B** or vice versa in 60 s which is much slower than the average elastic collision time of 5 s at this density. After each change of trap a spectrum is measured to determine the number of atoms and the degeneracy parameter.

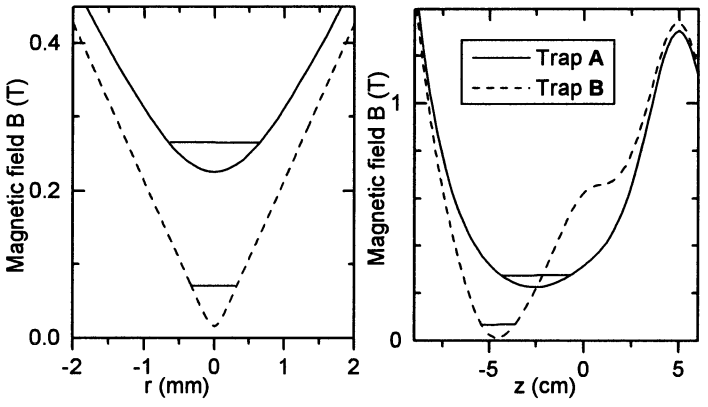

Figure 6.1: Magnetic field profile of trap **A** and **B** radially cut through the field minimum (left) and cut along the principal axis of the trap (right). The horizontal lines indicate the measured thermal energy T. Trap **A** has a depth of 0.72 K and a field minimum B_0 of 226 mT, Trap **B** has a depth of 0.85 K and a field minimum B_0 of 12 mT.

Changing the trap configuration from **A** to **B**, the temperature increased reversibly from $T_A \approx 46$mK to $T_B \approx 60$mK. Both T_A and T_B showed an upward drift of ~ 10mK to the final values mentioned above reached after 5000 s. In Fig. 6.2 we plot the degeneracy parameter $n\Lambda^3$ versus time for a sample cycled between trap **A** and trap **B**. It can be seen that the phase-space density differs by a constant factor 2.05 ± 0.13 between trap **A** and trap **B**.

The number of trapped atoms N versus time is plotted in the right graph of Fig. 6.2. Although T and n differ considerably between the two traps, the measured value for N is seen to be conserved within experimental error. The slow decay of N was found to be described by $N(t) = N(0)/[1 + N(0)Gt]$ as one would expect for a second-order decay process. The effective rate constant G is an average of the (field dependent) intrinsic rate constant g (defined such that $g = -\dot{n}/n^2$ for a uniform gas) times a trap- and temperature-dependent factor[11]. Inverting this average is impracticable. However, the theoretical decay[13] under the conditions of trap **A**, $g = 4.1 \times 10^{-15}$ cm^3 s^{-1}, would give $G = 1.1(3) \times 10^{-14}$ s^{-1} for this trap. For trap **B**, $g = 2.7 \times 10^{-15}$ cm^3 s^{-1} which would give $G = 1.3(5) \times 10^{-14}$ s^{-1}. Hence the observed $G = 1.34(5) \times 10^{-14}$ s^{-1}, for a trap alternating between **A** and **B**, is consistent with intrinsic relaxation.

Our results can be understood within a dilute gas model for N atoms at temperature T trapped in a deep external potential, so that evaporation is negligible. Collisions keep the gas in internal thermal equilibrium. The number of particles in the gas is sufficient to enable a thermodynamic description. Since we change the trap potential slowly compared to the thermalization time, thermodynamic processes proceed reversibly. Since there is no exchange

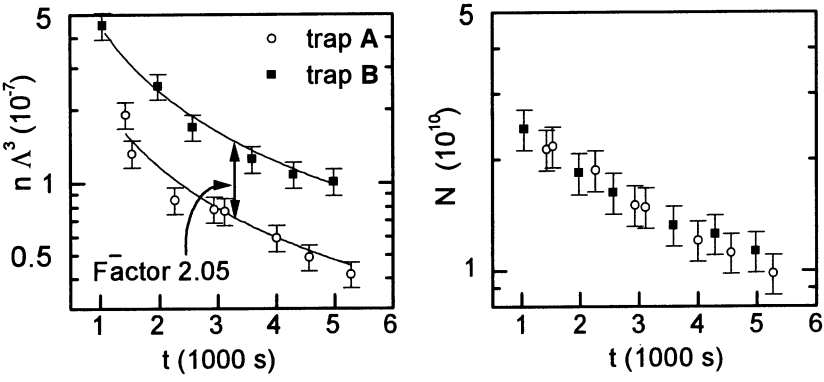

Figure 6.2: Experimentally determined phase-space densities of trapped atomic hydrogen (left graph), and number of atoms N in the trap (right graph) as a function of time, while the trapping potential was alternated between trap **A** and **B**. The curves are fits to a second order decay, with the constant ratio 2.05 ± 0.13 of phase-space density between the two traps.

of heat or particles with the environment, the thermodynamic entropy S of the gas is constant. In our experiment, the influence of quantum statistics is small and interactions between atoms do not influence thermodynamics as the mean-field interaction energy is much smaller than T. The degeneracy parameter can be expressed in terms of the single-particle partition function Z_1 and the total number of particles N as $n\Lambda^3 = N/Z_1$ [7].

The internal energy E can be calculated from the partition function to give [8]

$$E = \left(\frac{3}{2} + \gamma\right) NT, \tag{6.1}$$

where $\gamma = (T/V_e)\partial V_e/\partial T$, with $V_e \equiv N/n = Z_1\Lambda^3$ the effective volume. Here γT is the average potential energy per particle. For many trapping potentials γ is a constant independent of T and V_e scales like T^γ. For example, for a box $\gamma = 0$, for a harmonic trap $\gamma = 3/2$, and for a spherical quadrupole trap $\gamma = 3$. The canonical partition function $Z_1^N/N!$ can be written as the exponential of $-(E - TS)/T$ (see, e.g., [14]) to arrive at the following expression for the degeneracy parameter:

$$n\Lambda^3 = \exp\left(\frac{5}{2} + \gamma - \frac{S}{N}\right). \tag{6.2}$$

Since in an adiabatic process S and N are constant, the phase-space density does not change unless γ changes. It immediately follows that many of the most obvious ways of changing the trapping potential, like isotropic or anisotropic scaling of a harmonic trap, do *not* influence phase-space density. If we change γ adiabatically (e.g., experimentally, by changing B_0 in a Ioffe trap), $n\Lambda^3$ will change as e^γ. In an extreme case, by slowly changing the trap shape from

square well to spherical quadrupole the phase-space density in the center of the trap can be increased by as much as a factor $e^3 \approx 20$.

For the two traps used in our experiment the value of γ is weakly temperature dependent. For the measured temperatures we find $\gamma_A \approx 1.79$ for trap **A** and $\gamma_B \approx 2.53$ for trap **B**, the difference $\Delta\gamma = \gamma_B - \gamma_A$ after changing trap shape always being 0.74 ± 0.01. This implies a change in phase-space density by a factor $\exp[\Delta\gamma] = 2.10 \pm 0.02$ in good agreement with the measured value of 2.05 ± 0.13.

We emphasize that it should be possible to achieve considerable changes in the degeneracy parameter also around the BEC transition. For this purpose we extend our theoretical consideration to the case of a noninteracting Bose gas in the degenerate regime. This is a good approximation also for a weakly interacting Bose gas as long as the gas parameter $na^3 \ll 1$, where a is the scattering length. Below the critical temperature we have the additional condition that $n_0\tilde{U} \ll T$, with $\tilde{U} = 4\pi\hbar^2 a/m$ the scattering strength and n_0 is the condensate density. Expressions obtained for the entropy of an ideal Bose gas are still good approximations around and above the critical temperature of a non-ideal Bose gas. Interactions will change the shape of the condensate, but its entropy will always be zero. Because the influence of the interactions on the entropy of the above-condensate particles is negligible in the binary collision regime the interactions only become important when the condensate fraction becomes so large that the mean field energy of the condensate changes the effective potential for the above-condensate particles. Gases used in current investigations, such as Rb, Li, Na and H are sufficiently close to this ideal gas limit that thermodynamics are essentially unaffected by interactions, unless the condensate fraction becomes appreciable.

In the degenerate regime we continue to assume quasiclassical motion of the atoms. For clarity we restrict ourselves to the case of a power-law potential, although our expressions can easily be generalized to include the Ioffe trap. A power-law trap is characterized by a density of states of the type $\rho(\epsilon) = A\epsilon^{1/2+\delta}$ (See [15] and [16] for details). The scaling parameter A determines the size of the trap. E.g. for a harmonic trap $A = \frac{1}{2}(\hbar\omega)^{-3}$, where ω is the trap frequency. The parameter δ governs the shape of the trap. It can be shown that in the Boltzmann regime $\gamma = \delta$ independent of T for all power-law traps.

The internal energy of a Bose gas in a power-law trap above and below the critical temperature T_c[17] is given by

$$E = NT\left(\frac{3}{2}+\delta\right)\frac{g_{\frac{5}{2}+\delta}(z)}{g_{\frac{3}{2}+\delta}(z)} \quad ;T \geq T_c, \tag{6.3}$$

$$E = NT\left(\frac{3}{2}+\delta\right)\frac{g_{\frac{5}{2}+\delta}(1)}{g_{\frac{3}{2}+\delta}(1)}\left(\frac{T}{T_c}\right)^{\frac{3}{2}+\delta} \quad ;T \leq T_c, \tag{6.4}$$

where the Bose-Einstein integrals are expressed in polylogarithms $g_\alpha(x) = \sum_{l=1}^{\infty} x^l l^{-\alpha}$. The fugacity $z = \exp(\mu/T)$ with μ the chemical potential [18]. Note that as we have $T_c^{3/2+\delta} \propto N$,

Eq. (6.4) is in fact independent of the number of atoms. Above T_c the fugacity is given implicitly by

$$N = AT^{\frac{3}{2}+\delta}\Gamma(\frac{3}{2}+\delta)g_{\frac{3}{2}+\delta}(z), \tag{6.5}$$

with $\Gamma(x)$ the Euler gamma function. Below T_c, $z = 1$ and the number of atoms in the condensate, N_0, is given by $N_0/N = 1-(T/T_c)^{3/2+\delta}$. In the high temperature (Boltzmann) limit the parameter $n\Lambda^3$ introduced earlier reduces to the fugacity z. The specific heat at constant particle number and constant trap potential can now be found by taking the derivative of E with respect to temperature. We obtain

$$C = N\left(\frac{3}{2}+\delta\right)\left(f_{\frac{5}{2}+\delta}(z) - f_{\frac{3}{2}+\delta}(z)\right); \quad T > T_c, \tag{6.6}$$

$$C = N\left(\frac{3}{2}+\delta\right) f_{\frac{5}{2}+\delta}(1)\left(\frac{T}{T_c}\right)^{3/2+\delta}; \quad T < T_c, \tag{6.7}$$

where we have introduced $f_\kappa(z) \equiv \kappa g_\kappa(z)/g_{\kappa-1}(z)$. For $\delta = 0$, $\frac{3}{2}$ and 3 we find $f_{5/2+\delta}(1) = 1.284$, 3.602 and 5.346, respectively. In Eq. (6.6) the second term gives rise to a discontinuity in the heat capacity at T_c as already found by Bagnato et al. [16], which appears only for $\delta > 1/2$ because for $\delta < 1/2$ the function $g_{1/2+\delta}$ diverges, and hence $f_{3/2+\delta}$ tends to zero, as $T \to T_c$. This jump in the heat capacity was recently observed by the JILA group [19]. The entropy S obeys $dS/dT = C/T$, and hence has a kink at T_c for $\delta > 1/2$. We find that

$$S = N\left(f_{\frac{5}{2}+\delta}(z) - \ln(z)\right); \quad T \geq T_c, \tag{6.8}$$

$$S = Nf_{\frac{5}{2}+\delta}(1)\left(\frac{T}{T_c}\right)^{\frac{3}{2}+\delta}; \quad T \leq T_c. \tag{6.9}$$

For the homogeneous case ($\delta = 0$) these expressions can be found in standard statistical mechanics textbooks (e.g.[18]). The entropy as a function of T/T_c is plotted in Fig. 6.3.

It is noteworthy that the ideal Bose gas in a power-law trap in three space dimensions is isomorphic to the uniform Bose gas in $2\delta + 3$ dimensions. There is no heat capacity jump when the effective dimension is less than four. Remarkably, the processes which change the degeneracy parameter are just those which correspond to adiabatic changes of dimensionality!

If one moves along an isentropic line in Fig. 6.3 by increasing δ, one can take a dilute gas close to BEC through the transition. For example, by varying δ from 0 to 3 it is possible to Bose condense a gas that had initially a temperature 12 times higher than the critical temperature for that trap and given N. Eqs. (6) allow one to calculate the fraction of condensate particles N_0/N. Starting with a Bose gas in an ideal harmonic potential at $T = T_c$, and reversibly changing the trapping potential to an ideal spherical-quadrupole, we would arrive below T_c with a condensate fraction of 0.33. For the Ioffe trap, starting at $T = T_c$ at the limit of high B_0, we expect a condensate fraction of 0.25 in the trap at the limit of low B_0. Of course in these case T/T_c may already be so low that the influence of interactions can no longer be neglected.

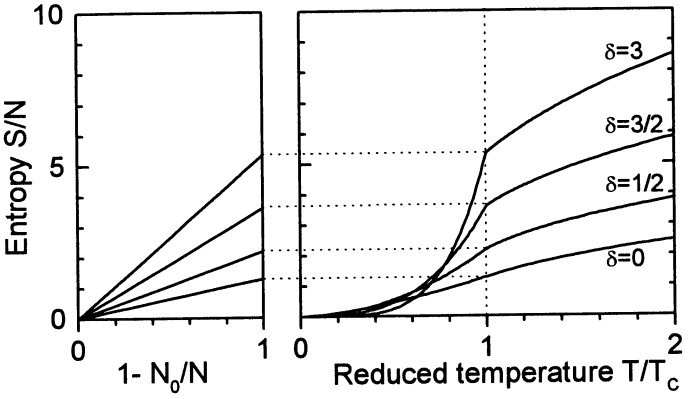

Figure 6.3: Entropy of an ideal Bose gas in power-law traps as a function of T/T_c (right) and, below T_c, also as a function of the above condensate fraction (left).

Our method allows one to control the degeneracy of a Bose gas and gently pull it across T_c and back. Cycling times are only limited by the elastic collision rate which for the alkali atoms has been demonstrated to be much faster than for hydrogen. Combined with non destructive diagnostics [9] this yields the unique possibility to study both condensate formation and destruction and to establish the presence or absence of asymmetries and hysteresis.

This work is part of a research program of the Stichting voor Fundamenteel Onderzoek der Materie (FOM), which is a subsidiary of the Nederlandse Organisatie voor Wetenschappelijk Onderzoek (NWO). M.W. acknowledges a TMR grant by the European Commission. The research of M.W.R. is supported by the Royal Netherlands Academy of Arts and Sciences (KNAW).

Bibliography

[1] M.H. Anderson, J.R. Ensher, M.R. Matthews, C.E. Wieman, and E.A. Cornell, Science **269**, 198 (1995).

[2] K.B. Davis, M.-O. Mewes, M.R. Andrews, N.J. van Druten, D.S. Durfee, D.M. Kurn, and W. Ketterle, Phys. Rev. Lett. **75**, 3969 (1995).

[3] C.C. Bradley, C.A. Sackett, and R.G. Hulet, Phys. Rev. Lett. **78**, 985 (1997); see also C.C. Bradley, C.A. Sackett, J.J. Tollet, and R.G. Hulet, Phys. Rev. Lett. **75**, 1687 (1995).

[4] D.S. Jin, J.R. Ensher, M.R. Matthews, C.E. Wieman, and E.A. Cornell, Phys. Rev. Lett. **77**, 420 (1996); M.-O. Mewes, M.R. Andrews, N.J. van Druten, D.M. Kurn, D.S. Durfee, C.G. Townsend, and W. Ketterle, *ibid.*, 988 (1996).

[5] C.G. Townsend, N.J. van Druten, M.R. Andrews, D.S. Durfee, D.M. Kurn, M.-O. Mewes and W. Ketterle in *Atomic Physics 15, Proceedings of the 15th International Conference on Atomic Physics*, Amsterdam, The Netherlands, 5-9 August 1996, edited by H.B. van Linden van den Heuvell, J.T.M. Walraven, and M.W. Reynolds (World Scientific, Singapore, 1997).

[6] H.F. Hess, Phys. Rev. B **34**, 3476 (1986).

[7] J.T.M. Walraven in *Proceedings of the SUSSP 44 Conference on Quantum Dynamics of Simple Systems*, edited by G.-L. Oppo, S.M. Barnett, E. Riis and M. Wilkinson (Insitute of Physics Publishing, Bristol, 1996); W. Ketterle and N.J. van Druten in *Advances in Atomic, Molecular and Optical Physics*, edited by B. Bederson and H. Walther (Academic Press, San Diego, 1996), Vol. 37, p. 181.

[8] O.J. Luiten, M.W. Reynolds, and J.T.M. Walraven, Phys. Rev. A **53**, 381 (1996).

[9] M.R. Andrews, M.-O. Mewes, N.J. van Druten, D.S. Durfee, D.M. Kurn, and W. Ketterle. Science **273**, 84 (1996).

[10] W. Ketterle and D.E. Pritchard, Phys. Rev. A **46**, 4051 (1992).

[11] R. van Roijen, J.J. Berkhout, S. Jaakkola, J.T.M. Walraven, Phys. Rev. Lett. **61**, 931 (1988).

[12] O.J. Luiten, H.G.C. Werij, I.D. Setija, M.W. Reynolds, T.W. Hijmans, and J.T.M. Walraven, Phys. Rev. Lett. **70**, 544 (1993); Appl. Phys. B. **59**, 311 (1994).

[13] A. Lagendijk, I.F. Silvera, and B.J. Verhaar, Phys. Rev. B **33**, 626 (1986) ; H.T.C. Stoof, J.M.V.A. Koelman, and B.J. Verhaar, Phys. Rev. B **38**, 4688 (1988).

[14] F. Reif, *Fundamentals of Statistical and Thermal Physics* (McGraw-Hill, New York, 1965).

[15] This includes the important examples of square ($\delta = 0$), spherical-quadrupole ($\delta = 3$) and harmonic traps ($\delta = 3/2$), the low and high B_0 limits of the Ioffe trap [8] and all traps with potentials that can be written as $U(x, y, z) = a\,|x|^{1/\delta_1} + b\,|y|^{1/\delta_2} + c\,|z|^{1/\delta_3}$ with $\delta = \sum_i \delta_i$.

[16] V. Bagnato, D.E. Pritchard, and D. Kleppner, Phys. Rev. A **35**, 4354 (1987).

[17] T.W. Hijmans, Yu. Kagan, G. Shlyapnikov, and J.T.M. Walraven, Phys. Rev. B **48**, 12886 (1993).

[18] K. Huang, *Statistical Mechanics* (Wiley, New York, 1963).

[19] C.E. Wieman, E.A. Cornell, D. Jin, J. Ensher, M. Matthews, C. Myatt, E. Burt, R. Ghrist, in *Atomic Physics 15, Proceedings of the 15th International Conference on Atomic Physics*, Amsterdam, The Netherlands, 5-9 August 1996, edited by H.B. van Linden van den Heuvell, J.T.M. Walraven, and M.W. Reynolds (World Scientific, Singapore, 1997).

Chapter 7

One-dimensional evaporative cooling of magnetically trapped atomic hydrogen

We report experiments on evaporative cooling of spin-polarized atomic hydrogen gas confined in a cryogenic magnetic trap and present a model of the trapped gas based on a generalized truncated Boltzmann approximation for the phase-space distribution function. The model takes into account the dimension of the evaporation (3D or 1D) and the time dependence of both the depth and the shape of the confining potential. Our observations are consistent with 1D evaporative cooling. To attain maximal phase-space density, we used the model assuming 1D evaporative cooling to optimize the evaporation procedure. With this work, the low dimension of evaporation was identified as the bottleneck thus far preventing attainment of Bose-Einstein condensation of trapped atomic hydrogen.
[P.W.H. Pinkse, A. Mosk, M. Weidemüller, M.W. Reynolds, T.W. Hijmans, and J.T.M. Walraven, to be published.]

7.1 Introduction

Since its introduction for magnetically trapped atomic hydrogen [1, 2, 3], evaporative cooling has proven to be a powerful technique to increase the phase-space density of trapped gases. It was used, in the case of alkali vapors, to reach the critical density required for Bose-Einstein condensation (BEC) [4]. As the only cooling technique currently applicable at high phase-space density, it plays a central role in the rapidly expanding field of BEC in ultracold gases[5].

Evaporative cooling occurs when energetic atoms are lost from a trap as a result of elastic interatomic collisions. These atoms carry with them a disproportionate share of the thermal energy and the remaining trapped atoms collisionally equilibrate to a lower temperature. The availability of energetic atoms decreases exponentially as the ratio of trap depth to temperature

increases, so to keep evaporation going it is necessary to decrease the trap depth to track the temperature (forced evaporation).

The most efficient form of evaporative cooling is plausibly "ergodic" evaporation, in which all atoms acquiring a total energy exceeding the depth of the trap are quickly lost. In this case the rate of evaporation is just the rate at which interatomic collisions promote atoms to energies higher than the trap depth. Experimentally, efficient evaporation can result when an equipotential surface of the trap is made absorbing, for example with material walls [6], a microwave resonance [7], or an optical resonance [8]. Then, atoms with sufficient energy to reach the equipotential are efficiently pumped from the trap and the evaporation is almost ergodic [9].

However, evaporation can be much less efficient than in the ideal situation. As discussed by Surkov *et al.*, whether the collisionless motion of the atoms in the magnetic trap is regular or stochastic can have profound consequences for the efficiency of evaporative cooling [10]. An important notion is the "effective dimension of evaporation" [10]. Ergodic evaporation is "three dimensional" (3D), since the criterion for the escape of an atom from the trap is based on the total energy of the atom. In the situation where the motional degrees of freedom of the atom are uncoupled and the energy of motion in only one direction determines the escape, the evaporation is "one dimensional" (1D). All other things being the same, the rate of 1D evaporation is slower than that of 3D evaporation by a factor approximately four times the dimensionless ratio of the trap depth to the temperature of the gas [10]. To compete with other processes that lead to atom loss and heating, fast cooling is necessary.

It is hard to realize true three-dimensional evaporative cooling[5]. For example, for the heavier alkalis gravity will displace the surface of constant potential energy from the surface of microwave (rf) resonance which removes the energetic atoms and in this way will reduce the dimensionality of the evaporation. Despite its expected ubiquity, no investigation of 1D evaporation has yet been reported.

In this paper we present a detailed analysis of our evaporative cooling experiments and present a model of the trapped gas based on a generalized truncated Boltzmann approximation for the phase-space distribution function. The model can be configured to describe 3D or 1D evaporative cooling, including the time dependence of both the depth and the shape of the confining potential. Our observations are consistent with the 1D evaporative-cooling version of our model. To attain maximal phase-space density, we optimized the evaporation procedure, using the knowledge that the evaporation process is consistent with 1D evaporation.

The paper is organized around two main parts: the first part describes the experiments, the second is devoted to the description of the 1D and 3D evaporation model. After a brief introduction of our assumptions and terminology in section 7.2.1, and trapping potentials in section 7.2.2, we present the apparatus (section 7.3.1) and the experiments showing the low dimensionality of the evaporation (section 7.3.2). Following this, we present measurements

of forced evaporative cooling experiments (section 7.3.3) that were optimized to reach a high phase-space density. The second part of the paper starts with a general discussion of the evaporation model (section 7.4), followed by the details for the 1D (section 7.5) and the 3D case (section 7.6). Finally, we discuss the implications of the dimensionality of evaporation for the attainment of Bose-Einstein condensation of atomic hydrogen in our apparatus.

7.2 Preliminaries

7.2.1 Physical picture

The description of evaporative cooling in this paper is based on the model introduced by Luiten *et al.*[11] and Walraven[12]. We consider a nondegenerate Bose gas, confined by an external potential $U(\mathbf{r})$ in which the atoms move quasi-classically. The gas is described by the distribution of atoms in phase-space (the space of atomic position $\mathbf{r}$ and momentum $\mathbf{p}$). The energy of an atom, ϵ, is given by $\epsilon = p^2/2m + U(\mathbf{r})$, where m is the atom mass. Interactions between the atoms provide collisions, but we neglect their contribution to the energy, as the density of atoms is low. We assume that the phase-space distribution is thermal, characterized by a temperature T, in the generalized sense of Ref. 12, even when the trap depth is finite and the gas is evaporating. This means that in the part of phase space occupied by trapped atoms the phase-space density is proportional to $\exp(-\epsilon/kT)$, with k the Boltzmann constant. In contrast to the assumptions in Refs. 11 and 12, the condition that discriminates the trapped atoms from the untrapped atoms is not only a function of the total energy. The peak phase-space density (often called simply "phase-space density") is written $n_0\Lambda^3$, where n_0 is a real-space atom density, called the "reference density", and Λ is the thermal De Broglie wavelength defined by $\Lambda = (2\pi\hbar^2/mkT)^{1/2}$. Typically n_0 is approximately equal to the actual real-space density at the center of the trap; this equality becomes exact in the limit of an infinitely deep trap. For a given trapping potential, the state of the gas is completely determined by the extensive variables n_0 and T, which form a natural basis for a thermodynamic description of evaporative cooling. The number of atoms in the trap, N, is related to the reference density by the effective volume V_e, defined by $V_e = N/n_0$. The external potential can be usefully characterized by the exponent γ which describes how V_e varies with temperature: $V_e \propto T^\gamma$. From a perfectly isolated, infinitely deep trap, atoms can only escape by internal decay processes. In our experiments spin-dipole relaxation[13] was the dominant loss process. Dipolar relaxation leads to loss of particles and to heating. Because it is a two-body process, it becomes more important at high densities. In order to cool the gas to low temperatures and high densities, an efficient cooling process, such as evaporative cooling, is required.

The simplest way to model evaporative cooling is to consider a fixed potential with a variable cutting edge, that determines the depth of the trap, as was done in Refs. 11 and 12. However,

in many situations (including our experiments) it is impossible to lower only the trap depth without changing the rest of the trapping potential. The question addressed in this paper is: what happens under a general potential change of a trap of finite depth? A quantitative answer will be given in later sections. Here we discuss this point qualitatively, in order to define the different processes and to clarify the terminology.

In our modeling we assume that states can be categorized as trapped or untrapped. *Evaporation* occurs when atoms are promoted to untrapped states by collisions with other atoms. Atoms in untrapped states are assumed to leave the trap before colliding with another atom (no collisional recapture). For this, the gas should be in the Knudsen regime – the mean free path of an atom should exceed the size of the gas cloud, which is a typical situation for most experiments. The 3D and 1D evaporation processes differ in the criterion, (the escape criterion) which distinguishes trapped states from untrapped states. For 3D evaporation the criterion involves simply the total energy of the atom, for 1D evaporation it is the energy associated with the motion of an atom in a particular direction (the escape direction).

It is worth mentioning that in reality the question whether the evaporation is 3D or 1D can depend on the gas density, even when maintaining the condition of having a Knudsen gas. When the collision time is longer than the ergodic mixing time at low density (giving 3D evaporation) it may be shorter at high density (giving 1D evaporation if there is a single escape direction). To avoid dealing with this crossover between 3D and 1D evaporation, we assume in this article that the degrees of freedom of the collisionless motion of atoms are either completely mixed (full ergodicity), or not mixed at all.

Atoms that are lost because the trap becomes too shallow to confine them are said to be *spilled* [12]. In a quantum mechanical picture these are the particles that occupy states that are removed from the trap. Spilling is a single particle process that is independent of collisions. If spilling is done quickly (faster than the collision rate) it can be used to analyze the energy distribution of the trapped atoms [14]. In forced evaporative cooling the trap depth is lowered to increase the evaporation rate. It is important to bear in mind that the atoms spilled as a direct result of this lowering are not, properly speaking, evaporated and they do not change the temperature directly. They are simply lost, leaving the rest of the distribution function unchanged.

A simple case of spilling occurs when only the trap depth is lowered in an otherwise unchanged potential. We refer to this case as "pure spilling". Spilling in most alkali experiments is pure spilling, because the trap depth is lowered by reducing the frequency of the rf field, which can be realized independently from the magnetic trapping field. On the other hand, it is not necessary to decrease the trap depth to spill atoms. For instance, when adiabatically compressing a gas, e.g., by increasing the spring constant of a harmonic trap, but keeping the trap depth constant, the level splitting increases and states are forced out of the trap.

Work is done by (or on) the trapped gas if the trapping potential is varied. We consider

variations of the potential on a timescale sufficiently slow in comparison with the collision time that the thermal character of the distribution is not appreciably disturbed. In this case, for example, increasing the spring constants of a harmonic trap leads to adiabatic compression and heating of the gas. If work is done sufficiently slow, it is a reversible process that does not change the entropy of the gas. This holds also for slow adiabatic changes of the trapping potential that change γ, in which case the phase-space density can be changed in a reversible way[15].

7.2.2 Trapping potentials

In our experiments evaporation is 1D because the longitudinal and transverse degrees of freedom of atomic motion are uncoupled and only the longitudinal motion of the atoms determines their escape from the trap. Our trap is of the Ioffe type [16], and its potential can be approximated by

$$U(x,y,z) = \sqrt{\alpha^2(x^2+y^2) + [U_0 + U_z(z)]^2} - U_0 \tag{7.1}$$

where $U_z(z_0) = 0$, with z_0 the coordinate of the trap minimum. The potential offset parameter U_0 is determined by the magnetic field at the trap minimum. The potential along the symmetry axis, $U_z(z)$, is determined by the axial coils and can have a complicated shape. The leading off-axis behavior is described by the transverse potential gradient α due to the Ioffe bars. An important special case is the trap we call Ioffe-Quadrupole (IQ), for which the axial potential U_z is harmonic, $U_z(z) = \beta z^2$. For an infinitely deep IQ trap the three parameters U_0, α, β describe the potential completely.

In addition to the supposed infinitely extending magnetic trapping potential, usually a surface is present at which atoms are removed from the trap. We assume here that this surface coincides with an equipotential surface of truncation energy ϵ_t. Atoms with a trajectory crossing this surface are thought to be removed from the trap immediately. Note that if the potential energy is chosen to be zero at the trap minimum, as we will assume throughout this paper, ϵ_t is just the depth of the trap (in the direction of the pumping surface, at least).

As shown by Surkov *et al.* [17], when $U_0 > \epsilon_t$ the transverse and longitudinal degrees of freedom in a Ioffe trap are effectively uncoupled. This conclusion was reached considering the Ioffe potential including small terms beyond the approximation of Eq. 7.1. It is noteworthy that for typical Ioffe traps the ratio of transverse and longitudinal oscillation frequencies is large, which makes this uncoupling a robust phenomenon. When working at ultralow temperatures the condition $U_0 \gg kT$ is inevitable in our Ioffe trap and because ϵ_t is not so very much greater than kT, one can easily appreciate that uncoupling is essentially unavoidable in practice.

When U_0 is much larger than ϵ_t the potential is separable in its variables – to a very good approximation – and we may write the potential as

$$U(x,y,z) = U_\perp(x,y) + U_z(z), \tag{7.2}$$

the sum of the longitudinal potential $U_z(z)$ and a transverse potential which is essentially harmonic, $U_\perp(x,y) = m\omega_\perp^2(x^2+y^2)/2$. The oscillation frequency for the transverse motion is given by $\omega_\perp = \alpha/\sqrt{mU_0}$. If the potential is separable, the energy ϵ of an atom can be considered to be the sum of a transverse energy, $\epsilon_\perp$, and a longitudinal energy, ϵ_z, which are uncoupled (between collisions) and conserved (for a constant trap). In our 1D evaporation model we will discuss traps of the form of Eq. 7.2 with evaporation determined by the longitudinal potential U_z. We will give expressions for general U_z and harmonic $U_\perp$.

A general class of separable potentials was analyzed by Bagnato *et al.* [18]. These potentials are of the form

$$U(x,y,z) = (x/\lambda_x)^{1/\delta_x} + (y/\lambda_y)^{1/\delta_y} + (z/\lambda_z)^{1/\delta_z} \tag{7.3}$$

where, e.g., λ_x sets the length scale in the x direction and δ_x sets the power law. The harmonic trap is a special case, with $\delta_x = \delta_y = \delta_z = 1/2$, and, e.g., $\lambda_x = \omega_x\sqrt{2/m}$. We will give expressions for this class of traps as well.

7.3 Experiments

7.3.1 Apparatus

In our experiments we use the cryogenic Ioffe trap which has been described in detail elsewhere [19]. It consist of four racetrack (oval) shaped coils providing radial confinement and a set of four cylinder-symmetric axial confinement coils, creating magnetic field profiles such as that shown in Fig. 7.1. The potential is approximately given by Eq. 7.1.

The trap is loaded with atomic hydrogen produced by dissociation of molecular hydrogen in a cryogenic discharge and thermalized into the trap by collisions of the atoms with the helium-coated wall and with each other. To obtain high densities, the superfluid ^{4}He film was covered with a monolayer of ^{3}He. A typical sample just after loading consists of 10^{12} atoms at a temperature of 70 mK. At the start of the evaporation the trap depth can be determined by the wall of the experimental cell as in Ref. [6], but the sample quickly cools away from the wall and the depth will be determined by a maximum of a magnetic field barrier as will be assumed in the rest of this paper. Evaporative cooling is performed by varying the currents in the axial coils to reduce the depth of the trap. Atoms escaping from the trap are cryopumped away.

It is important to note that our trap is constructed with superconducting coils optimized primarily to sustain a high trap depth with minimal dissipation (using persistent current switches) rather than fine control over the field. The uncertainties in the trap depth are estimated to be of order 0.5 mT. Careful attention had to be paid to current lag because of the high self inductances of the coils and the finite resistance of the normal-state persistent current switches. Fortunately most of these parameters are known and the current lag in the coils can be anticipated when programming a field change by integrating the differential equations connecting

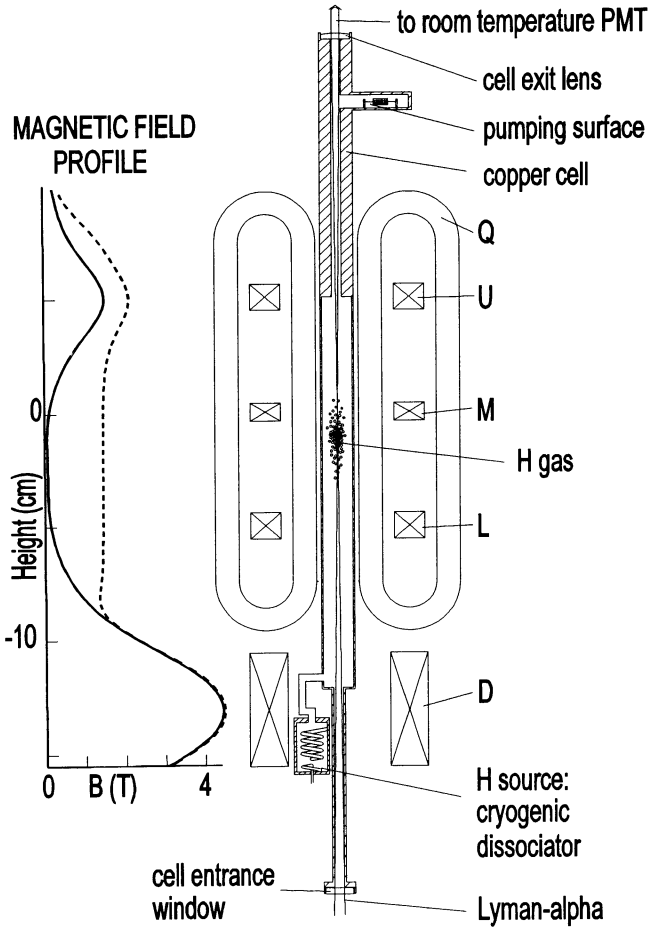

Figure 7.1: Schematic of the apparatus. On the left side an overview of the experimental cell is sketched together with the superconducting coils forming the magnetic trap. The axial confinement coils are labeled, from top to bottom, "U" (Upper),"M" (Middle), "L"(Lower) and "D"(Dissociator). The set of four racetrack coils creating the radial confining field are indicated with "Q". Also shown is the Lyman-α beam path for optical spectroscopy of the trapped gas. On the left side a possible field profile, along the axis and along the wall, is indicated.

the magnet power supply currents with the actual currents in the coils, taking into account the relaxation time due to the protection and switch resistors which shunt the superconducting coils [21].

The trapped gas is probed optically, using narrow-band light resonant with the Lyman-α transition (wavelength $\lambda = 122\,\mathrm{nm}$). The light beam is passed through the gas (see Fig. 7.1)

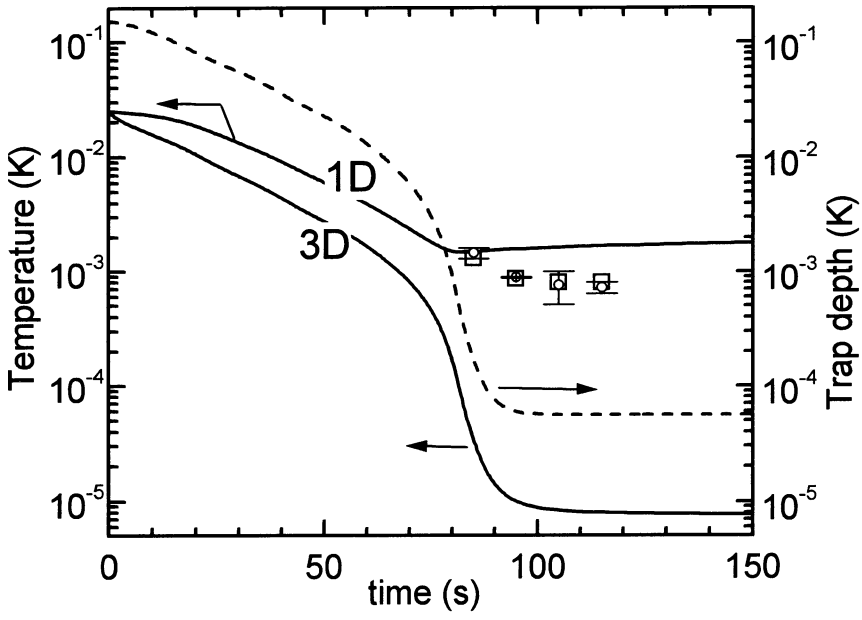

Figure 7.2: Plot of trap depth and the temperatures predicted by the 3D and 1D evaporation models versus time, during lowering the current through one of the axial confinement coils. The symbols are measured data points. The initial condition is a density of $3 \times 10^{12}\,\mathrm{cm}^{-3}$ and a temperature of 25 mK. The conditions are chosen such as to accentuate the difference between 1D and 3D evaporation.

and the total transmission is measured as a function of frequency. Comparison with theoretical spectra enables us to characterize the trapped gas by, e.g., its temperature and peak density. Details of the spectroscopic technique can be found in [20].

7.3.2 Experimental evidence of 1D evaporation

The question whether evaporation in our experimental situation is better described by 1D evaporation or by 3D evaporation was answered by the experiment described in this section. An evaporation experiment was performed starting with samples of 1.7×10^{11} atoms at 25 mK with a density of $3 \times 10^{12}\,\mathrm{cm}^{-3}$, as determined by Lyman-α spectroscopy. Next, the trap depth was reduced from 0.15 K to a value less than 0.1 mK (dashed line in Fig. 7.2), by lowering the upper confinement barrier. In this case this was done by reducing the current in the M-coil in four linear sweeps. As a consequence the trap depth changes relatively fast at the end. After the reduction of the trap depth, the sample was probed by taking Lyman-α spectra of 10 s duration and found to have temperatures of about 1 mK.

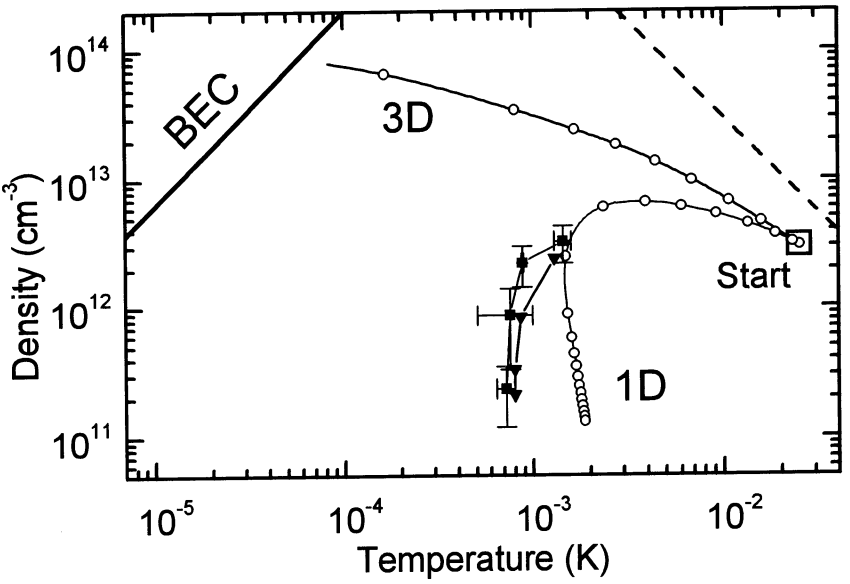

Figure 7.3: The same results as in Fig. 7.2 now plotted in the T-n_0 plane, showing results of simulation employing 3D and 1D evaporation. The open circles are spaced 10 s apart. The dashed line indicates the slope for a trajectory without atom loss (assuming a harmonic potential). The solid symbols are experimental points, starting at $t = 85$ s, spaced 10 s apart, in two series of measurements. The error bars on one of the series are obtained by fitting with different approximations to the Lyman-α beam profile.

We simulated the evolution of the gas using two versions of our evaporation model, one simulating 3D evaporation and the other simulating 1D evaporation. Both versions of the model will be described later in this paper in detail. For computational efficiency we assume that the trap is effectively harmonic in the z-direction (IQ trap). The full expressions for the field are used to find the truncation energy ϵ_t and from the behavior of $U(\vec{r})$ near its minimum, the trap parameters α, β and U_0. The real trap was then approximated by a IQ trap with these parameters. In the 1D case we found no significant difference when the full z-dependence was replaced by the IQ approximation. We do not expect significant differences in the 3D case either.

The results of the simulations are shown in Fig. 7.3, together with temperature and density obtained from the spectra. The evolution calculated for 3D evaporation predicts a monotonously increasing density and decreasing temperature, while the 1D evaporation gives rise to a sharp decline in density after an initial modest increase. Once the trap depth is lower than the "temperature", cooling ceases (in the 1D case) because an evaporating particle carries away

insufficient energy. In this case the momentum distribution of atoms in the trapped gas cloud is a disk perpendicular to the trap axis. One might well expect that the models, based on the truncated Boltzmann distribution, will become inaccurate when η (the ratio of trap depth to temperature) becomes of order unity. It is hence not surprising that the data are not in quantitative agreement with either model. The data are, however, consistent with the 1D evaporation model, and not at all with the 3D evaporation model. The 1D truncation of the phase-space distribution is taken into account when calculating theoretical Lyman-α spectra for the determination of temperature and density from the data. Using a 3D-truncated distribution leads to even lower derived densities and makes the discrepancy between the 3D model and this data even larger.

Although we cannot conclude with certainty from the comparison between this data and the models that the evaporation is purely one-dimensional, it does show that a model based on 1D evaporation describes the forced evaporation in our Ioffe trap at low temperatures much better than a model based on 3D evaporation.

7.3.3 Optimized 1D evaporation

Armed with the knowledge that evaporation in our Ioffe trap is more 1D than 3D, we aimed to arrive at the highest attainable phase-space density, using the model (described in detail later) based on 1D evaporation to optimize the trajectory through phase space. The optimal model trajectory was found by computer optimization of the evaporation process to obtain the highest phase-space density. In this optimization the currents through four of the five magnets were used as adjustable parameters, taking into account the starting conditions and the technical constraints imposed by the apparatus.

High radial confinement during loading of the trap maximizes the number of trapped atoms and assures the highest initial densities for the evaporation experiment. On the other hand, tight radial confinement leads to very small samples at low temperatures, making the optical thermometry difficult. Therefore we reduce the α coefficient during the first stages of the ramp. The ramp-down rate of the radial confinement coils was limited by the risk of quenching of the superconducting wires. The final current configuration was fixed to be sure that a trap of finite depth remained at the end.

To simplify the calculation of the optimal ramp settings further, the ramp was divided into 7 linear current sweeps. Both the duration of every linear sweep and the destination currents were optimized using a computer program based on the one-dimensional evaporation model, but including the full z-dependence of the field. It was checked that in both the radial and the axial directions $\epsilon_t/\hbar\omega$ decreased monotonically, with ω the radial or axial trap oscillation frequency. This indicates that no empty trap states are introduced, which is necessary for the model to be valid, as will be discussed in Sect. 7.6.3.

The effect of adiabatic compression or decompression of the trap is also taken into account in the model. However, because the product of curvatures $\omega_\perp^2 \omega_z$ in the optimized ramp turns out to be constant within 20%, this hardly influences the result. We also found that during the simulated evolution the effective-volume exponent γ remains in the narrow range $1.4 < \gamma < 1.6$. This means that adiabatic changes of the phase-space density[15] do not play an essential role in the present experiments.

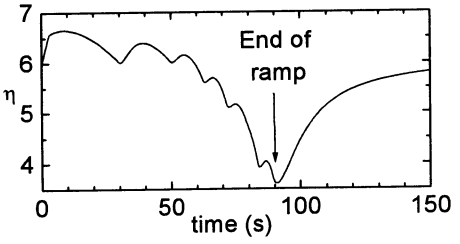

Figure 7.4: Calculated evolution of the truncation parameter η in a ramp optimized using the model based on 1D evaporation.

It is interesting to look at the evolution of the truncation parameter η during the optimized ramp. This is depicted in Fig. 7.4. Note that the value of η is, apart from some oscillations, steadily decreasing. This reflects the need for accelerated evaporation due to the increasing importance of dipolar heating with decreasing temperature. The oscillations are a result of the linear sweeps which form the building blocks of the total ramp. This indicates that, in principle, a better optimized ramp would be possible by using another optimization scheme which can deal with more complicated (smoother) ramps, or simply a larger number of linear ones. However, the fact that the wiggles in η are hardly reflected in Fig. 7.3 indicates that this could not have gained more than a few percent in, e.g., the density, because evaporation at a certain η corresponds to a certain slope in the T-n_0 plane.

We typically start with 4×10^{12} atoms loaded into the trap at a density of 7×10^{12} cm^{-3} and a temperature of 0.11 K. Because spectroscopy is difficult if the trapping field is changing, we repeated the ramp a number of times, the first time stopping after the second linear sweep, the next time stopping after the third linear sweep until the total ramp of 7 sweeps, in order to map out the complete trajectory. Every time that we broke off the ramp, the currents in the magnets were allowed to relax to the currents set by the power supplies at that moment. We simulated these partial ramps too, to compare with data. Before every (partial) ramp, we reloaded the cell with atomic hydrogen. The loading procedure leads to roughly the same starting conditions, but because the loading depends on the temperature of the cell, variations of order 30% in density can occur. Fig. 7.5 shows the ramps to step 2,3,...7. The curve labeled 7 is the complete optimized ramp. There is reasonable agreement between the data and the 1D model for the ramps to step 5. The discrepancy between the model and the data at step 6 and

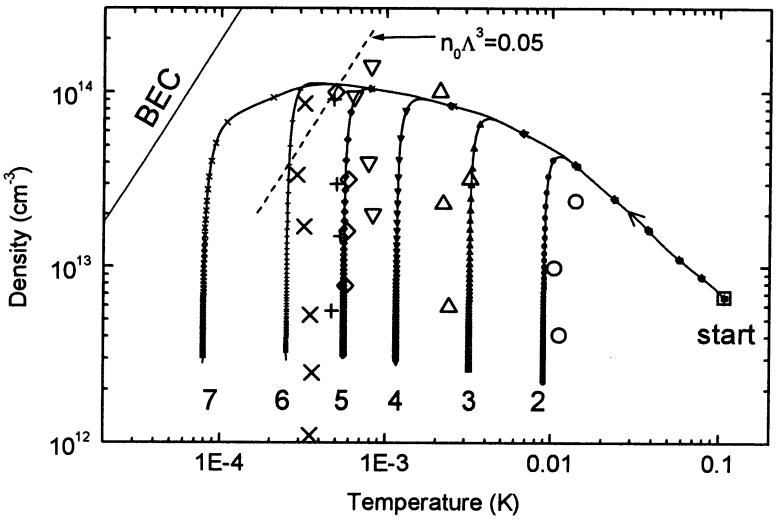

Figure 7.5: Evolution of trapped gas on the n_0-T plane. The curves are simulations based on 1D evaporation. The solid symbols on the theoretical curves are spaced 10 seconds apart. The larger, open symbols are experimental data points. The solid squares are measured in a ramp to step 2. The corresponding theoretical curve has open squares etc.

7 are probably due to the fact that the spectroscopy becomes less sensitive to the temperature below 1 mK. Spectroscopy is better at determining the number of atoms and, as can be seen in Fig. 7.6, the discrepancy is smaller. Also, deviation of the trap depth due to the stray fields becomes more important at small trap depths, as well as errors in the estimation of the calculated currents due to, e.g., neglect of the mutual inductances of the coils, and noise of the power supplies. Other possible sources of systematic errors are heating of the cloud by the probe light and heating by background gas produced by the eddy-current heating of the cell when ramping the magnets. The highest phase-space density achieved can be found in the upper left corner of Fig. 7.5: $n_0\Lambda^3 \simeq 0.05$, a little more than an order of magnitude short of BEC. This represents, we believe, the limit of the present apparatus. At the end of this paper we will discuss how this limit might be circumvented.

7.4 Modeling the trapped gas

7.4.1 Introduction

The first descriptions of evaporative cooling assumed that the trapped atoms had energies distributed according to a Boltzmann distribution truncated at the trap depth [22, 23, 24,

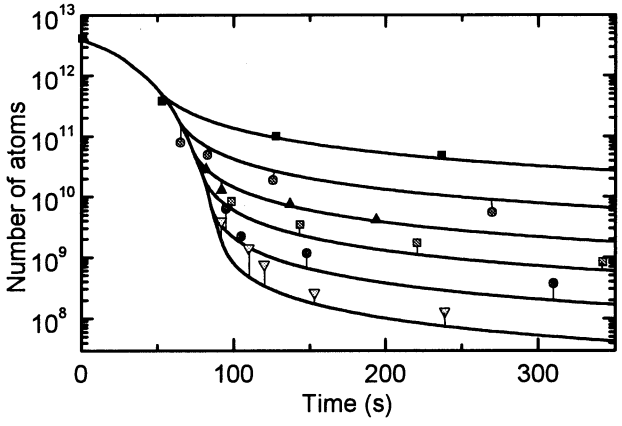

Figure 7.6: Evolution of the number of atoms as a function of time. The curves are simulations based on 1D evaporation. The experimental data points are connected with the corresponding theoretical curve by a vertical line.

25]. Luiten *et al.* [11] showed by numerical solution of the Boltzmann equation that for non-degenerate Bose gases the evaporation process conserves the truncated Boltzmann distribution indeed rather accurately. They went on to give a detailed thermodynamic description of the evaporating gas based on the truncated Boltzmann approximation, calculating the rate of evaporation from kinetic theory. Walraven extended this description by incorporating the effect of continuously reducing the trap depth, introducing the notion of spilling [12]. Berg-Sørensen discussed how to incorporate a time dependent trap strength into this approach [26].

Detailed modeling of evaporative cooling is possible using the direct simulation Monte Carlo (DSMC) method [27, 28]. This powerful method, originally introduced for calculations of gas dynamics [29], does not require any assumptions regarding the form of the distribution function. The DSMC method has been used to study the difference between 3D and 1D evaporation [27], including the effect of quantum statistics [28]. It is also well suited to study evaporative cooling in complicated situations, such as when the collision cross section is energy dependent or when the mean free path of the atoms is comparable to the size of the gas cloud. It demands, however, rather fast computers, especially if evaporation ramps are to be optimized.

Here we will work with the thermodynamic description, generalizing it to include evaporative cooling in two limiting cases (3D and 1D) and to include the time variation of both the depth of the trap and the shape of the confining potential. As explained in section 7.2.1, we limit our modeling of the trapped gas to the description of an ideal gas in the Knudsen regime. In this section we will discuss aspects of the modeling that are independent of the nature (dimensionality) of the truncation. Later, we discuss the variables and equations that are

specific to the 1D (section 7.5) or 3D case (section 7.6).

To include the time evolution of the trap in the formalism in a simple way, we introduce a single symbol, θ, which is an abbreviation for the set of independent control parameters needed to determine the trapping potential. In our case these are the five independently controllable currents through the different coil sets. In future experiments θ could include the frequency of an rf field applied for evaporation. In yet other versions of the model θ might represent a single parameter. For example, if only the truncation energy ϵ_t is varied then θ can be identified with ϵ_t. The trapping potential is, in general, a function of $\mathbf{r}$ which depends parametrically on θ. With the passage of time θ varies, as determined by the ramp program imposed upon the power supplies.

7.4.2 Thermodynamics

We describe the trapped gas by its classical phase-space distribution of atoms $f(\mathbf{r}, \mathbf{p})$, which we normalize as in Ref. 11, such that the total number of atoms, N, is given by

$$N = (2\pi\hbar)^{-3} \int d^3r\, d^3p\, f(\mathbf{r}, \mathbf{p}) \tag{7.4}$$

(Note that, with this normalization, f corresponds with quantum mechanical occupation numbers. We consider here a non-degenerate gas, i.e., with $f \ll 1$.) To induce a thermodynamic description we use a generalization of the truncated Boltzmann approximation employed in Ref. 11. We assume that an atom can be identified as "trapped" or "untrapped" on the basis of its instantaneous position in phase space, that the untrapped atoms are efficiently removed, and that the trapped atoms are described by a thermal distribution. More precisely, the phase-space distribution is assumed to have the form of an equilibrium distribution

$$f(\mathbf{r}, \mathbf{p}) = n_0 \Lambda^3 e^{-U(\mathbf{r})/kT} e^{-p^2/2mkT} \tag{7.5}$$

for $\mathbf{r}, \mathbf{p}$ such that the atom is trapped and to be zero elsewhere. This distribution is characterized by two parameters: the (maximum) phase-space density $n_0\Lambda^3$ and the temperature T. The only difference between the distribution in the case of 1D and 3D evaporation is the criterion for truncation. In the case of 1D evaporation, an atom leaves the trap if its z-energy $\epsilon_z = U_z(z) + p_z^2/2m$ exceeds ϵ_t and, hence, $f = 0$ for $\epsilon_z > \epsilon_t$. In the case of 3D evaporation an atom escapes the trap if its total energy $\epsilon = U(\mathbf{r}) + p^2/2m$ exceeds ϵ_t and, hence, $f = 0$ for $\epsilon > \epsilon_t$.

Although a true thermal equilibrium does not exist in an evaporating gas, the truncated Boltzmann approximation for the phase-space distribution allows us to adopt many of the methods and results of statistical mechanics. A central quantity is the effective volume $V_e(T, \theta)$, defined by $V_e = N/n_0$. The effective volume is Λ^3 times the single-particle partition function (see Ref. 11) and hence can be used to calculate all thermodynamic functions. In particular, the energy E of the trapped gas is given by [30]

$$E = \left(\frac{3}{2} + \gamma\right) NkT \tag{7.6}$$

where $\gamma = (T/V_e)\,(\partial V_e/\partial T)_\theta$, the partial derivative being evaluated at constant θ (i.e., holding the trap fixed). For a full thermal (not truncated) distribution an atom has an average kinetic energy $(3/2)kT$ and an average potential energy γkT. For a truncated distribution, this interpretation of the two terms in Eq. 7.6 is not legitimate, although their sum is still the total energy. The entropy S of the trapped gas is given by

$$S = Nk\left(\frac{5}{2} + \gamma - \ln n_0 \Lambda^3\right). \tag{7.7}$$

This expression can be derived from the partition function [15] even when the partition function refers to a truncated phase-space distribution. The entropy of a truncated gas is smaller than the entropy of a gas with the same N and E in thermal equilibrium in a deep trap [31].

The energy and entropy of the trapped gas are functions of N, T, and θ, which leads to the following useful differential relations:

$$\dot{E} = \left(\frac{3}{2} + \gamma\right) kT\dot{N} + C\dot{T} + \left(\frac{\partial \gamma}{\partial \theta}\right)_T NkT\dot{\theta} \tag{7.8}$$

and

$$\frac{\dot{S}}{k} = \left(\frac{S}{kN} - 1\right)\dot{N} + C\frac{\dot{T}}{T} + \left\{\left(\frac{\partial \gamma}{\partial \theta}\right)_T + \frac{1}{V_e}\left(\frac{\partial V_e}{\partial \theta}\right)_T\right\} N\dot{\theta} \tag{7.9}$$

with the heat capacity $C \equiv (\partial E/\partial T)_{N,\theta}$ given by the usual expression [11]

$$C = \left(\frac{3}{2} + \gamma + T\frac{\partial \gamma}{\partial T}\right) kN. \tag{7.10}$$

The last term in Eq. 7.8 is, in the special case that only the trap depth ϵ_t is varied and the potential is otherwise unchanged, the product of $\dot{\epsilon}_t$ and the "heat of truncation" [12, 26].

7.4.3 Differential equations for the evolution of the gas

To characterize the trapped gas in our numerical work, we employ the number of trapped atoms, N, and the temperature, T, as fundamental variables. To determine the time evolution of the trapped gas we should integrate (numerically) differential equations for N and T:

$$\dot{N} = \dot{N}_{\rm ev} + \dot{N}_\theta + \dot{N}_{\rm rel} \tag{7.11}$$

$$C\dot{T} = \dot{E}_{\rm ev} + \dot{E}_\theta + \dot{E}_{\rm rel} - \left(\frac{3}{2} + \gamma\right) kT\dot{N} - \left(\frac{\partial \gamma}{\partial \theta}\right)_T NkT\dot{\theta} \tag{7.12}$$

Eq. 7.11 simply reflects that $\dot{N}$ is the sum of the independent contributions $\dot{N}_{\rm ev}$, $\dot{N}_\theta$ and $\dot{N}_{\rm rel}$ for the rate of change of the number of trapped atoms due to evaporation, trap changes (spilling) and dipolar relaxation, respectively. In Eq. 7.12 the rate of change of the energy of the trapped gas is also written as a sum of the independent contributions $\dot{E}_{\rm ev}$, $\dot{E}_\theta$ and $\dot{E}_{\rm rel}$,

for the rate of change of energy due to evaporation, trap changes (spilling and work), and dipolar relaxation, respectively. At each time step $\dot{N}$ and $\dot{T}$ are calculated – all contributions and auxiliary quantities are either known functions of N, T, and θ or can be determined by numerical differentiation [32]. We will now consider the contribution of evaporation, trap changes, and dipolar relaxation in turn.

7.4.4 Evaporation

Elastic collisions between the trapped atoms lead to evaporation by promoting atoms to untrapped states. We assume isotropic (s-wave) scattering with a velocity-independent collision cross section $\sigma = 8\pi a^2$, where a is the scattering length. Evaporation causes a rate of change of atom number, $\dot{N}_{\rm ev}$, and energy, $\dot{E}_{\rm ev}$, which we can express in terms of effective volumes $V_{\rm ev}$ and $W_{\rm ev}$ introduced as follows [11]:

$$\dot{N}_{\rm ev} = -n_0^2 \sigma \bar{v} e^{-\eta} V_{\rm ev} \tag{7.13}$$

$$\dot{E}_{\rm ev} = \dot{N}_{\rm ev} \left(\eta + \frac{W_{\rm ev}}{V_{\rm ev}} \right) kT, \tag{7.14}$$

with $\eta = \epsilon_t / kT$ and the thermal velocity defined as $\bar{v} = \sqrt{8kT/\pi m}$. This shows explicitly the dependence on the atomic collision cross section σ and the gas temperature T and reference density n_0. The effective volumes depend only on the trapping potential, the truncation parameter η, and the nature of the phase-space truncation (dimensionality of evaporation). For 1D truncation we derive these volumes in section 7.5. For 3D truncation this was done in Ref. 11; for convenience we reproduce the expressions as [33].

7.4.5 Spilling and work

If the trapping potential is changed, some atoms are lost from the trap due to spilling and the remaining atoms may change their energy (i.e., do work on the magnet power supplies). Spilling is distinct from evaporation – it occurs even in the absence of collisions. In the 1D situation where the transverse and longitudinal motions of the atoms are dynamically uncoupled, spilling can lead to anisotropic energy distributions with $T_z < T_\perp$ if the potential $U_z(z)$ is varied on a timescale short compared to the thermalization time of the trapped gas, but slowly compared with the oscillation period for z motion [17]. This was partially the case in the experiment distinguishing 1D from 3D evaporation, presented in section 7.3.2. In our other experiments, however, we typically have variations of the trapping potential slow compared to the collision time scale and in our model will assume that the gas distribution is described by a single temperature.

By changing the trapping potential or trap depth (via the control parameters θ) we induce a rate of change $\dot{N}_\theta$ in the number of trapped atoms and $\dot{E}_\theta$ in the total energy. These quantities

depend upon the nature of the phase-space truncation (3D or 1D). In principle, they can be derived from the Boltzmann equation for a gas in a time-dependent potential, at least for the case of 3D truncation [26]. Here we choose a more intuitive approach.

Atoms are spilled from the trap because they occupy quantum bound states which are lost from the trapping potential. The rate of change of the number of trapped atoms due to spilling, $\dot{N}_\theta$, is found straightforwardly by counting the atoms in the lost states. Expressions are derived for 1D truncation in section 7.5.3 and for 3D truncation in section 7.6.3. For fixed trap shape, $\dot{N}_\theta$ is simply related to the rate of change of the trap depth [12]. This is not true in general, because variation of the shape of the trapping potential can lower the energy of atoms near the trap edge (adiabatic expansion) and prevent them from being spilled even if their original energy exceeded the final trap depth.

To calculate the rate of change of the energy of the trapped gas due to changing the trap, $\dot{E}_\theta$, we must account for the energy of the spilled atoms and for the effect of trap variations on the energy of those atoms which remain trapped (i.e., the work done by the trapped gas against the confining potential). For a deep trap, changes in the trap shape can even lead to adiabatic variations of the peak phase-space density (degeneracy) of the gas [15]. The simplest way to derive $\dot{E}_\theta$ is through consideration of the entropy of the gas. As the trap is varied, entropy is carried away by the spilled atoms. Within the truncated Boltzmann approximation, changing the trap does not cause any other entropy changes because the phase-space distribution is always thermal. Hence, the rate of change of the entropy of the trapped gas due to variation of the trapping potential, $\dot{S}$, is proportional to $\dot{N}_\theta$. We write

$$\dot{S}_\theta = \dot{N}_\theta s_\theta \tag{7.15}$$

where the entropy removed per spilled atom, s_θ, depends on the nature of the truncation. We calculate s_θ for 1D truncation in section 7.5 and for 3D truncation in section 7.6.

Once we know s_θ, the rate of change of the energy of the trapped gas follows from substituting $\dot{T}$ obtained from Eq. 7.9 into Eq. 7.8. This gives

$$\dot{E}_\theta = \dot{N}_\theta \left(s_\theta + k \ln n_0 \Lambda^3\right) T - \frac{NkT}{V_e} \left(\frac{\partial V_e}{\partial \theta}\right)_T \dot{\theta}. \tag{7.16}$$

This expression for $\dot{E}_\theta$ can then used in Eq. 7.12 for the evolution of the temperature of the trapped gas.

An easy way to calculate s_θ is by considering the special case of pure spilling (reducing the truncation energy ϵ_t while preserving the trapping potential seen by the trapped atoms). In this case T and n_0 are constant, allowing us to easily determine s_θ as a function of T, n_0, θ, and the nature of the truncation. For more complicated changes of the trapping potential s_θ will be the same. All that matters is that spilled atoms come from the truncation edge.

In an infinitely deep trap ($\dot{N}_\theta = 0$), the last term of Eq. 7.16 gives rise to adiabatic (de)compression of the thermal cloud, and the derivative of γ in Eq. 7.12 gives rise to a varia-

tion of $n_0\Lambda^3$ proportional to e^γ [15]. In a finite depth trap these effects cannot be separately attributed to these two derivatives, but it can easily be verified for, e.g., a generic power-law trap, that here also, $n_0\Lambda^3 \propto e^\gamma$ if no atoms are lost. Of course, for a real gas in a finite-depth trap the collisions required to maintain the truncated Boltzmann distribution will also lead to evaporative cooling which will tend to obscure the adiabatic contribution to changes of the phase-space density.

7.4.6 Dipolar relaxation

Inelastic collisions between atoms are also important for the evolution of the trapped gas. For atomic hydrogen, spin relaxation in binary collisions is the dominant inelastic process. The contributions due to dipolar relaxation of the atoms in binary collisions, $\dot{N}_{\rm rel}$ and $\dot{E}_{\rm rel}$, are calculated assuming a temperature independent rate constant G depending upon magnetic field as calculated in the literature [34]. The loss rate follows from $\dot{N}_{\rm rel} = -n_0^2 G V_{2e}$, where $V_{2e} = \int d^3r[n(\mathbf{r})/n_0]^2$ is the effective volume for binary collisions. For the determination of $\dot{E}_{\rm rel}$, given by $\dot{E}_{\rm rel} = (3/2 + \gamma_2)kT\dot{N}_{\rm rel}$, we use the two-atom energy parameter, $\gamma_2 \equiv (T/2V_{2e})\partial V_{2e}/\partial T$. Because the average energy that particles take away after an inelastic collision is much less than the trap depth and because collisions predominantly occur in the core of the distribution, the truncation is not important for the determination of γ_2.

7.5 1D Model details

In this section we will discuss the features specific to the model with 1D evaporation, which we have used to analyze and optimize our experiments.

7.5.1 1D Thermodynamics

In the case of 1D evaporation, the phase-space distribution $f(\mathbf{r}, \mathbf{p})$ is truncated on the basis of the z-energy of the atom, given by $\epsilon_z \equiv U_z(z) + p_z^2/2m$. That is, it has the Boltzmann form Eq. 7.5 in the region of phase space where $\epsilon_z < \epsilon_t$, and is zero elsewhere. In this case the density distribution of atoms in position space, given by $n(\mathbf{r}) = (2\pi\hbar)^{-1}\int d^3p\, f(\mathbf{r}, \mathbf{p})$, is

$$n(\mathbf{r}) = n_0 e^{-U(\mathbf{r})/kT} \mathrm{erf}\sqrt{\frac{\epsilon_t - U_z(z)}{kT}}. \tag{7.17}$$

The error function $\mathrm{erf}\,(x) \equiv 2\,\pi^{-1/2}\int_0^x \exp(-t^2)dt$ may also be written as $P(1/2, x^2)$, where P is the incomplete gamma function [35]. This density distribution is used in the calculation of the optical spectrum of the trapped gas in our experiments.

For a trap potential which is separable into a transverse and longitudinal part, the effective volume V_e can be written as the product of an effective area A_e (transverse), given by

$$A_e = \int_{-\infty}^{\infty}\int_{-\infty}^{\infty} dx\, dy\, e^{-U_\perp(x,y)/kT} \tag{7.18}$$

and an effective length L_e (longitudinal), given by

$$L_e = \int_{z_1}^{z_2} dz\, e^{-U_z(z)/kT} \mathrm{erf}\sqrt{\frac{\epsilon_t - U_z(z)}{kT}}, \tag{7.19}$$

where z_1 and z_2 are the turning points – the two solutions for z of the equation $\epsilon_t = U_z(z)$. When the transverse confinement is harmonic, we have $A_e = 2\pi kT/m\omega_\perp^2$. For the case of a potential of the form of Eq. 7.3 the effective area is given by

$$A_e = 4\lambda_x\lambda_y\Gamma(\delta_x+1)\Gamma(\delta_y+1)(kT)^{\delta_x+\delta_y} \tag{7.20}$$

and the effective length is given by

$$L_e = 2\lambda_z\Gamma(\delta_z+1)P(\delta_z+1/2,\eta)(kT)^{\delta_z}. \tag{7.21}$$

The average energy of a trapped atom, E/N, given by Eq. 7.6 is determined by T and γ. In the case of a separable potential we can write $\gamma = \gamma_\perp + \gamma_z$, with $\gamma_\perp = (T/A_e)\partial A_e/\partial T$ and $\gamma_z = (T/L_e)\partial L_e/\partial T$. For harmonic transverse confinement $\gamma_\perp = 1$. For power-law potentials of the form given by Eq. 7.3 we have $\gamma_\perp = \delta_x + \delta_y$ and

$$\gamma_z = -\frac{1}{2} + a\frac{P_{a+1}}{P_a} \tag{7.22}$$

with $a = \delta_z + 1/2$ and the abbreviation $P_a \equiv P(a,\eta)$ for the incomplete gamma function evaluated at the dimensionless trap depth η [36]. The effective exponent γ_z always lies between $-\frac{1}{2}$ (for $\eta = 0$) and δ_z (for $\eta = \infty$). For general $U_z(z)$, we evaluate γ_z by numerical integration along the trap axis.

For a general power-law potential Eq. 7.3 the specific heat (at constant θ and N) is given by

$$C = Nk\left\{1 + \delta_x + \delta_y + a\frac{P_{a+1}}{P_a}\left[(a+1)\frac{P_{a+2}}{P_{a+1}} - a\frac{P_{a+1}}{P_a}\right]\right\}. \tag{7.23}$$

In our modeling we use expressions appropriate to a harmonic transverse potential $U_\perp$ and evaluate longitudinal quantities like L_e and γ_z by numerical integration. The derivative $(\partial\gamma/\partial T)_\theta$ needed for the specific heat is found by numerical differentiation of γ.

7.5.2 1D Evaporation rate

Evaporation contributes to particle and energy loss according to Eqs. 7.13 and 7.14. Here we employ kinetic theory to calculate the effective volumes V_{ev} and W_{ev} for the case of 1D

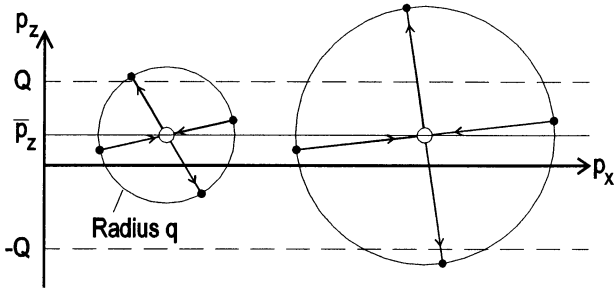

Figure 7.7: Collision spheres for calculation of 1D evaporative cooling, projected onto the x-z plane. Atoms are trapped if their z-momentum lies between $-Q$ and Q. The sphere radius is the relative momentum q. Left: $Q - \bar{p}_z < q < Q + \bar{p}_z$, only one atom can evaporate. Right: $q > Q + \bar{p}_z$, one or both atoms can evaporate.

evaporation. The volume $V_{\rm ev}$ is found by considering all pair collisions which occur per unit time in a gas described by the z-truncated Boltzmann distribution, summing all atoms which are promoted to longitudinal energy $\epsilon_z > \epsilon_t$. The calculation of the "excess energy" volume $W_{\rm ev}$ is analogous, but the total energy of the escaping atoms is summed.

Consider a collision, at position $\mathbf{r}$, of an atom of momentum $\mathbf{p}_1$ with an atom of momentum $\mathbf{p}_2$. To simplify matters we introduce the average momentum $\bar{\mathbf{p}} = (\mathbf{p}_1 + \mathbf{p}_2)/2$ and the relative momentum $\mathbf{q} = (\mathbf{p}_1 - \mathbf{p}_2)/2$. Collisions conserve $\bar{\mathbf{p}}$ and reorient $\mathbf{q}$ (according to an isotropic distribution for s-wave scattering). The number of collisions in volume d^3r at $\mathbf{r}$ during time dt involving a pair of atoms with average momentum in volume $d^3\bar{p}$ at $\bar{\mathbf{p}}$ and relative momentum in volume d^3q at $\mathbf{q}$ is equal to $\Gamma(\mathbf{r}, \bar{\mathbf{p}}, \mathbf{q}) d^3r\, d^3\bar{p}\, d^3q\, dt$, where

$$\Gamma = \frac{8\sigma}{(2\pi\hbar)^6} \left|\frac{\mathbf{q}}{m}\right| f(\mathbf{r}, \bar{\mathbf{p}} + \mathbf{q}) f(\mathbf{r}, \bar{\mathbf{p}} - \mathbf{q}). \tag{7.24}$$

The atoms are treated as distinguishable – to sum all collisions we integrate over all of the six dimensional $(\bar{\mathbf{p}}, \mathbf{q})$ space.

Figure 7.7 shows the relevant collision geometry in momentum space. For a given axial position in the trap, z, an atom will escape if it acquires a z-momentum whose magnitude exceeds the local escape momentum $Q(z)$ given by $Q^2/2m = \epsilon_t - U_z(z)$. The relevant quantities are $\bar{p}_z$ (the z component of the average momentum, conserved in collision), q (the magnitude of the relative momentum, also conserved), q_z (the z component of the relative momentum before collision), and q'_z (the z component of the relative momentum after collision). By symmetry we need only consider $\bar{p}_z, q_z, q'_z > 0$. Because the distribution of relative momentum after collision is isotropic, q'_z is distributed uniformly between 0 and q. Depending on the momenta involved, one or two atoms can escape in a collision (in contrast to 3D evaporation where only one atom can be lost per collision). The left sphere in Fig. 7.7, where $Q - \bar{p}_z < q < Q + \bar{p}_z$ depicts the

first situation where only one atom can be lost from the trap. The second situation is depicted by the right sphere in Fig. 7.7, where $q > Q + \bar{p}_z$ and two atoms can be lost.

The rate at which atoms are lost from the trap is the integral, over position and average and relative momenta, of the product of the collision kernel Γ given by Eq. 7.24 and the mean number of atoms leaving the trap per collision. For the left sphere in Fig. 7.7 ($q < Q(z) + \bar{p}_z$) the mean number is just

$$\int_{Q(z)-\bar{p}_z}^{q} \frac{1}{q}\, dq'_z. \tag{7.25}$$

For the right sphere ($q > Q(z) + \bar{p}_z$) two contributions should be added, yielding the mean number

$$\int_{Q(z)-\bar{p}_z}^{Q(z)+\bar{p}_z} \frac{1}{q}\, dq'_z + \int_{Q(z)+\bar{p}_z}^{q} \frac{2}{q}\, dq'_z. \tag{7.26}$$

In addition, we note that the $\int d^3q$ integration over relative momenta before the collision (with $q_z > 0$) can be written as

$$\int d^3q = 2\pi \int_0^{Q(z)-\bar{p}_z} dq_z \int_{Q(z)-\bar{p}_z}^{\infty} q\, dq, \tag{7.27}$$

where the dq_z integration is limited to select those collisions which occur in a truncated distribution. The dq integration should be split further into two parts corresponding to the two situations of Fig. 7.7.

From the above considerations we find the following explicit expression (exact within the 1D truncated Boltzmann approximation) for the rate of change of number of trapped atoms, $\dot{N}_{\rm ev}$, and their energy, $\dot{E}_{\rm ev}$:

$$\begin{aligned}
\begin{pmatrix} \dot{N}_{\rm ev} \\ \dot{E}_{\rm ev} \end{pmatrix} &= \frac{64\pi\sigma n_0^2 \Lambda^6}{(2\pi\hbar)^6 m} \int_{-\infty}^{\infty}\int_{-\infty}^{\infty} dx\, dy\, e^{-2U_\perp/kT} \int_{z_1}^{z_2} dz\, e^{-2U_z/kT} \int_{-\infty}^{\infty}\int_{-\infty}^{\infty} d\bar{p}_x\, d\bar{p}_y\, e^{-(\bar{p}_x^2+\bar{p}_y^2)/mkT} \\
&\quad \int_0^{Q} d\bar{p}_z e^{-\bar{p}_z^2/mkT} \int_0^{Q-\bar{p}_z} dq_z \left\{ \int_{Q-\bar{p}_z}^{Q+\bar{p}_z} dq\, q e^{-q^2/mkT} \int_{Q-\bar{p}_z}^{q} dq'_z \begin{pmatrix} 1 \\ \epsilon_+ \end{pmatrix} \right. \\
&\quad + \left. \int_{Q+\bar{p}_z}^{\infty} dq\, q e^{-q^2/mkT} \left[\int_{Q-\bar{p}_z}^{Q+\bar{p}_z} dq'_z \begin{pmatrix} 1 \\ \epsilon_+ \end{pmatrix} + \int_{Q+\bar{p}_z}^{q} dq'_z \begin{pmatrix} 2 \\ \epsilon_+ + \epsilon_- \end{pmatrix} \right] \right\},
\end{aligned} \tag{7.28}$$

where z_1 and z_2 are the two solutions for z of the equation $\epsilon_t = U_z(z)$. The energy of the atom (after collision) on the upper (+) or lower (−) hemisphere in Fig. 7.7 can be taken as $\epsilon_\pm = U_\perp + U_z + (\bar{p}^2 + q^2 \pm 2\bar{p}_z q'_z)/2m$. Only the $\bar{p}_z q'_z$ cross term need appear in the kinetic energy because $\bar{p}_x q'_x$ and $\bar{p}_y q'_y$ will integrate to zero. The prefactor in Eq. 7.28 comprises the factors appearing in Eq. 7.5 and 7.24, a factor of 4 due to the restriction to positive q_z and $\bar{p}_z$, and a factor 2π from the integral of azimuthal directions of $\mathbf{q}$ before collision.

In the calculation of $\dot{N}_{\rm ev}$ the integration over transverse average momentum may be done immediately. The integration over the transverse position contributes to the prefactor of the

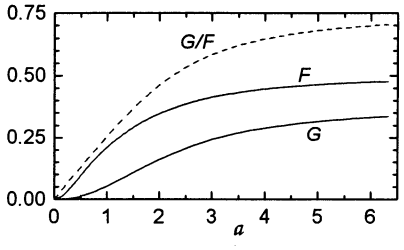

Figure 7.8: Functions F and G used in calculation of 1D evaporation rate from an arbitrary trap. In the limit $a \to \infty$, $F \to 1/2$ and $G \to 3/8$. Also shown is the ratio G/F, which lies between 0 and 3/4.

remaining integrals the two-body effective area

$$A_{2e} = \int_{-\infty}^{\infty}\int_{-\infty}^{\infty} dx\, dy\, e^{-2U_\perp/kT} \tag{7.29}$$

Similarly, in the integration for $\dot{E}_{\rm ev}$ one can extract that part of the energy of an atom which involves transverse coordinates. The transverse energy associated with colliding (hence, including evaporating) atoms is found to be $(5/4+\gamma_{2\perp})kT$, with $\gamma_{2\perp} = (T/2A_{2e})\partial A_{2e}/\partial T$. Since the transverse distribution is not truncated, we may use $A_{2e}(T) = A_e(T/2)$ and $\gamma_{2\perp}(T) = \gamma_\perp(T/2)/2$. With a harmonic potential for the x-y motion, $A_{2e}(T) = \pi kT/m\omega_\perp^2$ and $\gamma_{2\perp} = 1/2$.

After further manipulations, we obtain the effective volumes for 1D evaporation from an arbitrary separable trap as follows:

$$V_{\rm ev} = A_{2e}\int_{z_1}^{z_2} dz\, e^{\kappa-\eta} F(\sqrt{2\kappa}) \tag{7.30}$$

$$W_{\rm ev} = \left(\frac{5}{4}+\gamma_{2\perp}\right) V_{\rm ev} + A_{2e}\int_{z_1}^{z_2} dz\, e^{\kappa-\eta} G(\sqrt{2\kappa}) \tag{7.31}$$

where the local trap depth parameter is given by $\kappa(z) \equiv [\epsilon_t - U_z(z)]/kT$ and the functions F and G are given by

$$F(a) = \int_0^a dx\, e^{a^2/2-x^2}(a-x)\frac{\mathrm{erfc}(a-x)+\mathrm{erfc}(a+x)}{\sqrt{2}} \tag{7.32}$$

$$G(a) = \int_0^a dx\, e^{a^2/2-x^2}(a-x)\left[\frac{e^{-(a-x)^2}(a+x)+e^{-(a+x)^2}(a-x)}{2\sqrt{(2\pi)}}+\left(\frac{x^2-a^2}{2}\right)\frac{\mathrm{erfc}(a-x)+\mathrm{erfc}(a+x)}{\sqrt{2}}\right] \tag{7.33}$$

with $\mathrm{erfc}(x) = 1 - \mathrm{erf}(x)$. The argument a is the local escape momentum Q in units of the one-dimensional r.m.s. thermal momentum $\sqrt{mkT}$. Eqs. 7.30 and 7.31 are consistent with the approximate expressions given for a particular trap shape in Ref. 10. The functions F and G are plotted in Fig. 7.8. For efficient calculations approximations of F and G are given in [37].

7.5.3 1D Spilling and work

To find the rate at which atoms are spilled from the trap as the potential is varied, we count the atoms in the quantum states of z-motion which are lost from the trap. First, we need to count the states. The number of states of one-dimensional motion bound in the potential $U_z(z)$, which we denote $\mathcal{N}_z$, is given by the quasiclassical expression

$$\mathcal{N}_z = \frac{2(2m)^{1/2}}{2\pi\hbar} \int_{z_1}^{z_2} \sqrt{\epsilon_t - U_z(z)}\, dz. \tag{7.34}$$

For example, if $U_z(z)$ is harmonic, we have the simple result $\mathcal{N}_z = \epsilon_t/\hbar\omega_z$. The number of quantum states in the trap is a function only of the trap shape, parametrized by the set of independent coordinates θ.

Second, we need to count the atoms associated with each state. Eq. 7.4 for the number of trapped atoms can be written in terms of an integral involving the density of states (see Ref. 11), which, for a separable potential, factors into a transverse and a longitudinal part:

$$N = \int_0^\infty d\epsilon_\perp \rho_\perp(\epsilon_\perp) \int_0^{\epsilon_t} d\epsilon_z \rho_z(\epsilon_z)\, n_0 \Lambda^3 e^{-(\epsilon_\perp + \epsilon_z)/kT}. \tag{7.35}$$

The transverse integral can be expressed in terms of the effective area A_e, giving

$$N = \int_0^{\epsilon_t} d\epsilon_z \rho_z(\epsilon_z) A_e n_0 \Lambda e^{-\epsilon_z/kT} \tag{7.36}$$

We see that the number of atoms associated with each z-state of energy ϵ_z is $A_e n_0 \Lambda e^{-\epsilon_z/kT}$.

It is now straightforward to see that the rate of change of the number of trapped atoms due to trap changes is given by

$$\dot{N}_\theta = A_e n_0 \Lambda e^{-\eta} \dot{\mathcal{N}}_z, \tag{7.37}$$

i.e., the product of the number of atoms associated with each z-state at the trap edge and the rate of change of the number of these states [38].

We require that $\dot{\mathcal{N}}_z < 0$, otherwise empty states are introduced at the trap edge and the picture of a truncated Boltzmann distribution would be destroyed. The model hence can only describe situations in which the trap becomes shallower in the sense of supporting fewer bound states. This criterion is easily met when dealing with forced evaporation.

The rate of change of energy due to trap changes, $\dot{E}_\theta$, is calculated using the entropy argument discussed in section 7.4. The entropy carried away by spilled atoms is found by considering the case of pure spilling (the trap edge is lowered while the potential shape is held constant). In this case, the rate of change of energy is given by

$$\dot{E}_\theta = (1 + \gamma_\perp + \eta)\, kT \dot{N}_\theta \tag{7.38}$$

because a particle barely escaping over the z-barrier will on average take away kT of transverse kinetic energy, $\gamma_\perp kT$ of transverse potential energy and exactly ϵ_t of z-energy. We have verified

explicitly, for a general power-law potential and for a IQ potential, that Eq. 7.38 follows from taking the derivative of $(3/2+\gamma)NkT$ with respect to ϵ_t. Eq. 7.6 and 7.7 allow us to write the entropy as $S = E/T + Nk(1 - \ln n_0\Lambda^3)$. Differentiating this expression with respect to time, bearing in mind that for pure spilling both T and $n_0\Lambda^3$ are constant, we immediately find that the entropy removed by an atom spilled from a 1D truncated distribution is

$$s_\theta = k\left(2 + \gamma_\perp + \eta - \ln n_0\Lambda^3\right). \tag{7.39}$$

Because s_θ is independent of what manner of trap change caused the spilling, we can use it for changes of the trap other than pure spilling. Eq. 7.16 gives the following expression for the rate of change of the energy of the trapped gas due to more general changes of the trapping potential:

$$\dot{E}_\theta = (2 + \gamma_\perp + \eta)\, kT\dot{N}_\theta - \frac{NkT}{V_e}\left(\frac{\partial V_e}{\partial \theta}\right)_T \dot{\theta}. \tag{7.40}$$

Eq. 7.37 and 7.40 are used in Eqs. 7.11 and 7.12 for the evolution of N and T for the evaporating gas in the 1D model.

7.6 3D Model details

In this section we consider 3D (ergodic) evaporation. As in the 1D case, we choose the Ioffe-Quadrupole (IQ) trap as an example to evaluate quantities analytically.

7.6.1 3D Thermodynamics

The phase-space distribution function $f(\mathbf{r},\mathbf{p})$ given by the Boltzmann form (Eq. 7.5) is now to be truncated on the basis of the total energy of the atom, as in Ref. 11. This leads to a real-space density distribution

$$n(\mathbf{r}) = n_0 e^{-U(\mathbf{r})/kT} P\left(\frac{3}{2}, \frac{\epsilon_t - U(\mathbf{r})}{kT}\right). \tag{7.41}$$

The reference density n_0 is related to the number of atoms N by $n_0 = N/V_e$, where the effective volume V_e for a IQ trap is given by

$$V_e = 6A_{IQ}\Lambda^3(kT)^4\left(P_4 + \frac{2}{3}\xi\eta P_3\right) \tag{7.42}$$

with $P_a \equiv P(a,\eta)$ [36]. Furthermore, $\xi \equiv U_0/\epsilon_t$, and the trap dependent constant $A_{IQ} = (2m\pi^2)^{3/2}/[2(2\pi\hbar)^3\alpha^2\sqrt{\beta}]$.

The parameter γ is obtained from Eq. 7.6 and the known expression for the total energy of an energy-truncated gas in a IQ trap [11], giving

$$\gamma = -\frac{3}{2} + \frac{12P_5 + 6P_4\xi\eta}{3P_4 + 2P_3\xi\eta}. \tag{7.43}$$

The heat capacity C (at constant trap depth and number of atoms) is calculated straightforwardly by differentiating the total energy. We find that

$$C = 12Nk\frac{15P_4P_6 - 12P_5^2 + (10P_3P_6 - 6P_4P_5)\xi\eta + (4P_3P_5 - 3P_4^2)\xi^2\eta^2}{(3P_4 + 2\xi\eta P_3)^2} \tag{7.44}$$

7.6.2 3D evaporation rate

The rate of change of the number of atoms and the energy in the trapped gas, $\dot{N}_{\rm ev}$ and $\dot{E}_{\rm ev}$, are given by Eqs. 7.13 and 7.14, with effective volumes for evaporation $V_{\rm ev}$ and $W_{\rm ev}$ calculated for three-dimensional truncation. For a IQ trap expressions for these volumes were first derived by Luiten *et al.* [11, 33].

Integral expressions for the volumes $V_{\rm ev}$ and $W_{\rm ev}$ for 3D evaporation from an arbitrary trap, analogous to Eqs. 7.30 and Eq. 7.31, can be found in Ref. 11.

7.6.3 3D Spilling and work

To obtain $\dot{N}_\theta$ in the case of three-dimensional truncation, we calculate the number of quantum states in the trap, $\mathcal{N}$, by integrating the density of states $\rho(\epsilon)$ from 0 to ϵ_t. For a IQ trap, for which $\rho(\epsilon) = A_{IQ}(\epsilon^3 + 2U_0\epsilon^2)$, this leads to

$$\mathcal{N} = A_{IQ}\left(\frac{1}{4}\epsilon_t^4 + \frac{2}{3}U_0\epsilon_t^3\right). \tag{7.45}$$

The rate of change of the number of trapped atoms due to spilling is then given by

$$\dot{N}_\theta = n_0\Lambda^3 e^{-\eta}\dot{\mathcal{N}}, \tag{7.46}$$

i.e., the product of the occupation number of states at the trap edge and the rate of change of the number of these states.

In the case of 3D truncation, to prevent the introduction of empty trap states it is not sufficient to assume that $\mathcal{N}$ decreases in time. Anisotropic variations of the trap can lead to introduction of empty states, spoiling the picture of a truncated Boltzmann distribution, even while decreasing the total number of states. However, during forced evaporation the trap depth is typically so strongly reduced that no significant introduction of empty states occurs due to variation of the shape of the trapping potential. In other words, states are lost from the trap in all directions. For a harmonic trap this concept can be made precise: empty states are not introduced if $\epsilon_t/\hbar\omega_x$, $\epsilon_t/\hbar\omega_y$, and $\epsilon_t/\hbar\omega_z$ are all decreasing functions of time.

The rate of change of energy of the trapped gas due to trap changes, accounting both for the spilling of atoms and for the work done by the trapped atoms as the trap is deformed, is determined, as in the 1D case, using the entropy argument introduced in section 7.4. To find the entropy carried away by the spilled atoms we consider "pure spilling", where the truncation

edge ϵ_t is reduced but the shape of the trap remains the same. In this case $\dot{E}_\theta = \epsilon_t \dot{N}_\theta$ and, because temperature T and (reference) density n_0 do not change, it is easily found that the entropy removed by each atom spilled over the trap edge is given by

$$s_\theta = k\left(1 + \eta - \ln n_0 \Lambda^3\right). \tag{7.47}$$

Eq. 7.16 can now be used to write the rate of change of energy due to more general trap changes as

$$\dot{E}_\theta = (1+\eta)\, kT\dot{N}_\theta - \frac{NkT}{V_e}\left(\frac{\partial V_e}{\partial \theta}\right)_T \dot{\theta}. \tag{7.48}$$

Eq. 7.46 and 7.48 are used in Eq. 7.11 and Eq. 7.12 for the evolution of N and T for the evaporating gas in the 3D model.

7.7 Conclusion

Our data show clearly that in an important class of trap geometries evaporation is bottlenecked by the non-ergodic motion of the trapped atoms when the selection of escaping atoms is based on the energy in one direction only (1D evaporation), as predicted by Surkov *et al.*[10]. This is in contrast to the situation at high temperatures, which was found to be described by a 3D evaporation picture [6].

We have derived an evaporation model based on the truncated Boltzmann approximation which can describe either 3D or 1D evaporation. For 1D evaporation we have calculated the evaporation rate from kinetic theory. The model improves on previously published models by describing processes such as atom spilling, adiabatic compression, and even adiabatic changes of the phase-space density. It is sufficiently fast to calculate that it can be used to optimize ramp trajectories for forced evaporation. For common traps analytic expressions are given for important quantities.

The existing experimental apparatus in Amsterdam is apparently not suited to attain Bose-Einstein condensation of atomic hydrogen. Using a ramp optimized using the model based on a 1D truncation we reached a phase-space density $n_0\Lambda^3 \approx 0.05$. The key reason for this shortfall is the low dimensionality of evaporation in accessible field geometries, exacerbated by the poor ratio of elastic to inelastic collisions arising from the low scattering length of H. Our model predicts that BEC is attainable provided one can arrange sustained 3D evaporation. The trapping geometry employed at MIT [39] is different from ours because it has a long flat bottom with a low B_0, which is favorable for mixing degrees of freedom of translational motion. However, it is probable that nonergodicity of motion will become important in this trap as the conditions for BEC are approached.

A promising idea to avoid the 1D evaporation bottleneck is to use microwave-induced (rf-induced) evaporation [7]. This would also allow evaporative cooling of the trapped gas without

varying the currents in the superconducting magnets. For atomic hydrogen, it appears feasible to use the $F = m_F = 1$ to $F = m_F = 0$ hyperfine transition, for example, to eject atoms from the trap. For low B_0, the transition frequency is the 1.4 GHz hyperfine splitting. To obtain efficient evaporation the rf need only pump energetic atoms to the untrapped hyperfine state on a timescale shorter than the mean time between collisions. Considerations such as those presented in Ref. 5 imply that a loop-gap resonator with a Q of 10^3 and a rf-field volume of order 1 cm^3 would yield efficient evaporation with a power dissipation of 1 μW, compatible with the cryo-environment. Another way to arrange 3D evaporation is to bring the high energy wings of the gas in contact with a material, pumping, surface.

Acknowledgements

We thank G.V. Shlyapnikov for interesting discussions. This work is part of a research program of the Stichting voor Fundamenteel Onderzoek der Materie (FOM), which is a subsidiary of the Nederlandse Organisatie voor Wetenschappelijk Onderzoek (NWO). M.W. acknowledges a TMR grant by the European Commission. The research of M.W.R. is supported by the Royal Dutch Academy of Arts and Sciences (KNAW).

Bibliography

[1] H.F. Hess, Phys. Rev. B **34**, 3476 (1986); C. Lovelace, C. Mehanian, T.J. Tommila, and D.M. Lee, Nature **318**, 30 (1985).

[2] H.F. Hess, G.P. Kochanski, J.M. Doyle, N. Masuhara, D. Kleppner, and T.J. Greytak, Phys. Rev. Lett. **59**, 672 (1987).

[3] N. Masuhara, J.M. Doyle, J.C. Sandberg, D. Kleppner, and T.J. Greytak, Phys. Rev. Lett. **61**, 935 (1988).

[4] M.H. Anderson, J.R. Ensher, M.R. Matthews, C.E. Weiman, and E.A. Cornell, Science **269**, 198 (1995).

[5] W. Ketterle and N.J. van Druten in *Advances in Atomic, Molecular and Optical Physics*, edited by B. Bederson and H. Walther (Academic Press, San Diego, 1996), Vol. 37, p. 181-236; and references therein.

[6] O.J. Luiten, H.G.C. Werij, I.D. Setija, M.W. Reynolds, T.W. Hijmans, and J.T.M. Walraven, Phys. Rev. Lett. **70**, 544 (1993).

[7] D.E. Pritchard, K. Helmerson, and A.G. Martin, in *Atomic Physics 11*, edited by S. Haroche, J.C. Gay, and G. Grynberg (World Scientific, Singapore, 1989), p. 179; T.W. Hijmans, O.J. Luiten, I.D. Setija, and J.T.M. Walraven, J. Opt. Soc. Am. B **6**, 2235 (1989).

[8] I.D. Setija, H.G.C. Werij, O.J. Luiten, M.W. Reynolds, T.W. Hijmans, and J.T.M. Walraven, Phys. Rev. Lett. **70**, 2257 (1993).

[9] Making a potential energy surface an absorber does not guarantee ergodic evaporation, since the atoms should reach the surface. A certain complexity of motion is also required. In a Ioffe trap this complexity is provided by the absence of complete axial symmetry.

[10] E.L. Surkov, J.T.M. Walraven, and G.V. Shlyapnikov, Phys. Rev. A **53**, 3403 (1996).

[11] O.J. Luiten, M.W. Reynolds, and J.T.M. Walraven, Phys. Rev. A **53**, 381 (1996).

[12] J.T.M. Walraven, in *Proceedings of the SUSSP 44 Conference on Quantum Dynamics of Simple Systems*, edited by G.-L. Oppo, S.M. Barnett, E. Riis, and M. Wilkinson (Institute of Physics Publishing, Bristol, 1996), p. 315-352.

[13] A. Lagendijk, I.F. Silvera, and B.J. Verhaar, Phys. Rev. B **33**, 626 (1986); H.T.C. Stoof, J.M.V.A. Koelman, and B.J. Verhaar, Phys. Rev. B **38**, 4688 (1988).

[14] J.M. Doyle, J.C. Sandberg, N. Masuhara, I.A. Yu, D. Kleppner, and T.J. Greytak, J. Opt. Soc. Am. B **6**, 2244 (1989).

[15] P.W.H. Pinkse, A. Mosk, M. Weidemüller, M.W. Reynolds, T.W. Hijmans, and J.T.M. Walraven, Phys. Rev. Lett. **78**, 990 (1997).

[16] T. Bergeman, G. Erez, and H.J. Metcalf, Phys. Rev. A **35**, 1535 (1987).

[17] E.L. Surkov, J.T.M. Walraven, and G.V. Shlyapnikov, Phys. Rev. A **49**, 4778 (1994).

[18] V. Bagnato, D.E. Pritchard, and D. Kleppner, Phys. Rev. A **35**, 4354 (1987).

[19] O.J. Luiten, H.G.C. Werij, I.D. Setija, M.W. Reynolds, T.W. Hijmans, and J.T.M. Walraven, in *Proc. 13th Int. Conf. on Atomic Physics*, edited by H. Walther, T.W. Hänsch, B. Neizert (American Institute of Physics, New York 1993), p. 167.

[20] O.J. Luiten, H.G.C. Werij, M.W. Reynolds, I.D. Setija, T.W. Hijmans, and J.T.M. Walraven, Appl. Phys. B **59**, 311 (1994).

[21] The L/R relaxation time is 1.2 seconds for the coil which determines the trap depth here.

[22] J.M. Doyle, Ph.D. thesis, Massachusetts Institute of Technology (1991), unpublished.

[23] J.M. Doyle, J.C. Sandberg, I.A. Yu, C.L. Cesar, D. Kleppner, and T.J. Greytak, Physica B **194**, 13 (1994).

[24] K.B. Davis, M.-O. Mewes, and W. Ketterle, Appl. Phys. B **60**, 155 (1995).

[25] O.J. Luiten, Ph.D. thesis, University of Amsterdam (1993), unpublished.

[26] K. Berg-Sørensen, Phys. Rev. A **55**, 1281 (1997). Implies that several equations in Ref. 11 are in error. However, the two papers merely use different definitions of ξ. An erratum is to appear in Phys. Rev. A.

[27] H. Wu and C.J. Foot, J. Phys. B **29**, L321 (1996).

[28] H. Wu, E. Arimondo and C.J. Footfoot, Phys. Rev. A **56**, 560 (1997).

[29] G.A. Bird, *Molecular Dynamics and the Direct Simulation of Gas Flows* (Clarendon Press, Oxford, 1994).

[30] *Nota bene*: E/N, the average energy of a trapped atom, is not the chemical potential as unfortunately implied in Ref. 11. The chemical potential is, as usual, given by $\mu = kT\ln(n_0\Lambda^3)$ for a gas far from degeneration.

[31] Davis *et al.* [24] model ergodic evaporative cooling by a series of steps in which the high energy tail of the energy distribution is cut off instantaneously, after which the gas rethermalizes to a full distribution. In our terminology this is a phase-space density conserving truncation of the high energy tail which removes energy and entropy, followed by a rethermalization in which phase-space density is gained even though entropy increases. If we begin with a truncated distribution, instantly set $\epsilon_t \to \infty$, and allow the gas to thermalize, the entropy will of course increase. For a power-law trap, the change of entropy ΔS is given by $\Delta S/Nk = a[1 - P_{a+1}/P_a + \ln(P_{a+1}/P_a)] - \ln P_a$, with $a = 3/2+\delta$ and $P_a \equiv P(a,\eta)$. This entropy change on thermalization is a monotonically decreasing positive function of η.

[32] In the computer simulation employing numerically determined magnetic fields, it is convenient to calculate the partial derivatives of temperature-dependent quantities such as γ with respect to θ using, e.g., $(\partial\gamma/\partial\theta)_T\dot{\theta} = (\gamma' - \gamma)/\Delta t$, where γ' is calculated "in between" time steps, using the trap of time $t + \Delta t$ but the temperature of time t.

[33] $V_{\rm ev} = \Lambda^3\zeta^0_\infty\{\eta - 5 + \xi\eta(2\eta/3 - 8/3) + e^{-\eta}[\eta^4/24 + \eta^3/3 + 3\eta^2/2 + 4\eta + 5 + \xi\eta(\eta^3/9 + 2\eta^2/3 + 2\eta + 8/3)]\}, W_{\rm ev} = \Lambda^3\zeta^0_\infty\{\eta - 6 + \xi\eta(2\eta/3 - 10/3) + e^{-\eta}[\eta^5/120 + \eta^4/12 + \eta^3/2 + 2\eta^2 + 5\eta + 6 + \xi\eta(\eta^4/36 + 2\eta^3/9 + \eta^2 + 8\eta/3 + 10/3)]\}$, with $\zeta^0_\infty \equiv 6A_{IQ}(kT)^4$.

[34] H.T.C. Stoof, J.M.V.A. Koelman, and B.J. Verhaar, Phys. Rev. B **38** , 4688 (1988). Simplified expressions can be found in: R. van Roijen, Ph.D. thesis, University of Amsterdam (1989), unpublished.

[35] *Handbook of Mathematical Functions*, edited by M. Abramowitz and I.A. Stegun (Dover, New York, 1972).

[36] For integer a, $P_a = 1 - e^{-\eta}\sum_{m=0}^{a-1}\eta^m/m!$.

[37] The functions $F(a)$ and $G(a)$ can be approximated by $F(a) \approx 1/(1.946+2.82a^{-1.617})$ and $G(a) \approx 1/(2.707+16.20a^{-2.211})$. The relative deviations of these approximations are less than 1 % in the region $1 < a < 6$ (i.e., for $1/2 < \eta < 18$).

[38] A classical description of spilling is also possible. Consider the action $\oint p_z\,dz$ associated with the z motion of an atom (the integral is over one cycle of z-motion). The maximum action for a given trap is the action for an atom of z-energy equal to ϵ_t. Slowly lowering the depth of the trap, the action of each atom is constant and the rate of spilling is just the rate at which atoms are left behind by the decreasing maximum action.

[39] J.M. Doyle, J.C. Sandberg, I.A. Yu, C.L. Cesar, D. Kleppner, and T.J. Greytak, Phys. Rev. Lett. **67**, 603 (1991).

Samenvatting

Dit proefschrift heeft twee hoofdthema's: door resonantie versterkte twee-fotonspectroscopie aan magnetisch gevangen atomair waterstof (H), en verdampingskoeling van dit atomaire gas. Het achterliggende doel van deze experimenten is het bereiken van hogere fase-ruimtedichtheden (lagere temperaturen en hogere dichtheden) dan tot nu toe mogelijk was in Amsterdam, met als einddoel het bereiken van kwantumontaarding. Om de detectiegrens te verleggen naar lagere temperaturen en kleinere preparaten, is de optische diagnostiek van het koude gas verbeterd, zowel door verbetering van de optische aparatuur, als door de introductie van door resonantie versterkte twee-foton spectroscopie (afgekort "RETS"). Om de hogere fase-ruimtedichtheden te bereiken is de methode van verdampingskoeling geïmplementeerd, bestudeerd en geoptimaliseerd voor onze experimentele situatie.

De in situ diagnostiek van het gas is gebaseerd op het vergelijken van de optische spectra van het gas met berekende spectra. De absorptielijnen in het spectrum zijn verbreed door verschuivingen van de optische resonanties ten gevolge van de thermische beweging van de atomen (Doppler-effect) en ten gevolge van het inhomogene magneetveld waarmee het atomaire gas wordt opgesloten (Zeeman-effect). Rond de 2 mK worden deze verbredingsmechanismen van de zelfde grootte als de 100 MHz natuurlijke lijnbreedte van de $1S - 2P$ overgang (L_α, golflengte 121.57 nm), zodat thermometrie gebaseerd op L_α licht niet meer mogelijk is beneden die temperatuur. RETS overkomt deze intrinsieke beperking van L_α spectroscopie. Het is gebaseerd op de $1S - 3S$ of de $1S - 3D$ twee-fotonovergang, gebruik makend van één foton met een frequentie dicht bij L_α, en één dicht bij Balmer-α (H_α, golflengte 656.47 nm). Door het bijna resonante tussenliggende $2P$ niveau zijn relatief lage lichtintensiteiten voldoende voor deze twee-fotonexcitatie. Met de $3S$ and $3D$ toestanden is een natuurlijke lijnbreedte geassocieerd van 1 MHz, respectievelijk 10 MHz, beide nauw genoeg om de temperatuur te kunnen bepalen aan de hand van de Doppler-verbreding van de optische resonanties tot in het kwantumontaarde regime (ongeveer 100 μK voor dichtheden van $10^{14}\,\mathrm{cm}^{-1}$). Een ander voordeel van RETS is dat de resonante optische dichtheid van het gas naar believen kan worden gevarieerd door het kiezen van een andere verstemming van het licht ten opzichte van het tussenliggende $2P$ niveau.

Om de fase-ruimtedichtheid te verhogen maken we gebruik van verdampingskoeling. In de experimentele situatie wordt dit gedaan door de hete deeltjes uit de val te laten ontsnappen over een magnetische barrière in één richting uit de val. Het blijkt dat deze manier van verdampingskoeling niet zo effectief is als verwacht op basis van "ergodische" ééndeeltjesbeweging, waar met "ergodische beweging" bedoeld wordt dat alle delen van de faseruimte met de zelfde energie met gelijke kans bezocht worden. Bij ergodische ééndeeltjesbeweging zullen alle deeltjes met een energie die de ontsnappingsenergie overschrijdt, de val verlaten. Deze situatie wordt "3-dimensionale (3D) verdamping" genoemd, in tegenstelling tot het geval van "1-dimensionale

(1D) verdamping", waar alleen die deeltjes uit de val ontsnappen waarvan de energie geassocieerd met één van de vrijheidsgraden de ontsnappingsenergie overschrijdt. Het blijkt dat de verdamping in ons experiment consistent is met 1D verdamping.

Het proefschrift begint met een algemene inleiding waarin het onderzoek in een breder perspectief wordt geplaatst en het verband tussen de verschillende hoofdstukken wordt uitgelegd. Daarna wordt in hoofdstuk 2 ingegaan op de grondbeginselen van het magnetisch vangen van atomair H. Aan de orde komen het laden van de val, veldgeometrieën voor het vangen van het gas en de basis van de thermodynamische beschrijving van het gas in de magnetische val.

In hoofdstuk 3 wordt de apparatuur beschreven die gebruikt is voor de experimenten beschreven in dit proefschrift. Hier wordt beschreven hoe de kwaliteit van de L_α bundel, de bundelafmetingen en de optische toegang tot de cel zijn verbeterd. De opstelling voor de opwekking, stabilisatie, controle en detectie van het L_α en H_α licht en de cryogene opstelling worden besproken.

In hoofdstuk 4 komen vervalsprocessen aan de orde, zowel theoretisch als aan de hand van experimenten, die leiden tot de afname van het aantal gevangen deeltjes. Een deel van dit hoofdstuk is gewijd aan een verliesproces (Majorana-verlies) waarbij de richting van het magneetveld snel verandert ten opzichte van het magnetische moment van een atoom. Dit is een proces dan normaal gesproken goed onderdrukt kan worden door het magneetveld overal voldoende van nul te laten verschillen, maar in sommige experimenten kan het nuttig zijn het veld in het centrum van de val laag te kiezen. De levensduur van het gas wordt in enkele situaties afgeschat en vergeleken met experimentele resulaten.

Hoofdstuk 5 is gewijd aan de beschrijving van L_α spectroscopie en RETS. Een eerste vereiste hiervoor is kennis van de atomaire niveaus in de aanwezigheid van een extern magnetisch veld. De verschuiving van de optische overgangsfrequenties ten gevolge van het sterke H_α licht wordt besproken en geïllustreerd met de waarneming van een "Autler-Townes-doublet" in het absorptiespectrum van magnetisch gevangen H. Vervolgens wordt de vorm van de twee-foton lijnen besproken en de verbredingsprocessen die dit beïnvloeden, waarna de basis van de spectrum berekening wordt uitgelegd. Een serie RETS spectra genomen tijdens een verdampingskoelmeting wordt geanalyseerd.

In hoofdstuk 6 wordt uitgelegd hoe de fase-ruimtedichtheid van een gevangen Bose-gas adiabatisch en reversibel veranderd kan worden door het veranderen van de vorm van de magnetische potentiaal. Dit wordt gedemonstreerd met een experiment.

Tenslotte wordt in hoofdstuk 7 een model gepresenteerd dat de evolutie van een verdampend gas beschrijft gebaseerd op de benadering dat het gas kan worden beschreven door een afgekapte Bolzmann-verdeling, voor zowel 1D als 3D verdamping, en deze worden vergeleken met experimenten.

Nawoord

Dit proefschrift heeft alleen maar tot stand kunnen komen dankzij de hulp en steun die ik kreeg van vele collega's, vrienden en kennissen. In de eerste plaats wil ik mijn promotor, Jook Walraven, noemen. Ik ben hem zeer dankbaar voor alle steun en mogelijkheden die hij mij geboden heeft. Jook, ik heb ontzettend veel van je geleerd en wens je heel veel succes toe als directeur van het AMOLF. Naast de dagelijkse begeleiding zorgde Tom Hijmans jarenlang voor een niet aflatende stroom "ideetjes", opgedist met een ongeëvenaard humoristisch sausje en was zo een grote inspiratiebron. Ik heb ook grote bewondering voor Meritt Reynolds, die, altijd bescheiden, de ene na de andere essentiële bijdrage heeft geleverd aan zowat ieder resultaat van de waterstofgroep. Henri Werij wijdde mij in in de geheimen van de lasers. I thank Claus Zimmermann for his contributions to the two-photon project. Matthias Weidemüller vond feilloos de juiste toon om elk resultaat te kunnen presenteren en ik waardeer het aanstekelijke plezier waarmee hij hier werkte enorm. Ik had me geen betere collega-promovendus kunnen wensen dan Allard Mosk. Zijn aanwezigheid veraangenaamde de lange meetsessies die mede succesvol waren dankzij zijn kennis en inzicht. Ik zal bijvoorbeeld nooit vergeten hoe hij, ondanks het aanvankelijke ongeloof van de hele groep, ons één voor één heeft weten te overtuigen dat fase-ruimtedichtheid niet zo behouden is als iedereen dacht. Jom Luiten en Irwan Setija lieten een opstelling in een zeer goede staat achter, ruim voorzien van nuttige en minder nuttige documentatie ("Pas op, misschien verontreinigd met lucht!" en "Ik ben een hapje eten.").

Nico Jonker leste onze onverzadigbare dorst aan cryogene vloeistoffen. Afgezien van het lessen van die andere dorst nam Joost Overtoom vele technische klussen voor zijn rekening. Bert Zwart verhielp met veel enthousiasme heel wat vacuümtechnische problemen. Ik denk ook met veel genoegen terug aan de uren die ik samen met Otto Höpfner heb doorgebracht als er voor de bouw van iets nieuws weer eens gebrainstormd moest worden. Als er iemand is waarop ik de woorden "vakmanschap is meesterschap" helemaal van toepassing vind, dan ben jij dat, Otto. Veel te danken heb ik ook aan Michiel Groeneveld, die de delicate VUV optiek in goede staat wist te polijsten. Dankzij Ton Jongeneelen en Edwin Baaij konden we onze lasers stabiel aansturen. Naast het verrichten van allerlei hand- en spandiensten ontfermde Bert Holsbeeke zich over de lasers. Voor hun technische ondersteuning wil ik verder nog bedanken: Matthijs Bakker, Jan Dekker, Johan van de Ridder, Huybert van de Stadt, Ton Riemersma, Hugo Schlatter, Flip de Leeuw, Theo van Lieshout, Piet Sannes en Alof Wassink. Jaap Berkhout, Paul Langemeijer, Thijs Post en Henk Pot stonden mij bij in mijn strubbelingen met hard- en software. Administratieve zaken waren altijd in goede handen bij Ineke Baay, Jenny Batson en Friedje Witzenhausen.

I always enjoyed the discussions with and the company and the stories of Gora Shlyapnikov and Peter Fedichev. Kai Dieckmann heeft menige mensahap opgevrolijkt met zijn aanwezigheid.

Kai and Igor, I wish you both good luck with Bose-condensing rubidium atoms. Studenten Tycho Sonnemans, Susan Krieger en Giannis Zacharakis en Catherine Garrec wil ik bedanken voor hun bijdragen. Giannis, I think I owe it to you and your Greek friends that I begin to like olives. Catherine, dat ik deze woorden in het Nederlands schrijf is een uiting van mijn bewondering voor de snelheid waarmee je hier o.a. het Nederlands oppikte.

Met Bas, Ben, Cor, Dirk, Frederik, Klaas en Robert had ik vele leerzame discussies. Ad Lagendijk en zijn groep "Spectroscopie van de verdichte materie" zorgden voor een stimulerende omgeving, in welk verband speciaal de werkbesprekingen op vrijdagmiddag moeten worden genoemd. Carlos, Dirk, Frank, Gerard, Gijs, Jaime, Johannes, Judith, Mark, Mark (die mij een aantal keer heeft laten genieten van schitterende muziek), Mischa, Pedro, Peter (waarmee ik met veel plezier een kamer heb gedeeld), Rik, Rudolf, Willem (die mij letterlijk naar grote hoogtes leidde), en Wim, bedankt voor de aangename tijd, zowel binnen als buiten het lab.

Allen die voor de broodnodige afleiding zorgden buiten het werk wil ik hier bedanken, maar toch in het bijzonder die vrienden waarmee ik de vreugdevolle momenten kon vieren en waarbij ik aan kon kloppen als het eens iets minder ging. Tenslotte wil ik mijn ouders en mijn broers bedanken voor hun niet aflatende steun en voor de warme inhoud die ze aan het begrip "thuis" hebben gegeven.